

INAUGURAL-DISSERTATION

Zur Erlangung der Doktorwürde
der Naturwissenschaftlich-Mathematischen Gesamtfakultät
der
Ruprecht-Karls-Universität
Heidelberg

vorgelegt von
Dipl. –Chem. Fanny Caroline Liu
aus Yogyakarta/Indonesien

Tag der mündlichen Prüfung: 11. Februar 2011

**Entwicklung LSPR-basierter optischer Biosensoren zum
markierungsfreien Nachweis biomolekularer Wechselwirkungen in
hochintegrierten Peptidbibliotheken**

Gutachter:

Prof. Dr. rer. nat. Reiner Dahint

Prof. Dr. rer. nat. Joachim Spatz

**Development of LSPR-based Optical Biosensors
for the Label-Free Detection of Biomolecular Interactions
in High-Density Peptide Arrays**

Referees:

Prof. Dr. rer. nat. Reiner Dahint

Prof. Dr. rer. nat. Joachim Spatz

CONTENTS

CONTENTS	1
ABSTRACT	5
LIST OF PUBLICATIONS	8
ABBREVIATIONS	9
1. INTRODUCTION	11
2. THEORY	14
2.1. <i>In situ</i> peptide synthesis	14
2.1.1 Photolithographic synthesis	15
2.1.2 SPOT synthesis	16
2.1.3. Particle-based synthesis	16
2.2. Surface plasmon resonance as a tool in molecular biosensing	19
2.2.1. Surface plasmon resonance.....	19
2.2.1.1. Theory of propagating surface plasmon	19
2.2.1.2. Theory of localized surface plasmon.....	21
2.2.2. Surface plasmons in optical sensing	21
2.2.2.1. Excitation of surface plasmons.....	21
2.2.2.2. Quantitative interpretation of SPR response.....	23
2.2.2.3. Methods of measurements	25
2.2.2.4. Application of surface plasmons in biosensing	26
2.3. Protein-resistant films	26
2.3.1. Poly(ethylene glycol) (PEG).....	27
2.3.2. Immobilizing PEG onto surfaces	29
2.3.2.1. Chemisorption	29
2.3.2.2. Covalent grafting.....	29
2.3.2.3. Physisorption	30
2.3.2.4. Atom Transfer Radical Polymerization	31
2.3.2. Zwitterionic polymers.....	33
2.4. Surface analysis methods	34
2.4.1. Excitation and detection of surface plasmons	34
2.4.2. X-ray Photoelectron Spectroscopy (XPS).....	35
2.4.3. Scanning Electron Microscopy (SEM)	37
2.4.3.1. Basic Principle.....	38
2.4.3.2. Sample-Beam Interactions.....	38
3. MATERIALS AND METHODS	40
3.1. Fabrication of LSPR biosensors based on optical responsive materials	40

3.1.1. Materials	40
3.1.2. Deposition of the bottom gold layer	40
3.1.3. Deposition of the dielectric layer	41
3.1.3.1. By simple incubation	41
3.1.3.2. By spin coating	41
3.1.3.3. By floating	42
3.1.3.4. By thermal evaporation	43
3.1.4. Deposition of the upper gold layer	43
3.1.4.1. By metallization	43
3.1.4.2. By Physical Vapor Deposition	43
3.2. Synthesis of protein-resistant coatings on the LSPR biosensor via Atom Transfer Radical Polymerization (ATRP)	44
3.2.1. Materials	44
3.2.2. Direct synthesis of a protein-resistant coating on the LSPR biosensor	45
3.2.2.1. Direct attachment of ATRP initiators on the LSPR biosensor	45
3.2.2.2. Synthesis of a graft polymer film on the LSPR biosensor via ATRP	45
3.2.3. Indirect synthesis of a protein-resistant coating on the LSPR biosensor	45
3.2.3.1. Synthesis of a silica gel on the LSPR biosensor	45
3.2.3.2. Synthesis of a graft polymer film on the silica gel-coated LSPR biosensor	45
3.2.3.2.1. Attachment of ATRP initiators on the silica-gel coated LSPR biosensor	45
3.2.3.2.2. Synthesis of a graft polymer film on the silica-gel coated LSPR biosensor via ATRP	46
3.2.3.2.3. Functionalization of the protein-resistant coating on the LSPR biosensor	47
3.3. Preparation of biomolecule arrays onto the protein resistant LSPR biosensor	48
3.3.1. Materials	48
3.3.2. Fabrication of antibody arrays on the LSPR biosensor by the spotting technique	48
3.3.3. Fabrication of peptide arrays on the polymer coated LSPR biosensor by the particle-based technique	49
3.3.3.1. Synthesis of amino acid toner particles for the particle-based synthesis	49
3.3.3.2. Partial synthesis of peptide arrays on the polymer coated LSPR biosensor by the particle-based technique	49
3.3.3.2.1. Liquid-phase peptide synthesis	49
3.3.3.2.2. Particle-based peptide synthesis	49
3.3.3.2.3. Immunostaining with fluorescence-labeled antibodies	50
3.3.3.3. Total synthesis of peptide arrays on the polymer coated LSPR biosensor by particle-based technique	51
3.3.3.3.1. Particle-based peptide synthesis	51
3.3.3.3.2. Immunostaining with infrared-labeled antibodies	51
3.4. Excitation and detection of surface plasmons	51
3.5. Analytical measurements	53
3.5.1. Scanning Electron Microscopy (SEM)	53
3.5.2. X-ray Photoelectron Spectroscopy (XPS)	53
4. RESULTS AND DISCUSSION	55
4.1. Overview and introduction	55
4.2. Study of LSPR based biosensors as a solid support for peptide arrays and a detection tool in the antibody assay	55
4.2.1. Introduction	55
4.2.2. Deposition of the intermediate dielectric layer	57
4.2.2.1. Silica nanoparticle monolayer as the dielectric layer in the LSPR biosensor	57

4.2.2.2. Homogeneous polycrystalline silica film as the dielectric layer in the LSPR biosensor	64
4.2.2.3. A composite structure of a polycrystalline silica film and a silica particle monolayer as the dielectric layer in the LSPR biosensor	64
4.2.3. Deposition of the upper gold layer	65
4.2.3.1. Deposition of the upper gold layer by seeding and plating	65
4.2.3.2. Deposition of the upper gold layer by Physical Vapor Deposition (PVD)	66
4.2.4. Localized Surface Plasmon Resonance (LSPR) Spectra	67
4.2.4.1. Interpretation of the LSPR spectra of the nanoparticle-based biosensor	67
4.2.4.2. Plasmon resonance line shape	68
4.2.4.3. Optical homogeneity	72
4.2.4.4. Optical sensitivity	78
4.2.4.5. Conclusion	82
4.3. Synthesis of protein-resistant coatings on LSPR biosensor via Atom Transfer Radical Polymerization (ATRP)	85
4.3.1. Direct synthesis of protein-resistant coating on LSPR biosensor	85
4.3.2. Indirect synthesis of protein-resistant coating on the LSPR biosensor	86
4.3.2.1. Synthesis of silica gel on the LSPR biosensor	86
4.3.2.2. Synthesis of a protein-resistant film on the silica gel-coated LSPR biosensor via ATRP	90
4.3.2.2.1. Attachment of ATRP initiators on the silica gel-coated LSPR biosensor	90
4.3.2.2.2. Surface initiated ATRP on the silica gel-coated LSPR biosensor	92
4.3.2.2.3. LSPR response of graft copolymer films with different thicknesses	97
4.3.2.2.4. Functionalization of the protein-resistant coating on the LSPR biosensor	98
4.3.3. Stability of the protein-resistant polymer -coated LSPR biosensor in the peptide printing procedure ...	99
4.3.3.1. Blocking of residual hydroxyl groups of the polymer film	99
4.3.3.2. Removal of Fmoc protection groups by piperidine	100
4.3.3.3. Removal of side-chain protecting groups by trifluoroacetic acid	101
4.3.3.4. Treatment of graft polymer-coated LSPR biosensor with acetic acid, piperidine, and trifluoroacetic acid	101
4.3.4. Conclusion	102
4.4. Label-free detection of antigen-antibody interactions occurring on a LSPR biosensor coated with a protein-resistant layer	104
4.4.1. LSPR biosensor as label-free detection tool	104
4.4.2. Fabrication of an antibody array on a LSPR biosensor by spotting technique	105
4.4.1.1. Qualitative analysis by LSPR imaging	106
4.4.1.2. Quantitative analysis by LSPR resonance shift	109
4.4.2. Fabrication of a peptide array on a LSPR biosensor by particle-based technique for peptide synthesis	110
4.4.2.1. Generation of a peptide array on a LSPR biosensor by partial particle-based synthesis	110
4.4.2.2. Total synthesis of a peptide array on a LSPR biosensor by particle-based technique	113
4.4.3. Conclusion	119
5. OPTICAL BIOSENSORS BASED ON WGM	121
5.1. Introduction	121
5.2. Theory	121
5.2.1. Basic equations	121
5.2.2. Approximation for $q = 1$ mode	123
5.2.3. Q-factor	123
5.2.4. WGM for biosensing	124
5.2.5. Excitation of WGM	124

5.2.6. Determination of the sphere radius	125
5.3. Materials and Methods	125
5.3.1. Chemicals	125
5.3.2. Inking.....	125
5.3.3. Deposition of polyelectrolytes	125
5.3.4. Raman measurement.....	125
5.4. Results and Discussion	126
5.5. Summary and Conclusion	127
6. SUMMARY AND CONCLUSION.....	129
6.1. Optical biosensor based on localized surface plasmon resonance (LSPR).....	129
6.2. Protein resistant coating on the LSPR biosensor based on poly(ethylene glycol).....	131
6.3. Label-free detection of biomolecular interactions on the polymer coated LSPR biosensors	134
6.4. Optical biosensors based on Whispering Gallery Modes (WGM)	137
BIBLIOGRAPHY	138
ACKNOWLEDGEMENT	147

Abstract

Peptide or protein chips which can track hundreds or thousands of distinct proteins from a blood or urine sample at a single step are highly desired. It will allow the diagnosis of diseases in their formative, treatable stages just by detecting proteins that are markers for these specific diseases. To simultaneously and efficiently detect where blood's proteins bind on the grid, label-free detection methods are favorable in order to reduce time and cost demands and facilitate the detection of low-affinity binding events. In this work, a label-free biosensor based on localized surface plasmon resonance (LSPR) was developed and specifically optimized regarding its application as a solid substrate in the synthesis of high-density peptide arrays, and in the detection of molecular interactions occurring on the sensor surface. Three main issues which are crucial in achieving this goal have been covered in this work: (i) development and optimization of the LSPR biosensor, (ii) Synthesis of a protein resistant layer on the LSPR biosensor, (iii) Label-free detection of biomolecular interactions on the polymer coated LSPR biosensors.

For this purpose, a LSPR-based biosensor was first constructed. It consists of two gold layers and an intermediate dielectric layer in-between. The LSPR biosensor shows several pronounced resonance peaks in the UV-visible region of the electromagnetic spectrum, which are highly sensitive to changes in the refractive index of the surrounding medium. The LSPR biosensor was optimized in terms of plasmon resonance line shape, optical homogeneity, and sensitivity to facilitate its application in the label-free detection of biomolecular interactions in array format.

In a second step, a poly(ethylene glycol) based polymer was synthesized on the sensor surface at mild reaction conditions by using Atom Transfer Radical Polymerization (ATRP). The sensor was first coated with a silica gel to stabilize the sensor and provide a sufficiently high number of functional groups. ATRP initiators were immobilized on the silica gel surface in 2 steps by silanization and esterification to enhance the coupling efficiency. Subsequently, polymerization was carried out with oligo(ethylene glycol) methacrylate (OEGMA) as the monomer resulting in a poly(ethylene glycol) methacrylate (PEGMA) polymer film. In the second approach, a graft copolymer film was synthesized on the sensor surface with methyl methacrylate (MMA) as the diluting monomer in order to reduce the protein-resistance of the sensor coating and further enhance the sensor stability. Graft copolymer films with 10% PEGMA/ 90% MMA and a thickness of 50-60 nm were successfully synthesized by setting the polymerization time between 9.5 and 10.5 hours. This thickness regime is required to ensure a high-loading of amino functional groups, which serve as the starting point for the subsequent peptide array synthesis. At the same time, this film thickness does not exceed the surface sensitivity regime of the LSPR biosensor.

To test the performance of the LSPR biosensor, an array of fluorescent-labeled antibodies was formed on its surface by a spotting robot. The LSPR image displays an array of spots which corresponds to the fluorescence image. Moreover, the quantity of antibody bound to the sensor surface was correctly predicted based on the measured wavelength shifts in the quadrupole regime and a mass sensitivity factor known from literature. This shows that the LSPR biosensor described in this thesis has the potential to allow the detection of molecular interactions in a miniaturized array format in a quantitative manner.

In the final part of this thesis, the polymer-coated LSPR biosensor was successfully utilized as the solid substrate in the synthesis of a peptide array via a novel laser printing technique developed at the Cancer Research Center Heidelberg (DKFZ). An array with 9x20 variants of hemagglutinin/HA (YPYDVPDYA) epitope was synthesized on a polymer-coated LSPR

biosensor and incubated with IR-dye conjugated specific antibody. The LSPR image was generated by evaluating the wavelength shift in the octapole resonance peak and has successfully displayed the entire peptide array formed on the sensor surface.

In a separate study, the potential of single, small particles for biosensing applications in miniaturized format was investigated. Whispering gallery modes (WGM) of fluorescence-doped sulfonated polystyrene (PS) particles with a diameter of 2 μm were studied with respect to their resonance shift after adsorption of polyelectrolyte multilayers. The resonance shifts were plotted as a function of the film thickness and a slope of 0.038 nm/Å was obtained from a linear fit to the experimental data. This sensitivity factor can be translated into a detection limit of 3 fg by assuming a spectral resolution of 0.1 nm and a polyelectrolyte mass density¹⁷ of 0.81 g/cm³.

Kurzfassung

Peptid- oder Proteinchips, die Hunderte oder Tausende unterschiedliche Proteine aus einer Blut- oder Urinprobe in einem einzigen Schritt aufspüren können, sind in der medizinischen Diagnostik von großem Interesse. Sie bieten die Möglichkeit, die Diagnose von Krankheiten in einem frühen, behandelbaren Stadium durch den Nachweis spezifischer Proteine zu ermöglichen, die Indikatoren für die betreffende Krankheit darstellen. Bei der parallelen und effizienten Erkennung spezifischer Proteine sind markierungsfreie Detektionsmethoden von Vorteil, da sie einerseits zeit- und kosteneffizient sind und andererseits auch schwache Bindungen nachweisen können. In dieser Arbeit wurde ein markierungsfreier Biosensor entwickelt, der auf lokalisierter Oberflächenplasmonenresonanz (LSPR) basiert, und insbesondere bezüglich seiner Anwendung als ein festes Substrat in der Synthese hochintegrierter Peptidbibliotheken sowie der Erkennung biomolekularer Wechselwirkungen optimiert. Drei zentrale Fragen, die zur Erreichung dieses Ziels entscheidend sind, wurden in dieser Arbeit behandelt: (i) die Herstellung und Optimierung des LSPR-Biosensors, (ii) die Herstellung einer protein-resistenten Beschichtung auf dem LSPR-Biosensor, und (iii) die markierungsfreie Detektion biomolekularer Wechselwirkungen auf dem Polymerbeschichteten LSPR-Biosensor.

Zu diesem Zweck wurde zunächst ein LSPR-basierter Biosensor entwickelt. Der Sensor besteht aus zwei Goldschichten und einer dazwischen liegenden dielektrischen Schicht. Der LSPR-Biosensor zeigt mehrere ausgeprägte Resonanzpeaks im UV-Vis Spektrum, die hochempfindlich auf Änderungen des Brechungsindex des umgebenden Mediums reagieren. Der LSPR-Biosensor wurde im Hinblick auf die Linienform der Plasmonenresonanz sowie seine optische Homogenität und Empfindlichkeit optimiert, um seinen Einsatz beim markierungsfreien Nachweis von biomolekularen Wechselwirkungen im Arrayformat zu ermöglichen.

Im zweiten Schritt wurde ein Polyethylenglykol (PEG) basierter Polymerfilm als protein-resistente Beschichtung auf dem LSPR-Biosensor bei milden Reaktionsbedingungen mit Hilfe der Atom Transfer Radikal Polymerisation (ATRP) synthetisiert. Der Sensor wurde hierbei zuerst mit einem Silikagel beschichtet, um dem Sensor Stabilität zu verleihen und eine hohe Anzahl von Hydroxylgruppen anzuknüpfen. ATRP-Initiatoren wurden auf der Silikageloberfläche durch Silanisierung und anschließende Veresterung immobilisiert, um die Kopplungseffizienz zu steigern. Anschließend wurde die Polymerisation mit Oligoethylenglykolmethacrylat (OEGMA) als Monomer durchgeführt, wodurch ein reiner Polyethylenglykolmethacrylat (PEGMA)-Polymerfilm erzeugt wurde. Im zweiten Ansatz wurde ein Copolymer auf der Sensoroberfläche mit Methacrylsäuremethylester (MMA) als sekundärem Monomer synthetisiert, um die Proteinresistenz der Sensorbeschichtung zu

reduzieren und die Stabilität des Sensors weiter zu erhöhen. Copolymerfilme mit 10% PEGMA/ 90% MMA und einer Filmdicke von 50-60 nm wurden erfolgreich durch die Einstellung der Polymerisationszeit auf 9,5 bis 10,5 Stunden synthetisiert. Diese Filmdicke ist erforderlich, um eine ausreichende Anzahl funktioneller Amino-Gruppen zu gewährleisten, welche als Ausgangspunkt für die anschließende Synthese eines Peptidarrays dienen. Gleichzeitig bleibt die Schichtdicke im Empfindlichkeitsbereich des LSPR-Biosensors.

Um die Leistungsfähigkeit des LSPR-Biosensors zu überprüfen, wurde ein Array fluoreszenzmarkierter Antikörper auf dessen Oberfläche gespottet. Das LSPR-Bild zeigt eine Reihe von Spots, die mit dem Fluoreszenzbild korreliert. Außerdem konnte die Menge der oberflächengebundenen Antikörper anhand der gemessenen Wellenlängenverschiebung in der Quadrupolresonanzpeak und einem aus der Literatur bekannten Empfindlichkeitsfaktor korrekt vorhergesagt werden. Dies zeigt, dass der in dieser Arbeit optimierte LSPR-Biosensor das Potenzial besitzt, molekulare Wechselwirkungen in einem miniaturisierten Arrayformat quantitativ nachzuweisen.

Im letzten Teil dieser Arbeit wurde der polymerbeschichtete LSPR-Biosensor erfolgreich als festes Substrat für die Synthese eines Peptidarrays mithilfe einer neuen Laserdrucktechnik eingesetzt, die am Krebsforschungszentrum Heidelberg entwickelt wurde. Ein Array mit 9x20 Varianten des HA Epitops (YPYDVPDYA) wurde auf einer polymerbeschichteten LSPR-Biosensor synthetisiert und mit einem IR-Farbstoff konjugierten anti-HA Antikörper inkubiert. Die Bindungsereignisse auf dem Sensor wurden dann mittels eines IR-Scanners und markierungsfreiem LSPR-Imaging nachgewiesen. Das LSPR-Bild wurde durch Auswertung der Wellenlängenverschiebung des Octapolresonanzpeaks erzeugt und konnte erfolgreich den gesamten Peptidarray auf der Sensoroberfläche darstellen.

In einer separaten Studie wurde das Potenzial einzelner kleiner Teilchen für biosensorische Anwendungen im Miniaturformat untersucht. Hierzu wurden sogenannte Whispering Gallery Modes (WGM) in Fluoreszenz-dotierten sulfonierten Polystyrol (PS) Partikeln mit einem Durchmesser von 2 μm erzeugt und ihre Resonanzverschiebung nach der Adsorption von Polyelektrolyten untersucht. Bei einer Auftragung der gemessenen Resonanzverschiebung als Funktion der Schichtdicke ergibt sich ein linearer Zusammenhang, der sich durch eine Gerade mit einer Steigung von 0,038 nm/Å anpassen lässt. Dieser Empfindlichkeitsfaktor ergibt unter der Annahme einer spektralen Auflösung von 0,1 nm und einer Polyelektrolytdichte von 0,81 g/cm³ eine Nachweisgrenze von 3 fg für diesen Einzelpartikelsensor.

List of Publications

- [1] M. Himmelhaus, **F. Caroline**, H. Takei in Proceedings of SPIE - Physical Chemistry of Interfaces and Nanomaterials II, **2003**, 5223 *Routines for Controlling Nanoparticles at Surfaces and Interfaces*, 31-37.
- [2] A. Weller, **F. C. Liu**, R. Dahint, M. Himmelhaus in Applied Physics B: Lasers and Optics **2008**, 90(3-4), 561-567 *Whispering Gallery Mode Biosensors in the low-Q Limit*, 561-567.
- [3] **F. C. Liu**, T. Felgenhauer, N. Waly, H. O. Guvenc, V. Stadler, R. Bischoff, F. Breitling, R. Dahint: *LSPR-based Optical Biosensors for the Label-Free Detection of Biomolecular Interactions in High-Density Peptide Arrays* (in preparation).

Abbreviations

AEM	2-aminoethyl methacrylate
APTES	(3-aminopropyl)triethoxysilane
ATR	attenuated total reflection
ATRP	atom transfer radical polymerization
Boc	<i>t</i> -butyloxycarbonyl
CRT	cathode ray tube
CuBr	copper(I) bromide
CuCl	copper(I) chloride
CuCl ₂	copper(II) chloride
DCM	dichloromethane
DIC	<i>N,N</i> -diisopropyl carbodiimide
DIPEA	<i>N,N</i> -diisopropylethylamine
DMF	<i>N,N</i> -dimethylformamide
DNA	desoxyribonucleic acid
EDC	<i>N</i> -(3-dimethylaminopropyl)- <i>N</i> -ethylcarbodiimide hydrochloride
EM	electromagnetic
ESA	acetic anhydride
Fmoc	9-fluorenylmethoxycarbonyl
HCl	hydrogen chloride
IgG	immunoglobulin G
IR	infrared
LED	light-emitting diode
LSPR	localized surface plasmon resonance
MMA	methyl methacrylate
MPTES	(3-mercaptopropyl)trimethoxysilane
MWD	molecular weight distribution
NHS	<i>N</i> -hydroxysuccinimide
NMI	<i>N</i> -methyl-imidazole
OEGMA	oligo(ethylene glycol) methacrylate
OPC	organic photoconducting
OPfp	pentafluorophenyl ester
PAH	poly(allylamine hydrochloride)
PDMS	poly(dimethylsiloxane)

PEG	poly(ethylene glycol)
PEGMA	poly(ethylene glycol) methacrylate
PEI	polyethyleneimine
PET	poly(ethylene terephthalate)
PLL	poly-L-lysine
PMDETA	1,1,4,7,7-pentamethyldiethylenetriamine
polySBMA	poly(sulfobetaine methacrylate)
PSS	poly(sodium 4-styrenesulfonate)
PVD	physical vapor deposition
RI	refractive index
RNA	ribonucleic acid
SA	11-mercaptoundecylsulfonic acid
SAM	self-assembled monolayer
SCMF	single-chain mean-field
SEM	scanning electron microscopy
SI-ATRP	surface-initiated atom transfer radical polymerization
SPR	surface plasmon resonance
TBS	tris-buffered saline
TBS-T	tris-buffered saline with Tween 20
TE	transverse electric
TEGMME	tri(ethylene glycol) monomethyl ether
TFA	trifluoroacetic acid
TIBS	triisobutylsilane
TM	transverse magnetic
TMA	11-mercapto- <i>N,N,N</i> -trimethylammonium chloride
UV	ultra violet
Vis	visible
WGM	whispering gallery modes
XPS	x-ray photoelectron spectroscopy

1. Introduction

When medical visionaries talk about the future, many offer up the image of a computer chip or CD-ROM that stores a human's complete DNA sequence. The odds of getting e.g. Alzheimer's disease or breast cancer could then be revealed by reading the DNA sequences. In most cases, however, it is more significant to know a person's current health condition rather than the possibility of getting a specific disease in the future. In this case, studying one's proteins instead of DNA and genes might provide immediate answers.

Proteins reflect the chemistry taking place inside cells, chemistry that is altered in potentially diagnostics ways by different diseases. By detecting proteins that are markers for specific diseases, researchers could then spot diseases in their formative, treatable stages.

To perform such a complex diagnostic, protein-chips that can track hundreds or thousands of distinct proteins from a blood or urine sample at a single step are required. Thousands of molecules designed to capture specific proteins should be immobilized at specific sites on these chips. The resulting pattern of the binding events would reveal the patient's health condition (Fig. 1-1).¹⁸⁻¹⁹ To simultaneously and efficiently detect where blood's proteins bind on the grid, label-free analyzing methods should be used as they reduce time and cost demands and are favorable with respect to the detection of low-affinity binding events.

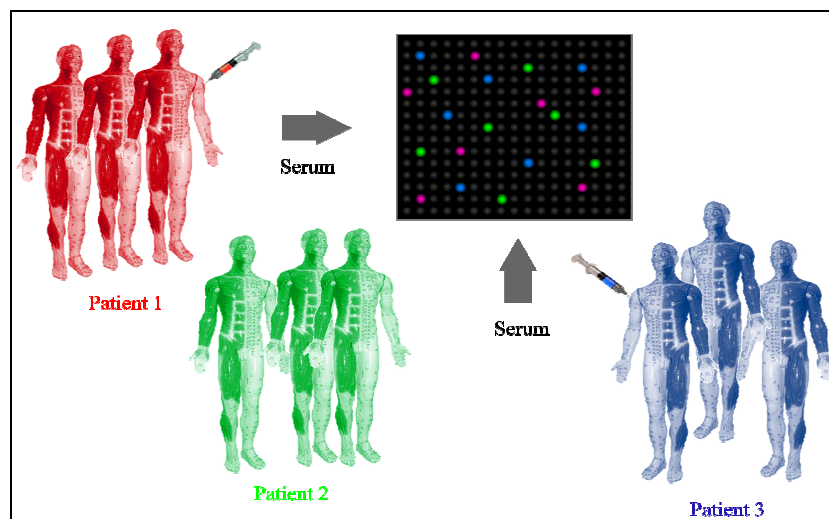


Figure 1-1. Patterns of binding events from patient's serums should reveal the health condition

In many cases, the biological activities of the proteins can be recapitulated by shorter peptides that are taken from the primary sequences, although often with partial loss of activity. Hence, peptide arrays can be used instead of protein chips to screen diverse biochemical interactions in the cells.

Aim and Organization

The goal of this thesis is to develop an optical biosensor which should serve simultaneously as a solid support in the synthesis of high-density peptide arrays, as well as in the detection of antibody-antigen interactions occurring on the peptide chips.

Several issues that have made peptide arrays challenging to implement include the expense of preparing large number of peptides, the development of chemistries and supports that give

good control in presenting immobilized peptides, the prevention of non-specific interactions at the surface, and development of analytical methods to detect activities on the chips. All these crucial points in the preparation and application of peptide chips will be covered in this dissertation work.

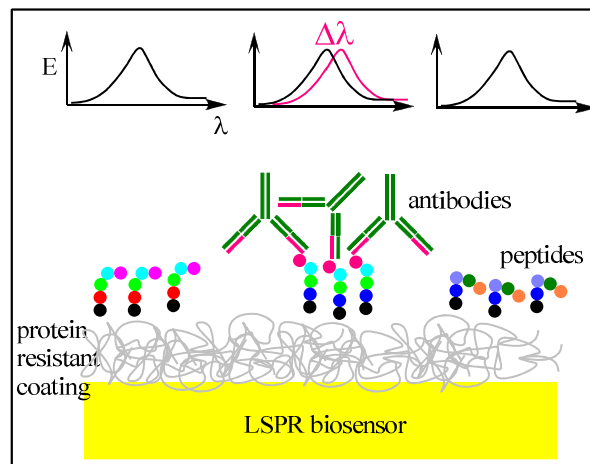


Figure 1-2. Protein resistant coated, LSPR based biosensor in combination with peptide arrays. Coupling of antibodies on the peptide array can be detected as a shift in the extinction spectrum.

High density peptide arrays

The two general approaches for parallel on-chip peptide synthesis are photolithographic synthesis and SPOT synthesis. The lithographic technique translated *Merrifield's* solid phase methods for peptide synthesis directly to the array support by developing photolabile protecting groups that would allow synthesis to proceed only at regions of the surface that are illuminated. In the SPOT synthesis, peptides are synthesized by sequential spotting of small (typically microliter) volumes of activated amino acids to a porous membrane. The arrays may be assembled either by manual or robotic distribution of reagents, making this method accessible to researchers in the biological sciences.

To generate customized peptide arrays at high density, high speed, and low cost, our cooperation partner (research group "Chip-based Peptide Libraries") at the German Cancer Research Center Heidelberg (DKFZ) is developing a novel method using a modified color laser printer. The printer is capable of printing the 20 amino acids at defined positions on a glass support. Presently the printing resolution is limited to 160 000 spots in an area of 20x20 cm.^{16,19} This "particle-based synthesis" should be used in this dissertation work to fabricate a high-density peptide array.

Label-free detection of bio-molecular interactions

To interrogate antibody-antigen interactions occurring on the peptide chips, a detection method is required. The use of radioactive and fluorescent labels has been the most important, but recent work has introduced 'label-free' methods that offer wider utility. These latter methods have the principal advantages that the assays are more straightforward because they avoid the steps associated with applying and processing the label and they can identify unanticipated activities. One technique under development is the localized surface plasmon resonance (LSPR) on gold, which is extensively studied and optimized in this dissertation work regarding its application as a detection tool in combination with peptide arrays.

Under just the right conditions, photons in a beam of light incident upon a gold-dielectric material interface “resonate” with the electrons in the gold. As a result, instead of the light simply reflecting off the gold surface, photon energy is converted to a wave of “plasmons” in the gold, which is then observed as a maximum in the extinction spectrum.

LSPR can be used to detect binding events on a surface because adding material to the surface changes the resonance frequency. This detection method is quantitative - the change in resonance frequency is proportional to the change in mass on the surface.²⁰

Protein resistant films to prevent non-specific interactions

In diagnostic assays based on specific recognition of antigen/antibody pairs, suppression of nonspecific protein adsorption is crucial for achieving sufficiently low detection limits. Nonspecific protein adsorption can be reduced by using a system where repulsive interactions between proteins and the surface overcome the attractive ones.

Surface modification by poly(ethylene glycol) (PEG) is a well-known strategy for rendering surfaces protein resistant. The protein repelling character has been attributed to steric repulsion and excluded-volume effects between proteins in solution and the PEG-modified surface.²¹

In this work, PEG-based protein resistant films have been prepared on the biosensor surface via Atom Transfer Radical Polymerization (ATRP). Its mild reaction conditions should enable the application of ATRP on the chemically sensitive SPR biosensor. Polymer films synthesized by ATRP have a three-dimensional layer geometry, providing a high loading of functional groups for the linkage of the generated peptides.

Thus, this dissertation work is divided into three parts:

1. Development and optimization of biosensors based on LSPR.
2. Synthesis of protein resistant coatings on the LSPR biosensor via ATRP.
3. Synthesis of high density peptide array via “particle-based synthesis” on the protein resistant-coated LSPR biosensor and the label-free detection of bio-molecular interactions on the peptide array.

Biosensors based on Whispering Gallery Modes (WGM)

Optical label-free detectors, such as the well-established surface plasmon resonance (SPR) sensor, are generally favored for their ability to obtain quantitative data on intermolecular binding. However, sensitivity to single binding events has not materialized due to the problem that a given photon in the exciting light interacts only once with an adsorbate.²²⁻²³ Optical microcavities have been introduced as a powerful tool to achieve label-free detection of single molecules because the resonant recirculation of light within a microcavity allows the light to interact with the adsorbate molecules many more times.

In a joint project with Andreas Weller et al. the potential of small particles with diameters below 6 μm for biosensing applications in miniaturized format was investigated. These particles support the excitation of Whispering Gallery Modes and may act as optical microcavities, which sensitively respond to molecule adsorption.

2. Theory

The excitement for peptide microarrays – together with protein, carbohydrate and small molecule arrays - stems from the impact that oligonucleotide arrays have had in basic and applied research. A significant benefit of the arrays is that they allow biochemical interactions to be identified from thousands of possibilities and have in turn motivated many researchers to pursue discovery-driven, rather than hypothesis-driven research.^{18-19,24}

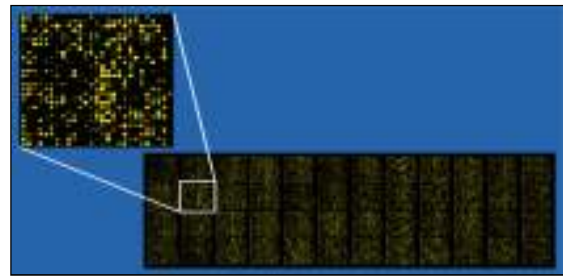


Figure 2-1. DNA-chip⁷

Compared to the relative ease of DNA microarray synthesis, peptide and protein chips are fundamentally different in their preparation chemistry and applications. In particular, there are 20 natural amino acids compared to only four natural DNA or RNA nucleotides.

Nucleid acids have the distinct advantage of complementary binding, in which one strand of RNA or DNA binds specifically to another with the corresponding sequence of bases. To make an array, researchers simply synthesize strands of nucleid acids complementary to the sequences searched for, and attach them in a grid pattern to a substrate.

Proteins and peptides, in contrast, bind to their target on the three-dimensional shape of each, as well as may undergo a myriad of chemical interactions. Thus, for each spot on an array, researchers must come up with a unique and specific molecule to capture a desired protein target.

However, the diverse chemical properties of peptides and proteins make them suitable for a broad range of applications. Peptide chips provide versatile tools for probing antigen-antibody, protein-protein-, and peptide-ligand interactions, and should find key applications for therapeutic target identification, protein function assay, drug discovery, and diagnostics.

Several issues that have made peptide arrays challenging to implement include the expense of preparing large numbers of peptides, the development of chemistries and supports that give good control in presenting immobilized peptides, the prevention of non-specific interactions at the surface, and the development of analytical methods to detect activities on the chips. All these crucial points in the preparation and applications of peptide chips will be covered in this dissertation work.

2.1. *In situ* peptide synthesis

Methods for fabrication of peptide microarrays can be classified by the assembly of peptides on the surface – *in situ* peptide synthesis or immobilization of functionalized presynthesized peptides onto chips.

Immobilization of peptides that have been previously synthesized is preferred when only small numbers of peptides are needed in the array or when the peptides will be used to prepare large numbers of identical arrays. However, the expense and time required to prepare hundreds of peptides — including the purification of those peptides before immobilization — prohibit routine applications. These considerations have motivated the development of *in situ* peptide synthesis, which benefits from using small amounts of reagents and avoiding

purification and immobilization of peptides. Two general approaches for parallel on-chip peptide synthesis are photolithographic synthesis and SPOT synthesis. In the last few years a new method for *in-situ* peptide synthesis has been developed at German Cancer Research Center Heidelberg, which is based on amino acids toner particles.^{16,19}

2.1.1 Photolithographic synthesis

The photolithographic approach was first reported by Fodor et al. in 1991.²⁵ This group translated solid phase methods for peptide synthesis directly to the array support by utilizing photolabile protecting groups that would allow synthesis to proceed only at regions of the surface that are illuminated.

The synthesis involves multi-cycles with each cycle using light irradiation through a photomask followed by coupling one type of amino acid to specific locations where the photo-labile protecting group on the terminal of the growing chain has been removed upon light irradiation.

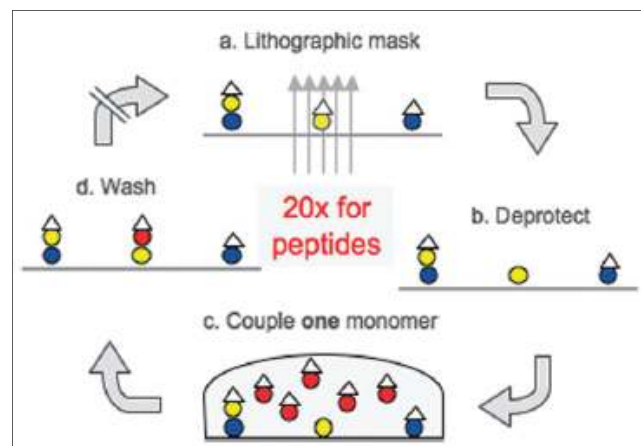


Figure 2-2. Photolithographic synthesis of a peptide array. (a) A pattern of light defines specific areas on a 2D solid support. (b) By illumination, the transient protection group at the top of the growing oligomer chain is removed. (c) The whole support is covered with one of the 20 different C-terminally activated amino acid derivatives. (d) After coupling, excess monomers are washed away.¹⁶

Although this method seems promising for high-density peptide chips, it has practical limitations: photomasks are expensive and time consuming to produce and their fabrication requires expensive equipment and a high grade clean room environment; the preparation of the monomers containing photo-labile protecting groups is not an easy task. These groups perform poorly in terms of repetitive coupling yield when compared to conventional *t*-butyloxycarbonyl (Boc) or 9-fluorenylmethoxycarbonyl (Fmoc) protection groups.

Another drawback of this method is the large number of coupling cycles that must be performed, since only a single kind of monomer can be coupled at a time. For example, up to 20 x 10 coupling cycles are necessary to synthesize a 10meric peptide array. This large number of coupling cycles makes it very difficult to avoid the accumulation of unwanted side reactions.

Thus, for peptide synthesis, this method proved to be too difficult to be used in a regular laboratory setting and too costly to afford. However, it has been successfully applied to DNA chip fabrication, where the limited number of different monomers (4 bases instead of 20 amino acids) significantly reduces the number of preparation cycles required. Today, oligonucleotide arrays with thousands of oligonucleotides per cm², made by photolithographic synthesis, are commercially available.²⁶

2.1.2 SPOT synthesis

The second technique used for *in situ* peptide synthesis is the SPOT method, first reported by Frank in 1992. In the SPOT synthesis, peptides are synthesized by sequential spotting of small (typically microliter) volumes of activated amino acids onto a derivatised cellulose sheet. The amino acids in the successively deposited droplets react with the free amino groups of the growing peptide chains that are linked to the cellulose support. Each droplet defines a small reaction sphere. The SPOT peptide microarray is then incubated with the sample solution and the assays require only milliliters of the sample volume.²⁷

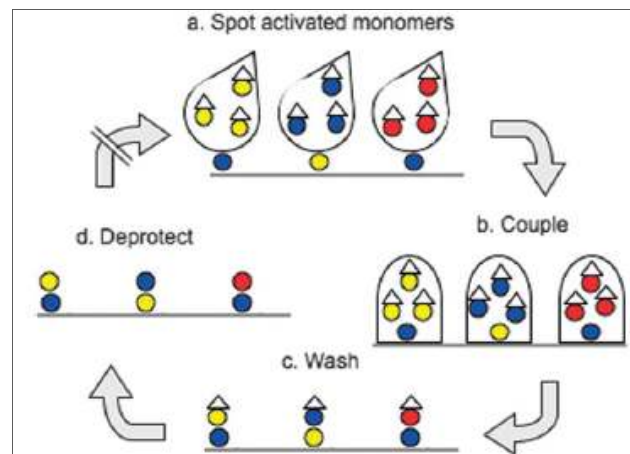


Figure 2-3. SPOT synthesis of a peptide array. (a) A spotter positions the 20 different C-terminally activated amino acid derivatives, all contained within liquid droplets, to define specific areas on a solid support. (b) The amino acids are coupled to the support. (c) Excess monomers are washed away. (d) The transient protection group is removed.¹⁶

This method has gained wide acceptance in scientific community to allow screening epitope sequences, enzymatic reaction substrates, and protein binding ligands at a low cost. Compared to the lithographic approach it significantly reduces the number of coupling cycles as one complete monolayer of monomers can be prepared in one cycle. Thus, only 10 instead of 20 x 10 preparation cycles are required for the synthesis of a 10meric peptide array.

However, the SPOT synthesis method is limited in its ability to produce peptide arrays with densities that exceed about 25 peptide spots per cm^2 , mainly due to difficulties in handling the amino acids droplets that can evaporate or spread over the array.²⁸⁻²⁹

2.1.3. Particle-based synthesis

The latest progress in synthesizing high-density peptide array is provided by a technique that is based on 20 different solid amino acid particles. These triboelectrically charged particles are selectively positioned on a 2D support using electrical fields generated by either a laser printer or a computer chip. Once positioned, the whole layer of amino acid particles is melted to initiate the coupling reaction. Washing and deprotection steps complete the cycle.^{2,16,30}

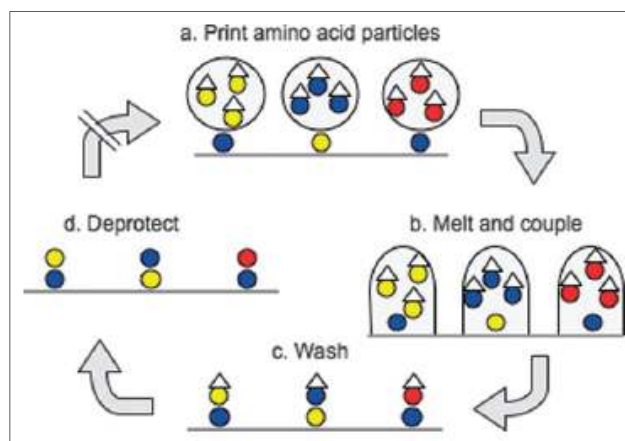


Figure 2-4. Particle-based synthesis of a peptide array by means of a laser printer. (a) A laser printer positions Fmoc-amino acid-OPfp esters embedded within solid toner particles onto a solid support. (b) The toner particles are melted to couple the amino acid derivatives onto the support. (c) Excess monomers are washed away. (d) The Fmoc protection groups are removed.¹⁶

The highly reactive amino acid derivatives are embedded within a solid particle matrix that completely blocks their diffusion and prevents chemical coupling to a reaction partner. This solid particle matrix consists of diphenyl sulfoxide, toner resin, and charge control reagents e.g. Fe(III)- or Al(III)-complexes. All 20 different amino acid particles use conventional Fmoc chemistry and have a C-terminal OPfp-ester as the activating group. These amino acid derivatives proved to be stable for months at room temperature when embedded in toner particles, with the exception of Fmoc-arginine-OPfp. This compound decayed with a rate of 4 % per month.

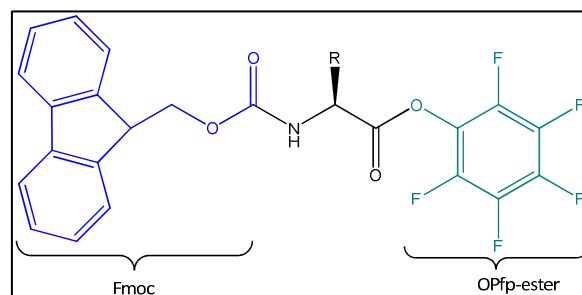


Figure 2-5. C-terminally activated, N-terminally protected amino acid derivatives, which are embedded in the toner particles used for particle-based peptide array synthesis.

This method differs from SPOT synthesis in the use of a solid solvent at room temperature, which prevents the spreading of the reaction reagents as well as uncontrolled evaporation of solvent, which changes the concentration of the chemicals involved in the coupling reactions. It also provides a more accurately defined reaction sphere. The available reaction time is accurately controlled by temperature. These features should allow to significantly scale down the area of individual synthesis sites, resulting in a higher peptide density.

The peptide laser printer used in positioning the particles, is conceptually based on the color laser printer OKI C7400, but accommodates 20 instead of 4 printing units (Fig. 2-6). Each unit contains a particular amino acid toner. The printer operates a drive and mounting that enable the repeated exact positioning ($\pm 5 \mu\text{m}$) of the solid support.



Figure 2-6. Peptide printer based on a color laser printer OKI C7400, equipped with 20 printing units, each containing one particular type of amino acid toner particles.²

The OPC (organic photoconducting) drum is charged evenly by a corona (yellow, Fig. 2-7). A light source (light-emitting diode (LED) row, orange) illuminates and thereby neutralizes selected areas of the OPC drum. Triboelectrically charged toner particles are then transferred to these neutralized areas. Finally, the toner particles delivered by the OPC drum are collected by a strong electric field (4 kVmm^{-1}) on a solid support, and heated to release the amino acid derivatives embedded in the particles. Thus, the electrostatic pattern is transformed into the corresponding amino acid pattern.

The LED row provides approximately 10 000 illumination steps per 20 cm, resulting in a two-dimensional light pattern comprising around 100 million pixels per $(20 \times 20) \text{ cm}^2$.

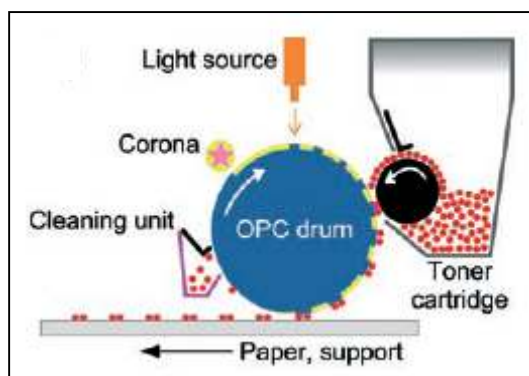


Figure 2-7. Schematic diagram showing the principle of operation of a laser printer.²

The first experiments resulted in a printing resolution of 160 000 peptide spots in an area of $(20 \times 20) \text{ cm}^2$. This density (400 spots per cm^2) significantly exceeds the state-of-the-art in peptide array synthesis (SPOT synthesis: 25 spots per cm^2 ; photolithographic synthesis: 144 spots per cm^2) but is still lower than the millions of different peptides that this method could generate. Fabrication of customized peptide arrays with high density at high speed and low cost, using the particle based-printing method, is expected for the near future.

2.2. Surface plasmon resonance as a tool in molecular biosensing

The majority of techniques currently employed to interrogate biomolecular interactions require some type of radio-, enzymatic- or fluorescence labeling to report the binding event. Since labeling molecules involves chemical modifications, there is a risk that the function may be impacted by the label, a particular problem for proteomics research. The labeling step also imposes additional time and cost demands, and prohibits an *in situ* detection process. Moreover, additional incubation and washing steps that are usually required in between the interaction and detection process may prohibit the detection of low-affinity binding events. Therefore, label-free detection systems such as optical, acoustic, and thermic biosensors are the preferred approach for functional analysis of protein interactions.^{20,31-32}

2.2.1. Surface plasmon resonance

Materials that possess a negative real and small positive imaginary part of the dielectric constant, such as metals, are capable of supporting surface plasmon resonance (SPR). This resonance is a coherent oscillation of the surface conduction electrons excited by electromagnetic (EM) radiation.^{1,33}

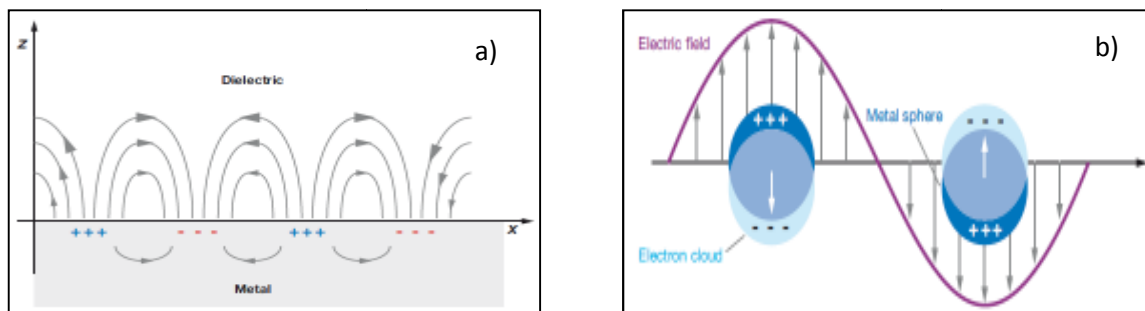


Figure 2-8 illustrates the difference between *propagating* and *localized* surface plasmons. In the first case, plasmons propagate in the x- and y-directions along the metal-dielectric interface, for distances on the order of hundreds of nanometers to hundreds of microns, and decay evanescently in the z-direction with $1/e$ decay lengths on the order of 200 nm.

For the case of localized surface plasmons, electromagnetic radiation interacts with particles much smaller than the incident wavelength. This leads to a plasmon that oscillates locally around the nanoparticle – an effect which is called localized surface plasmon resonance (LSPR).

2.2.1.1. Theory of propagating surface plasmon

The light propagation in planar metal/dielectric waveguides can be analyzed by solving Maxwell's equations using the modal method.³⁴

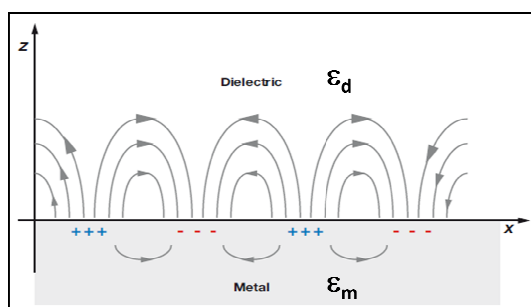


Figure 2-9. A metal-dielectric waveguide. ϵ_m , ϵ_d denote the complex permittivity of the metal and the dielectric layer.¹

The solution of the eigenvalue equation for the transverse magnetic modes is given by

$$k_{sp} = \frac{\omega}{c} \sqrt{\frac{\varepsilon_d \varepsilon_m}{\varepsilon_d + \varepsilon_m}} \quad (\text{Eq. 2-1})$$

where k_{sp} denotes the propagation constant of a mode, c is the speed of light in vacuum, $\varepsilon_m = \varepsilon'_m + i\varepsilon''_m$ the complex permittivity of the metal-, and $\varepsilon_d = \varepsilon'_d + i\varepsilon''_d$ the complex permittivity of the dielectric layer.

For lossless metal and dielectric ($\varepsilon''_m = \varepsilon''_d = 0$), this equation represents a guided mode, providing that the permittivities ε'_m and ε'_d are of opposite sign, and that $\varepsilon'_m < -\varepsilon'_d$. As the permittivity of dielectric materials is usually positive, for this mode to exist, the real part of the permittivity of the metal needs to be negative.

Following the free-electron model for metals

$$\varepsilon_m = \varepsilon_0 \left(1 - \frac{\omega_p^2}{\omega^2 + i\omega\nu} \right)$$

where ν is the collision frequency, ω_p the plasma frequency

$$\omega_p = \sqrt{\frac{Ne^2}{\varepsilon_0 m_e}}$$

N the concentration of free electrons, and e and m_e the electron charge and mass, the equation 2.1 is fulfilled for frequencies lower than the plasma frequency of the metal.

Metals such as gold, silver and aluminum exhibit a negative real part of permittivity in the visible (Vis) and near infrared (NIR) region of the spectrum. Therefore, surface plasmon resonance bands can be observed in the Vis-spectrum of these materials, which enables their application as sensors by using a simple UV-Vis excitation source and detection apparatus.

The propagation length L , which is defined as the distance in the direction of propagation at which the energy of the surface plasmon decreases by a factor of $1/e$, is a function of the wavelength. In the wavelength range 550-1000 nm, typical propagation lengths of surface plasmons are 0.6-50 μm , 4-50 μm , and 6-14 μm for gold, silver and aluminum.

The electromagnetic field of a surface plasmon reaches its maximum at the metal-dielectric interface and decays into both media. The field decay in the direction perpendicular to the metal-dielectric interface is characterized by the penetration depth L_p , which is defined as the distance from the interface at which the amplitude of the field decreases by a factor of $1/e$. The penetration depth of a surface plasmon is dependent on the wavelength of the incident light and on the dielectric constants of both layers. The spectral dependence of L_p at the interface between gold and a dielectric medium with a refractive index of 1.32 is shown in Fig. 2-10.

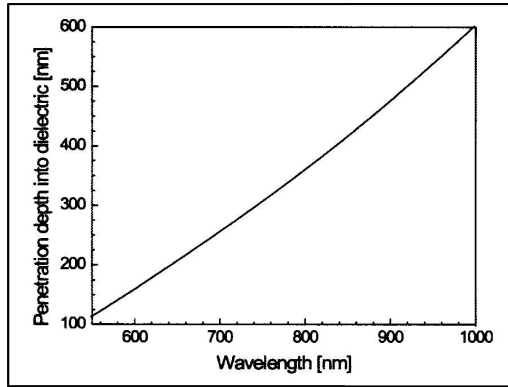


Figure 2-10. Wavelength dependence of the penetration depth L_p at the interface between gold and a dielectric medium with a refractive index of 1.32.³⁴

For a gold film, a typical penetration depth L_p is on the order of a few hundred nanometers into the dielectric layer for excitation with visible light. This makes SPR a surface sensitive technique and measurements can be made even when a large excess of analyte is present. Any species that is further away from the metal/dielectric interface than the penetration depth L_p will not significantly affect the generation and propagation of the surface plasmons.³⁵

2.2.1.2. Theory of localized surface plasmon

The absorption spectra of localized surface plasmons can also be explained by solving the Maxwell's equations to find the electric and magnetic fields in all regions of space.^{1,36}

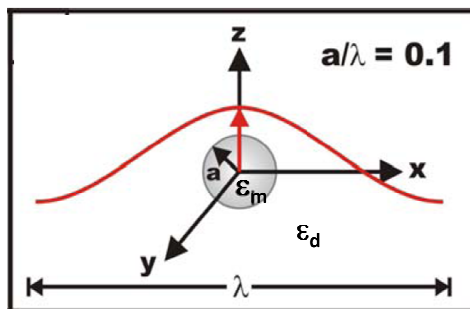


Figure 2-11. A metal sphere with radius a and dielectric constant ϵ_m , embedded in a dielectric medium ϵ_d .¹

The extinction spectrum of a spherical metal particle of radius a that is irradiated by z -polarized light of wavelength λ , with $a/\lambda < 0.1$, is given by

$$E(\lambda) = \frac{24\pi^2 N a^3 \epsilon_d^{3/2}}{\lambda \ln(10)} \left[\frac{\epsilon_m''(\lambda)}{(\epsilon_m'(\lambda) + 2\epsilon_d)^2 + \epsilon_m''(\lambda)^2} \right] \quad (\text{Eq. 2-2})$$

ϵ_m' and ϵ_m'' are the real and imaginary components of the metal dielectric function, and ϵ_d is the dielectric constant of the dielectric environment.

2.2.2. Surface plasmons in optical sensing

2.2.2.1. Excitation of surface plasmons

Surface plasmons cannot be directly excited by light, because their wave vector is longer than that of light of the same energy. In this chapter, the momentum-matching condition for surface plasmon resonance will be studied in details.

The momentum of a free photon propagating in a dielectric medium,

$$k_{ph} = \frac{\omega}{c} \sqrt{\epsilon_d}$$

is always smaller than the momentum of a surface plasmon mode, k_{sp} , propagating along an interface between that same medium and the metal (Fig. 2-12).⁵

$$k_{sp} = \frac{\omega}{c} \sqrt{\frac{\epsilon_d \epsilon_m}{\epsilon_d + \epsilon_m}}$$

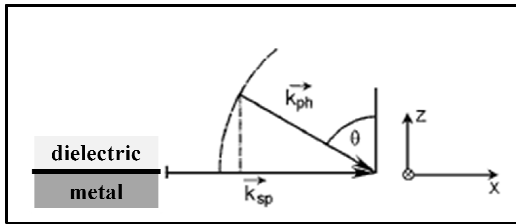


Figure 2-12. Momentum relation between a surface plasmon, (\vec{k}_{sp}), propagating along x and a photon, (\vec{k}_{ph}), incident at a metal/dielectric interface at an angle θ . At any angles θ , $|\vec{k}_{ph}| < |\vec{k}_{sp}|$.⁵

For the excitation of surface plasmons, only the photon wave vector projection to the x-direction is the relevant parameter. This means that by changing the angle of incidence, θ , one can tune $k_{ph}^x = k_{ph} \sin \theta$ from zero at normal incidence (Point 0 at Fig. 2-13) to the full wave vector $k_{ph}^x = k_{ph}$ at grazing incidence (Point A at Fig. 1-13), for a simple reflection of a photon with energy $E = \hbar\omega_L$ at a planar dielectric/metal interface. However, this is not sufficient to fulfill the momentum-matching condition for surface plasmon excitation (dashed curve at Fig. 1-13).

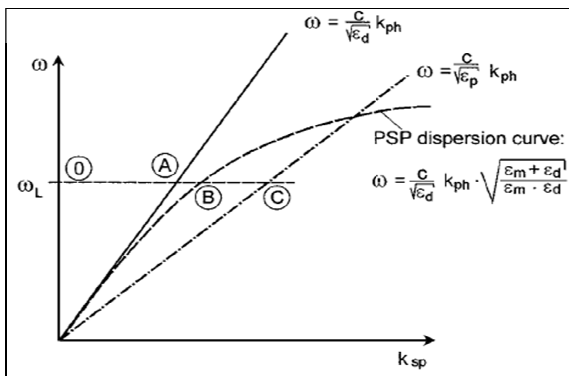


Figure 2-13. Dispersion relation of a photon travelling as a plane wave in the dielectric medium (full line), and of a photon propagating in the prism (dash-dotted line). Dispersion of the surface plasmon mode propagating along the metal/dielectric interface is represented by the dashed curve.⁵

One way to overcome this problem is by means of a prism coupler and the attenuated total reflection method (ATR). In the Otto geometry of the ATR method (Fig. 2-14, left), photons are not coupled directly to the metal/dielectric interface, but via the evanescent tail of light totally internally reflected at the base of a high-index prism ($\epsilon_p > \epsilon_d$).³⁴ This light is characterized by a larger momentum (dashed-dotted line at Fig.1-13) that for a certain spectral range can exceed the momentum of the surface plasmon to be excited at the metal surface. So, by choosing the appropriate angle of incidence θ_0 (Point B at Fig. 2-13), resonant coupling between evanescent photon and surface plasmons can be obtained.

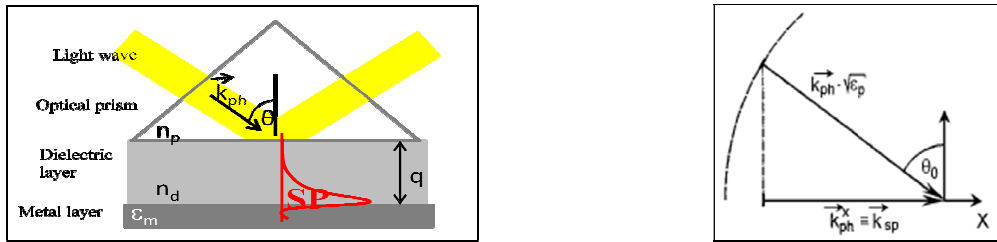


Figure 2-14. Excitation of surface plasmons in Otto geometry of the attenuated total reflection (ATR) method (left). Wavevector matching condition for the resonant coupling of photons traveling in the prism: at the incident angle θ_0 , the photon projection along the x-coordinate, \vec{k}_{ph}^x , matches the surface plasmon wavevector \vec{k}_{sp} (right).

The coupling between the incident light's evanescent wave and the surface plasmon corresponds to an attenuation of the reflected light intensity and can be observed as a maximum in the extinction spectrum.

2.2.2.2. Quantitative interpretation of SPR response

The angle θ and wavelength λ , at which surface plasmon resonance occurs, vary extremely sensitively with the refractive index (RI) n or the dielectric constant ε of the medium in contact with the sensor surface ($n = \sqrt{\varepsilon\mu}$, μ is the permeability of the material).

Thus, shifts in these parameters yield quantitative measurements of changes in the RI, Δn , of the medium to be interrogated. However, the medium may possess a more complex structure instead of a uniform RI, such as an adsorbed film in a liquid solution. In this case, the sensor response reflects some sort of average RI.¹⁰

1. SPR response to bulk solutions

Over a narrow range, the sensor response (R) to changes in bulk index of refraction in the absence of adsorption from the solution, can be approximated as linear

$$R = m \Delta n = m(n_{final} - n_{initial})$$

The magnitude of the slope, m , can be thought of as a sensitivity factor for the sensor (Fig. 2-15).

Over a larger range of n , a low-order polynomial equation should be used to describe the sensor response more explicitly

$$R = m_1 \Delta n + m_2 \Delta n^2$$

2. SPR response to adsorbed films

Figure 2-16 shows an idealized bilayer structure, wherein a thin adsorbed film of uniform thickness d and index of refraction n_a is bonded to the metal surface of an SPR sensor. Above this adsorbate layer there is a bulk liquid solution of index n_s .

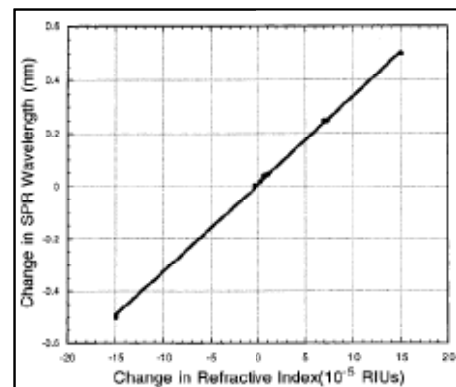


Figure 2-15. Measured SPR response (change in extinction maxima) over a narrow range of the bulk index of refraction near that for water ($n=1.330$). RIU=refractive index unit.¹⁰

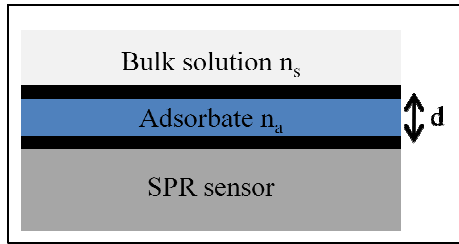


Figure 2-16. Schematic diagram of a bilayer structure involving an adsorbate a of thickness d and refractive index n_a directly on the SPR sensor surface. A solution s of refractive index n_s lies above the adsorbate film.¹⁰

The estimated SPR response can be appointed by the equations:

$$R = m(n_{eff} - n_s)$$

or

$$R = m_1 (n_{eff} - n_s) + m_2 (n_{eff} - n_s)^2$$

with n_{eff} as an effective refractive index for the bilayer, which can be calculated by averaging the index of refraction over the depth of the whole bilayer structure:

$$n_{eff} = (2/I_d) \int_0^{\infty} n(z) \exp(-2z/I_d) dz = n_s + (n_a - n_s)[1 - \exp(-2d/I_d)]$$

with I_d as the characteristic decay length in the direction perpendicular to the sensor surface, d the adsorbate layer thickness, and $n(z)$ the index of refraction at height z .

For linear calibration plot of SPR response versus bulk RI the equation becomes

$$R = m(n_{eff} - n_s) = m(n_a - n_s)[1 - \exp(-2d/I_d)]$$

and for more complex nonlinear calibration curve, the SPR response is determined by

$$\begin{aligned} R &= m_1 (n_{eff} - n_s) + m_2 (n_{eff} - n_s)^2 \\ &= m_1 (n_a - n_s)[1 - \exp(-2d/I_d)] + m_2 \{(n_a - n_s)[1 - \exp(-2d/I_d)]\}^2 \end{aligned}$$

It should be noted that the constants m , m_1 and m_2 would be determined first from calibration curves using bulk solutions (Fig. 2-17).

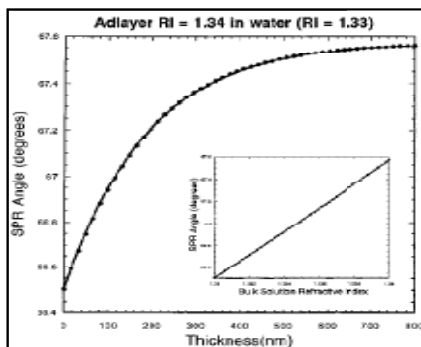


Figure 2-17. Calculated SPR response versus adlayer thickness for the bilayer structure of Fig. 1-14, for the special case where $n_a=1.330$, $n_s=1.340$, and $\lambda=825$ nm. Insert: calculated SPR response versus bulk index of refraction of a homogeneous solution for the special case where $\lambda=825$ nm. The sensitivity factor m is 107 per RIU.¹⁰

This simple but quantitative mathematical formalism for interpretation of surface plasmon resonance signals can be used to estimate adsorbed film thicknesses, surface coverages, or surface concentrations from the SPR response.

2.2.2.3. Methods of measurements

Commonly, SPR measurements are collected in one of these three modes: i) wavelength shift, ii) angle shift, and iii) imaging (Fig. 2-18). In the first two modes, the reflectivity of light from the metal surface can be measured as a function of either wavelength (at constant angle of incidence) or angle of incidence (at constant wavelength). The third method uses light of both constant wavelength and incident angle to interrogate a two-dimensional region of the sample, mapping the reflectivity of the surface as a function of position. This last method is commonly referred to as Surface Plasmon Resonance Imaging.³⁷

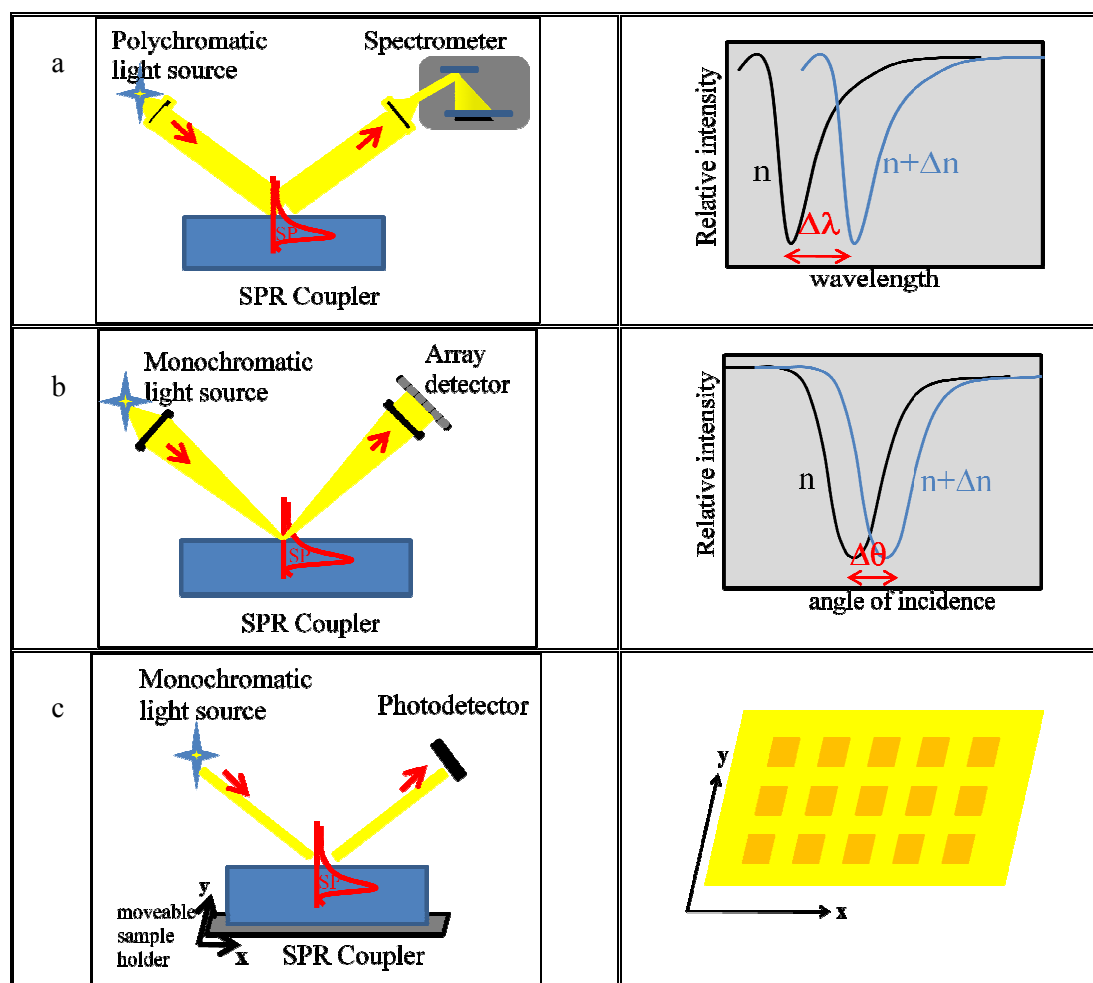


Figure 2-18. Methods of measurement in SPR-sensing: based on (a) wavelength shift, (b) angle-resolved, (c) imaging (see also Fig. 1-19).

The contrast in the SPR imaging is based on the different reflectance of the analyte and its background. Fig. 2-19 illustrates the generation of an SPR image. Since the location of the plasmon resonance shifts to higher angles upon adsorption of molecules, more light is reflected at a specific angle of incidence (α_{inc}) from the reactant dots (r_R) than from the regions of gold (r_{Au}). An additional shift of the SPR curve occurs upon interaction of analyte molecules with the reactant dot, which leads to a higher reflectance r_A .³⁸

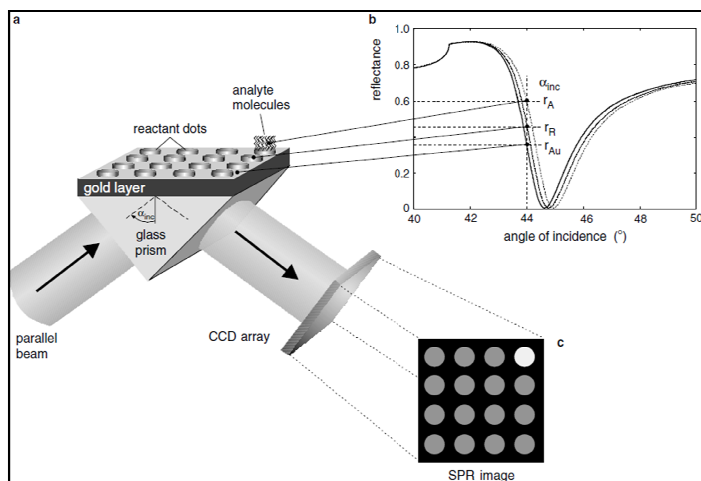


Figure 2-19. (a) Schematic diagram of SPR imaging. (b) Calculated SPR reflectance curves for a pure gold surface (solid line), a reactant dot (dashed line) and adsorbed analyte molecules on a reactant dot (dotted line). (c) The contrast of the SPR image is based on the different reflectance $r_A > r_R > r_{Au}$.³⁸

2.2.2.4. Application of surface plasmons in biosensing

The study of both propagating- and localized surface plasmons, have enabled a variety of applications, such as biological and chemical sensing, due to the dependency of the plasmon resonance condition on the interaction between the metal surface-confined electromagnetic wave and its molecular environment.

The immense usefulness of SPR imaging in monitoring the binding of analytes to arrays of bound species simultaneously, which saves time and sample volume, has been demonstrated in the work of Brockman et al.^{37,39} Detecting protein-DNA interactions was made possible by using a combination of multicomponent oligonucleotide arrays and SPR imaging.

Using SPR imaging and an antibody microarray with array element sizes varying from 750 μm down to 200 μm , Lee et al has successfully detected two clinically important protein biomarkers, β_2 -microglobulin and cystatin C, at solution concentrations down to 1 nM.⁴⁰

Van Duyne et al. demonstrated biomedically highly relevant application of LSPR sensing in their work, where a biomarker for Alzheimer's disease, amyloid-beta-derived diffusible ligand (ADDL), has been detected using LSPR spectroscopy. The limit of detection was estimated to be ~ 10 pM.⁴¹

Thus, LSPR technology is a very promising detection technique in clinical research, which can allow the diagnosis of diseases at their early stage utilizing an associated biomarker/antibody pair (such in ovarian cancer).

2.3. Protein-resistant films

One of the greatest challenges to biomaterials scientists is preventing the nonspecific, noncovalent surface adsorption of proteins, the well-known first step in undesirable reactions of the body to foreign materials, such as immune responses, blood coagulation, or bacterial adhesion, which can trigger inflammation in the vicinity of artificial organs or implants.

In diagnostic assays and biosensors based on specific recognition of antigen/antibody pairs, suppression of nonspecific protein adsorption is crucial for achieving sufficient bioassay selectivity and sensitivity.

Another example of the importance of preventing protein adsorption is in contact lenses. The elimination of lysozyme build-up on the surface of the lenses can improve their quality and reduce the need for cleaning.

Elimination of protein adsorption requires a system where repulsive interactions between proteins and the surface overcome the attractive ones. Due to the diversity of the interactions between proteins and surfaces, a preferred strategy for blocking the adsorption of proteins is to immobilize polymers in the form of well-solvated brushes, such as poly(ethylene glycol), on the surface. The polymer layer shields the surface, introducing a high activation barrier for the proteins to adsorb.

2.3.1. Poly(ethylene glycol) (PEG)

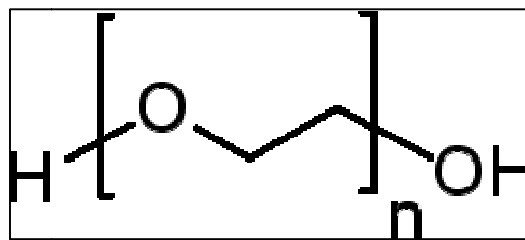


Figure 2-20. Poly(ethylene glycol) (PEG)

Poly(ethylene glycol) (PEG) is a synthetic, water-soluble polymer which is widely used in the chemical and biomedical field. PEG is nontoxic and does not harm active proteins or cells although it interacts with cell membranes. It can be modified chemically and readily attached to other molecules and surfaces. When attached to other molecules it has little effect on their chemistry but controls their solubility and increases their size. These properties have led to the application of PEG in a variety of cosmetics, lotions, soaps, and drug formulations.⁴²⁻⁴³

The ability of surface coatings containing poly(ethylene glycol) to prevent non-specific protein adsorption and cell adhesion has been recognized for decades and has resulted in many biomedical applications of this class of materials. However, the molecular mechanisms underlying protein resistance of grafted PEG have not yet been fully identified.

Several different aspects of the problem which are generally considered in understanding the protein repelling character of PEG are:

1. Steric repulsion

Jean and Andrade calculated the steric repulsion of grafted polymers on the adsorption of proteins on surfaces, based on the Alexander-de Gennes theory of polymer brushes. This approach is valid for very long polymer chains ($n > 1000$) and for relatively high surface coverage.^{11,44}

In this approach, PEG is assumed to be a neutral homopolymer with linear and flexible chains terminally attached to a hydrophobic substrate in water. Proteins are treated as homogeneous, infinite particles, and are thus considered as a plate in water (Fig. 2-21). The crucial parameters are the distance D between the terminally attached PEG chains,

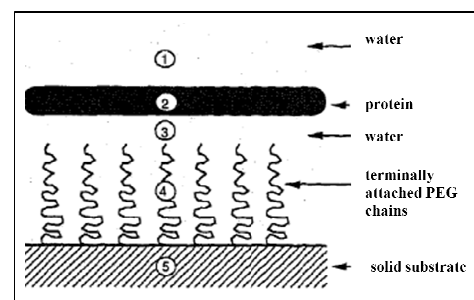


Figure 2-21. Schematic drawing of terminally attached PEG chains to a solid substrate with a protein of infinite size in water solvent; model for the Alexander-de Gennes theory of polymer brushes.¹¹

an extent of the surface density; and the degree of polymerization, N , a measure of the chain length.

To calculate the steric repulsion free energy per unit surface area, two effects – osmotic pressure and elastic restoring force – are taken into account. The contribution of each effect is taken as the proportionality constants k_1 and k_2 , which are different for each polymer-solvent system. Hence, the steric repulsion free energy is given by

$$\frac{F_s(z)}{k_B T} = \frac{k_1}{a^2} \left(\frac{7 k_2}{5 k_1} \right)^{5/12} N \sigma^{11/6} \left[\left[\left(\frac{h}{z} \right)^{5/4} - 1 \right] + \frac{5}{7} \left[\left(\frac{z}{h} \right)^{7/4} - 1 \right] \right]$$

with h as the height of the brush and is given by $h = \left(\frac{5}{7} k_1 / k_2 \right)^{1/3} a N \sigma^{1/3}$, a the monomer size- and σ the surface density of PEG, $k_B T$ is the product of Boltzmann constant and the temperature of the system.

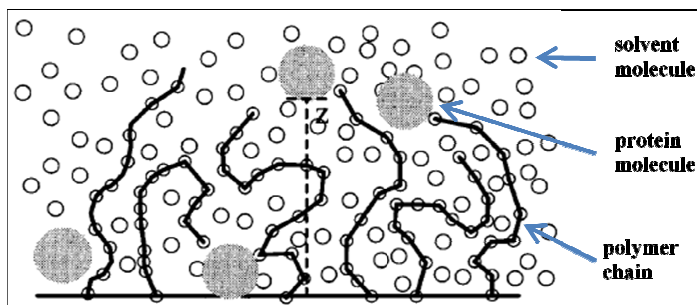


Figure 2-22. Schematic drawing of the single-chain mean-field (SCMF) model. The connected circles represent the polymer chains, the small circles are the solvent molecules, and the large circles are the protein molecules.¹¹

On the other hand side, thermodynamic and structural properties of grafted polymer layers composed of intermediate-chain-length molecule ($30 \leq n \leq 100$) was best described by the single-chain mean-field (SCMF) theory.⁴⁵⁻⁴⁶

Szleifer calculated the potential of mean force between a surface and a protein in the presence of the polymer layer based on the SCMF theory (Fig. 1-22)⁴⁷⁻⁴⁸, which is given by

$$U(z) = \int_z^\infty \pi(z') v_p(z') dz' + \int_z^\infty \epsilon_{pg} a_{p,z}(z') \langle \phi_g(z') \rangle dz' + U_{ps}(z)$$

where $\pi(z')$ and $\langle \phi_g(z') \rangle$ are the lateral pressure and the polymer density profile of the polymer layer, $v_p(z') dz'$ is the volume that a protein occupies at z' , ϵ_{pg} is the strength of the protein-polymer attraction, and $a_{p,z}(z') dz'$ is the area of contact of a protein at z' with the solution. The first term represents the average repulsions felt by the protein molecule due to the grafted polymers, the second term represents the attractive protein-polymer-interactions, and the last term is the bare surface-protein-attractive interaction.

2. Hydration shell

When the molecular weight of the PEG exceeds a certain number, it will be able to fold on itself. This folding will permit a loose sharing of bound water molecules within the folds, averaging approximately 2-3 water molecules per repeat unit. The sharing of bound water creates an excluded volume from which protein will be repelled. If a protein molecule attempts to compress this hydrated PEG coil, it will take energy to remove the bound water molecules, while at the same time the PEG coil will lose entropy. Thus, even though the released water molecules would gain entropy, the overall free energy of the system will rise

and this process will not occur spontaneously. This thermodynamic model explains the increasing protein resistance of PEG with higher chain-length.⁴²

3. Protein binding sites

The lack of protein binding sites (ionic and hydrophobic) on PEG help in lowering the affinity of proteins to adsorb onto a PEG coated surface.

2.3.2. Immobilizing PEG onto surfaces

PEG coatings on surfaces can be prepared following two main strategies: (i) the *grafting to* and (ii) the *grafting from* strategies. The *grafting to* strategy involves the attachment of presynthesized polymers via either physisorption or chemisorption. In the *grafting from* approach, the polymerization is directly initiated from initiator-functionalized surfaces.⁴⁹

2.3.2.1. Chemisorption

A dense film of poly(ethylene glycol) on a gold surface can be formed by immersing a gold-coated wafer for 12 h to 1 week in ethanolic solutions of the PEG-terminated alkanethiols in a concentration regime of several millimole per liter.

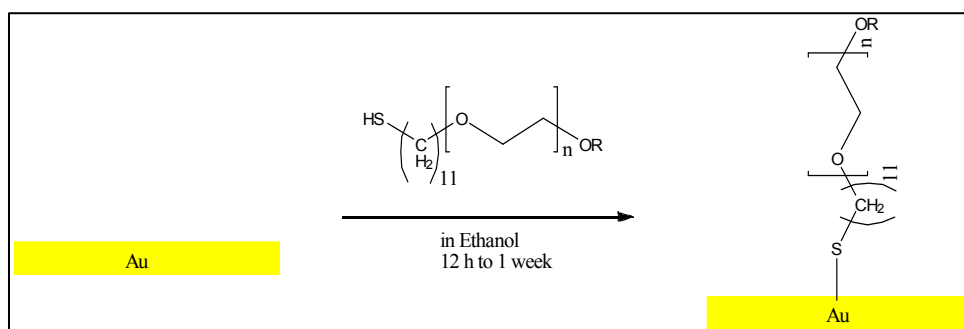


Figure 2-23. Self-assembled monolayer of PEG molecules on gold

These self-assembled monolayers (SAMs) of PEG-terminated alkanethiols form a dense “non-fouling” brush that confers protein resistance to the gold surface, and are arguably the best non-fouling systems that are currently available.⁵⁰⁻⁵¹

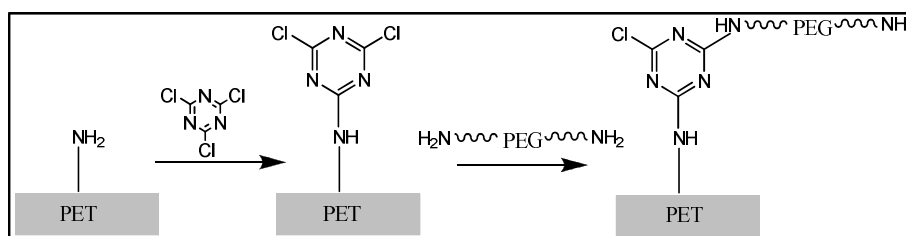
Although poly(ethylene glycol) SAMs on gold exhibit significantly better protein resistance than a PEG film prepared by physisorption or covalent grafting, they have several limitations: because SAMs are a single molecular layer, they have limited robustness, which is further exacerbated by the existence of defects in the SAM and the propensity of the chemisorbed thiolate to oxidize. An additional problem with PEG surfaces prepared by simple adsorption techniques is their tendency to elute off the surface, particularly in a solution containing proteins which are highly surface active agents.

2.3.2.2. Covalent grafting

More stable films have been prepared by covalently bonding PEG directly to a substrate. Direct attachment of PEG to a substrate usually requires derivatizing the hydroxyl tailgroups of the PEG molecule with an active coupling agent. Alternatively, the hydroxyl tailgroups on of PEG can be reacted with active coupling agents which have been immobilized onto the

surface. In some cases both of these approaches can be combined (i.e., reacting a derivatized PEG molecule with an activated substrate).

Gombotz et al. created a stable layer of PEG on a poly(ethylene terephthalate) (PET) film using cyanuric chloride activation chemistry. The PET film was first functionalized with amino groups by exposure to an allylamine plasma. The surface amino groups were next activated with cyanuric chloride and then reacted with bis-amino PEG molecules.⁵²



2.3.2.3. Physisorption

Another approach to immobilize PEG onto surfaces is the grafting of PEG side chains to a polymer backbone, resulting in the formation of a comb-like structure. This copolymer is then attached to the surface through electrostatic interaction. For example, graft copolymers of poly-L-lysine with PEG side chains (PLL-PEG) have shown the ability to adsorb onto a variety of substrate materials including glass and metal oxides (Fig. 2-25). The positively charged PLL backbone sticks to the negatively charged substrates, providing stability for the adsorbed layer. The PEG side chains stretch away from the surface, forming a protein-resistant layer.^{21,43}

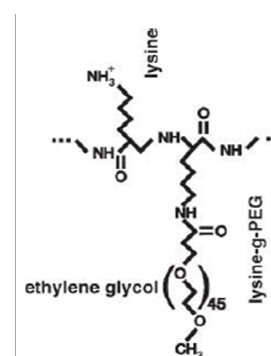


Figure 2-25. Chemical structure of poly-L-lysine-graft-poly(ethylene glycol) (PLL-PEG).¹³

Despite the widely demonstrated applicability of PLL-PEG for surface blocking such as for generating protein patterns and gradients, the use of PLL-PEG suffers from the fact that it is rather expensive. In 2010 a low-cost PLL-PEG analog was introduced by Ionov et al.

A random copolymer of 2-aminoethyl methacrylate and poly(ethylene glycol) methyl ether methacrylate (AEM-PEG) comprises a positively charged backbone and PEG side chains, thus, mimicking the structure of PLL-PEG (Fig. 2-26). The protein resistance of AEM-PEG functionalized glass substrates is comparable to the surface blocking based on PLL-PEG.¹³

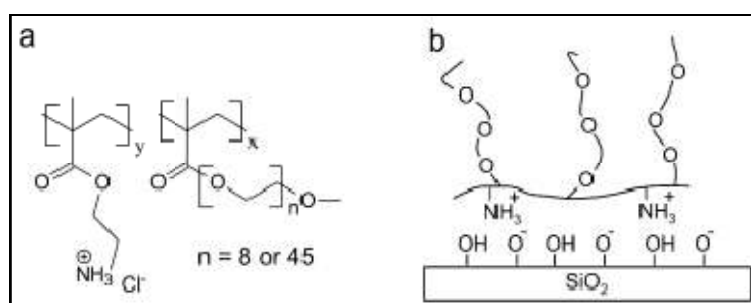


Figure 2-26. (a) Chemical structure of 2-aminoethyl methacrylate hydrochloride and poly(ethylene glycol) methyl ether methacrylate. The number of monomer units are denoted by x and y and the number of the PEG side chains is given by n . (b) Schematic representation of AEM-PEG adsorption onto negatively charged surfaces.¹³

By using ionic interactions, Kidambi et al. demonstrated the fabrication of patterned SAMs of m-d-poly-(ethylene glycol) (m-dPEG) molecules (cf. Fig. 2-27) on polyelectrolyte multilayers (PEMs). First, PEMs are formed using the layer-by-layer (LbL) assembly technique⁵³⁻⁵⁴ by immersing a glass slide for 20 minutes in a polyelectrolyte solution. This process was repeated to build up multiple layers. Afterwards, patterned SAMs on PEMs were created by using microcontact printing (μ CP).⁵⁵⁻⁵⁷ An elastomeric stamp, made from poly(dimethylsiloxane) (PDMS), was immersed in a solution of m-dPEG for 20 minutes and brought into contact with the substrate for 10-15 min at room temperature.¹⁵

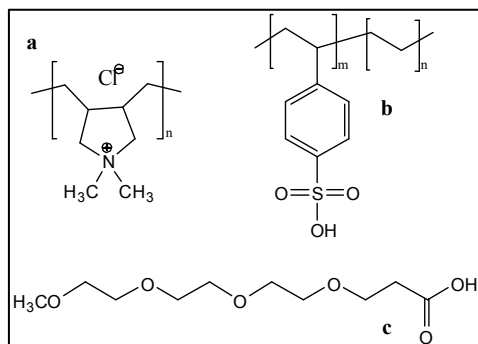


Figure 2-27. Strong polyelectrolytes are used to form polyelectrolyte multilayers (PEM): (a) sulfonated polystyrene and (b) poly(diallyldimethylammonium chloride); (c) m-d-poly(ethylene glycol) (m-dPEG) acid.¹⁵

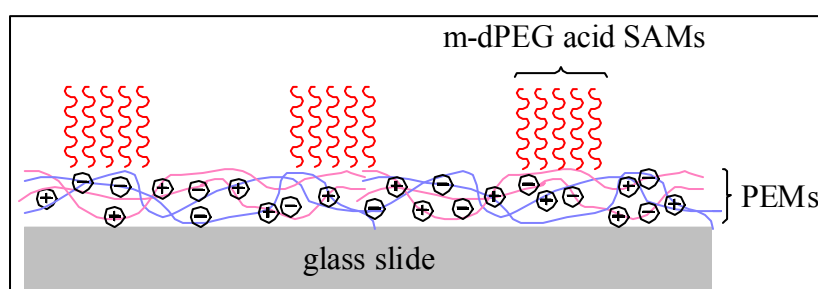


Figure 2-28. Attachment of PEG molecules onto surfaces by physisorption.

Selective deposition can be achieved by introducing alternating regions of different chemical functionalities on a surface (Fig. 2-28). Here, an m-dPEG molecule with an activated carboxylic acid group at the end can be stamped directly onto multilayer films to form a patterned SAM, by carefully selecting surface chemistry and taking advantage of electrostatic interactions between the top surface of the multilayer film and the stamped molecule.

After transferring m-dPEG monolayer patterns onto the PEM surfaces, subsequent deposition of PEMs resulted in 3-D heterostructures on the non-m-dPEG-SAM regions. These new patterned and structured surfaces have potential applications in micro-electronic devices, electro-optical and biochemical sensors.

Physisorption or covalent grafting (the -grafting to- approach) typically results in a low surface density of PEG chains (e.g., $< 4 \mu\text{g cm}^{-2}$), due to steric repulsion between polymer chains which hamper the formation of dense polymer brushes. Furthermore, with increasing polymer molecular weight, the reaction between the polymer end-group and the complementary group on the substrate surface becomes less efficient. An exception was the carboxy-functionalized PEG-alkanethiols $[\text{HOOC-CH}_2\text{-(OCH}_2\text{-CH}_2\text{)}_n\text{-O-(CH}_2\text{)}_{11}\text{-SH}$, $n=22-45$], which utilize a two-step adsorption mechanism when adsorb on polycrystalline gold. The globular thiol molecules first adsorb from solution to form an amorphous film at low grafting density and then transformed into a dense brushlike state.⁵⁸

2.3.2.4. Atom Transfer Radical Polymerization

Surface-initiated atom transfer radical polymerization (SI-ATRP) offers another, complementary route for the in-situ synthesis of a highly-dense PEGylated polymer on a surface.^{12,59-63} The protein-resistant film formed by using SI-ATRP combines the advantages of SAMs, namely their high surface density and ease of formation, with those of polymers —

thicker and more robust films with versatile architecture and chemistry. SI-ATRP is one example of the *grafting from* strategy in preparing polymer brushes on surfaces.

Atom Transfer Radical Polymerization (ATRP) belongs to the class of living polymerization and has proved to be one of the methods for precision polymer synthesis. Since the initiation is faster than or at least comparable to the propagation rate, the obtained polymers have a narrow molecular weight distribution (MWD). Hence, a polymer film generated on a surface by ATRP will have an almost equal overall thickness.

ATRP can be carried out under mild reaction conditions and allows a wide range of functional groups to be present in the monomer, solvent, or initiator, and thus can be applied to a broad spectrum of polymeric systems.

The reaction is initiated by the homolytic cleavage of the carbon-halogen bond in the organic halide via one electron oxidation of the metal center ($M^nX_nL_m$) to form an initiating radical species ($R\bullet$). The $R\bullet$ reacts with the unsaturated species (monomer) to generate a radical species $[R-CH_2-C(R_1)(R_2)\bullet]$. This radical intermediate attacks the next monomer successively and generates a polymer chain (Fig. 2-29). The key factors in preventing a high polydispersity index are the low concentration of the radical intermediates and their fast but reversible transformation into a dormant species before undergoing successive addition to monomers.

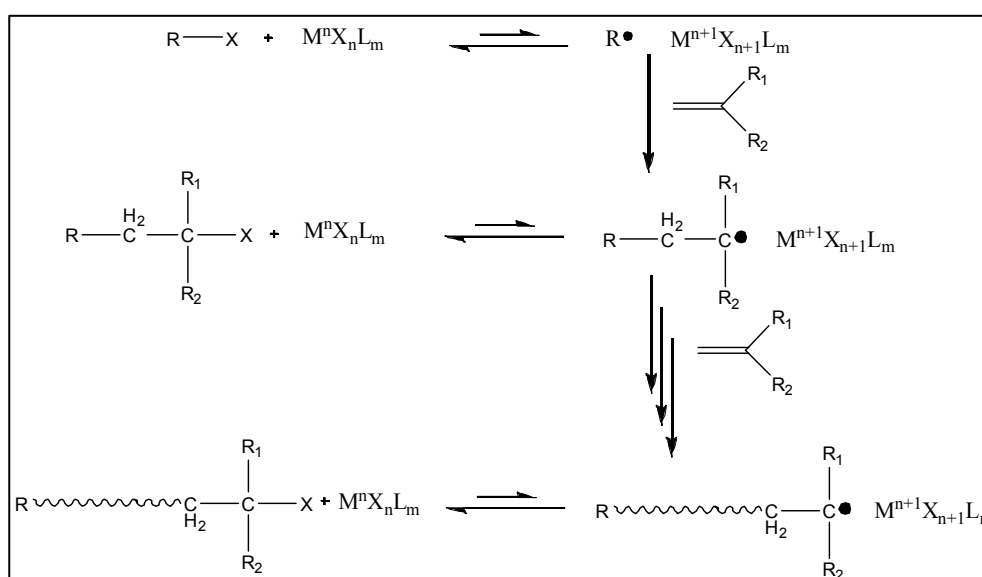


Figure 2-29. Mechanism of ATRP by Kamigaito et al.¹²

ATR-polymerization on a surface is realized by the immobilization of the initiator molecules onto a surface, followed by polymerization of the desired monomer solely from the surface with help of a transition-metal catalyst (Fig. 2-30).¹²

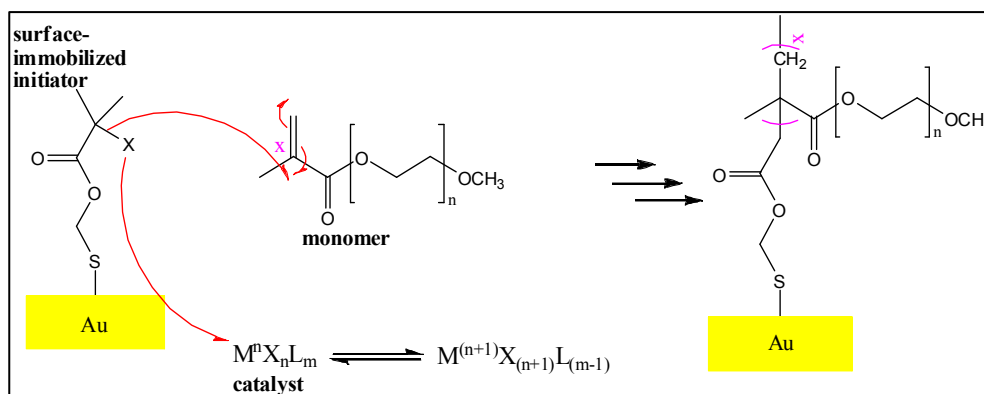


Figure 2-30. Scheme of surface initiated atom transfer radical polymerization (SI-ATRP) on gold.

Ma et al. reported that oligo(ethylene glycol) methyl methacrylate (OEGMA) could be polymerized from an alkanethiol SAM on gold that was functionalized with a terminal ATRP initiator. The resulting poly(OEGMA) brushes grown from the surface reduced the adsorption of proteins from 100% serum to below the 1 ngcm^{-2} detection limit of SPR spectroscopy.

Stadler et al. synthesized various graft copolymer films of poly(ethylene glycol) methacrylate (PEGMA) and methyl methacrylate (MMA) on silicon to examine the dependency of protein-surface interactions on grafting composition. A breakdown of the protein-repelling properties was only observed for 15% PEGMA and lower, which indicated a prevalence of the sterical repulsion by PEG side chains over the attractive hydrophobic interaction of proteins with a surface. This result might lead to applications of PEGMA/PMMA coatings in biomaterials, which combine the biocompatibility of PEGMA with the higher stability of PMMA.

2.3.2. Zwitterionic polymers

In recent years, zwitterionic polymers containing the pendant groups phosphobetaine, sulfobetaine, and carboxybetaine have received growing attention for use in a new generation of blood-contacting materials because of their good plasma-protein-fouling resistance. When a plasma protein approaches an interface, electrical neutrality plays an important role in minimizing the electrostatic interactions, and the absence of hydrogen-bond donors helps in minimizing the hydrogen-bonding interactions.⁶⁴ Thus, surfaces grafted with zwitterionic polymers are ideal for resisting nonspecific protein adsorption when the surface density and chain length of the zwitterionic groups are controlled, yielding excellent properties with respect to antithrombogenic response.

There are two types of zwitterionic polymer brushes: (i) homopolymer brushes such as poly(sulfobetaine methacrylate) (polySBMA), with a methacrylate main chain and an analog of taurine betaine as the pendant group,⁶⁵ (ii) mixed-charge copolymer brushes such as an polyampholyte system. A copolymer brush derived from the combination of the positively charged 11-mercapto-*N,N,N*-trimethylammonium chloride (TMA) and negatively charged 11-mercaptoundecylsulfonic acid (SA) was presented by Chang et al. as an example of the pseudozwitterionic polyampholytes.⁶⁶ Both polymers were synthesized on surfaces by using SI-ATRP.

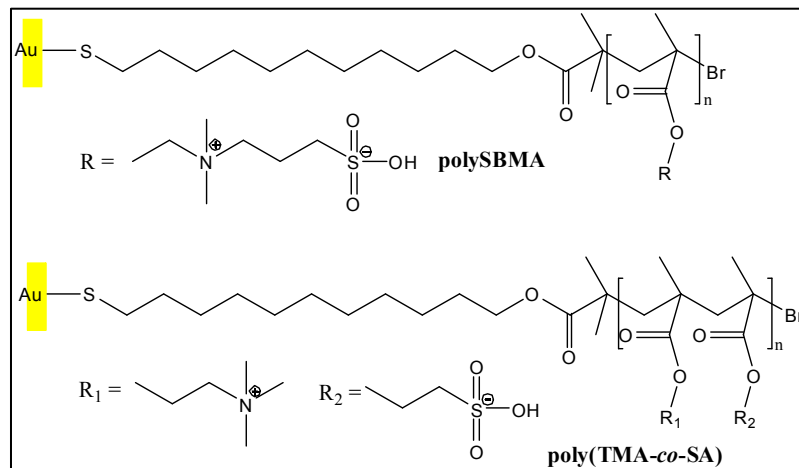


Figure 2-31. Chemical structures of gold surfaces with polySBMA polymer brushes, and mixed-charge poly(TMA-co-SA) copolymer brushes.

2.4. Surface analysis methods

2.4.1. Excitation and detection of surface plasmons

Surface plasmons -propagating along an interface between a metal and a dielectric material can be excited by light in the UV-Visible regime. The wavelengths, at which surface plasmons are excited, is analyzed using a UV-Vis-spectrometer. The main components of the corresponding set-up –light source, spectrometer and optical fibers to guide the incoming and reflected light- are discussed in the following.⁶⁷

Light source

Exciting the surface plasmons on the LSPR biosensor requires a *continuum light source* which produces a continuous spectrum in the UV and visible regions. In the UV and visible regions, lamps utilizing a gas discharge are frequently applied. In the tube the gas is ionized, and free electrons, accelerated by the electrical field in the tube, collide with gas and metal atoms. Some electrons circling around the gas and metal atoms are excited by these collisions, bringing them to a higher energy state. When the electron falls back to its original state, it emits a photon, resulting in visible light or ultraviolet radiation.

Spectrometer

The resolving power R of a spectral resolution instrument is defined by

$$R = \frac{\lambda}{\delta\lambda}$$

where $\delta\lambda$ is the resulting linewidth of the spectral apparatus when using monochromatic light of wavelength λ . The most widely used types of spectrometers are the prism- and the grating spectrometers. In the optical arrangement for the detection of reflected light on the LSPR biosensor a grating spectrometer is applied.

A reflection grating is used for the spectral separation in a *grating spectrometer*. The resolving power R of the grating is determined by the total number of illuminated lines N and by the diffraction order m .

$$R = \frac{\lambda}{\delta\lambda} = N \cdot m$$

Optical Fiber Waveguide

The basic principle of optical fiber waveguide is the waveguiding of light in a planar three layer guide, which can be described by Snell's law of refraction coupled with the phenomenon of total internal reflection (Fig. 2-32).⁶⁸

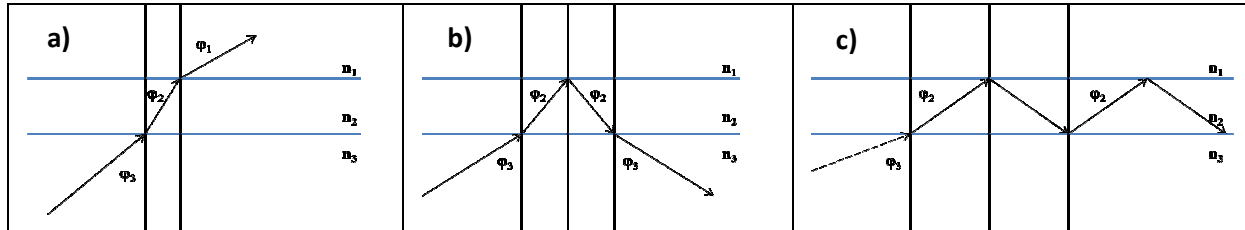


Figure 2-32. Light path for (a) air radiation mode, (b) substrate radiation mode, (c) guided mode.

The angles of incidence and refraction, φ_i ($i = 1, 2, 3$), are measured with respect to the normals to the interface planes. From Snell's law

$$\sin \varphi_1 / \sin \varphi_2 = n_2 / n_1$$

and

$$\sin \varphi_2 / \sin \varphi_3 = n_3 / n_2.$$

Wenn φ_3 is small, the light ray passes freely through both interfaces, suffering only refraction (Fig. 1-34a). As φ_3 is increased beyond the point at which φ_2 exceeds the critical angle for total internal reflection at the $n_2 - n_1$ interface, that light wave becomes partially confined as shown in Fig. 1-34b, corresponding to a substrate radiation mode. The condition for total internal reflection at the $n_2 - n_1$ interface is given by

$$\varphi_2 \geq \sin^{-1}(n_1/n_2)$$

$$\varphi_2 \geq \sin^{-1}\left(\frac{n_1}{n_3 \sin \varphi_3 / \sin \varphi_2}\right)$$

$$\Leftrightarrow \varphi_3 \geq \sin^{-1}(n_1/n_3).$$

As φ_3 is further increased beyond the point at which φ_2 also exceeds the critical angle for total internal reflection at the $n_2 - n_3$ interface, the light wave becomes totally confined, corresponding to a guided mode. In this case, the critical angle is given by

$$\varphi_2 \geq \sin^{-1}(n_3/n_2).$$

2.4.2. X-ray Photoelectron Spectroscopy (XPS)

A photon of sufficiently high energy can ionize an atom, producing an ejected free electron. The kinetic energy **KE** of the electron (the photoelectron) depends on the energy of the photon $h\nu$ expressed by the Einstein photoelectric law:⁶⁹⁻⁷⁰

$$h\nu = E_b + \text{KE} + \Phi$$

where E_b is the binding energy of the particular electron to the atom concerned and Φ the work function of the instrument. Since $h\nu$ is known, a measurement of KE determines E_b .

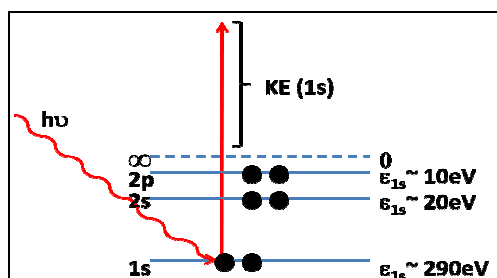


Figure 2-33. Schematic representation of the electronic energy levels of a C atom and the photoionization of a C 1s electron.

Since the binding energy is elemental characteristic, the XP-spectrum contains specific informations about the chemical environment on top of the substrate. Depending on the energy range of the radiation (typically 200-2000 eV), the material, and the collection angle, XPS enables a surface analysis for a penetration depth of approx. 10 nm.

Surface sensitivity analysis

Electrons in XPS can travel only short distances through solids before losing energy due to collisions with atoms. Only photoelectrons ejected from atoms close-by the surface escape unscattered and appear in the XPS peaks. Electrons originating from deeper regimes have correspondingly reduced chances of escaping unscattered and mostly end up in the background at lower KE after the XPS peak, as shown in Fig. 2-34a. Thus, the peaks originate mostly from atoms near the surface, the background mostly from the deeper regime of the sample. This is the reason for the surface sensitivity of XPS.

The inelastic mean free path length (λ_e), which determines quantitatively exactly how surface sensitive the measurement is, depends on the kinetic energy KE of the emitted electron and the material through which it travels. Empirical relationships between KE and λ_e are plotted in Fig. 2-34b for a variety of elements.

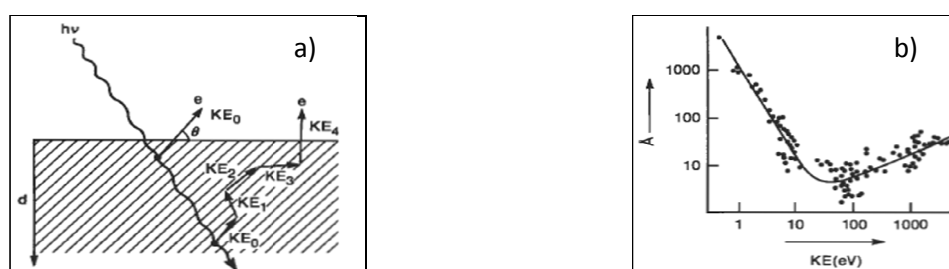


Figure 2-34. (a) Schematic of inelastic electron scattering occurring as a photoelectron tries to escape the solid, starting at different depths. (b) Mean free path lengths λ_e as a function of the kinetic energy of the emitted electrons.⁶⁹

Quantitative analysis

XPS can also be used for quantitative analysis since the intensities of the photoelectron peaks are related to the amount of each element. The intensity expected in a photoelectron line at kinetic energy KE from a pure reference sample of element A is given by:

$$I_A^0 = \sigma_A(h\nu) J_0 L_A(\nu) Q(KE) N_A^0 \lambda_A(KE) \cos \theta$$

where $\sigma_A(h\nu)$ is the cross section for photoemission for the line of interest from element A at photo energy $h\nu$, J_0 is the X-ray photon flux at the sample surface, $L_A(\gamma)$ is the angular asymmetry parameter for the photoelectron line concerned and an include angle γ between the incoming photons and the outgoing photoelectrons, $Q(KE)$ is a term describing the transfer characteristics of the spectrometer, N_A^0 is the number density of atoms in the pure reference sample, $\lambda_A(KE)$ is the attenuation length for photoelectrons of kinetic energy KE in element A, and θ is the angle of emission of the photoelectrons measured from the sample normal.⁷¹ XPS measurements are normally performed with a take-off angle of zero degree, thus $\cos \theta$ equals one.

Instrumentation

An XPS spectrometer schematic is shown in Fig. 2-35. The X-ray source is usually an Al- or Mg-coated anode struck by electrons from a high voltage (10-15 kV) source. AlK_{α} or MgK_{α} radiation lines are chosen as the beam source due to their relatively high energy and narrow width (Table 2-1).

Table 2-1. General properties of Mg K_{α} and Al K_{α} X-ray radiation source⁷²

X-ray source	Energy (eV)	Width (eV)
Mg K_{α}	1253.6	0.70
Al K_{α}	1486.6	0.85

The X-rays flood a large area ($\sim 1 \text{ cm}^2$). The beam's spot size can be reduced to about 100- μm diameter by focusing the electron beam onto the anode and passing the X rays through an X-ray monochromator. Electron lenses slow the electrons before entering the analyzer to improve the energy resolution. The most popular analyzer consists of two concentric hemispheres with a voltage applied between them. The XPS spectrum is produced by varying the voltages on the lenses and the analyzer so that the trajectories of electrons ejected from the sample at different energies are brought to a focus at the analyzer exit slit. A channeltron type electron multiplier behind the exit slit of the analyzer amplifies individual electrons by 10^5 - 10^6 , and each such pulse is transferred to an external conventional pulse counting electronics and into a computer. The computer also controls the lens and analyzer voltages. A plot of electron pulses counted against analyzer voltage yields the photoelectron spectrum.

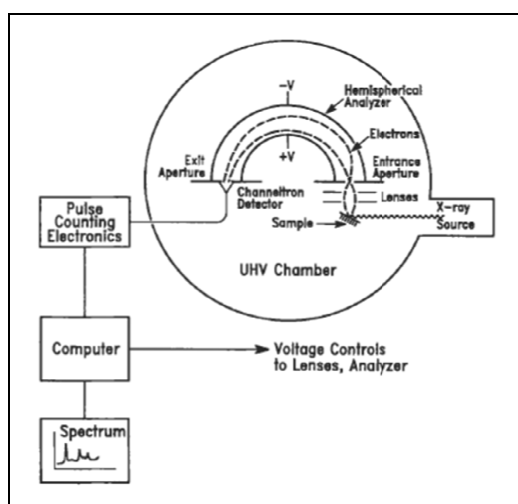


Figure 2-35. Schematic of an X-ray photoelectron spectrometer

2.4.3. Scanning Electron Microscopy (SEM)

A scanning electron microscope is a type of electron microscope that images the surface of a sample by scanning it with a focused high-energy beam of electrons in a raster scan pattern.^{8,69,73}

The theoretical limit to an instrument's resolving power is determined by:

$$r = \frac{\lambda}{2NA}$$

where r is the resolving power, λ is the wavelength of light used, and NA is the numerical aperture of the system. As a consequence of de Broglie relation $E = h\frac{c}{\lambda}$ with E as the energy, h the Planck's constant, and c the speed of light in vacuum, the wavelength of high-energy electrons used in SEM (typically 1-10 keV) lies in the regime of hundreds nanometers. Thus, the resolution of the SEM can approach a few nm.

2.4.3.1. Basic Principle

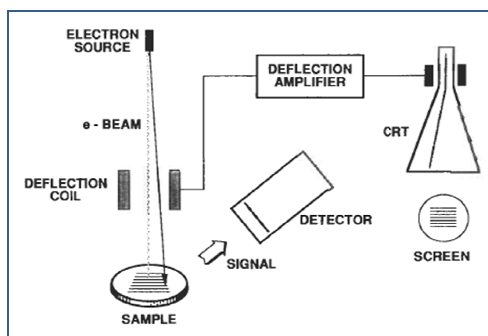


Figure 2-36. Schematic operation of SEM⁸

In the SEM, electrons are focused in vacuum into a fine beam that is scanned over the surface of the specimen. As the electrons penetrate the surface, different types of interactions can occur which result in the emission of electrons or photons from the surface. Emitted electrons are collected by the detectors, and the output is used to modulate the brightness of a cathode ray tube (CRT). In this way an image is produced on the CRT; every point that the beam strikes on the sample is mapped directly onto a corresponding point on the screen.

The main features of the SEM instrument are the electron column containing the electron source (i.e., the gun), the magnetic focusing lenses, the sample vacuum chamber and stage region (at the bottom of the column) and the electronics console containing the control panel, the electronic power supplies and the scanning modules.

2.4.3.2. Sample-Beam Interactions

The volume (both depth and width) of the sample-beam interaction varies directly with the accelerating voltage and inversely with the average atomic number of the sample.⁸

Secondary electron images

When a primary electron interacts with an atom, it undergoes either inelastic scattering with atomic electrons or elastic scattering with the atomic nucleus. In an inelastic collision with an electron, some amount of energy is transferred to the other electron. Because of their low energy, SEs are strongly absorbed by the sample. Thus, only the secondary electrons produced near the surface of the sample can escape because of the decreased path length to the surface.

The escape of SEs contributes to the topographical image in the SEM. Small projections on the sample surface have areas of shorter path length for the escape of secondary electrons than flat areas. Such areas appear bright on the image. Because the secondary electrons escape from a small volume of the total sample-beam interaction volume, the secondary electrons produce the image of highest resolution (~ 4 nm).

Backscattered electron images

Higher energy electrons are primary electrons that have been scattered elastically by the nucleus of an atom. The higher the atomic number of a material, the more likely it is that backscattering will occur. Consequently the image brightness will increase by increasing atomic number. BSEs are therefore very useful in detecting the presence of differences in average atomic number of a sample.

BSEs are produced from nearly entire area of sample-beam interaction and are not strongly absorbed by the sample because of their high energy. Because of the large width of escape, the resolution for an SEM image using backscattered electrons exceeds that of SE image (15 nm).

3. Materials and Methods

3.1. Fabrication of LSPR biosensors based on optical responsive materials

3.1.1. Materials

Clean room cleaned glass coverslips were purchased from Schott (Jena, Germany).

Gold (99.99%), titanium (99.995%) and silicon oxide granulate (99.99%) were obtained from Kelpin (Leimen, Germany).

Amino-functionalized silica nanospheres with diameters of 510 nm and 970 nm were received as solids from Polysciences, Inc. (Warrington, PA, USA).

16-mercaptohexadecanoic acid (99%), *N*-hydroxysuccinimide (NHS, 97%), *N*-(3-dimethylaminopropyl)-*N*-ethylcarbodiimide hydrochloride (EDC, 98%), and Triton X-100 were purchased from Sigma-Aldrich (Munich, Germany). Methanol p.a. was obtained from AppliChem GmbH (Darmstadt, Germany).

Hydrogen tetrachloroaurate(III) trihydrate (99.9+%), trisodium citrate dehydrate (99+%), sodium borohydride (99%), hydroxylamine hydrochloride (99.9999%), polyethyleneimine (PEI, MW=25000 Da), and phosphate-buffered saline (PBS, pH 7.4) were obtained from Sigma-Aldrich (Munich, Germany).

Millipore cartridges from Millipore GmbH (Eschborn, Germany) were used to purify water to a resistivity of $18.2 \text{ M}\Omega\text{cm}^{-1}$.

All materials were used without further purification.

A 150 W mercury vapor pressure lamp (TQ 150) from Heraeus Noblelight (Hanau, Germany) was used for UV radiation.

3.1.2. Deposition of the bottom gold layer

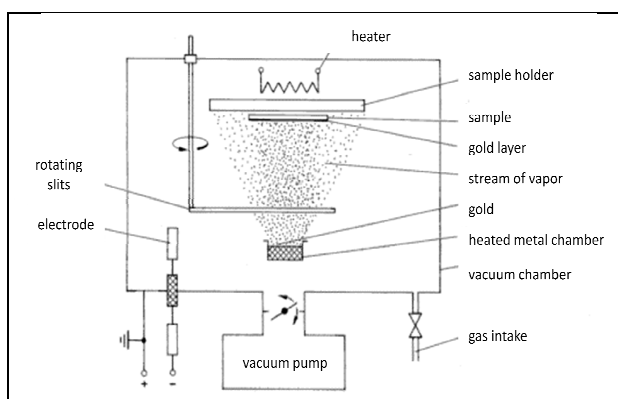


Figure 3-1. Design of the home-built thermal evaporator⁹

Consecutive layers of titanium (5 nm) and gold (100 nm) were sputtered on top of a glass coverslip by physical vapor deposition (PVD). Thin titanium films are applied to promote adhesion between the gold layer and the substrate.

A home-built thermal evaporator (Fig. 3-1) was used for evaporation at a base pressure of $2 \cdot 10^{-8}$ Torr. The growth rate was monitored by a quartz crystal micro balance and adjusted to $15\text{-}20 \text{ \AA/s}$.⁹

3.1.3. Deposition of the dielectric layer

3.1.3.1. By simple incubation

The gold-coated glass was covered with a COOH-terminated self-assembled alkanethiolate monolayer adsorbed from a 1 mM aqueous solution of 16-mercaptohexadecanoic acid after cleaning the substrates by UV irradiation.

The surface-bound thiols were activated by transforming the carboxylic acid groups exposed on the surface into ester groups. For this purpose, the substrate was immersed in a freshly prepared solution of 0.05 M NHS and 0.2 M EDC in a 1:1 volume ratio for 7 min.

In the next step the substrate was incubated in a 0.1 g/ml solution of amino-functionalized silica particles in Millipore water for 1 hour, then removed from the solution, rinsed with Millipore water, and dried in a stream of nitrogen.

3.1.3.2. By spin coating

Two-dimensional (2-D) colloidal assemblies have been investigated for applications including anti-reflection coatings, gratings, and photolithographic masks. Densely close-packed 2-D particle monolayers could be fabricated using spin-coating, Langmuir Blodgett (LB)-techniques, thin laminar flow liquid film, monolayer transfer, and electrophoretic deposition.⁷⁴

Spin coating is a simple and fast procedure used to apply uniform thin films to flat substrates (Fig. 3-2). An excess amount of a particle solution is placed on the substrate, which is then rotated at high speed in order to spread the fluid by centrifugal force. The sizes of the highly ordered domains are dictated by the spinning parameters and composition of the coating fluid, e.g. addition of the appropriate surfactant concentration.

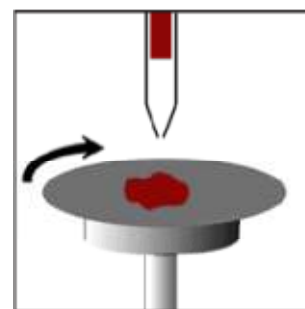


Figure 3-2. Spin coating

Surfactants are amphiphilic molecules, which contain both hydrophobic hydrocarbon chains and hydrophilic moieties (Fig. 3-3). Surfactants can adsorb to a significant extent even at a very low concentration. Above a threshold concentration, they can also form aggregates in solution and at solid/liquid interfaces by hydrophobic interactions. Such adsorption of surfactants on a solid can lead to changes in a variety of interfacial properties such as wetting behavior (oil displacement, flotation, detergency) and colloid stability (dispersion, flocculation).⁷⁵ Triton X-100, which was mixed into the silica particle suspension, belongs to the class of non-ionic surfactants.

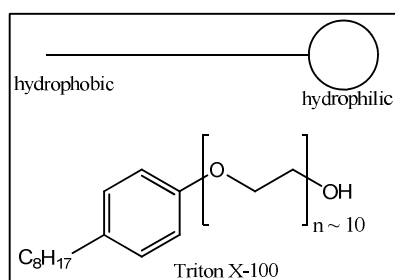


Figure 3-3. Surfactant molecule (Triton X-100) containing a hydrophilic head and a hydrophobic tail.

Deposition of the dielectric layer by spin coating

Gold-coated glass substrates (100 Au on 5 nm Ti) were first cleaned by UV irradiation, and subsequently functionalized with 16-mercaptohexadecanoic acid from a 1 mM aqueous solution. The substrate was immersed into a freshly prepared aqueous mixture of 0.05 molar NHS and 0.2 molar EDC (1:1) for 7 min to activate the surface-bound carboxyl groups.

The substrate was then placed onto the spin coater (TT 200-8 spin from LP-Thermtech AG, maximum rotation speed 6600 rpm) and covered with 2 ml of the coating solution. Samples were then rotated with a velocity of 6000 rpm for 300 s.

Three spin coating parameters were optimized in order to obtain the highest coverage and homogeneity of the particle layer: the rotation speed, the solvent of the silica suspension, and the incubation time.

1. Rotation speed

The gold coated substrates were spin-coated with an aqueous suspension of silica nanoparticles (diameter $d = 0.97 \mu\text{m}$) at a concentration of 0.1 g/ml. The incubation time, which denotes the time period in-between deposition of the silica particle suspension onto the substrates and the start of the spin coating process, was set to 1 min.

Three different rotation speeds were tested: 2000, 5000, and 6000 rpm.

2. Solvent

All samples were spin-rotated for 300 s with a rotating speed of 6000 rpm and varying incubation time (1, 2, and 15 min).

Two types of suspensions were used to prepare the silica monolayer: aqueous suspensions of amino-functionalized silica particles with a concentration of 0.1 g/ml, as well as a mixture of an aqueous silica particles suspension (0.1 g/ml) and a surfactant solution (Triton-X 100: methanol=1:400)⁷⁶ in a 1:1 volume ratio.

3. Incubation time

All samples were incubated with 0.1 g/ml silica suspensions in a Triton X-100/water-mixture (1:400) and spun at 6000 rpm for 300 s.

Six different incubation times were tested: 1, 2, 10, 11, 13, 15 min.

Calculation of surface coverage

SEM images were recorded for each type of sample and the percentage of surface coverage was calculated using Adobe Photoshop CS4.

3.1.3.3. By floating

The generic approach to produce silica monolayers by the floating technique starts with the deposition of a silica suspension drop on the initial glass substrate (“parent substrate”). After drying the deposited dispersion, the particles are floated on the air/water interface by slow immersion of the parent substrate under a shallow angle. The silica particles detach from the substrate and forming a close-packed monolayer at the air/water interface.

Subsequently, the floating layer of silica particles was picked up by the gold-coated glass substrate (“receiving substrate”). For this purpose, the receiving substrate is immersed into the water and slowly withdrawn at a shallow angle, just to reverse to the immersion process. Finally, the receiving substrate is kept at a fixed angle until all liquid is evaporated.

Further details on silica monolayers prepared by floating of silica nanoparticle can be found in another doctoral thesis from our group.⁷⁷

3.1.3.4. By thermal evaporation

Silicon dioxide layers were evaporated onto the gold-coated glass substrates using the home-built thermal evaporator (Fig. 3-1) at a base pressure of 2×10^{-7} Torr. The growth rate was monitored by a quartz crystal micro balance and adjusted to 3 Å/s.

3.1.4. Deposition of the upper gold layer

3.1.4.1. By metallization

Metallization of the dielectric layer was achieved by adsorption of isolated gold nanoparticles (seeding) and growing these metal seeds by electroless plating.

Preparation of the seeding solution

Colloidal gold particles with sizes of 3 nm were synthesized according to a well-known procedure.⁷⁸ 1 mL of 1 % aqueous $\text{HAuCl}_4 \cdot 3\text{H}_2\text{O}$ was added to 100 mL of H_2O with vigorous stirring, followed by addition of 1 mL of 1 % aqueous sodium citrate 1 min later. After an additional minute, 1 mL of 0.075 % NaBH_4 in 1 % aqueous sodium citrate was added. The solution was stirred for 5 min and then stored at 4 °C until needed. All aqueous solutions were prepared with freshly produced Millipore water.

Seeding and plating

Samples were immersed in a solution of 2 mg/ml polyethyleneimine (PEI) for 20 min to invert the charge of the dielectric silica layer. Then, negatively charged gold nanoparticles (diameter ~ 3 nm) were adsorbed onto the PEI-coated silica layer via electrostatic interaction (“seeding”). To this end, the samples were incubated in a colloidal suspension of citrate-stabilized gold particles for 12 h. After removal of the solution, the seeding step was repeated. The samples were subsequently exposed to an aqueous solution of 0.1 % $\text{HAuCl}_4 \cdot 3\text{H}_2\text{O}$ and 0.04 M NH_2OH to grow the gold clusters into a contiguous metal shell (electroless plating). After 3 min, the substrates were rinsed with Millipore water and dried in a stream of nitrogen.

3.1.4.2. By Physical Vapor Deposition

Consecutive layers of titanium (5 nm) and gold (50 nm) were evaporated on top of a silica particle monolayer by physical vapor deposition (PVD).

3.2. Synthesis of protein-resistant coatings on the LSPR biosensor via Atom Transfer Radical Polymerization (ATRP)

3.2.1. Materials

2-Bromo-*N*-(3-triethoxysilyl)propyl isobutyramide and 11-mercaptoundecyl 2-bromo-2-methylpropanoate were obtained from our collaborating group affiliated with the German Cancer Research Center (Chip-based peptide synthesis group, DKFZ Heidelberg).

Synthesis of bromosilane:

2.02 g freshly distilled triethylamine (20 mmol) and 4.21 g 3-aminopropyltriethoxysilane (19 mmol) were dissolved in 65 ml anhydrous dichloromethane in a Schlenk flask under a nitrogen atmosphere and cooled to -80 °C. A mixture of 4.60 g 2-bromoisobutyryl bromide (20 mmol) in 30 ml anhydrous dichloromethane was prepared and slowly added to the cooled solution with constant stirring. The solution was warmed up into room temperature and the solvent was removed under reduced temperature. The residue was then dissolve in 50 ml anhydrous *n*-hexane and stirred for 30 min under nitrogen atmosphere. The solution was filtered through a fritted funnel (fine pore size) under nitrogen atmosphere to remove the ammonium salts, and washed several times with anhydrous *n*-hexane. Remaining solvent was then removed under reduced pressure and the remaining red oil was distilled twice under vacuum. The product is a colorless oil.

Dichloromethane (anhydrous, analytical grade), ethanol (analytical grade), methanol (analytical grade) were purchased from AppliChem GmbH (Darmstadt, Germany).

Poly(ethyleneglycol) methacrylate (PEGMA, mol. wt., ~360 g/mol), 2,2-bipyridyl (bipy, 98%), copper(I) bromide (analytical grade), *N,N*-dimethylformamide (DMF; anhydrous, dried over 0.4-nm molecular sieve) were obtained from Sigma-Aldrich (Munich, Germany).

(3-mercaptopropyl)trimethoxysilane (MPTES, 95%) and hydrogen chloride (HCl, 0.1 M) were purchased from Sigma-Aldrich (Munich, Germany).

(3-aminopropyl)triethoxysilane (APTES, ≥ 98%), triethylamine (≥ 99%, dried over potassium hydroxide pellets), and bromoacetyl bromide (≥ 98%) were purchased from Sigma-Aldrich (Munich, Germany).

Methyl methacrylate (MMA, 99%) was received from VWR International (Darmstadt, Germany) and tri(ethylene glycol) monomethyl ether (TEGMME, p.a.) was obtained from Th. Geyer (Renningen, Germany). 1,1,4,7,7-pentamethyldiethylenetriamine (PMDETA, 99+%) were obtained from Acros Organics (Geel, Belgium). Copper(I) chloride (≥ 99.995%) and copper(II) chloride (≥ 99.995%) were purchased from Sigma Aldrich (Munich, Germany).

Fmoc-β-alanine (>99%) was purchased from Iris BioTechnology; (<http://www.irisbiotech.com/>). *N,N*-diisopropyl carbodiimide (DIC, purum) and *N*-methylimidazole (NMI, analytical grade) were purchased from Sigma-Aldrich.

Acetic anhydride (analytical grade), *N,N*-diisopropylethylamine (DIPEA, analytical grade), piperidine (≥99%), triisobutylsilane (TIBS; ultrapure) and chloroform (analytical grade) were purchased from Sigma-Aldrich (Munich, Germany). Trifluoroacetic acid (TFA, 99%) was obtained from Acros Organics, Geel, Belgium.

3.2.2. Direct synthesis of a protein-resistant coating on the LSPR biosensor

3.2.2.1. Direct attachment of ATRP initiators on the LSPR biosensor

LSPR biosensors were incubated in a 10 mM solution of 11-mercaptopundecyl 2-bromo-2-methylpropanoate in anhydrous dichloromethane over night. The reaction was stopped by addition of ethanol (p.a.), followed by extensive rinsing with ethanol and distilled water. The slides were then carefully dried in a stream of nitrogen.

3.2.2.2. Synthesis of a graft polymer film on the LSPR biosensor via ATRP

In a Schlenk flask, 141 mg 2,2'-bipyridyl (bipy, 0.90 mmol) were dissolved in 10 ml of 1:1 methanol/water. 5 ml PEGMA (15.3 mmol) and 64 mg CuBr (0.45 mmol) were added to the mixture. The brown-colored reaction mixture was immediately degassed three times under vacuum. The mixture was then sonicated for 3 min to dissolve the copper catalyst.

The activated LSPR biosensors were placed in a glass petri dish inside a desiccator. The polymerization reaction mixture was added to the petri dish and the desiccator was immediately evacuated three times and flushed with nitrogen. The slides stayed in the polymerization mixture overnight.

The slides were rinsed intensively with Millipore water and DMF inside the petri dish to remove residues of the polymerization solution. The slides were incubated for 15 min each in Millipore water and then DMF, and subsequently washed twice for 2 min with methanol on a rocking shaker.

3.2.3. Indirect synthesis of a protein-resistant coating on the LSPR biosensor

3.2.3.1. Synthesis of a silica gel on the LSPR biosensor

A sol-gel solution containing MPTES, 0.1 M HCl, and methanol p.a. in 1:1:1 volume ratio was prepared and sonicated for 10 min. After 2 h of pre-gelation, fabricated LSPR biosensors were immersed in the sol-gel solution for 2 days. The sensors were then carefully removed from the sol-gel and rinsed thoroughly with methanol. Samples were strongly shaken in methanol four times for 5 min each to remove any non-chemisorbed silica gel.

3.2.3.2. Synthesis of a graft polymer film on the silica gel-coated LSPR biosensor

3.2.3.2.1. Attachment of ATRP initiators on the silica-gel coated LSPR biosensor

1-step initiator immobilization

LSPR biosensors were incubated in a 10 mM solution of 2-bromo-2methyl-*N*-propyltrimethoxysilyl isobutyramide in anhydrous dichloromethane over night. The reaction was stopped by addition of ethanol (p.a.), followed by extensive rinsing with ethanol and distilled water. The slides were then carefully dried in a stream of nitrogen. To achieve full condensation of silanol groups, silanized LSPR biosensors were heated for 1 h at 100 °C in an oven.

2-step initiator immobilization

ATRP initiators were immobilized on the LSPR biosensor by two reactions: silanization and esterification.

1. Silanization

LSPR biosensors were incubated in a solution of 2.9 v% APTES, 2.4 v% distilled water and 94.7 v% absolute ethanol over night. The slides were then washed in absolute ethanol 4 times, each time for 5 min, to remove physisorbates. Finally, the slides were thoroughly rinsed with absolute ethanol. To achieve a full condensation of the silanol groups, silanized LSPR biosensors were heated for 1 h at 100 °C in an oven.

2. Esterification

Silanized LSPR biosensors were immersed in a solution of 400 µl triethylamine and 20 ml anhydrous dichloromethane and kept at a temperature of 0 °C. 100 µl bromoacetyl bromide in 1 ml anhydrous dichloromethane was slowly added to the reaction solution. The slides stayed overnight in the reaction mixture. The slides were then thoroughly rinsed with acetone and absolute ethanol, and dried in a stream of nitrogen.

3.2.3.2.2. Synthesis of a graft polymer film on the silica-gel coated LSPR biosensor via ATRP

Graft polymer film with 100 % PEGMA

141 mg 2,2'-bipyridyl (bipy, 0.90 mmol) were dissolved in 10 ml of 1:1 methanol/water in a Schlenk flask. 5 ml PEGMA (15.3 mmol) and 64 mg CuBr (0.45 mmol) were added to the mixture. The brown-colored reaction mixture was immediately degassed three times under vacuum. The mixture was then sonicated for 3 min to dissolve the copper catalyst.

The activated LSPR biosensors were placed in a glass petri dish inside a vacuum desiccator. The polymerization reaction mixture was added to the petri dish and the desiccator was immediately evacuated three times and flushed with nitrogen. The slides remained overnight in the polymerization mixture.

The slides were rinsed intensively with Millipore water and DMF inside the petri dish to remove all residue of the polymerization solution. The polymer-coated LSPR biosensors were incubated in Millipore water and DMF for 15 min each, and then washed twice with methanol on a rocking shaker for 2 min.

Graft copolymer film with 50 % PEGMA and 50 % MMA

In a Schlenk flask, 22 ml PEGMA (67.5 mmol), 7 ml MMA (67.5 mol) and 314 µl PMDETA (3 mmol) were mixed. 25 mg CuCl (0.25 mmol) and 85 mg CuCl₂ (0.63 mmol) were then added to the reaction mixture. The reaction mixture was immediately degassed three times under vacuum. The mixture was then sonicated for 3 min to dissolve the copper catalyst. In contrast to CuBr/bipy in MeOH/H₂O, the polymerization mixture was colored deep blue.

The activated LSPR biosensors were placed in a glass petri dish inside a vacuum desiccator. The polymerization reaction mixture was added to the petri dish and the desiccator was immediately evacuated three times and flushed with nitrogen. The slides remained overnight in the polymerization mixture.

The slides were rinsed intensively with Millipore water and DMF inside the petri dish to remove all residue of the polymerization solution. The polymer-coated LSPR biosensors were incubated in Millipore water and DMF for 15 min each, and then washed twice with methanol on a rocking shaker for 2 min.

Graft copolymer film (10:90) with 10 % PEGMA and 90 % MMA

In a Schlenk flask, 23 ml PEGMA (70.6 mmol), 67 ml MMA, 110 ml TEGMME and 2048 μ l PMDETA (10 mmol) were mixed. 692 mg CuCl (7 mmol) were then added to the reaction mixture. The reaction mixture was immediately degassed three times under vacuum. The mixture was then sonicated for 3 min to dissolve the copper catalyst. The polymerization mixture took on a deeply green color.

The activated LSPR biosensors were placed in a glass petri dish inside a vacuum desiccator. The polymerization reaction mixture was added to the petri dish and the desiccator was immediately evacuated three times and flushed with nitrogen.

The incubation time was varied in order to optimize the thickness of the copolymer film choosing 5, 9.5, 10.5, 15.5, 20, and 22 h.

The slides were rinsed intensively with Millipore water and DMF inside the petri dish to remove all residue of the polymerization solution. The polymer-coated LSPR biosensors were incubated in Millipore water and DMF for 15 min each, and then washed with methanol twice on a rocking shaker for 2 min each.

3.2.3.2.3. Functionalization of the protein-resistant coating on the LSPR biosensor

Amino-functionalization

Polymer-coated LSPR biosensors were incubated in anhydrous DMF for 30 min to pre-swell the polymer film. In a Schlenk flask, 62.26 mg of Fmoc- β -alanine (0.2 M) and 37.2 μ l DIC (0.24 M) were mixed in 1 ml of dry DMF under nitrogen atmosphere and stirred for at least 5 min. 31.8 ml NMI (0.4 M) were then added to the reaction mixture.

Remaining DMF used for swelling was removed from the polymer-coated slides and the slides were incubated in the reaction solution under nitrogen for at least 16 h. The slides were then washed three times, each time for 2 min, with DMF.

Three β -alanine residues were coupled to the protein-resistant coating consecutively as a linker unit to provide better accessibility for the growing peptide chains.

Blocking of residual hydroxyl groups

The slides were incubated overnight in a glass petri dish on a rocking shaker in a solution consisting of 10 v% acetic anhydride, 20 v% DIPEA, and 70 v% DMF. The next day the blocking solution was removed and the slides were washed five times, each time for 2 min, with DMF.

Cleaving of Fmoc protection groups

To remove the Fmoc protection groups, the slides were incubated in a solution of 20 v% piperidine in DMF for 20 min. The slides were then washed three times with DMF, each time for 2 min, and two times in methanol, each for 2 min.

Removal of side-chain protecting groups

The slides were incubated in methylene chloride for 30 min to pre-swell the polymer coating. The amino side chains were removed by incubating the slides in a mixture of 51 v% TFA, 44

v% methylene chloride, 3 v% TIBS and 2 v% water three times for 30 min under stirring. The slides were then washed with methylene chloride and DMF twice for 5 min each.

3.3. Preparation of biomolecule arrays onto the protein resistant LSPR biosensor

3.3.1. Materials

Fmoc-protected, Opfp-activated amino acid derivatives were obtained from Novabiochem (Merck Biosciences, Bad Soden/Germany).

N,N-dimethylformamide (DMF, peptide grade) was purchased from Biosolve BV, Valkenswaard, The Netherlands and dried over molecular sieve. Methanol (p.a.), ethanol (p.a.), chloroform (p.a.), methylene chloride (p.a.), piperidine (99%), acetic anhydride (p.a.), *N,N*-diisopropylethylamine (DIPEA, p.a.), triisobutylsilane (TIBS, ultrapure) were purchased from Sigma Aldrich (Munich, Germany) and were used without further purification. Trifluoroacetic acid (TFA, 99%) was purchased from Acros Organics (Geel, Belgium).

Preparation of Tris-buffered saline with Tween 20 (TBS-T):

A 10x Tris-buffered saline (TBS) stock solution was prepared by mixing 0.1 M (12.11 g) Trizma base and 1.5 M (87.66 g) NaCl (adjusted to pH 7.6 with concentrated HCl). TBS-T was prepared by dilution of the 10x TBS stock solution with water in 1:10 ratio and addition of 0.05 v% Tween 20. Trizma base (99.9%) and Tween 20 were purchased from Sigma Aldrich (Munich, Germany).

Mouse monoclonal rabbit anti-HA was purchased from Sigma Aldrich (Munich, Germany). Alexa Fluor 647–conjugated goat anti-rabbit IgG (H+L) was purchased from Invitrogen (Karlsruhe, Germany). Monoclonal mouse anti-HA, conjugated with 800 CW, was provided by our collaborating group (Chip-based peptide synthesis, DKFZ Heidelberg). Dylight 680–conjugated goat anti-mouse IgG (H+L) was purchased from Thermo Scientific (Karlsruhe, Germany).

GenePix 4000B fluorescence scanner and GenePix Pro 4.0 microarray image analysis software were purchased from Molecular Devices (Sunnyvale, CA, USA)

Odyssey infrared scanner and Odyssey V3.0 microarray image analysis software were purchased from LI-COR Biosciences (Bad Homburg, Germany).

3.3.2. Fabrication of antibody arrays on the LSPR biosensor by the spotting technique

2 μ l of Alexa Fluor 647 goat anti-rabbit IgG (2 mg/ml) was diluted with 8 μ l TBS-T buffer. The antibody array was spotted onto a LSPR biosensor by a spotting robot (BioChip ArrayerTM, Perkin Elmer, Rodgau, Germany). An array of 25x25 spots was formed, with a spot volume of 2 nl and a center-to-center separation of 600 μ m.

Using the GenePix 4000B fluorescence scanner, a fluorescence read-out was performed at the appropriate wavelength (635 nm for Alexa Fluor 647 dyes) immediately after the spotting experiment. Fluorescence images were analyzed with GenePix Pro image analysis software.

3.3.3. Fabrication of peptide arrays on the polymer coated LSPR biosensor by the particle-based technique

3.3.3.1. Synthesis of amino acid toner particles for the particle-based synthesis

Amino acid particles were manufactured at the German Cancer Research Center, Heidelberg. Detailed information and composition can be found at Beyer et al.³⁰ and Stadler et al.⁷⁹

One of 20 different Fmoc-amino-acid-OPfp-esters (Merck Biosciences GmbH, Bad Soden, Germany, 10 w%), a toner resin (SEKISUI CHEMICAL, Tokyo, Japan; 84.5 w%), pyrazolone orange (ABCR GmbH, Karlsruhe, Germany; 4.5 w%) and an iron (III)-bis (naphthoic acid) complex (self-synthesized; 1 w%) were melted, mixed and finally solidified. The homogenized and crushed toner mass was then mixed with ~4 w% silica particles, and slowly fed into an air jet mill where grinded particles were collected within a narrow lattice.⁸⁰

3.3.3.2. Partial synthesis of peptide arrays on the polymer coated LSPR biosensor by the particle-based technique

3.3.3.2.1. Liquid-phase peptide synthesis

Polymer-coated LSPR biosensors were incubated in anhydrous DMF for 30 min to pre-swell the polymer film. A 0.1 M solution of the Fmoc-protected and Opfp-activated amino acid derivative in dry DMF was prepared in a Schlenk flask under nitrogen atmosphere and stirred for at least 5 min.

Remaining DMF used for swelling was removed from the polymer-coated slides and the reaction mixture was added to them. The slides were incubated in the reaction solution under nitrogen for at least 16 h. The slides were then washed three times with DMF, each time for 2 min.

In order to block residual OH-groups, the slides were incubated overnight in a glass petri dish on a rocking shaker in a solution consisting of 10 v% acetic anhydride, 20 v% DIPEA, and 70 v% DMF. The next day the blocking solution was removed and the slides were washed with DMF five times for 2 min.

To remove the Fmoc protection groups, the slides were incubated in a solution of 20 v% piperidine in DMF for 20 min. The slides were then washed three times with DMF, each time for 2 min, and two times in methanol for 2 min.

3.3.3.2.2. Particle-based peptide synthesis

Each type of amino acid microparticles was stored in a particular aerosol generator. For selective particle deposition, the particles were dispersed by a stream of dry air and charged by friction due to collisions with the plexiglas generator walls. Charged amino acid microparticles were addressed onto the polymer coated LSPR biosensor by directing electric forces.



Figure 3-4. Polymer-coated LSPR biosensors after deposition of amino acids particles via a modified laser printer.

After each deposition of a particular particle type, the LSPR sensor was briefly (<3 min) heated to fix the deposited particles onto the surface. The slides were transferred into a pre-warmed, nitrogen-flushed reaction chamber after all types of amino acid particles were printed on the slides. Here, the coupling reaction is initiated upon melting at 90 °C for 90 min under inert gas. The deposition of the amino acid particles is typically achieved with micron precision.

After cooling to room temperature, the slides were washed 1 min and then 20 min with 1 ml of a mixture of acetic anhydride, DIPEA and DMF (5:10:35) to remove residual particle material and to block residual amino groups. The slides were then washed five times with DMF for 5 min each and incubated with 1 ml of 20 v% piperidine in DMF to remove the N-terminal Fmoc protecting group, and washed again five times with DMF for 5 min each and two times with methanol for 5 min each. The slides were then dried in a stream of nitrogen.

This synthesis cycle was repeated as many times as necessary to complete the synthesis of the desired peptide sequence.

After the peptide synthesis was completed, the slides were incubated in methylene chloride for 30 min to pre-swell the polymer coating. The amino side chains were removed by incubating the slides in a mixture of 51 v% TFA, 44 v% methylene chloride, 3 v% TIBS and 2 v% water three times for 30 min under stirring. The slides were then washed twice with methylene chloride and DMF for 5 min each.

The slides were incubated in a 5 % (v/v) DIPEA in DMF for 30 min to neutralize any remains of TFA in the polymer coating. Finally, the slides were washed twice in DMF and in methanol for 5 min, and dried in a stream of nitrogen.

The slides were sonicated for 9 min to remove silica particle residues of the amino acids particles.

3.3.3.2.3. Immunostaining with fluorescence-labeled antibodies

The slides were incubated in 1 ml of TBS-T buffer for at least 30 min to rehydrate the polymer film. Immunostaining solution was prepared by diluting specific antibody (rabbit anti-HA) by 1:1000 in TBS-T buffer. The slides were then incubated in 1 ml of the antibody solution for 1 h at room temperature on a rocking shaker. Buffer solution was carefully removed and the slides were washed six times, each time for 5 min, in TBS-T with constant gentle shaking.

A secondary antibody (Alexa Fluor 647-conjugated goat anti-rabbit IgG) was diluted at a ratio of 1:1000 in TBS-T buffer and the slides were incubated in this solution for 1 h at room temperature on a rocking shaker. Buffered solution was carefully removed and the slides were washed six times in TBS-T, each time for 5 min with constant gentle shaking. The slides were then dried in a stream of nitrogen.

Positions of the fluorescence-labeled antibodies on the polymer-coated LSPR biosensor was detected by using the GenePix 4000B fluorescence scanner at appropriate wavelengths (635 nm for Alexa Fluor 647 dyes). Fluorescence images were analyzed with GenePix Pro image analysis software.

3.3.3.3. Total synthesis of peptide arrays on the polymer coated LSPR biosensor by particle-based technique

3.3.3.3.1. Particle-based peptide synthesis

The procedure for a full-sequence peptide synthesis by the particle-based technique is identical to that described in chapter 3.3.3.2.2.

3.3.3.3.2. Immunostaining with infrared-labeled antibodies

The slides were incubated in 1 ml of TBS-T buffer for at least 30 min to rehydrate the polymer film. Immunostaining solution was prepared by diluting specific antibody (800 CW-conjugated mouse anti-HA) by 1:1000 in TBS-T buffer. The slides were then incubated in 1 ml of the antibody solution for 2 h at room temperature on a rocking shaker. Buffered solution was carefully removed and the slides were incubated in a new solution of antibody for another hour. The slides were then washed six times in TBS-T, each time for 5 min with constant gentle shaking.

Infrared (IR) images of the samples were captured by using an Odysseus Infrared (IR) scanner at appropriate wavelength (800 nm for CW 800). IR scanning images were analyzed with Odyssey V3.0 image analysis software.

3.4. Excitation and detection of surface plasmons

Two optical set-ups were used to analyze the optical properties of the LSPR biosensor. The optical set-up shown in Figure 3-5a was used for macroscopic measurements. It consists of a moveable sample holder, a deuterium-halogen light source, an optical fiber bundle which both illuminated the sample and collected the reflected light, and a UV/Vis spectrometer. The spatial resolution of this set-up was determined by the diameter of the illuminating fiber bundle and amounts to ~3 mm.

Scanning measurements with an adjustable spatial resolution were performed by using the optical set-up shown in Figure 3-5b. Light from the source was guided through an optical fiber with a diameter of 200 μm to excite surface plasmons only in a small and confined area of the sample. Reflected light was collected using an optical waveguide with a diameter of 50 μm and transmitted to the spectrometer.

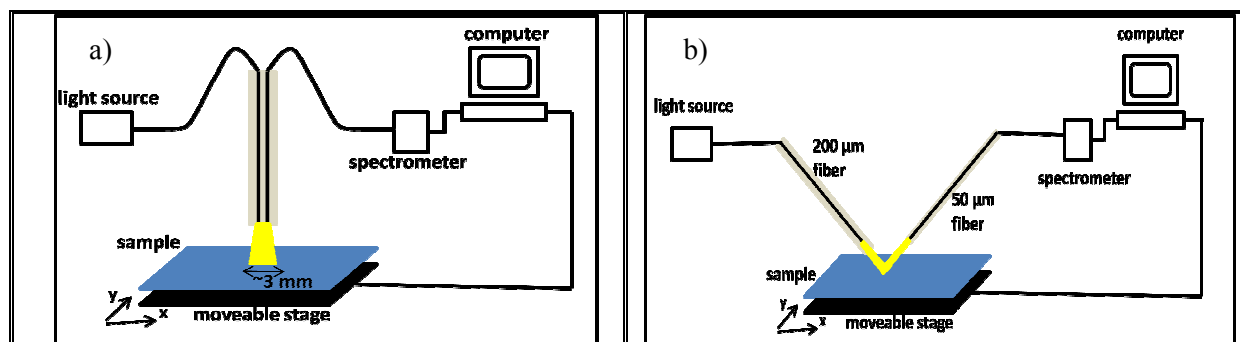
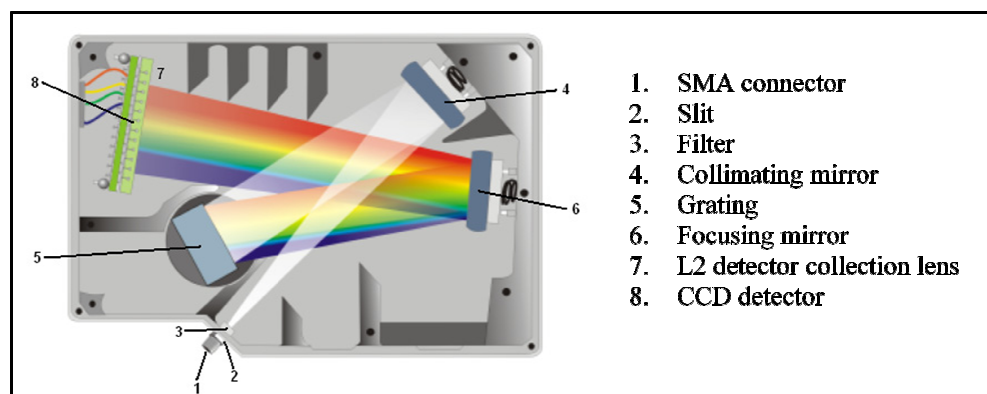


Figure 3-5. Optical constructions for UV-Vis measurements in (a) macroscopic and (b) scanning modes.

All UV-Vis absorption spectra in this study were measured using a lamp from Ocean Optics (DH-2000-BAL), which combined deuterium and tungsten halogen light sources in one optical path. The wavelength for the deuterium lamp ranged from 210 to 400 nm, while the tungsten-halogen lamp covered the region from 300 to 1500 nm.⁸¹



To determine the wavelength of the plasmon resonances, a high-resolution UV/Vis grating spectrometer from Ocean Optics is used (HR2000). The light pathway through the optical bench of an HR2000 spectrometer is shown in Figure 3-6.

For macroscopic measurements with low spatial resolution, fiber bundle R200-7-UV/Vis from Ocean Optics was purchased in which a tight bundle of 6 illumination fibers surround 1 read fiber with diameters of 200 μm . For measurements in scanning mode, optical waveguides of different sizes (core diameter = 50 and 200 μm) were purchased from Polymicro Technologies (FVP100110125UVM and FVP200220240UVM). These fibers are especially applicable for transmission of UV-Vis-NIR light in the region between 180 to 1150 nm due to the high percentage of hydroxyl groups on its core's silica surface (Fig. 3-7).⁸²

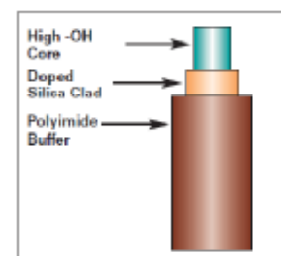


Figure 3-7. Construction of a silica optical fiber from Polymicro Technology.

Movements of the translation stage in x- and y-axis directions are controlled by two step motors with a minimum step size of 0.5 μm (purchased from OWIS GmbH). The motorized x-y stage enables point-by-point measurements in the scanning mode. Step motors and spectrometer operation were computerized using an in-house developed program written in Visual Basic.⁸³

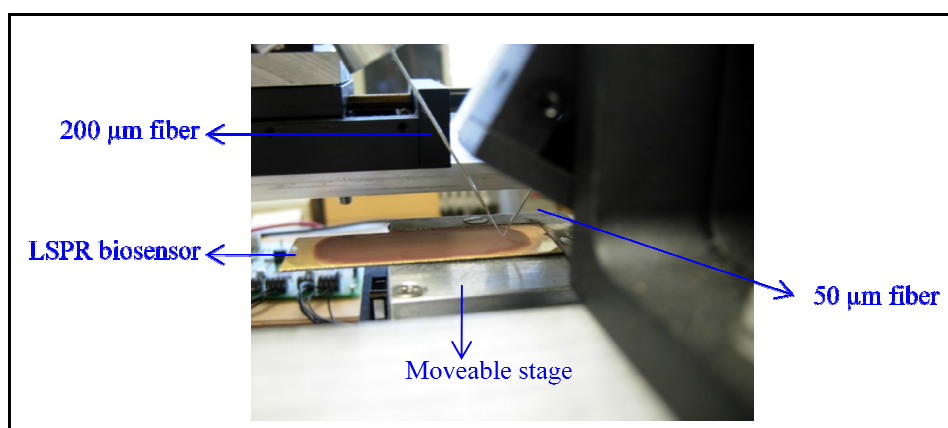


Figure 3-8. Surface scanning of a LSPR sensor with the optical construction shown in Fig. 3-5b

3.5. Analytical measurements

3.5.1. Scanning Electron Microscopy (SEM)

All SEM images displayed in this thesis were recorded with a LEO1530 Gemini electron microscope, mostly using the secondary electron detector. The EHT (Electron High Tension), which is the accelerating voltage, was set to 3 KV.

3.5.2. X-ray Photoelectron Spectroscopy (XPS)

XPS measurements in this work were conducted with the spectrometer MAX200 (Leybold-Heraeus). A non-monochromatic dual anode X-ray source was used. One anode face is coated with magnesium and the other one with aluminum. The design enables quick switching between the two types of X-ray radiation (Al $K\alpha$: 1486.6 eV, Mg $K\alpha$: 1253.6 eV). In this thesis, all XPS measurements were carried out using the Mg $K\alpha$ line. A concentric hemispherical electron-energy analyzer is used as detector.

All XPS measurements were performed by first taking a survey scan spectrum covering a range of 1000 eV, and then scanning the individual peaks in more detail over a smaller range of 20-40 eV. These detailed scans with high resolution were used for quantitative analysis. In order to compare the results obtained from measurements made on different days, all the important parameters (such as the scanning step, the dwell time for each step, the pass energy, and the amount of scans) were kept constant. The parameters used for all the measurements are listed in Table 3-1.

Table 3-1. Parameters for XPS measurements.

Orbitals	Start (eV)	End (eV)	Step (eV)	Dwell (s)	Pass Energy (eV)	Scans
Survey	1000	-5	0.4	0.01	96	3
Au4f	95	75	0.2	0.04	48	12
C1s	300	270	0.2	0.10	48	15
O1s	545	520	0.2	0.12	48	15
Si2s	175	135	0.2	0.25	48	20

S2p	175	135	0.2	0.25	48	20
N1s	420	395	0.2	0.25	48	20
Br3p	190	170	0.2	0.25	48	20

The position of photoelectron peaks shift by several eV when the investigated surface is electrically isolated. In this case, the binding energy scale of the spectrum has to be calibrated by the position of a standard peak. When the samples are prepared on a gold surface, the Au4f_{7/2} peak serves as the standard and is set to 84 eV.

After the data acquisition in XPS measurements, spectra are normalized according to the transmission function in order to compare the intensities of individual peaks and quantify the data.

There are two general methods to obtain the intensity (peak area) of the photoelectron peak. The first is called peak integration. Before integrating a curve and calculating the area under the peak, the background must be subtracted. Two kinds of background, Shirley and Tougaard, are commonly applied for quantification.⁷¹ The second method in determining the peak area is peak fitting. When a photoelectron peak of an element appears broad and asymmetric, it usually contains contributions from atoms in several different chemical environments. The asymmetric peak can then be fitted as a combination of several symmetric sub-peaks. In this dissertation, Gaussian functions were used for fitting each sub-peak and to obtain the position, height, width, and area of the peak. XPSPEAK41 software was downloaded from <http://www.wsu.edu/~scudiero/Xpspeak41.zip> and used for quantitative analysis of the XPS spectra.

4. Results and Discussion

4.1. Overview and introduction

The goal of this dissertation is the label-free detection of antibody-antigen interactions in high-density peptide libraries. To this end, an optical sensor based on localized Surface Plasmon Resonance (LSPR) was built and optimized. Subsequently a high-density peptide library was synthesized on the LSPR sensor using laser printer technology. Antibody-antigen interactions can then easily be detected by a shift of the extinction peak in the UV-VIS spectrum.

In the first part of this work (Chapter 4.2), optically responsive surfaces based on LSPR are constructed and optimized. These substrates are to serve simultaneously as solid platforms for the peptide arrays as well as sensors in detecting the binding events occurring on these arrays.

In order to prevent non-specific protein adsorption, it is necessary to coat the optically responsive substrates by a protein-resistant film. This has been achieved by synthesizing a protein-repelling coating on the LSPR biosensor based on poly(ethylene glycol) methyl methacrylate (PEGMA) graft polymer film by Surface Initiated Atom Transfer Radical Polymerization (SI-ATRP). This will be described in the chapter 4.3 of this thesis.

Peptide arrays are then synthesized on the polymer-coated LSPR biosensor by peptide printer technology using amino acid toner particles.

Finally, a qualitative comparison between label-based and label-free analysis is made in an antibody assay with respect to the performances of both techniques in detecting specific interactions between antibodies and peptide arrays in chapter 4.4.

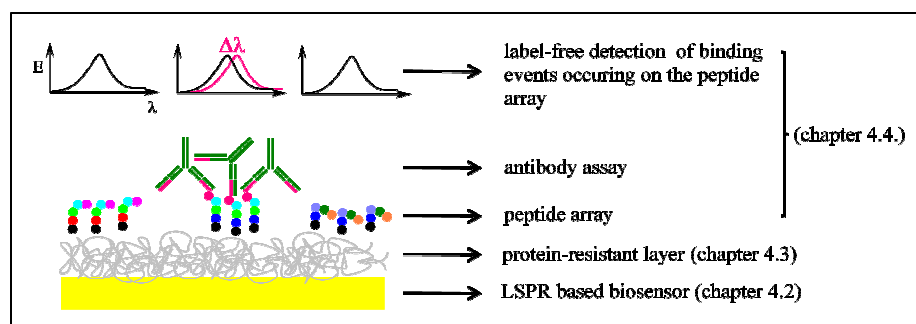


Figure 4-1. Schematic overview over the main work sections

4.2. Study of LSPR based biosensors as a solid support for peptide arrays and a detection tool in the antibody assay

4.2.1. Introduction

The basic principles for designing an optical sensor based on *propagating* and *localized* surface plasmons in gold was first reported in 2000 by Takei and Himmelhaus. They showed the sensing ability of cap-shaped gold nanoparticle films, which were formed by evaporating gold onto a randomly close-packed (rcp) monolayer of adsorbed *dielectric* polystyrene particles with a diameter of a few hundred nanometers. The samples exhibit an extinction peak in the visible region, which position is found to depend linearly on the refractive index of surrounding environment. When a solution of thiol molecules, known to selectively adsorb

on gold, was added, the resulting shift in the extinction peak was consistently toward longer wavelengths (Fig. 4-2).^{3-4,84}

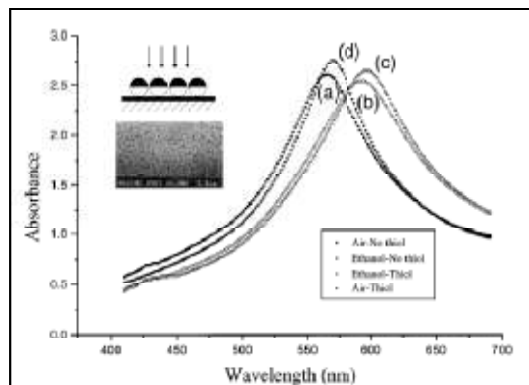


Figure 4-2. Schematic diagram showing the formation of optical biosensor based on Surface Plasmon Resonance of gold by Takei and Himmelhaus³⁻⁴

Previous work done by our group has suggested that two layers of metallic gold and an intermediate *dielectric* layer are required to succeed in combining propagating and localized SPR (Fig. 4-3).⁸⁵ The bottom gold layer was prepared by Physical Vapor Deposition (PVD) on a glass slide or a silicon wafer. The upper gold layer was formed by adsorbing gold colloids on the dielectric layer (“seeding”), which is then grown into a contiguous layer by electroless gold deposition from an electrolyte solution (“plating”).⁸⁶⁻⁸⁸ The intermediate dielectric layer was a nanoparticle film, which was formed by self-assembling of polystyrene or silica particles with a diameter of several hundred nanometers.

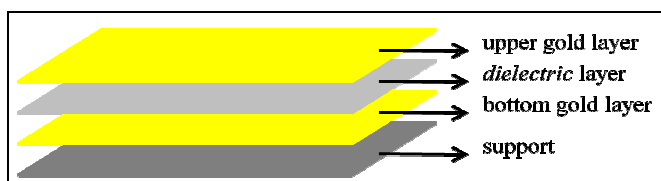


Figure 4-3. Biosensor based on propagating and localizing surface plasmon resonances of gold

In order to ensure its suitability as both a solid support for the peptide arrays and the detection of antibody-antigen interactions in a miniaturized format, several aspects in the fabrication of the LSPR nanobiosensor have to be taken into account:

1. Optical homogeneity

Binding events are detected by comparing the resonance maximum of occupied and unoccupied sites on the peptide array (Fig. 4-4). Therefore, it is necessary that both unoccupied and occupied binding sites show little variation in the resonance wavelength. Variation of the resonance wavelength higher than the adsorption-induced shift would prohibit the exact read-out of binding events.

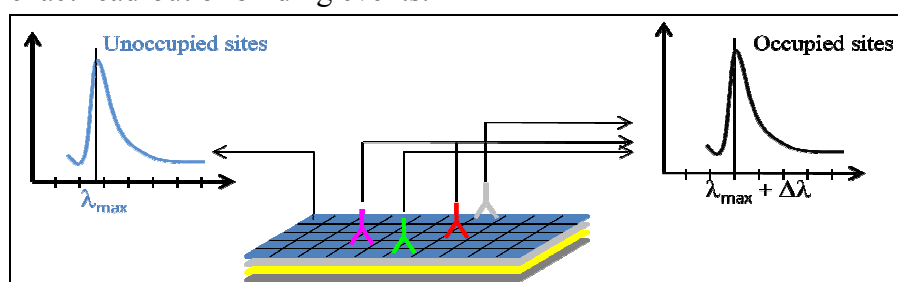


Figure 11-4. LSP-resonance peaks of occupied (blue) and unoccupied (yellow) sites on the sensor in an ideal case.

2. Sensitivity

A high sensitivity in detecting adsorbed analytes is essential for a miniaturized system due to low absolute amount of analyte in the system. In this work, resonance shifts due to fibrinogen

adsorption on the sensor surface were measured to test the sensitivity of each sensing geometry.

3. Plasmon line shape

The accuracy of a spectroscopic measurement is determined by the sharpness of the lines to be measured. A narrow resonance peak would facilitate the read-out of the maximum and help to analyze even small adsorption-induced shifts. Thus, resonance peaks with low FWHM (Full Width at Half Maximum) are preferred.

4. Stability

Serving as the support for the peptide array, the LSPR sensor has to undergo a multitude of processing cycles during the synthesis of the peptide array. Therefore, the sensor is required to be stable against harsh chemical conditions and temperature treatment. The chemical and mechanical stability of LSPR biosensor developed in this work will be demonstrated in the last chapter, by showing its function after enduring the whole process of PEG synthesis and peptide array fabrication.

Thus, the LSPR biosensor developed in this work was designed and optimized to meet the following criteria:

- high contrast in UV-VIS spectrum between occupied and unoccupied binding sites
- high sensitivity towards molecule binding
- a sharp peak profile in the UV-VIS spectrum
- high chemical, mechanical and temperature stability.

4.2.2. Deposition of the intermediate dielectric layer

One of the decisive issues in the fabrication of this optical sensor is the formation of the *dielectric* layer. Three geometries of the intermediate *dielectric* layer were investigated in the current work: silica nanoparticle monolayers (Fig. 4-5a), homogeneous polycrystalline silica films (Fig. 4-5b), and a composite structure of a homogeneous silica film and a silica particle monolayer on top (Fig. 4-5c).

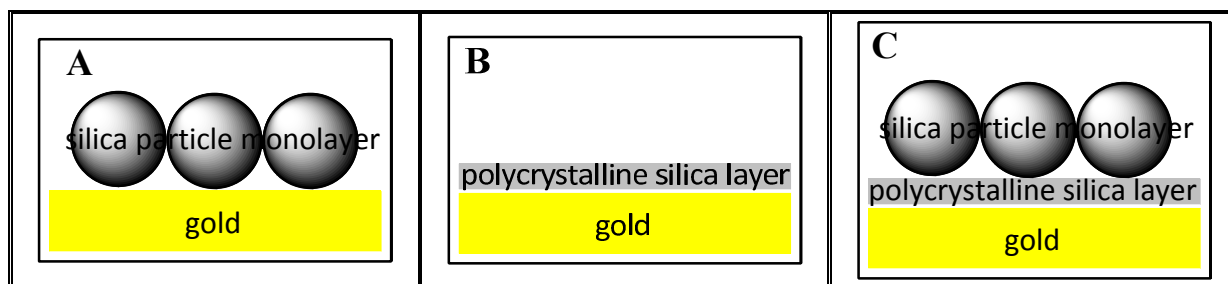


Figure 4-5. Geometries of the dielectric layer in the LSPR biosensor:
(a) monolayer of silica particles, (b) homogeneous polycrystalline thin silica film,
(c) composite structure of a homogeneous silica film and a silica particle monolayer on top

4.2.2.1. Silica nanoparticle monolayer as the dielectric layer in the LSPR biosensor

Silica nanoparticles were used in these experiments, because they are commercially available, inert to most organic solvents, and compatible with both peptide synthesis and biological processes.⁸⁹⁻⁹⁰ In this work, dielectric silica nanoparticles are bound *covalently* to the bottom gold layer in order to improve film stability. First, the underlying gold layer is coated by a self-assembled monolayer of carboxyl-terminated thiols, while the dielectric silica particles are functionalized by amino groups. The particle-bound amino groups react with the surface-bounded carboxyl group to create a peptide bond with EDC/NHS as the carboxyl-activating reagents (Fig. 4-6, left). In the first method, the coupling of amino-functionalized silica particle to the carboxyl-functionalized gold surface was achieved by a simple incubation technique.

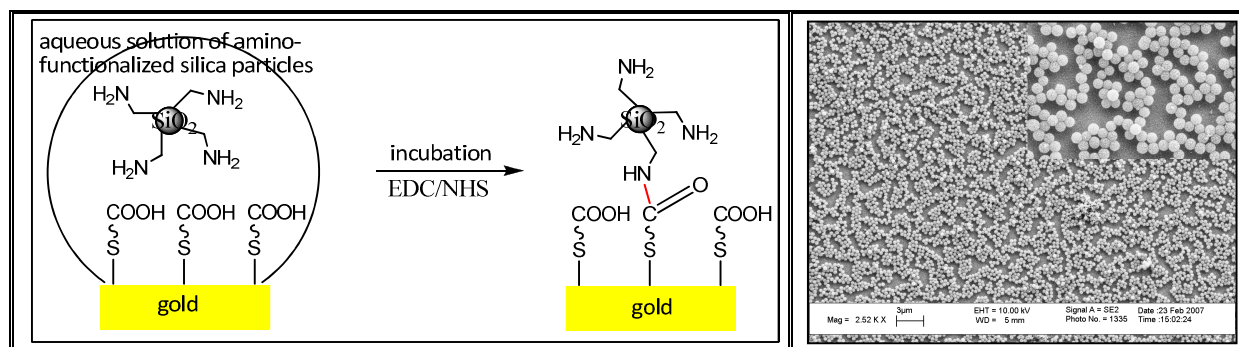


Figure 4-6. Schematic drawing (left) and SEM image (right) of silica nanoparticle ($d = 390$ nm) monolayers formed by simple incubation technique. Surface coverage was determined to be 57.5 %.

Scanning Electron Microscope images of the sample shows a monolayer of silica particles (Fig. 4-6, right). The surface area of the bottom gold layer which is covered by the silica particles was determined to be 57.5 %.

To achieve a higher density and better homogeneity of the silica particle monolayer, a spin coater was utilized while still maintaining the covalent binding between amino-functionalized silica particles and self-assembled carboxylthiols on gold (Fig. 4-7). The spin coating technique offers the advantage of covering large areas with a uniform layer within a small period of time.^{76,91}

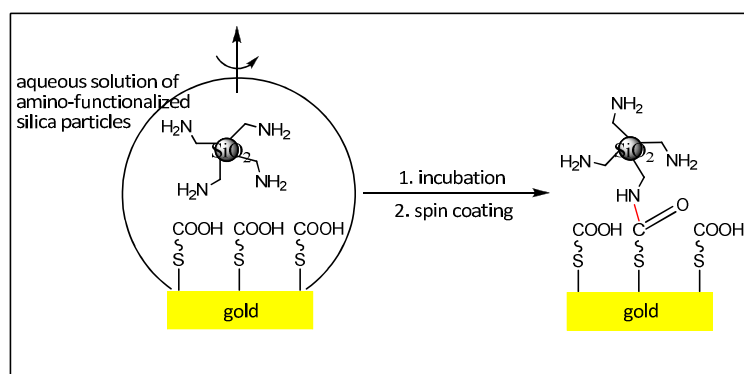


Figure 4-7. Deposition of silica particle on gold by spin coating

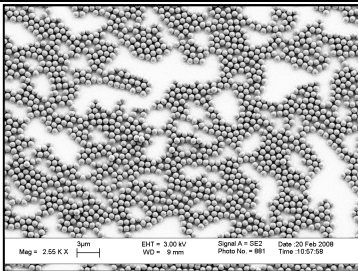
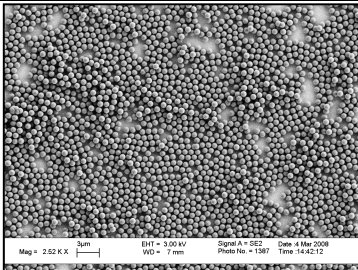
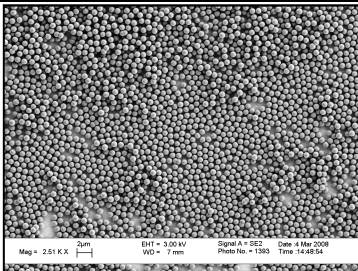
In the preparation of silica particle monolayers on gold by spin coating, three parameters have been optimized to obtain monolayers with high surface coverage: the solvent of the silica suspension, the incubation time, and the rotation speed.

1. Rotation speed

The first optimized parameter in the formation of nanoparticle monolayer by spin coating was the *rotation speed*. For these experiments, the gold coated substrates were spin-coated with an aqueous suspension of silica nanoparticles (diameter $d = 0.97 \mu\text{m}$) at a concentration of 0.1 g/ml. The incubation time, which denotes the time period in between the insertion of the substrates into the silica particle suspension and the start of the spin coating process, was set to 1 min.

Table 4-1. Optimization of particle surface density by variation of rotation speed.

By increasing the rotation speed from 2000 rpm to 6000 rpm, the surface coverage improves from 60.3 % to 83.1 %.

Rotation speed	SEM images	Surface Coverage
2000 rpm		60.3 %
5000 rpm		81.5 %
6000 rpm		83.1 %

The resulting surface densities of silica nanoparticles on the gold coated substrates as a function of the rotation speed are shown in Table 4-1. A rotation speed of 200 rpm gives a low surface density of ca. 60.3 %. The surface density can be increased by increasing the rotation speed to 4000 (surface density ca. 81.5 %) and 6000 rpm (surface density ca. 83.1 %), respectively. Concluding, a higher rotation speed was found to improve the spreading of the silica suspension, resulting in particle layers with fewer vacancies (Table 4-1). However, higher rotation speed also resulted in a higher tendency of multilayer forming.

2. Solvent

In achieving a homogeneous particle monolayer by spin coating, both the spreading behavior of the particles on the surface and the solvent evaporation rate play an important role. Both effects are controlled by the chemical properties of the solvent.

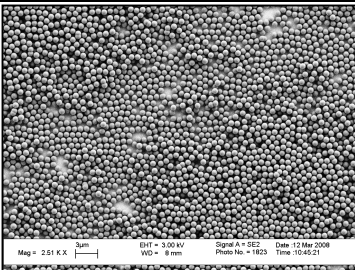
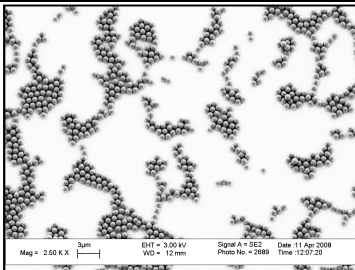
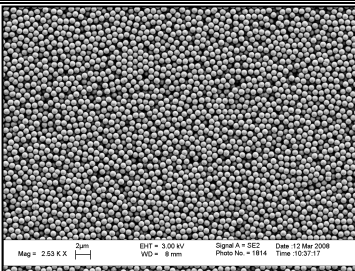
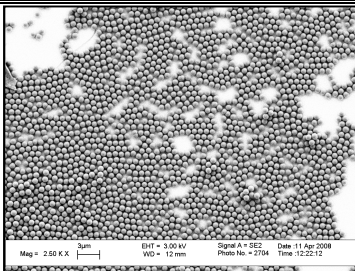
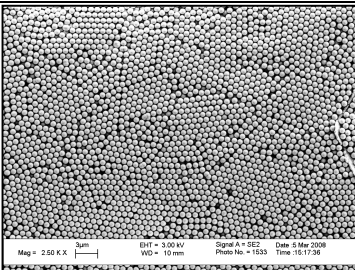
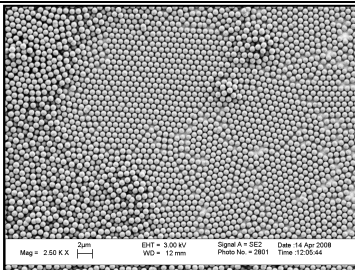
It is known that surfactant solutions exhibit a slower evaporation rate than pure water under the same conditions, which should accommodate the formation of close-packed monolayers.⁹²⁻⁹³ At the same time, addition of surfactants in the solvent should impact the spreading behavior of the particles.

In this thesis, the effect of surfactants added to the particle suspension was investigated in terms of monolayer formation. The amount and type of surfactant added to the silica particle solution were taken from Li et al.⁷⁶ SEM images below (Table 4-2) show the differences in the structure of silica particle layers, which were formed from silica particles suspended in water and a water/Triton X-100-mixture (400:1) with varying incubation time. All samples

were spin-rotated for 300 s with a rotating speed of 6000 rpm with a silica particle concentration of 0.1 g/ml.

Table 4-2. Optimization of silica particle ($d = 0.97 \mu\text{m}$) monolayer formation by adding surfactant into the particle suspension.

The left-hand column depicts a time series when using pure water as solvent, while results with added surfactant Triton X-100 are given on the right hand-side. It is seen that the addition of surfactants reduces the tendency of multilayers formation.

Incubation time prior to spin-coating	Solvent = water	Solvent = water/Triton X-100 (400:1)
1 min		
2 min		
15 min		

Overall, SEM images indicate that surfactant-free silica suspension have a higher tendency to form nanoparticle multilayers (Table 4-2, left column). For an incubation time of 1 min., a complete particle monolayer with an additional partial second layer is visible in Table 4-2. Higher incubation times, 2 and 15 min., result in even stronger multilayer formation.

Addition of surfactant in the solvent reduces the particle's tendency to form multilayers on surfaces (Table 4-2, right column). For an incubation time of 1 minute, a particle monolayer with low density is formed. Particle monolayers with higher density can be achieved by extending the incubation time to 2 and 15 minutes. Bilayer formation is only observed in comparatively small areas of the sample, even for an incubation time of 15 minutes.

These experimental results, which show the tendency of silica particles to form monolayers in the presence of surfactants, can be explained by the amphiphilic properties of surfactants. Surfactants possess both hydrophobic (commonly denoted as "tails") and hydrophilic groups (referred to as "heads"), and therefore are soluble both in organic solvents and water (Fig. 4-8, left).

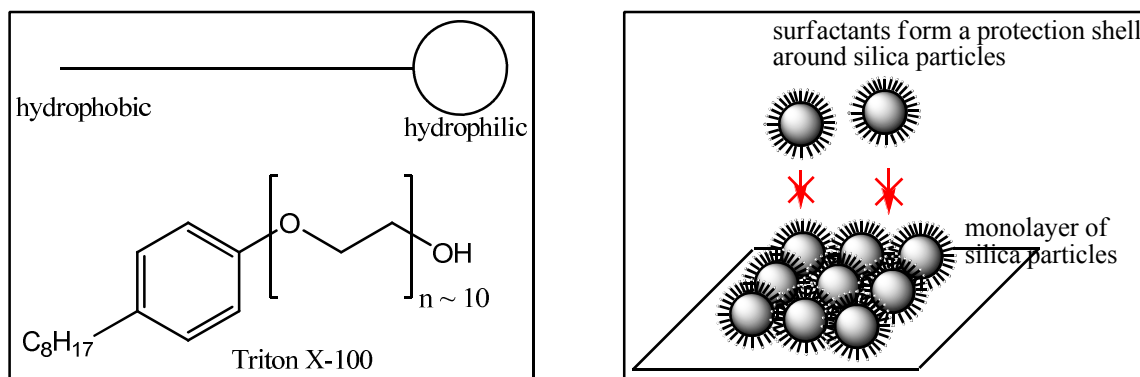


Figure 4-8. Surfactant molecules with hydrophilic head and hydrophobic tail (left). Mechanism in monolayer formation in the surfactant-containing silica suspension (right): Surfactant molecules form a protective shell around silica particles, which increases particle-particle repulsive interactions, preventing the formation of the second particle layer. Moreover, the surfactant improves the spreading behavior.

The addition of a surfactant reduces the surface tension of a liquid or the interfacial tension between two phases. This results in a lower energy demand to enlarge the interface area. As a consequence, silica particles suspended in a mixture of surfactant and water display a faster and more evenly spreading behavior. Another advantage when adding surfactants to the silica suspension is the ability of the surfactant molecules to build a protective shell around the silica particle. Particles show a stronger repulsive interaction, which reduce the formation of the second particle layer effectively (Fig. 4-8, right).

3. Incubation time

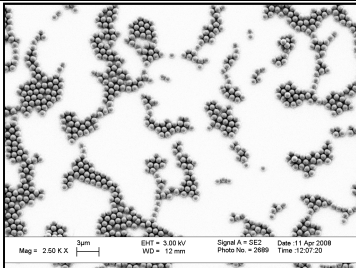
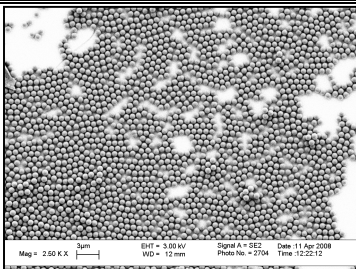
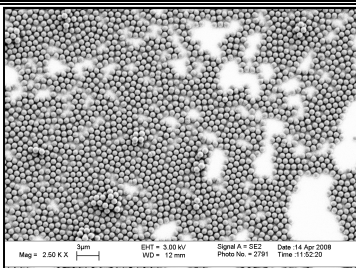
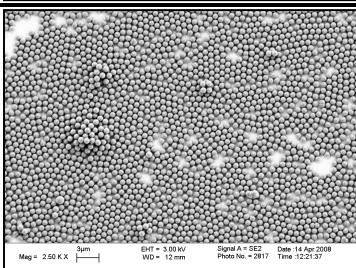
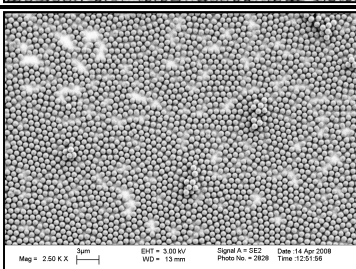
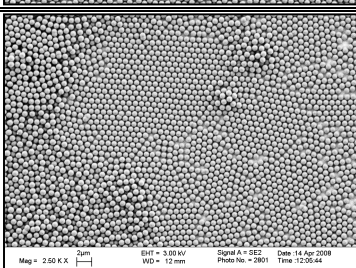
Samples were incubated with the surfactant-containing silica suspension for a certain period of time before being spun. The *incubation time* turned out to be the most important factor with respect to achieving a high surface density of particles in the monolayer.

In Table 4-3 both the SEM images of silica monolayers formed with different incubation time and the obtained surface coverage are listed. All samples were incubated in 0.1 g/ml silica suspension in surfactant/water-mixture (1:1) and spun at 6000 rpm for 300 s.

When increasing the incubation time from 1 to 13 minutes, the surface density of the nanoparticle layer increased from ca. 38.4 to 87.2 % (Table 4-3). Extending the incubation time further to 15 minutes resulted in the formation of a partial nanoparticle bilayer.

Table 4-3. Optimization of the particle surface density by incubation time.

Incubation time is varied from 1 min to 15 min. With increasing incubation time the surface density is increased, eventually yielding bilayer after 15 min of incubation. The optimum incubation time is 13 min.

Time	SEM images	Surface coverage
1 min		38.4 %
2 min		70.7 %
10 min		79.5 %
11 min		85.4 %
13 min		87.2 %
15 min		bilayer

The surface area covered by silica particles is given in Figure 4-9 as a function of the incubation time. Nanoparticle monolayers with the highest surface density were obtained when incubating the substrates in surfactant-containing silica suspension for 13 minutes before spin coating. An incubation time of 15 minutes already resulted in a nanoparticle coating with some degree of multilayer formation.

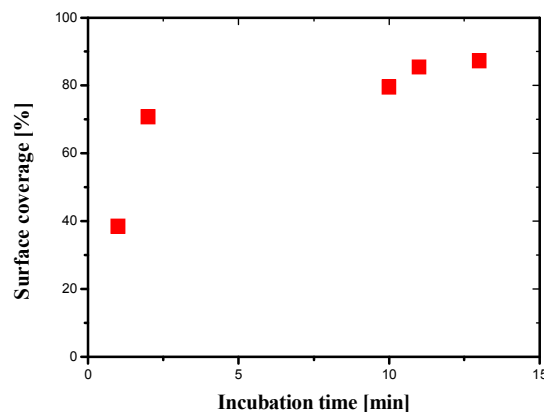


Figure 4-9. Surface area covered by silica particles as a function of incubation time before spin-coating. After 15 min of incubation bilayer formation emerged. The optimum incubation time for achieving the highest surface particle density while still maintaining a monolayer structure was found to be 13 min.

As a summary of the optimization procedures detailed above, it is concluded that silica nanoparticle monolayers prepared by spin coating achieved the highest surface density when applying the following preparation steps: first, amino-terminated silica nanoparticles are suspended in a mixture of Triton X-100 and water (1:400). The gold substrate, functionalized with a carboxylthiol-SAM, is then incubated with the silica suspension for 13 minutes, followed by spin coating with a rotation speed of 6000 rpm for 300 s.

Silica particle monolayers formed without as well as with the application of spin coating are compared in Fig. 4-10. Surface preparation without spin coating (Fig 4-10a) results in a surface particle coverage of 57.5 %, while samples prepared by optimized spin coating (Fig. 4-10b) achieve a surface coverage of 87.2 %. This strong increase on surface density will benefit the exact read-out of the extinction maxima by forming narrow plasmon resonance peaks, which facilitate the detection of binding events occurring on the sensor surface. The effect of surface particle coverage on the optical properties of the LSPR biosensor will be discussed in details in chapter 4.1.3.2.

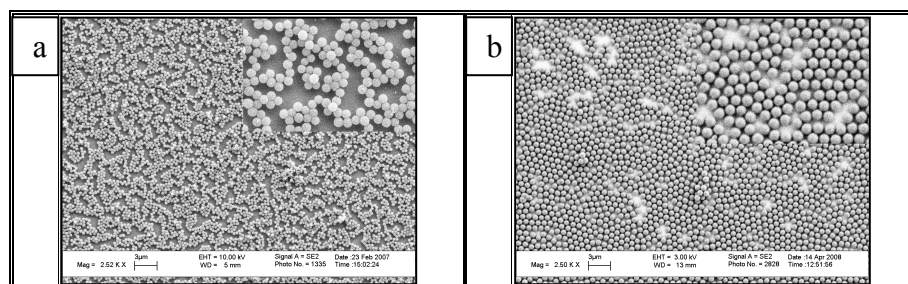


Figure 4-10. SEM images of the nanoparticle films: (a) before and (b) after optimization with spin coating. Preparation of nanoparticle films by spin coating with optimized parameters increased the surface coverage from 57.5 % to 87.2 %.

4.2.2.2. Homogeneous polycrystalline silica film as the dielectric layer in the LSPR biosensor

In an alternative approach to prepare LSPR biosensors, the nanoparticle monolayer was replaced by a polycrystalline silica film which served as the intermediate dielectric layer. For this purpose, a homogeneous silica layer with a thickness of 250 nm was deposited on the gold coated substrate by Physical Vapor Deposition (PVD). The thickness variation of the polycrystalline silica film was measured to be $\pm 5\%$.⁹

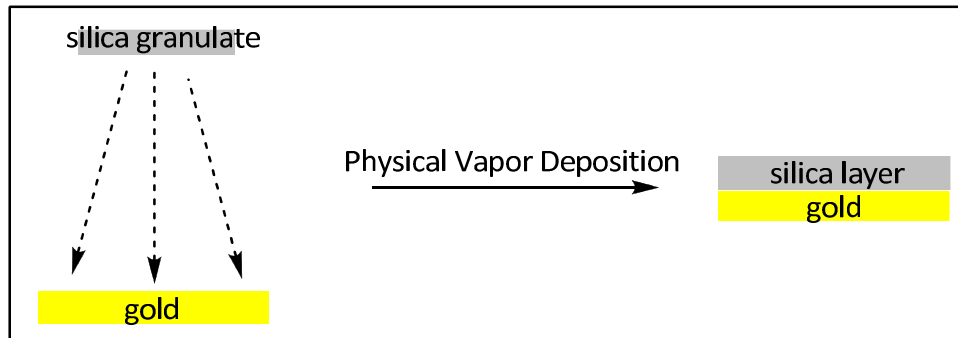


Figure 4-11. Deposition of polycrystalline silica film on gold by Physical Vapor Deposition (PVD)

4.2.2.3. A composite structure of a polycrystalline silica film and a silica particle monolayer as the dielectric layer in the LSPR biosensor

In the third approach, a composite structure of a homogeneous polycrystalline silica film and a silica nanoparticle monolayer was fabricated and used as the intermediate dielectric layer. First, a polycrystalline silica film (thickness = 40 nm) was deposited on a gold coated-substrate by PVD. The silica film was then coated with amino-functionalized silica nanoparticles ($d = 510$ nm) by a simple floating technique.

In the floating technique, monolayers of nanoparticles are formed at the air/water interface and transferred to a target substrate (Fig. 4-12).⁹⁴⁻⁹⁵ The optical characterization of LSPR biosensors prepared by floating of silica nanoparticle will be discussed in detail in another PhD thesis of our group.⁷⁷

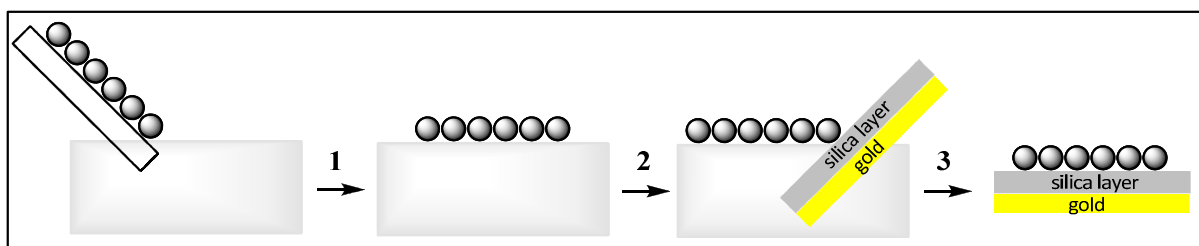


Figure 4-12. Deposition of silica particle monolayer by floating. (1) A glass substrate with silica particle solution is dipped into water and a monolayer of particle is formed on the water surface. (2) A target substrate is carefully dipped into the water. (3) The floating monolayers of silica particles are picked up by the target substrate.

4.2.3. Deposition of the upper gold layer

Two techniques for depositing the gold layer on top of the intermediate dielectric layer were investigated.

4.2.3.1. Deposition of the upper gold layer by seeding and plating

First, isolated gold colloids with a diameter of ~ 3 nm are adsorbed onto the intermediate dielectric layer (*seeding*). In a second step, the pre-adsorbed gold colloids serve as nucleation sites for electroless metal deposition from an electrolyte solution (*plating*). With increasing plating time, the gold nanoparticles become more and more interconnected, finally leading to a continuous metal shell around the dielectric film. This deposition technique was applied to all three geometries of intermediate dielectric layer: silica particle monolayers (Fig. 4-13a), polycrystalline silica layers (Fig. 4-13b), and the composite structure of both structural elements (Fig. 4-13c).

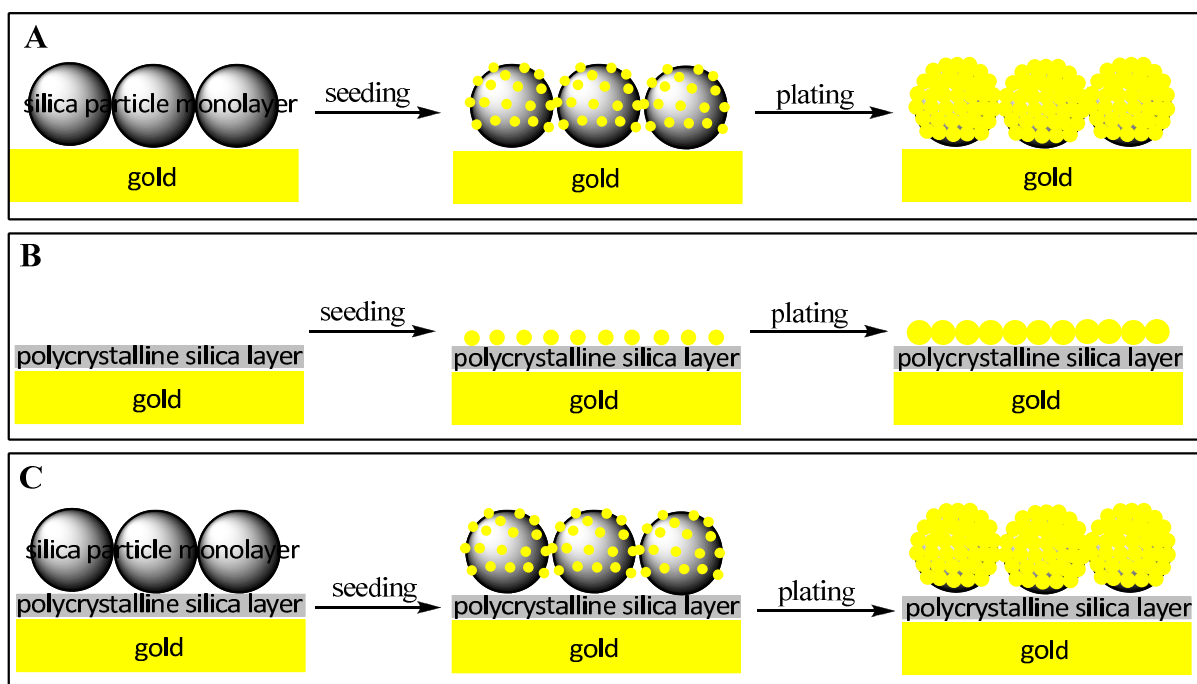


Figure 4-13. Schematic drawing of gold deposition onto the silica dielectric layer by seeding and plating. (a) A silica particle monolayer, (b) a polycrystalline silica layer, and (c) a composite structure of a polycrystalline silica layer and a silica particle monolayer serves as the intermediate dielectric film.

The results are given in Fig. 4-14. When gold is deposited via seeding and plating on surface-adsorbed silica particles – deposited either on a gold film or a silica film-, the silica particles will be entirely coated by gold clusters (Fig. 4-14a). In contrast, deposition of gold on a polycrystalline silica film by this technique provides a flat layer of gold clusters (Fig. 4-14b). Gold clusters formed on the dielectric layer after a 3-min plating obtain a diameter of ~ 50 nm.

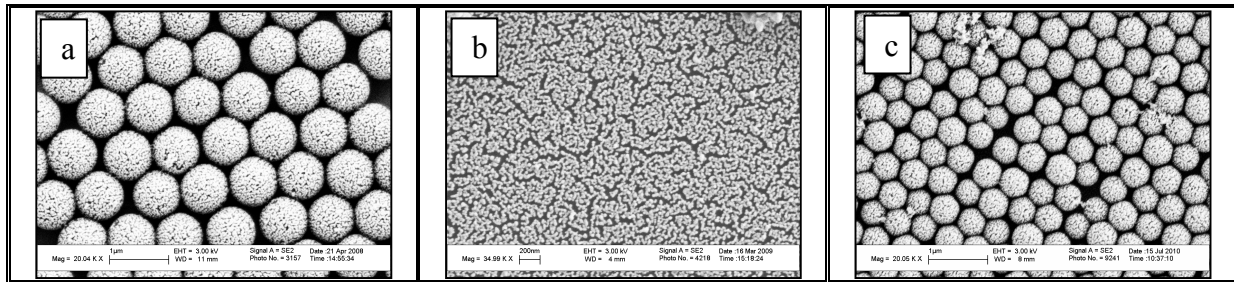


Figure 4-14. SEM images of the dielectric layer coated by gold via the seeding/plating deposition technique. (a) A silica particle monolayer, (b) a polycrystalline silica layer and (c) a composite structure of a polycrystalline silica layer and a silica particle monolayer serves as the intermediate dielectric film.

4.2.3.2. Deposition of the upper gold layer by Physical Vapor Deposition (PVD)

Alternatively, gold was evaporated onto the surface-adsorbed silica nanoparticles so that cap-shaped gold particles were formed (Fig. 4-15). For direct comparison to the gold layer produced by the seeding-plating technique, a layer thickness of 50 nm was selected in this gold deposition technique.

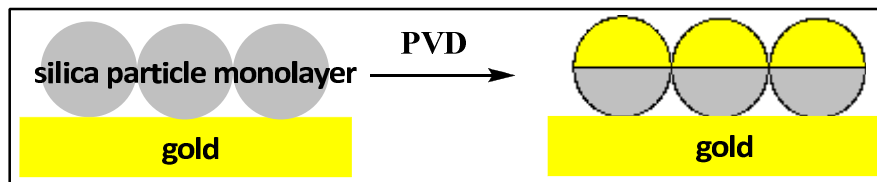


Figure 4-15. Schematic drawing of gold deposition onto the silica dielectric layer by PVD. A silica nanoparticle monolayer serves as the intermediate dielectric film.

By scanning electron microscopy, gold was found to cover only the top parts of the nanoparticles (Fig. 4-16). The boundary between the coated and the non-coated regions of the silica particle could be discerned and the area directly below a nanoparticle was clearly found to be shadowed.

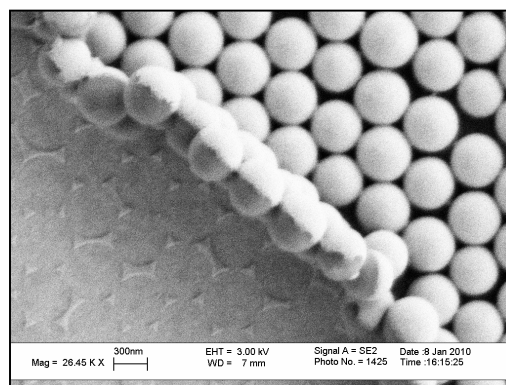


Figure 4-16. SEM image of the dielectric layer coated by the upper gold layer via PVD. A silica nanoparticle monolayer serves as the intermediate dielectric film.

4.2.4. Localized Surface Plasmon Resonance (LSPR) Spectra

As mentioned above (chapter 4.1.), three aspects in the optical property of the LSPR sensor are critical to its suitability as a detection tool in antibody-antigen-interaction: plasmon line shape, optical homogeneity, and sensitivity towards surrounding dielectric medium.

4.2.4.1. Interpretation of the LSPR spectra of the nanoparticle-based biosensor

Nanoparticle-based LSPR sensors (Fig. 4-17) are typically operated with direct optical transmission or reflection, since plasmon excitation on a subwavelength structure does not require evanescent wave excitation. For nanoparticles immobilized on a substrate, changes in the plasmon resonance due to modifications of the refractive index of the surrounding medium are detected as wavelength shifts of the plasmon resonance.

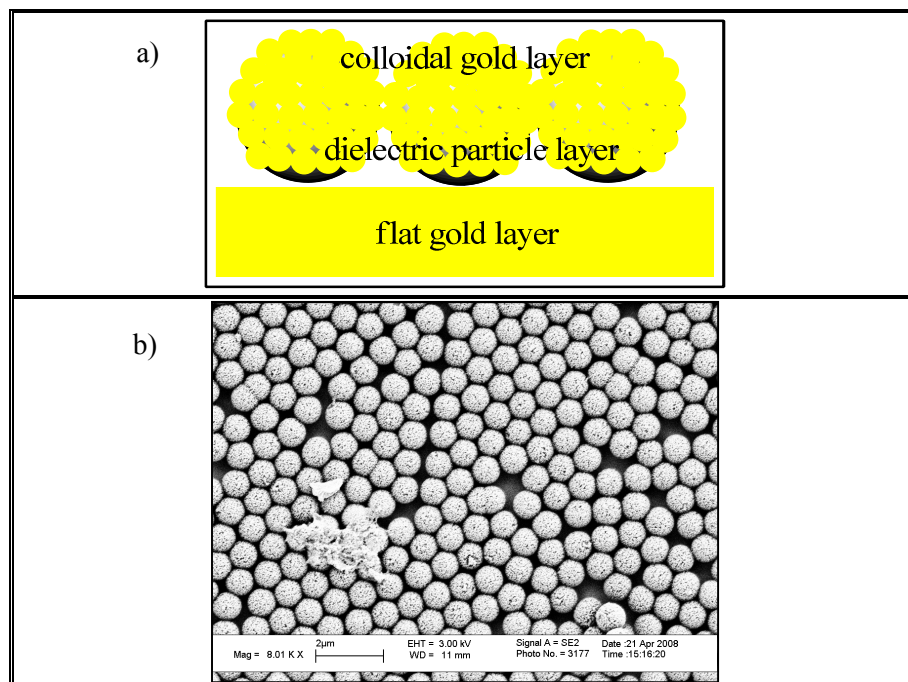


Figure 4-17. (a) Schematic drawing and (b) SEM image of nanoparticle-based LSPR sensor

Fig. 4-18a shows the extinction spectra of silica nanoparticle layers deposited on a thin gold film and coated with colloidal gold. Here, silica particles with varying diameters (400 nm and 1000 nm) were used. Fig. 4-18a displays three distinct resonance maxima for silica particles with a diameter of **400 nm** ($\lambda_{\max} = 355.7, 500.2, 730.4$ nm, solid curve). The peak with the largest wavelength (730.4 nm) represents the dipole resonance mode and the second largest peak (500.2 nm) is contributed by the quadrupole resonance mode.⁹⁶

In the extinction spectrum of LSPR biosensors made by silica particles with a diameter of **1000 nm** (Fig. 4-18a, dashed curve), five resonance maxima ($\lambda_{\max} = 346.3, 401.5, 469.7, 578.9, 813.9$ nm) are observed. Here, the dipole resonance mode is represented by the peak with the largest wavelength (813.9 nm) and the quadrupole resonance mode is represented by the second largest peak (578.9 nm).

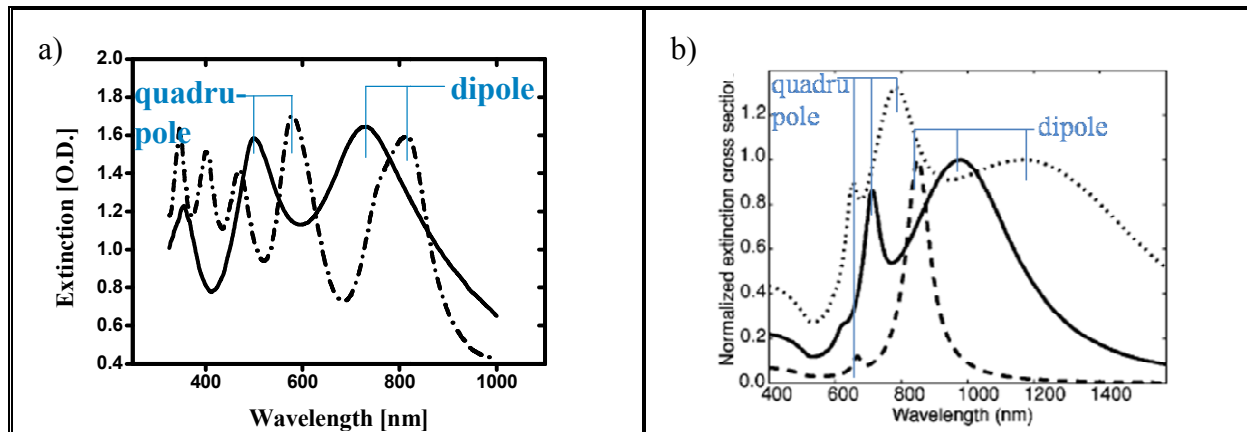


Figure 4-18. LSP-resonance spectra of

- (a) gold coated silica particles immobilized on a thin gold film (Fig. 4-17); diameter of silica core = 400 nm (solid) and 1 μm (dashed)
- (b) isolated silica-gold nanoshells in water (calculated by Westcott et al)⁹⁷; diameter of silica core = 90 nm (dashed), 183 nm (solid), and 270 nm (dotted)

These results indicate an increase in the number of the resonance peaks as well as a shift towards longer wavelength of the extinction maxima when the silica particle diameter is increased.

These experimental findings are in line with the theoretical predictions made by Westcott et al⁹⁷ based on Mie scattering theory. Westcott calculated the extinction spectra of silica-gold nanoshells in water with various core and shell radii (Fig 4-18b). As the diameter of the silica core is increased from 90 nm (dashed line) to 270 nm (dotted line), the dipole resonance peaks moved from ~800 nm to ~1200 nm. Additionally, his calculation indicates an increase in the number of excited resonance modes with increasing particle core size, exactly as observed in our experiments.

The number of resonance peaks depends on the size of the nanoparticles with respect to the wavelength of the light used for detection. A nanoparticle with a diameter much smaller than the wavelength of light will respond as a dipole in an optical field. Higher order multipolar contributions to the overall optical response can be excited for nanoparticles of sizes comparable to the wavelength of light due to the spatial variation of the electromagnetic field across the width of the nanostructure.

The increase in wavelength of the resonance maxima with increasing particle diameter can be explained if the surface plasmon resonances are considered as a homogenous electron gas oscillating over a fixed positively charged background. Here, induced surface charges provide a restoring force. When the core medium is a dielectric, it polarizes in response to the resulting field. This effectively reduces the strength of the surface charge and decreases the restoring force. Consequently, the plasmon energies are lowered and the resonance peaks appear at longer wavelength with increasing core size.⁹⁸

The above experimental results show that the optical properties of the LSPR sensor system, such as the position of the plasmon resonances, can be tuned by changing the dielectric core size. Furthermore, binding events can be monitored through the shifting of individual resonance peaks when using the LSPR sensor in biological systems.

4.2.4.2. Plasmon resonance line shape

To facilitate an exact read-out of the LSPR maximum position, a peak with high intensity and narrow linewidth is required. For this purpose the normalized full width at half maximum

(FWHM) of the peaks, defined as $L = \frac{FWHM \text{ (Full Width at Half Maximum)}}{I \text{ (Intensity)}}$, is calculated for each LSPR sensing geometry. A small value of L , corresponding to high intensity and narrow linewidth, is preferable for the detection of molecular binding on the sensor surface.

The full width at half maximum (FWHM) bandwidth of normalized quadrupole and dipole resonance peaks was quantified by fitting the spectra to a Pseudo-Voigt-function (Eq. 3-1):³

$$y = y_0 + A \left[m_u \frac{2}{\pi} \frac{\omega_L}{4(\lambda + \lambda_c)^2 + \omega_L^2} + (1 - m_u) \frac{\sqrt{4 \ln 2}}{\sqrt{\pi} \omega_G} e^{-\frac{4 \ln 2}{\omega_G^2} (\lambda + \lambda_c)^2} \right] \quad (\text{Eq. 3-1})$$

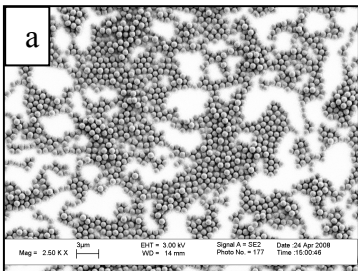
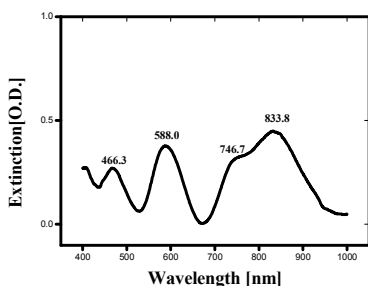
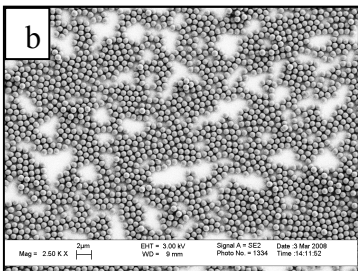
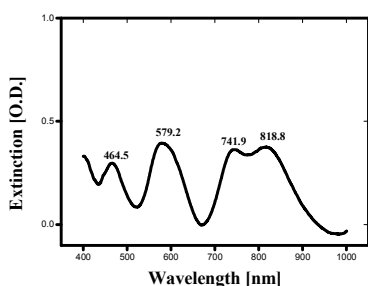
Here, y_0 and A are the offset and scaling coefficients, m_u is a weighting factor to balance Lorentzian and Gaussian contributions, λ_c is the center wavelength, and ω_L , ω_G are Lorentzian and Gaussian bandwidths.

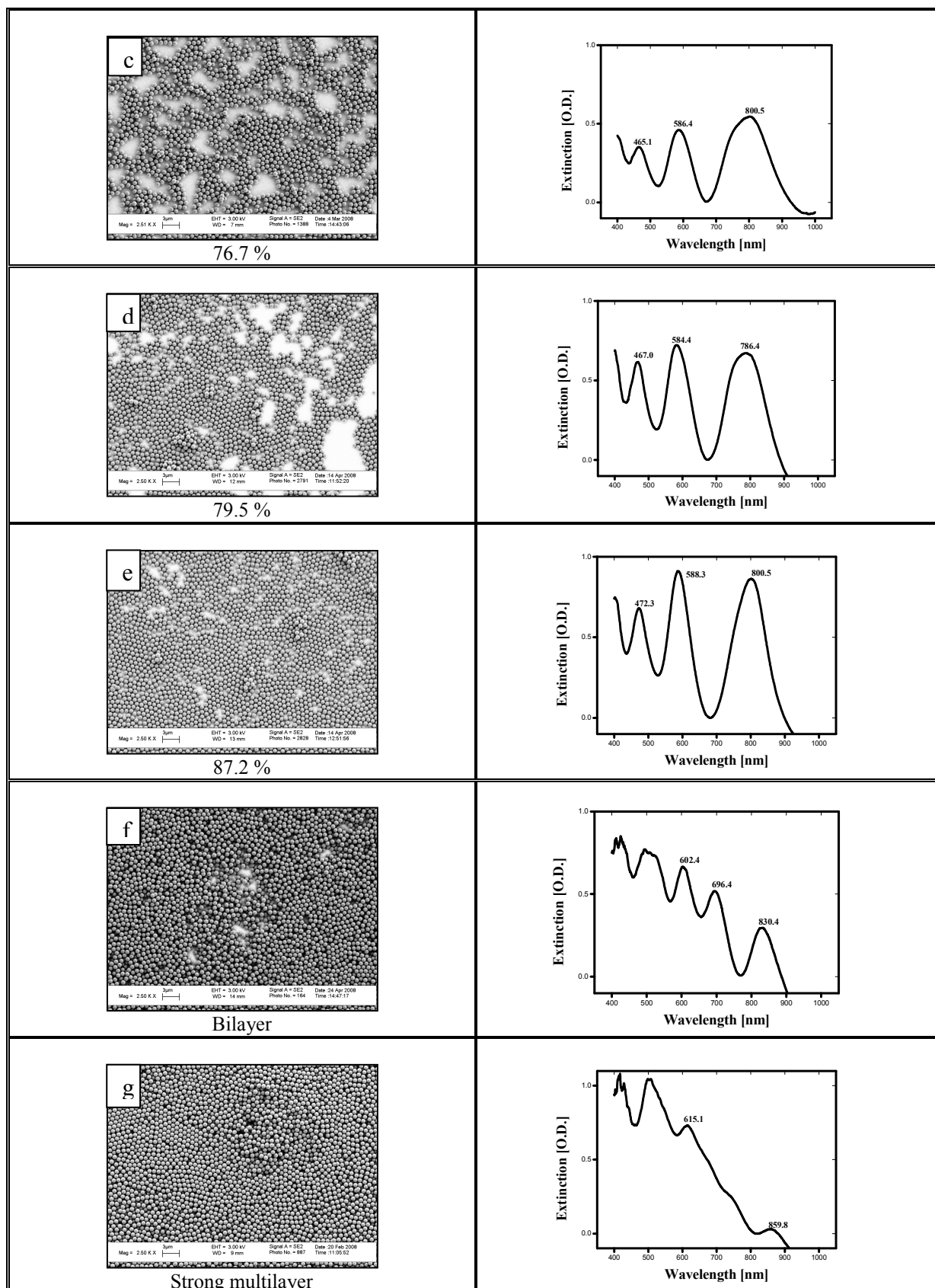
a. Dependence of the plasmon resonance line shape on the intermediate dielectric layer

The shape of both quadrupole and dipole resonance peak depend on the nanoparticle surface density. The effect of the particle surface density on the extinction spectra was investigated and optimized by the usage of spin coating for the deposition of the silica nanoparticles. The resulting data are given in Table 4-4. The upper gold layer was prepared by seeding/plating in the fabrication for all samples. The surface density (left column) on 1x1.5 cm² samples was varied from 65.6 % to 87.2 % with spin coating. Additionally, the LSPR spectrum of a bilayer sample as well as a strongly multiply layered sample was recorded. The corresponding UV-VIS extinction spectra are given in the right column of Table 4-4.

Table 4-4. Correlation of surface coverage and linewidth of the resonance peaks.

The nanoparticle surface coverage was varied from 65.6 % (a) to 87.2 % (e). Additionally, two samples with bi- and multilayer formation (f and g) are also shown in the Table. The UV-VIS extinction spectrum of each sample is shown in the right column.

SEM Images/Surface coverage	Extinction Spectra
 <p style="text-align: center;">65.6 %</p>	
 <p style="text-align: center;">75.3 %</p>	



Four resonance maxima in the 400 nm, 500 nm, 700 nm, and 800 nm regimes are observed for a particle density of 65.6 % and 75.3 %, respectively, from which the two peaks at 700- and 800 nm overlap and are not well resolved. Also, these particle densities result in extinction spectra with low intensity. For nanoparticle densities higher than 76.7 %, the

splitting of the peaks at the higher wavelength vanishes and higher extinction intensities are obtained (Table 4-4, c-e). The maximum extinction intensity is observed for a surface coverage of 87.2 %.

The extinction spectrum of the sample with a particle bilayer shows several resonance peaks between 600 and 900 nm (Table 4-4, f). These LSPR peaks are of very low intensity in comparison to the resonance peaks of the monolayered samples (Table 4-4, a-e). The effect of particle multilayer formation on the intensity of the resonance peaks is even more pronounced in the strongly multilayered sample (Table 4-4, g). These results indicate that silica nanoparticle multilayers are significantly less suitable as the intermediate dielectric layer in LSPR biosensors.

For a quantitative evaluation, the spectra from Table 4-4 were fitted to a Pseudo-Voigt-function (Eq. 3-1). The FWHM, intensity, and normalized FWHM of the dipole and quadrupole resonances are given in Table 4-5.

Table 4-5. FWHM, intensity, and normalized FWHM of the dipole and quadrupole resonances for LSPR biosensors with different surface coverage.

By increasing the surface coverage from 65.6 to 87.2 %, the normalized FWHM of the dipole and quadrupole resonances decreased from 222.9 to 95.2 (quadrupole), and from 358.4 to 135.5 (dipole).

Surface coverage	Quadrupole resonance			Dipole resonance		
	FWHM	I	<i>L</i>	FWHM	I	<i>L</i>
65.6 %	70.0 nm	0.314	222.9	173.1 nm	0.483	358.4
75.3 %	84.9 nm	0.368	230.7	164.4 nm	0.397	414.1
76.7 %	67.5 nm	0.413	163.4	143.9 nm	0.604	238.2
79.5 %	79.1 nm	0.611	129.5	146.9 nm	0.758	193.8
87.2 %	79.4 nm	0.834	95.2	140.0 nm	1.033	135.5

The normalized FWHM of both the dipole and quadrupole resonances decreases with increasing surface coverage of the particle monolayer. The *L* value for quadrupole resonance decreases from 222.9 to 95.2 by increasing the surface coverage from 65.6 % to 87.2 %. At the same time, the *L* value for the dipole resonances increased from 358.4 to 135.5. These trends are displayed graphically in Fig. 4-19.

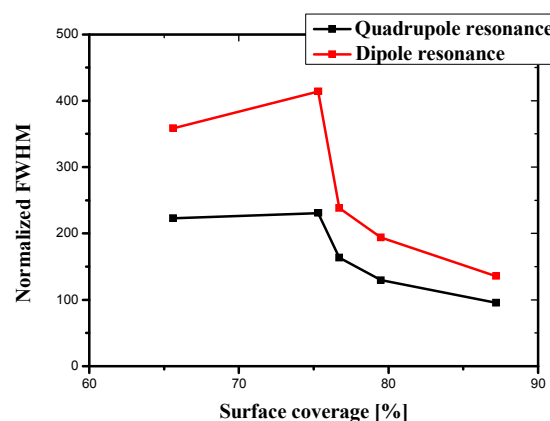


Figure 4-19. Normalized FWHMs of the dipole and quadrupole resonances as a function of the surface coverage. Both resonance modes show a decreasing normalized FWHM upon increasing surface coverage.

These results clearly show that both the dipole and quadrupole resonance peaks strongly depend on the surface coverage of the silica particle monolayer and that the normalized FWHM, which is an indicator for the sharpness of the resonance peaks, decreases with increasing surface coverage. Thus, samples with high particle density facilitate the

unambiguous determination of resonance peak positions and an exact read-out of potential changes in its position induced by biochemical interactions on the sensor surface. Furthermore, Fig. 4-19 indicates that the quadrupole plasmon resonance mode exhibits a lower normalized FWHM than the dipole resonance for each surface coverage, and therefore appears to be better suited for the detection of binding events on the sensor surface.

Another interesting aspect from these experimental results is that the broadening of both dipole and quadrupole resonance peaks due to small surface coverage is an analog to the observation of Westcott et al for gold nanoshells, where an inhomogeneous broadening of the plasmon line shape was observed due to core and shell size distributions.⁹⁷

b. Dependence of the plasmon resonance line shape on the upper gold layer

The plasmon resonance line shape of LSPR biosensors prepared by different gold deposition techniques, - seeding/plating as well as PVD -, is investigated by comparing the normalized FWHM of the dipole and quadrupole peaks.

Table 4-6 shows the FWHM, intensity, and normalized FWHM of the dipole and quadrupole resonances for LSPR biosensors prepared by seeding/plating and PVD in the fabrication of the upper gold layer. Here, a composite structure of a homogeneous silica film with a thickness of 50 nm and a silica particle monolayer ($d = 510$ nm) serves as the intermediate dielectric layer.

Table 4-6. FWHM, intensity, and normalized FWHM of the dipole and quadrupole resonances for LSPR biosensors prepared by seeding/plating and PVD in the fabrication of the upper gold layer. A composite structure of a silica particle monolayer and a homogenous silica layer serves as the intermediate dielectric layer.

Fabrication of the upper gold layer	Seeding/plating		PVD	
	Quadrupole	Dipole	Quadrupole	Dipole
FWHM	46.4	135.0	54.6	80.4
I	1.372	1.139	0.496	1.498
<i>L</i>	33.8	118.5	110.1	53.7

In line with the above discussion, a lower value for L is found for the quadrupole resonance peak (33.8) than for the dipole mode (118.5) for the seeding/plating technique. Interestingly, this behavior is reversed if PVD is used in the fabrication of the upper gold layer instead of seeding/plating. The LSPR biosensor fabricated by PVD exhibits a lower value for L in the dipole resonance peaks (53.7), compared to the quadrupole mode (110.1).

Concluding, the lowest normalized FWHM, which is an indicator for the sharpness of the resonance peaks, was accomplished in the quadrupole resonance mode of the LSPR biosensor prepared by seeding/plating in the fabrication of the upper gold layer, with a composite structure of a homogeneous silica film (thickness = 50 nm) and a silica particle monolayer ($d = 510$ nm) as the intermediate dielectric layer.

4.2.4.3. Optical homogeneity

a. Dependence of the optical homogeneity on the intermediate dielectric layer

The second criterion for application of the LSPR biosensor in the detection of antibody-antigen interactions in miniaturized format is the optical homogeneity of the sensor. In order to determine the optical uniformity of the prepared LSPR biosensor, extinction spectra of five arbitrarily selected positions on a 1×1.5 cm² sample were recorded and the variation in wavelength of the dipole and quadrupole resonance maxima was analyzed.

The fabrication techniques of the intermediate dielectric layer - simple incubation technique and optimized protocol for spin coating technique - are compared to each other in terms of optical homogeneity. Fig. 4-20 shows the extinction spectra of five different locations on LSPR biosensor prepared by the simple incubation technique using covalent bonding (cf. Fig. 4-6). Here, silica nanoparticles with a diameter of 0.97 μm were used and the upper gold layer was deposited by seeding/plating.

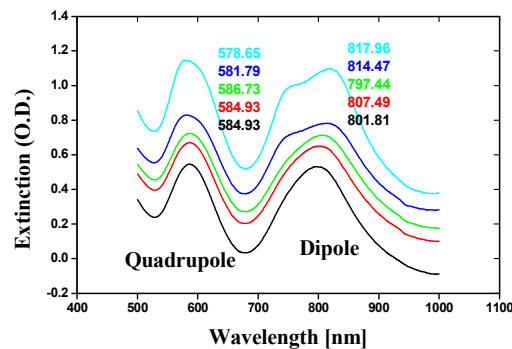


Figure 4-20. Dipole and quadrupole resonance peaks of a LSPR biosensor, the intermediate dielectric layer was prepared by simple incubation technique. The spectra were taken on a $1 \times 1.5 \text{ cm}^2$ sample in five arbitrarily selected positions.

All five positions display a dipole plasmon mode with a maximum at $\sim 810 \text{ nm}$ and a quadrupole plasmon mode with a maximum at $\sim 580 \text{ nm}$ in their extinction spectra.

Table 4-7. Dipole and quadrupole resonance maxima of the LSPR biosensor. The intermediate dielectric layer was prepared by simple incubation technique.

Position	Quadrupole resonance maximum	Dipole resonance maximum
1	578.6 nm	818.0 nm
2	581.7 nm	814.5 nm
3	586.7 nm	797.4 nm
4	584.3 nm	807.5 nm
5	584.9 nm	801.8 nm

The maximum of the quadrupole resonance shows a variation of 8.1 nm, with 578.6 nm as the lowest and 586.7 nm as the highest resonance wavelength. In the dipole resonance, a 20.6 nm-deviation was found around the maximum with 797.8 nm as the lowest and 818.0 nm as the highest wavelength (Tab. 4-7).

This result shows that a molecular binding on the LSPR sensor surface, prepared by simple incubation, can only be reliably detected by monitoring the shift in the dipole resonance peak, if the resulting adsorption-induced shift is larger than 20 nm. However, a binding event can be identified by monitoring changes in the quadrupole peak if the adsorption-induced shift surpasses the 8 nm-limit. This result shows the advantage of monitoring the quadrupole shift instead of the commonly monitored shift in the dipole resonance.

The optical homogeneity of a LSPR biosensor, which was prepared by an optimized spin coating process, is shown in Fig. 4-21. The diameter of the silica nanoparticles was 970 nm and seeding/plating was used for the deposition of the upper gold layer. Again, the wavelengths of the quadrupole and dipole resonance peaks were identified on a $1 \times 1.5 \text{ cm}^2$ sample at five arbitrarily selected positions. The obtained maxima of resonance peaks are compiled in Table 4-8.

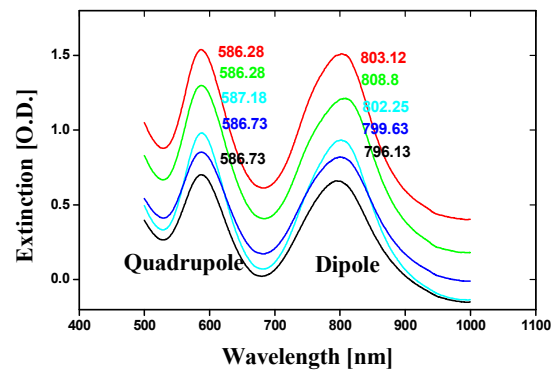


Figure 4-21. Dipole and quadrupole resonance peaks of a LSPR biosensor, the intermediate dielectric layer was prepared by optimized spin coating. The spectra were taken on a $1 \times 1.5 \text{ cm}^2$ sample in five arbitrarily selected positions.

The dipole resonance peaks show a variation of 12.7 nm in the wavelength of its resonance maximum while quadrupole resonance exhibits a variation of only 0.9 nm (see Table 4-8). These results are clearly in line with those for the simple incubation technique (see Table 4-7). Here, the variation in the wavelength of the quadrupole resonance maximum was also less than that of the dipole resonance.

Table 4-8. Dipole and quadrupole resonance maxima of the LSPR biosensor. The intermediate dielectric layer was prepared by optimized spin coating.

Position	Quadrupole resonance maximum	Dipole resonance maximum
1	586.28 nm	803.12 nm
2	586.28 nm	808.80 nm
3	587.18 nm	802.25 nm
4	586.73 nm	799.63 nm
5	586.73 nm	796.13 nm

In Table 4-9, the variation of the quadrupole and dipole resonance maximum in the LSPR biosensor prepared by simple incubation technique and spin coating are listed. Both techniques generate less variation of the maxima in the quadrupole resonance than in the dipole resonance. Spin coating shows a definite advantage as the fabrication method for the silica particle monolayer, because it exhibits a significantly lower variation of the maximum wavelength for both quadrupole and dipole resonances.

Table 4-9. Variation of the dipole and quadrupole resonances in LSPR biosensor, the intermediate dielectric layer was prepared by simple incubation and spin coating.

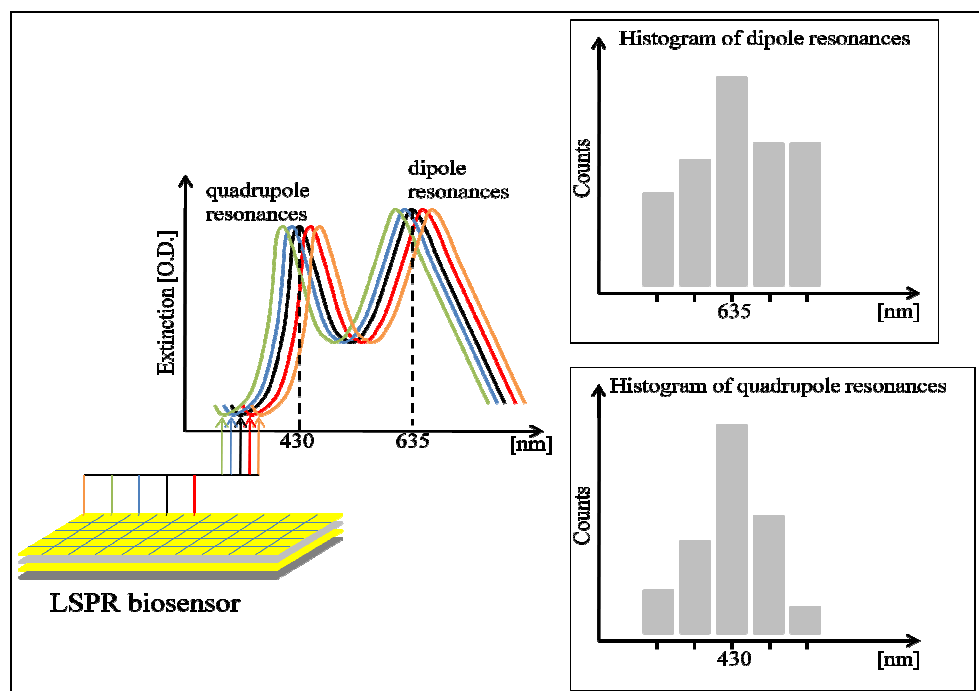
Fabrication of the intermediate dielectric layer	Variation of quadrupole resonance maximum	Variation of dipole resonance maximum
Simple incubation	8.1 nm	20.6 nm
Spin coating	0.9 nm	12.7 nm

However, larger areas of silica nanoparticle monolayer prepared by spin coating show a higher variation in the obtained particle surface density than found on a $1 \times 1.5 \text{ cm}^2$ sample. This suggests that strict control of humidity and temperature is required in order to achieve further improvement of sample preparation with the spin coating procedure in case of larger sample areas.

b. Dependence of optical homogeneity on the upper gold layer

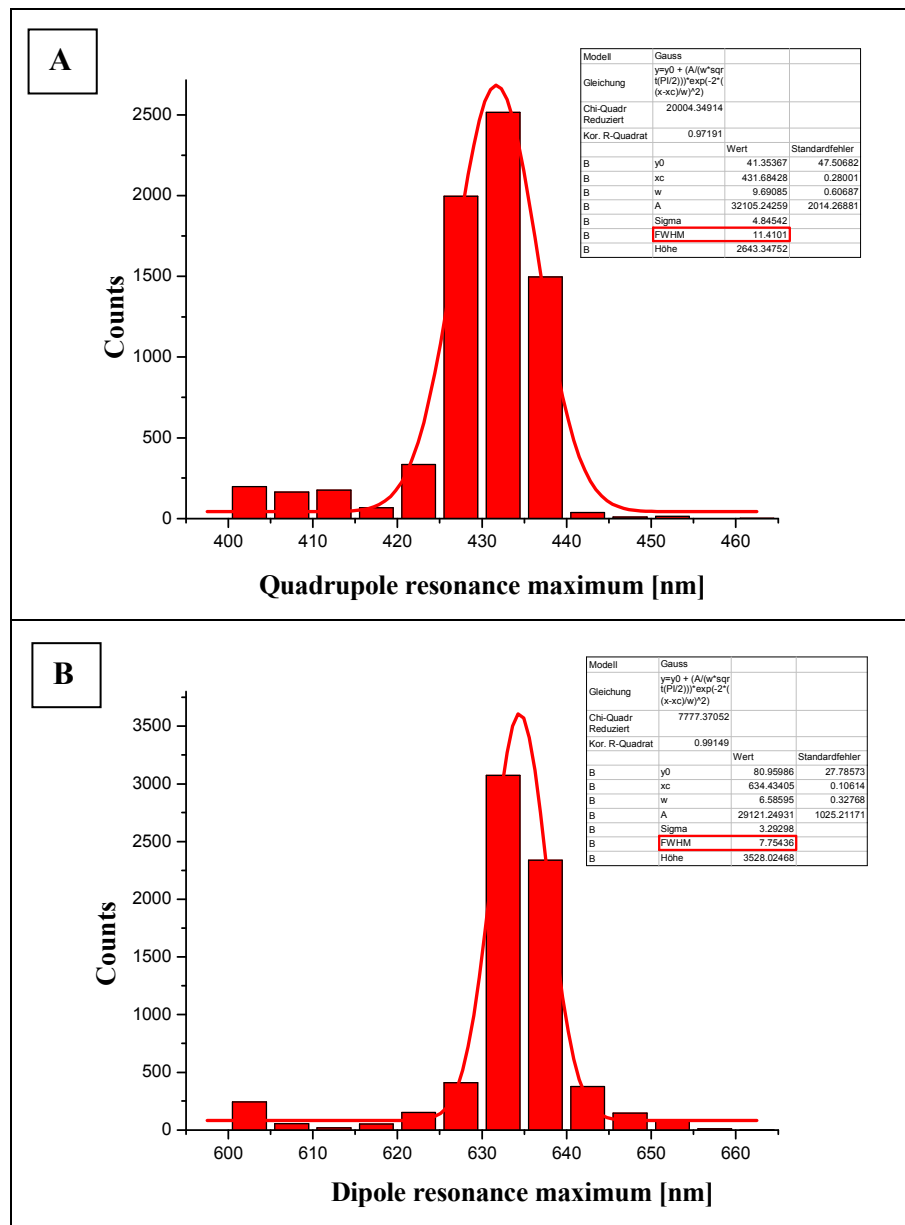
The deposition techniques for the upper gold layer - seeding/plating and PVD - are compared to each other in terms of optical homogeneity. In order to compare the optical homogeneity, LSPR biosensor surfaces were scanned in the UV-Vis spectrometer with a pixel size of $100\ \mu\text{m} \times 100\ \mu\text{m}$. An extinction spectrum was recorded for each measured pixel, and the wavelengths of the dipole and quadrupole resonance maxima are plotted in a histogram.

These histograms are fitted to a Gaussian function to determine their full width at half maximum (FWHM). The FWHM determines the distribution of the resonance maxima and, therefore, is an indicator for the optical homogeneity of the LSPR sensors. A low FWHM indicates a low variation in the wavelength of the resonance maxima. Figure 4-22 shows the generation principle of the histograms.



In Graph 4-1, the distribution of the quadrupole and dipole resonance maxima in a LSPR sensor prepared by the seeding/plating technique is displayed. Silica nanoparticles with a diameter of 510 nm served as the intermediate dielectric layer, which was prepared by the floating technique (cf. Fig. 4-12). A total number of 7738 pixels on the LSPR sensor surface were measured and displayed as histograms with a bin size of 5 nm.

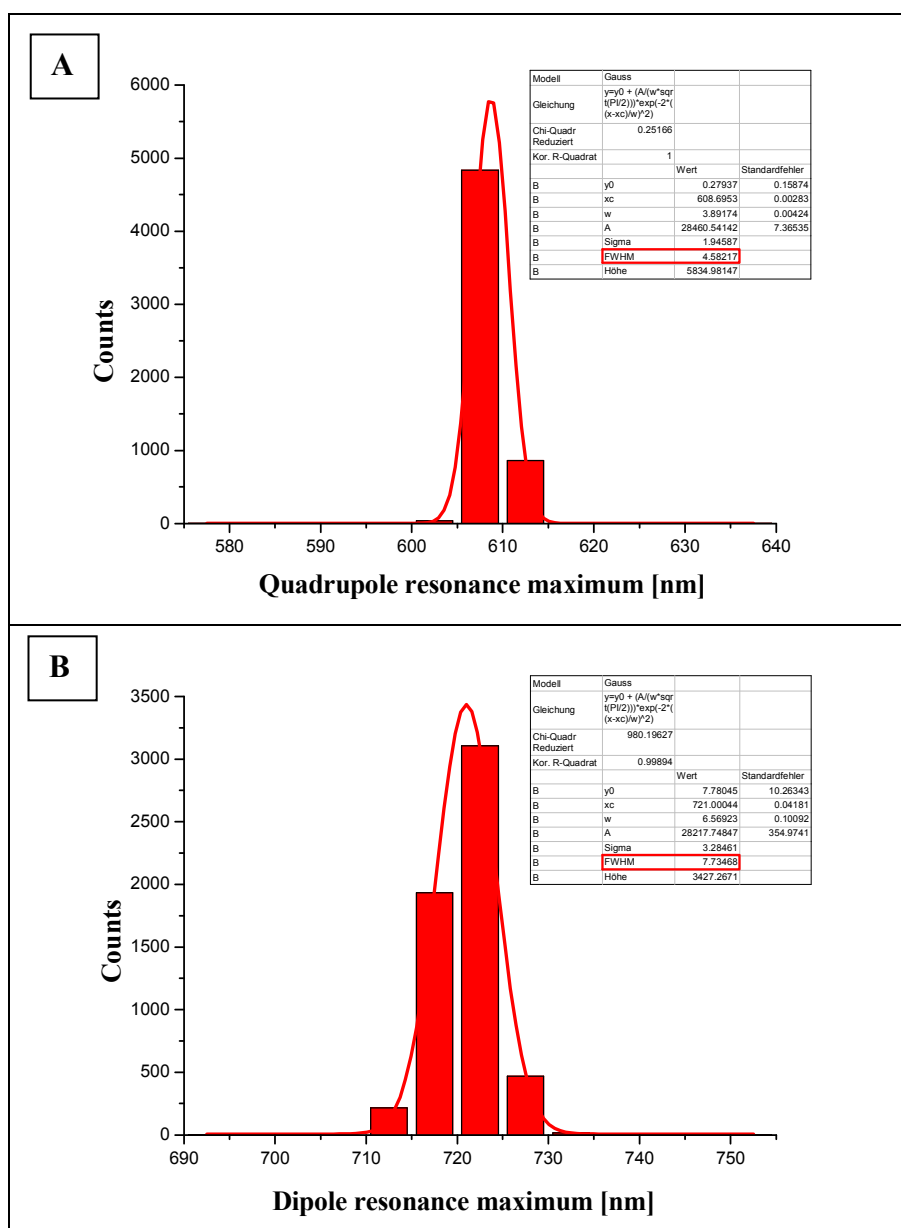
Fitting of the quadrupole resonance histogram to a Gaussian peak yields a FWHM of 11.41 nm (Graph 4-1A), while the FWHM of the dipole resonance histogram measures 7.75 nm (Graph 4-1B). This result implies that the dipole resonance has less variation in its maximum than the quadrupole resonance, which is in contrast to the results given in Table 4-9.



Graph 4-1. Distribution of the resonance maxima in a LSPR biosensor for (A) the quadrupole resonance peak and (B) the dipole resonance peak. The upper gold layer was prepared by seeding/plating.

In Graph 4-2, the distribution of the quadrupole and dipole resonance maxima in a LSPR sensor prepared by Physical Vapor Deposition (PVD) is displayed. Silica nanoparticles with a diameter of 510 nm constitute the intermediate dielectric layer, which was prepared by the floating technique. A total number of 5684 pixels on the LSPR sensor surface were measured and displayed as histograms with a bin size of 5 nm.

Gaussian fitting of the quadrupole resonances show a FWHM of 4.58 nm (Graph 4-2A), while the FWHM of the dipole gaussian function is 7.73 nm (Graph 4-2B). This indicates less variation of the resonance maxima for the quadrupole than for dipole resonances, which is in line with the results given in Table 4-9.



Graph 4-2. Distribution of the resonance maxima in a LSPR biosensor for (A) the quadrupole resonance peak and (B) the dipole resonance peak. The upper gold layer was prepared by PVD.

In Table 4-10, the FWHMs of the dipole and quadrupole resonances of both gold deposition methods are compiled. The quadrupole resonance peak of the LSPR biosensor prepared by PVD possesses the smallest overall FWHM. This small variance in the resonance maximum indicates a higher optical homogeneity of the LSPR biosensor prepared by PVD. This will be a significant advantage in the read-out/detection of binding events on the LSPR biosensor. However, the FWHM of the dipole resonances of both gold deposition techniques are very similar.

Table 4-10. FWHM of the dipole and quadrupole resonances in LSPR biosensor, the upper gold layer was prepared by seeding/plating and PVD.

Fabrication of the upper gold layer	FWHM of quadrupole resonance maximum	FWHM of dipole resonance maximum
Seeding/plating	11.41 nm	7.75 nm
PVD	4.58 nm	7.73 nm

Concluding, the optical homogeneity of the LSPR biosensor was optimized by variation in the fabrication of the intermediate dielectric layer and in the deposition of the upper gold layer. To this end, optical homogeneity was assessed by the variation in wavelength of the quadrupole and dipole resonance maxima. Less variation in resonance maxima of both the dipole as well as quadrupole resonances was observed for spin coating than for the simple incubation technique. The data thus indicate that the spin coating technique achieves a better optical homogeneity of silica particle monolayers than the simple incubation technique.

Regarding the deposition techniques of the upper gold layer, a smaller overall variation in the resonance maxima was observed for the PVD than for the seeding/plating technique.

4.2.4.4. Optical sensitivity

a. Dependence of optical sensitivity on the intermediate dielectric layer

The third criterion for the suitability of the LSPR biosensor in the detection of antibody-antigen interactions is the sensitivity of the sensor towards molecular binding events on its surface. The sensitivity tests were performed by incubating the sensors in a 1 mg/ml solution of fibrinogen for three hours and – after rinsing and drying – monitoring the adsorption-induced shift of the dipole and quadrupole resonance maxima.

Fig. 4-23 shows the extinction spectra before (black line) and after (red line) incubation in fibrinogen for a LSPR biosensor prepared by simple incubation technique. Silica particle monolayers were formed with 390 nm silica nanoparticles and seeding/plating was used to deposit the upper gold layer.

A red shift in both the dipole and quadrupole plasmon resonances is observed in Fig. 4-23a after the formation of a fibrinogen film. Figs. 4-23b and c indicate that the dipole resonance peak shows a higher red shift (7 nm) than the quadrupole resonance peak (5 nm).

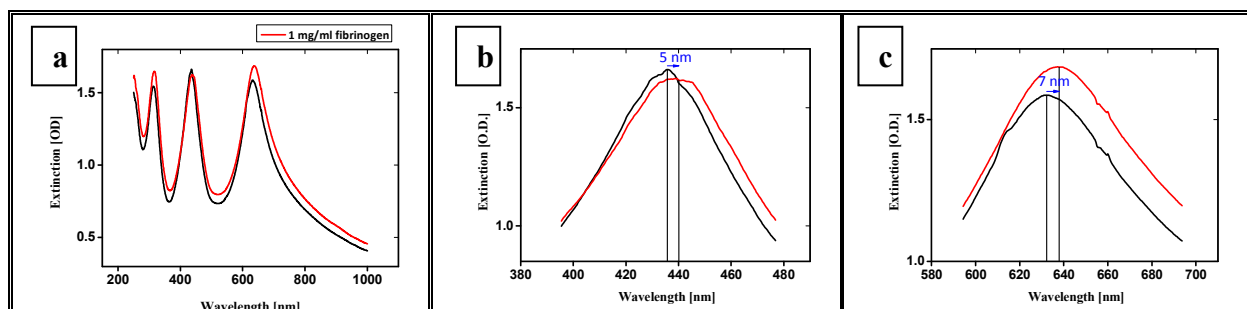


Figure 4-23. Extinction spectra of a LSPR biosensor before (black line) and after (red line) adsorption of fibrinogen. The intermediate dielectric layer was prepared by simple incubation technique with silica nanoparticles.
(a) overview (b) in quadrupole mode (c) in dipole mode

The red-shift of both the dipole and quadrupole resonance modes due to formation of the fibrinogen film arises from an increased polarizability of the surrounding dielectric media. Again, this can be rationalized by considering the surface plasmon resonances as a homogenous electron gas oscillating over a fixed positively charged background with induced surface charges providing a restoring force. The surrounding dielectric media polarizes in response to the resulting field and effectively reduces the strength of the surface charge. As a result, the restoring force decreased. Consequently, the plasmon energies are lowered and the resonance peaks appear in the longer wavelength as the dielectric constant of the surrounding medium grows.⁹⁸

Similar to the silica-gold nanoshell system (Fig. 4-17b) discussed by Westcott et al⁹⁷, the dipole resonance in the LSPR biosensor system developed in this work is more sensitive to changes in the surrounding dielectric media than the quadrupole mode. In order to understand this phenomenon, the extinction efficiency due to absorption and scattering of the incident light has to be taken into account.

The extinction efficiency for small particles is given by:

$$Q_{ext} = 4x \operatorname{Im} g_d$$

$$\text{with } g_d = \left(\frac{\varepsilon_m - \varepsilon_d}{\varepsilon_m + 2\varepsilon_d} \right)$$

Here, $x = 2\pi a(\varepsilon_0)^{1/2}/\lambda$; and $\varepsilon_m, \varepsilon_d$ are the dielectric constants of the metal particle and the surrounding dielectric media.⁹⁹⁻¹⁰⁰

For larger particles, higher multipoles in particular the quadrupole term become more important to the extinction spectra.

$$Q_{ext} = 4x \operatorname{Im} \left[g_d + \frac{x^2}{12} g_q + \frac{x^2}{30} (\varepsilon_m - 1) \right]$$

$$\text{with } g_q = \left(\frac{\varepsilon_m - \varepsilon_d}{\varepsilon_m + \frac{3}{2}\varepsilon_d} \right)$$

The factors g_d and g_q play the key role in determining the wavelength dependence of extinction efficiency, as the metal dielectric constant ε_m is strongly dependent on the wavelength.

Since $\operatorname{Im} \left(\frac{a-ib}{a^2+b^2} \right) = \left(\frac{-b}{a^2+b^2} \right)$, $\operatorname{Im} g_d$ can be solved to $\frac{\varepsilon_m' 3\varepsilon_d}{(\varepsilon_m' + 2\varepsilon_d)^2 + \varepsilon_m''^2}$. Therefore, the dipole resonance occurs when $(\varepsilon_m' + 2\varepsilon_d)^2 + \varepsilon_m''^2$ is minimal. Here, ε_m' is the real part and ε_m'' is the imaginary part of the metal dielectric constant.

Using the same argumentation, the condition for quadrupole resonance is fulfilled when $(\varepsilon_m' + 3/2 \varepsilon_d)^2 + \varepsilon_m''^2$ is minimal.

In Fig. 4-24, $(\varepsilon_m' + 2\varepsilon_d)^2 + \varepsilon_m''^2$ and $(\varepsilon_m' + 3/2 \varepsilon_d)^2 + \varepsilon_m''^2$ are plotted as a function of the wavelength to determine the resonance conditions for the dipole and quadrupole modes. The real (ε_m') and imaginary (ε_m'') dielectric constants for thin gold films¹⁰¹ are inserted in these equations. The resonance conditions for the LSPR biosensor on air ($\varepsilon_d = 1.00054$) and coated with a thiol-SAM ($\varepsilon_d = 2.7$) are then calculated.¹⁰²

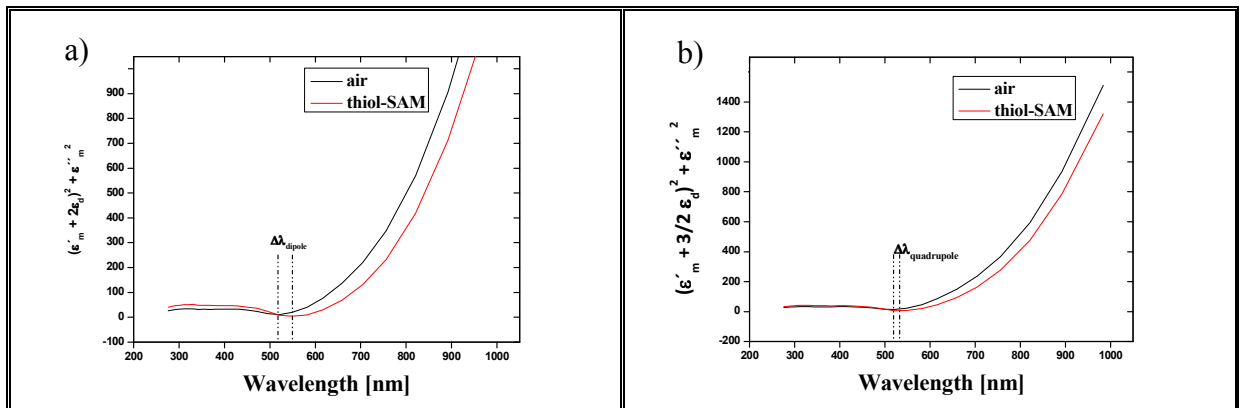


Figure 4-24. Plasmon resonance conditions for (a) dipole and (b) quadrupole mode, before (black line) and after (red line) formation of thiol SAM on the sensor surface.

It is clearly seen in Figure 4-24b that changes in the dielectric constant ϵ_d result in only small changes in quadrupole resonance wavelength. On the other hand, modification in surrounding medium of the sensor induces a much larger shift in the dipole resonance wavelength (Fig. 4-24a).

This rationalizes why the dipole resonance shift is much more sensitive towards the surrounding medium in comparison to the quadrupole mode. It should be noted at this point, however, that these results should be considered as qualitative only. For an exact theoretical calculation in determining the resonance wavelength, the real and imaginary parts of the dielectric constants of gold nanoshell should be used instead of those for thin gold film. Also, the dielectric constant of the surrounding medium has to be known with higher accuracy.

The stronger sensitivity of the dipole resonance on the medium compared to the quadrupole resonance observed in this work is consistent with results reported for other sensor systems, such as isolated silica-gold nanoshells and silver triangular nanoprisms.¹⁰³

Fig. 4-25 shows the extinction spectra of a LSPR biosensor before (black line) and after (red line) incubation in 1 mg/ml solution of fibrinogen. Here, the biosensor was prepared by spin coating instead of simple incubation technique. Silica nanoparticles with a diameter of 510 nm were used and the upper gold layer was deposited by seeding/plating. Again, dipole resonance modes show a higher sensitivity toward changes in the dielectric constant of the surrounding medium than the quadrupole mode. Adsorption of fibrinogen with a concentration of 1 mg/ml can be observed in the extinction spectra as a 16 nm-shift in the quadrupole resonance maximum and a 26 nm-shift in the dipole resonance maximum (Fig. 4-25b and c).

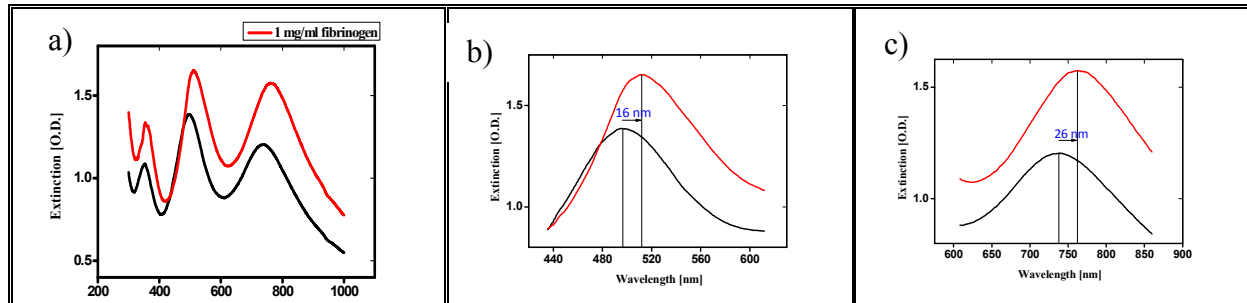


Figure 4-25. Extinction spectra of a LSPR biosensor before (black line) and after (red line) adsorption of fibrinogen. The intermediate dielectric layer was prepared by spin coating:
(a) overview (b) in quadrupole resonance mode (c) in dipole resonance mode

In Table 4-11, the fibrinogen-induced shift of the quadrupole and dipole resonance maximum of the LSPR biosensor, prepared by simple incubation and spin coating as the fabrication method of the intermediate dielectric layer, are listed. Both techniques generate a lower shift in the quadrupole resonance maxima than in the dipole resonance. However, application of spin coating as the preparation method of the intermediate dielectric layer improved the sensitivity of both quadrupole and dipole resonance peaks.

Table 4-11. Adsorption-induced shifts of the dipole and quadrupole resonances after adsorption of fibrinogen on the LSPR biosensor, the intermediate dielectric layer was prepared by simple incubation and spin coating.

Fabrication of the intermediate dielectric layer	Shift of quadrupole resonance maximum	Shift of dipole resonance maximum
Simple incubation	5 nm	7 nm
Spin coating	16 nm	26 nm

b. Dependence of optical sensitivity on the upper gold layer

The deposition techniques of the upper gold layer - seeding/plating and PVD - are also compared to each other in term of optical sensitivity by comparing the adsorption-induced shift of the dipole and quadrupole resonances.

Fig. 4-26 shows the extinction spectra of LSPR biosensor prepared by seeding/plating as the deposition method of the upper gold layer, before (black line) and after (red line) incubation in a 1 mg/ml solution of fibrinogen. The intermediate dielectric layer was fabricated by floating using 510 nm silica nanoparticles. Dipole resonance modes show a higher sensitivity toward changes in the dielectric constant of the surrounding medium than the quadrupole mode. Adsorption of fibrinogen with a concentration of 1 mg/ml can be observed in the extinction spectra as a 6 nm-shift in the quadrupole resonance maximum and a 52 nm-shift in the dipole resonance maximum (Fig. 4-26b and c).

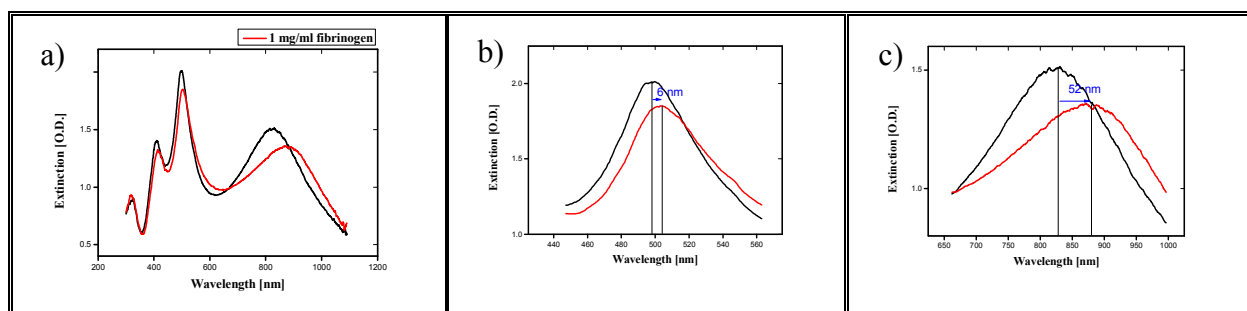


Figure 4-26. Extinction spectra of LSPR nanobiosensor before (black line) and after (red line) adsorption of fibrinogen. The upper gold layer was prepared by seeding/plating.
(a) overview (b) in quadrupole resonance mode (c) in dipole resonance mode

Fig. 4-27 shows the extinction spectra of a LSPR biosensor prepared by PVD as the deposition method of the upper gold layer, before (black line) and after (red line) incubation in a 1 mg/ml solution of fibrinogen. The intermediate dielectric layer was fabricated by floating using 510 nm silica nanoparticles. Again, the extinction spectra show a larger shift in the dipole resonance maximum than in the quadrupole resonance maximum. Adsorption of fibrinogen with a concentration of 1 mg/ml can be observed in the extinction spectra as a 16 nm -shift in the quadrupole resonance maximum and a 26 nm -shift in the dipole resonance maximum (Fig. 4-27b and c).

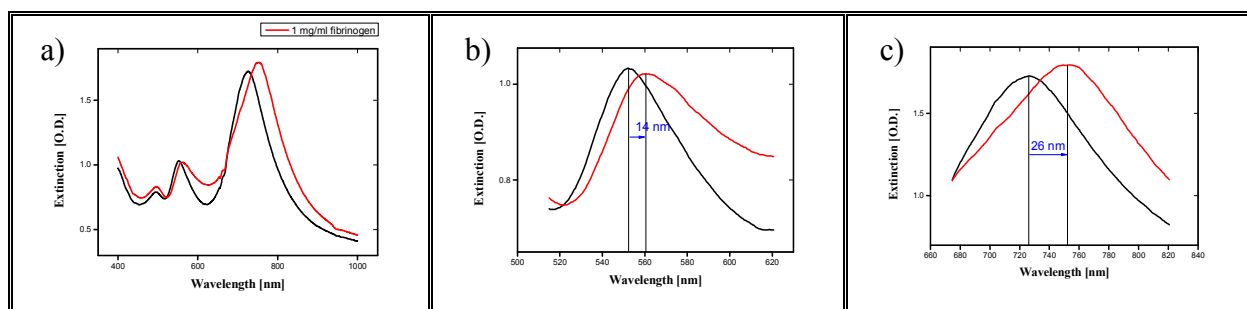


Figure 4-27. Extinction spectra of a LSPR biosensor before (black line) and after (red line) adsorption of fibrinogen. The upper gold layer was prepared by PVD.
(a) overview (b) in quadrupole resonance mode (c) in dipole resonance mode

In Table 4-12, the adsorption-induced shifts of the dipole and quadrupole resonances of LSPR biosensor prepared by the two gold deposition methods are compared. Both seeding/plating and PVD resulted in a higher sensitivity of the dipole resonances towards changes in the surrounding medium compared to quadrupole resonances. However, a larger adsorption-

induced shift in the dipole resonance was achieved by the seeding/plating method (52 nm) than in the LSPR sensors prepared by PVD (26 nm), while a higher shift in the quadrupole peak was achieved by the PVD as the gold deposition technique (14 nm) than in the sensors prepared by seeding/plating.

Table 4-12. Adsorption-induced shifts of the dipole and quadrupole resonances after adsorption of fibrinogen on the LSPR biosensor, the upper gold layer was prepared by seeding/plating and PVD.

Fabrication of the upper gold layer	Shifts of quadrupole resonance maximum	Shifts of dipole resonance maximum
Seeding/plating	6 nm	52 nm
PVD	14 nm	26 nm

In summary, the sensitivity of the LSPR biosensor prepared by different techniques was investigated. First, simple incubation and spin coating were compared to each other as the fabrication technique of the intermediate dielectric layer. The usage of spin coating in the preparation of silica nanoparticle monolayers improves the sensitivity of both dipole and quadrupole resonances compared to LSPR sensors prepared by the simple incubation method. In the comparison of seeding/plating and PVD as the deposition technique of the upper gold layer, both have advantage and disadvantages. Seeding/plating shows a higher sensitivity in the dipole resonance compared to PVD, while PVD technique generates a larger shift in the quadrupole resonance.

However, all LSPR biosensors prepared by different techniques show one distinct trend: they all generate higher adsorption-induced shifts in the dipole than in the quadrupole resonance. For this reason, the dipole resonance will be more sensitive to molecular interactions occurring on the sensor surface.

4.2.4.5. Conclusion

In this thesis, biosensors based on the localized and propagating surface plasmon resonances of gold have been successfully synthesized. The construction of the LSPR biosensors requires two gold layers and an intermediate dielectric layer between the two gold layers. Three geometries of the intermediate dielectric layer were investigated in this thesis: a silica nanoparticle monolayer, a homogeneous silica film, and a composite structure of a silica particle monolayer and a homogeneous silica film. While the lower gold layer was exclusively prepared by Physical Vapor Deposition (PVD), the two distinct techniques of PVD and seeding/plating were investigated in the deposition of the upper gold layer.

It was shown that the extinction spectra of the LSPR biosensors optimized in this dissertation, correlate with the theoretical calculations made by Westcott et al.⁹⁷ for silica-gold nanoshells in water based on Mie scattering theory. Importantly, it is shown that the number and the wavelength of the excited resonance modes on the sensor increase with increasing core size. This shows that the optical properties of the LSPR sensor system, such as the position of the plasmon resonances, can be tuned by modifying the dielectric core size. Two plasmon resonance modes, identified as quadrupole and dipole resonances, can be excited in the wavelength region from 400 to 900 nm. The properties of these two resonance peaks were investigated further in this work.

The described LSPR biosensors have been characterized and optimized in terms of three aspects essential for the application of the sensors in the detection of biomolecular interactions: plasmon line shape, optical homogeneity, and sensitivity towards the surrounding dielectric medium.

The plasmon line shape, which determines the accuracy of a spectroscopic measurement, was quantitatively assessed by the normalized Full Width at Half Maximum (FWHM), defined as $L = \frac{FWHM \text{ (Full Width at Half Maximum)}}{I \text{ (Intensity)}}$. A small L value will enable an exact read-out of the resonance maximum. Two important aspects were evaluated from the study of different LSPR biosensor structures. First, both the dipole and quadrupole resonance peaks strongly depend on the surface coverage on the silica particle monolayer and the normalized FWHM decreases with the increasing surface coverage. Second, the lowest normalized FWHM was accomplished in the quadrupole resonance mode of the LSPR biosensor prepared by seeding/plating in the fabrication of the upper gold layer, with a composite structure of a homogeneous silica film (thickness = 50 nm) and a silica particle monolayer ($d = 510$ nm) as the intermediate dielectric layer.

For parallel detection of binding events on a peptide array, it is necessary that surface areas with both unoccupied and occupied binding sites exhibit little variation in the resonance maximum position. To determine the optical homogeneity of the sensor, the extinction spectra of several arbitrarily chosen positions on a LSPR biosensor were recorded. The variations in the wavelength of the dipole and quadrupole resonances were then analyzed for different sensor preparation techniques. In a comparison between simple incubation and optimized spin coating in the preparation step for the intermediate dielectric layer, spin coating yielded a lower variation of the maximum wavelength for both quadrupole and dipole resonances. However, both techniques generate less variation of the maxima in the quadrupole resonance than in the dipole resonance. In the comparison of seeding/plating and PVD as the deposition technique for the upper gold layer, the quadrupole resonance peak of LSPR biosensor prepared by PVD shows the least variation.

A high sensitivity of the LSPR biosensors towards the surrounding medium is essential to detect biomolecular interactions in miniaturized format. Sensitivity tests were performed by observing the fibrinogen-induced shift of the dipole and quadrupole resonance maxima. Using spin coating in the preparation of silica nanoparticle monolayers has improved the sensitivity of both dipole and quadrupole resonances, compared to LSPR sensors prepared by the simple incubation method. In the comparison of seeding/plating and PVD as the deposition technique of the upper gold layer, both have advantages and disadvantages. Seeding/plating shows a higher sensitivity in the dipole resonance compared to PVD, while the PVD technique generates a larger shift in the quadrupole resonance.

A comparison of the different LSPR sensor geometries with respect to plasmon resonance line shape, optical homogeneity, and optical sensitivity is given in Table 4-13. Regarding these three aspects, the most suitable geometry for the application in label-free detection of biomolecular interactions is the LSPR biosensor which consists of a 100 nm gold film as the bottom gold layer, a 250 nm homogeneous silica film as the intermediate dielectric layer, and gold colloids prepared by seeding/plating as the upper gold layer (cf. Fig. 4-13b).

Table 4-13. Comparison of the different LSPR biosensor geometries with respect to the most important aspects for the application of the sensors in the detection of biomolecular interactions

	Plasmon resonance line shape	Optical homogeneity	Optical sensitivity
I. Intermediate dielectric layer			
1. silica nanoparticle layer	+	+	+
- by simple incubation	++	++	++
- by spin coating			
2. homogeneous silica film	+++	+++	++
3. composite structure of a silica nanoparticle layer and a homogeneous silica film	++	++	+++
II. Upper gold layer			
1. By seeding/plating	+++		+++ (dipole)
2. By PVD (Physical Vapor Deposition)		+++	+++ (quadrupole)

4.3. Synthesis of protein-resistant coatings on LSPR biosensor via Atom Transfer Radical Polymerization (ATRP)

In diagnostic assays and biosensors based on specific recognition of antigen-antibody pairs, suppression of nonspecific protein adsorption is crucial for achieving sufficient bioassay selectivity and sensitivity. Therefore, the successfully designed LSPR biosensor has to be coated by a protein-resistant layer, before it can be used as a solid support for the peptide array.

There are three requirements for the fabricated PEG-coated LSPR biosensor to be applicable as the solid substrate in the synthesis of peptide arrays by the printing technology: (i) a high stability against the chemical/mechanical stress occurring during the peptide array generation and the antibody assaying process, (ii) a high resistance against non-specific protein adsorption to enhance the signal-to-noise (S/N) ratios in the detection of antibody coupling, and (iii) to enable the integration of the peptides into the sensor surface.

Poly(ethylene glycol) (PEG), which is widely used in chemical and biomedical fields due to its nontoxic properties, was applied as the coating polymer on the sensor surface to prevent non-specific protein interaction. Instead of self-assembled monolayers of OEG-terminated alkanethiols, a protein-repelling coating based on a PEG graft polymer film was chosen to utilize the advantages of polymers such as thicker and more robust architecture and chemistry, and their three-dimensional layer geometries, providing a high loading of functional groups for the linkage of the generated peptides.

A poly(ethylene glycol) methacrylate (PEGMA) layer was synthesized on the sensor surface via Atom Transfer Radical Polymerization (ATRP) due to several considerations. Beside a high tolerance of functional groups, ATRP produces polymers with narrow molecular weight distributions, which provides a high control over the film thickness. Moreover, the mild reaction conditions should facilitate the application of ATRP on the chemically-sensitive LSPR biosensor.

4.3.1. Direct synthesis of protein-resistant coating on LSPR biosensor

In the first attempt to synthesize poly(ethylene glycol) methacrylate coating on the sensor surface via ATRP, initiator molecules are coupled directly onto the upper gold layer by thiol bonding.

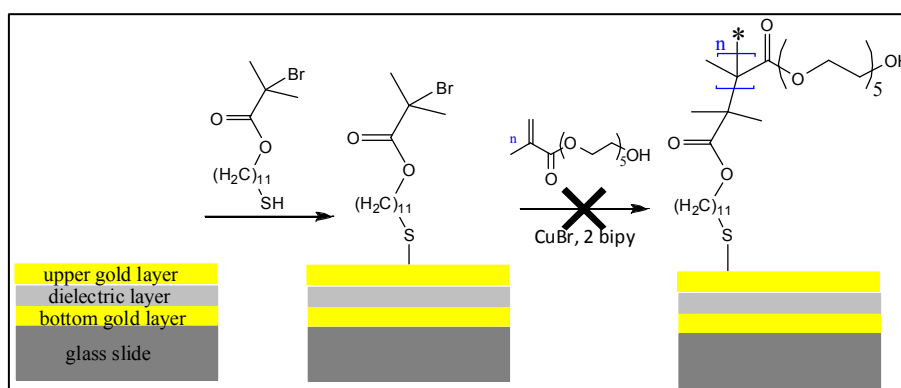


Figure 4-28. Direct synthesis of a PEGMA film on a LSPR biosensor via ATRP.

In the first step, an ATRP initiator (11-mercaptoundecyl 2-bromo-2methylpropanoate) was coupled directly onto the sensor surface. In the second step, the PEGMA monomer and catalyst were added.

Here, *11-mercaptoundecyl 2-bromo-2-methylpropanoate* acted as the ATRP initiator. Copper (I) bromide and 2,2'-bipyridine were added as ATRP catalyst. The direct synthesis of the PEGMA layer via ATRP was carried out on a LSPR biosensor utilizing colloidal gold as the upper metal layer and silica nanoparticles as the dielectric layer.

SEM images taken after the polymerization of OEGMA monomers on the LSPR biosensor show that a thick, undefined layer was formed on the sensor surface (Fig 4-29). However, the dielectric and upper gold layer of the LSPR biosensor, consisting of the gold-coated silica nanoparticles, were completely removed from the bottom gold layer. The silica nanoparticles were stripped from the gold colloids coating and trapped inside the polymer film.

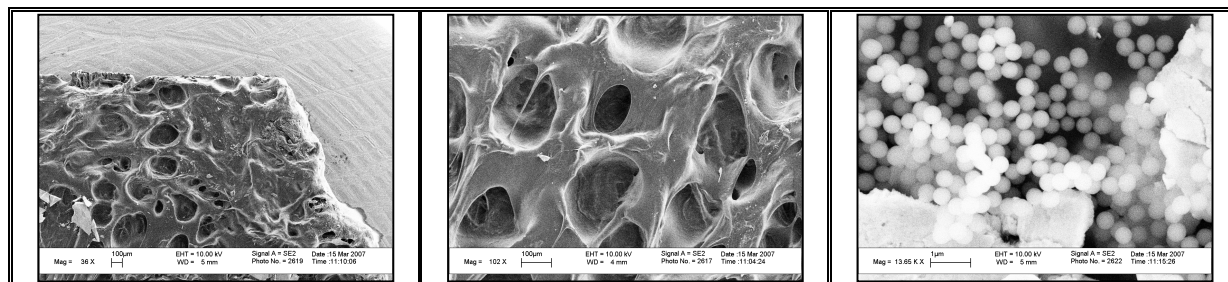


Figure 4-29. SEM images of polymer film directly synthesized on LSPR biosensor.

The direct synthesis of a protein-resistant coating on LSPR biosensor based on poly(ethylene glycol) methacrylate via ATRP failed, due to instability of the sensor towards chemical and mechanical stress.

4.3.2. Indirect synthesis of protein-resistant coating on the LSPR biosensor

In the second attempt to coat LSPR biosensor with a layer of protein-resisting PEG by ATRP, the sensor surface was first coated by a thin sol-gel film. This sol-gel film should stabilize the chemical and mechanically sensitive sensor and alleviate the attachment of the ATRP initiator molecules.

4.3.2.1. Synthesis of silica gel on the LSPR biosensor

A *gel* is an interconnected, rigid network with pores of submicrometer dimensions and polymeric chains whose average length is greater than a micrometer. A silica gel may be formed by network growth from an array of colloidal particles or by formation of an interconnected 3-D network by the simultaneous hydrolysis and polycondensation of an organometallic precursor.¹⁰⁴

There are seven processing steps in the fabrication of the silica sol-gel. In the first step, *mixing*, *sol* is formed by hydrolysis of the alkoxide precursor and condensation of the hydrated silica. A polycondensation reaction occurs and results in a SiO₂ network. In the second step, *casting*, the low-viscosity sol is casted into a mold. In the *gelation* step, the condensed silica species link together to become a three-dimensional network and the viscosity increases sharply. The fourth step, *aging*, involves maintaining the gel for a period of time, hours to days, completely immersed in liquid. Polycondensation continues along with localized solution and re-precipitation of the gel network, increasing the strength of the gel. During the fifth step, *drying*, the liquid is removed from the interconnected pore network. The sixth step is the *dehydration or chemical stabilization*, where the surface silanol (Si-OH) bonds are removed from the pore network resulting in a chemically stable ultraporous solid. In the last step, *densification*, the porous gel is heated at high temperature to eliminate the pores. The density ultimately becomes equivalent to fused quartz or fused silica.¹⁰⁴

The first approach for the formation of silica gel on metal surfaces based on the combination of sol-gel and self assembled monolayer (SAM) technologies was presented by Zanette *et al* in 1998, using two different preparation routes. The first avenue relies on the initial chemisorption of a thiolated precursor, while the second avenue involves the immersion of the sample in a sol-gel containing the thiolated precursor, along with the acid catalyst and methanol.¹⁰⁵

In this thesis, the coating of the LSPR biosensor by a silica gel was accomplished using the second preparation method with *(3-mercaptopropyl)trimethoxysilane* as the building block of the 3-D silica network (Fig. 4-30).

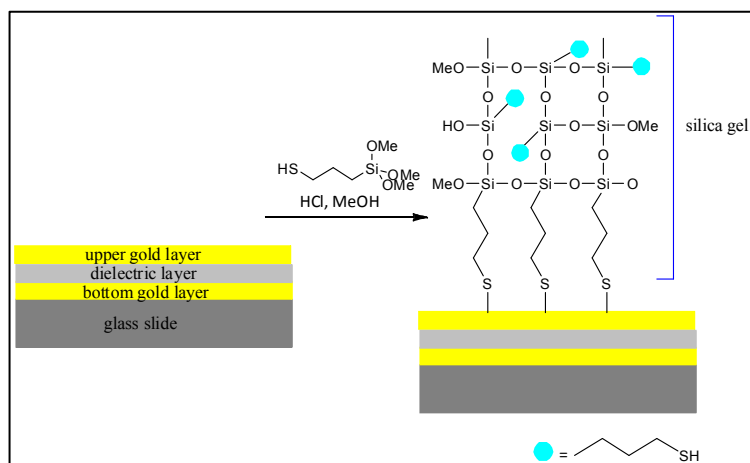


Figure 4-30. Synthesis of a three-dimensional silica gel on the LSPR biosensor via direct coupling of sol-gel and SAM technologies.

XPS revealed the formation of silica gel on the LSPR biosensors, indicated by intense C 1s- and O 1s signals. The elemental ratio of carbon, oxygen, sulfur and silicon of silica gel can be calculated using the following general equation:

$$\frac{I_X}{I_Y} = \frac{\sigma_X \lambda_X N_X}{\sigma_Y \lambda_Y N_Y} \quad (\text{Eq. 3-2})$$

In Equation 3-2, the peak area I can be calculated from XP spectra and the photoionization cross-section σ and the attenuation length λ can be obtained from literature or database. Thus, the elemental ratio, $\frac{N_X}{N_Y}$, can be calculated.

The attenuation length (λ) or the inelastic mean free path (IMFP) of the photoelectrons is a function of the kinetic energy and is dependent on the composition of the material. For calculation of the elemental peak ratio on the synthesized *silica gel*, IMFPs of photoelectrons in *poly(dimethylsiloxane)*¹⁰⁶ are applied in the equation, due to the similarities in film structure (Table 4-13).

Table 4-13. Estimated attenuation lengths of C 1s, O 1s, S 2p and Si 2p photoelectrons in poly(dimethylsiloxane)

Orbital	C1s	O1s	S2p	Si2p
E_{kin} [eV] for Mg $K\alpha$ radiation	970	724	1094	1150
λ [nm]	4.10	3.25	4.51	4.69

The peak ratios of carbon, oxygen, sulfur, and silicon were calculated using λ values taken from Table 4-13 and are presented in Table 4-14. The low sulfur peak intensity indicated that the silica gel was formed on top of the gold-thiolate bond (c.f. Fig. 4-30).

Table 4-14. Elemental ratio of carbon, oxygen, sulfur and silicon found in the XP spectra of silica gel coated LSPR biosensors indicating that the silica gel was formed on top of the gold-thiolate bond (c.f. Fig. 4-30).

C	O	S	Si
10	6	1	3.5

Fig. 4-31a shows a S 2p peak at 163.5 eV, which is consistent with the formation of a gold-thiolate bond as found in literature.¹⁰⁷⁻¹⁰⁹ A significant amount of unbound thiol was detected in the spectrum, revealed through the S 2p peak with a binding energy (BE) of 166.8 eV.

Three C 1s signals with BEs of 284.8, 288.1, and 289.9 eV were found by the peak fitting (Fig 4-31b). The peak at 284.8 eV corresponds to the carbon atom in the methylene group, which was surrounded by two other methylene groups. The 288.1 eV peak corresponds to methylene groups which are bound to a sulfur atom on one side and a methylene group on the other side. Carbon atoms of the methylene groups connected to an oxygen atom are revealed in the XP spectra as the C 1s peak with the highest binding energy, due to the strong electronegativity of O.

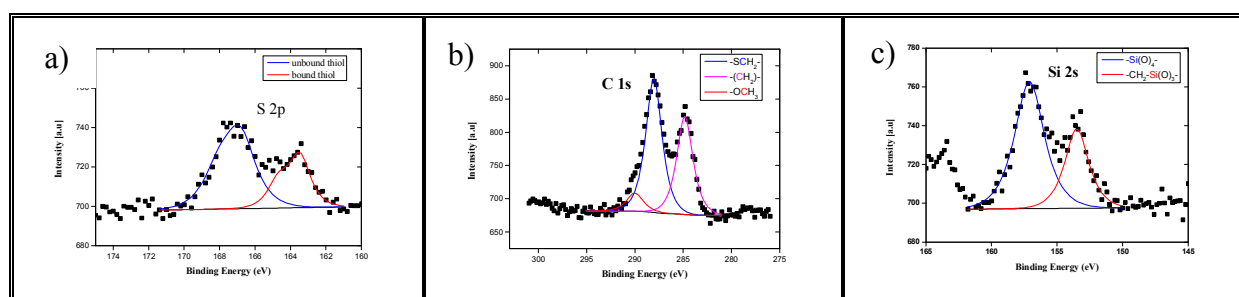


Figure 4-31. XPS spectra of silica gel coated LSPR biosensor of (a) S 2p, (b) C 1s, and (c) Si 2s electrons.

The XP spectra show two Si 2s peaks at 153.5 and 157.1 eV. The 153.5 eV peak corresponds to the silicon atoms surrounded by three oxygen atoms and one methylene group, while the peak at 157.1 eV indicates the silicon atoms bound to four oxygen atoms (Fig 4-31c).

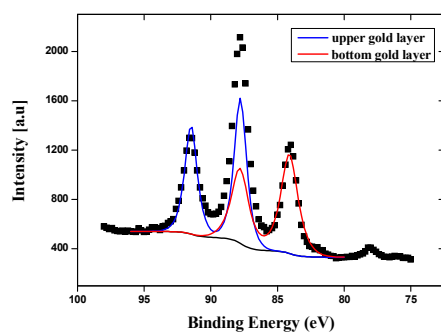


Figure 4-32. XPS Au 4f spectrum of silica gel coated LSPR biosensor.

Interestingly, the XP spectra show three instead of two visible peaks in the Au 4f region. The chemical shift of 3.7 eV, which is the exact value of $4f_{5/2} - 4f_{7/2}$ BE splitting, found between the right and middle peaks, indicates an overlap of two Au 4f signals originating from both upper and bottom gold layers (Fig. 4-32).

The $4f_{5/2}$ and $4f_{7/2}$ peaks with BEs of 87.8 and 84.1 eV arise from the bottom gold layer. The upper gold layer shows $4f_{5/2}$ and $4f_{7/2}$ peaks at 91.4 and 87.8 eV due to the charging effect.

The thickness of the silica gel on the LSPR biosensor was estimated using the Lambert Beer law, relating the reduction of electron number to the properties of the material through which the electrons are traveling.

$$I = I_0 \exp \left[\frac{-d}{\lambda \cos \theta} \right] \quad (\text{Eq. 3-3})$$

I = Intensity of the gold photoelectrons attenuated by a film; I_0 = intensity of gold photoelectrons from clean gold, i.e. uncoated gold film; d = thickness of the film; θ = the angle between the surface normal and the analyzer axis; λ = attenuation length.

The thickness of the silica gel is estimated by calculating the ratio of the Au 4p_{3/2} peak to the Au 4f peak, since both photoelectrons generate very intensive signals in the XP spectra.

$$\begin{aligned} \frac{I^{Au\ 4f}}{I^{Au\ 4p}} &= \frac{I_0^{Au\ 4f} \exp \left[\frac{-d}{\lambda^{Au\ 4f}} \right]}{I_0^{Au\ 4p} \exp \left[\frac{-d}{\lambda^{Au\ 4p}} \right]} \\ \exp \left[\frac{-d}{\lambda^{Au\ 4f}} + \frac{d}{\lambda^{Au\ 4p}} \right] &= \frac{I^{Au\ 4f}}{I^{Au\ 4p}} \frac{I_0^{Au\ 4p}}{I_0^{Au\ 4f}} \\ \exp \left[d \left(\frac{1}{\lambda^{Au\ 4p}} - \frac{1}{\lambda^{Au\ 4f}} \right) \right] &= \frac{I^{Au\ 4f}}{I^{Au\ 4p}} \frac{I_0^{Au\ 4p}}{I_0^{Au\ 4f}} \\ \exp \left[d \left(\frac{\lambda^{Au\ 4f} - \lambda^{Au\ 4p}}{\lambda^{Au\ 4p} \times \lambda^{Au\ 4f}} \right) \right] &= \frac{I^{Au\ 4f}}{I^{Au\ 4p}} \frac{I_0^{Au\ 4p}}{I_0^{Au\ 4f}} \\ d &= \left(\frac{\lambda^{Au\ 4p} \times \lambda^{Au\ 4f}}{\lambda^{Au\ 4f} - \lambda^{Au\ 4p}} \right) \ln \left[\frac{I^{Au\ 4f}}{I^{Au\ 4p}} \frac{I_0^{Au\ 4p}}{I_0^{Au\ 4f}} \right] \end{aligned}$$

For estimation of the silica gel thickness synthesized in this work, attenuation lengths of Au 4p and Au 4f photoelectrons in poly(dimethylsiloxane) were used in the equation (Table 4-15).¹⁰⁶

Table 4-15. Estimated attenuation lengths of Au 4p and Au 4f photoelectrons in poly(dimethylsiloxane)

Orbital	Au 4p	Au 4f
E_{kin} [eV] for Mg K α radiation	710	1168
λ [nm]	3.2	4.75

The ratio of $\frac{I_0^{Au\ 4p}}{I_0^{Au\ 4f}}$ was determined experimentally by measuring the gold peaks intensity of a clean gold film. Hence, the approximate thickness of the silica gel over the LSPR biosensor was

$$d = \left(\frac{\lambda^{Au\ 4p} \times \lambda^{Au\ 4f}}{\lambda^{Au\ 4f} - \lambda^{Au\ 4p}} \right) \ln \left[\frac{I^{Au\ 4f}}{I^{Au\ 4p}} \frac{I_0^{Au\ 4p}}{I_0^{Au\ 4f}} \right]$$

$$d = \left(\frac{3.2 \times 4.75}{4.75 - 3.2} \right) nm \ln \left[\frac{I_{Au\ 4f}^{9208}}{I_{Au\ 4p}^{45928}} \right]$$

$$d = 9.8 nm \ln \left[0.2 \frac{I_{Au\ 4f}}{I_{Au\ 4p}} \right] = 9.8 nm \ln \left[0.2 \frac{5620}{931} \right] = 1.85 nm$$

4.3.2.2. Synthesis of a protein-resistant film on the silica gel-coated LSPR biosensor via ATRP

After successfully coating and stabilizing the LSPR biosensor with a layer of 3-D silica network, a protein-resistant film based on poly(ethylene glycol) is introduced to the sensor surface by ATRP. In the first step, ATRP initiators should be attached onto the silica gel. In the second step, the polymerization proceeded on the sensor surface.

4.3.2.2.1. Attachment of ATRP initiators on the silica gel-coated LSPR biosensor

Two parameters are important for a successful ATRP initiating system. First, initiation should be fast in comparison with propagation. Second, the probability of side reactions should be minimized. There are several general considerations for the initiator choice. (1) The stabilizing group order in the initiator is roughly $CN > C(O)R > C(O)OR > Ph > Cl > Me$. Tertiary alkyl halides are better initiators than secondary ones, which are better than primary alkyl halides. (2) The general order of bond strength in the alkyl halides is $R-Cl > R-Br > R-I$. Thus, alkyl iodides should be the most efficient initiators. However, the use of alkyl iodides requires special precautions, since they are light sensitive, can form metal iodide complexes, and the R-I bond may possibly be cleaved heterolytically. (3) Successful initiation in the ATRP can depend strongly on the choice of catalyst.^{12,59}

In the first attempt to fabricate a PEG layer on the silica gel-coated LSPR nanobiosensor, *2-bromo-2methyl-N-propyltrimethoxysilyl isobutyramide* was applied as the immobilized initiator in the ATRP (Fig. 4-31). As a tertiary alkyl bromide, *2-bromo-2methyl-N-propyltrimethoxysilyl isobutyramide* was expected to be an efficient initiator, and attachment to the silica gel surface should be possible due to the terminal silyl group.

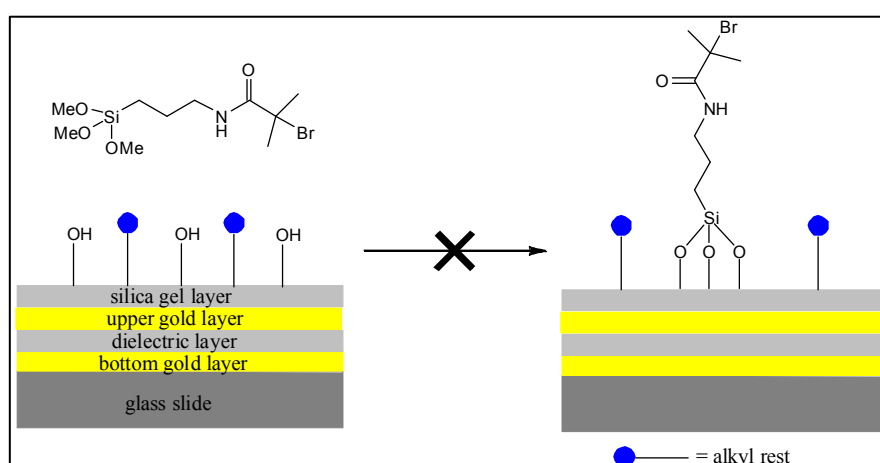


Figure 4-33. Direct attachment of ATRP initiator onto the sol-gel layer using 2-bromo-2methyl-N-propyltrimethoxysilyl isobutyramide

Although the same synthesis route has been successfully applied by Stadler *et al* to prepare a PEGMA coating on CMOS (complementary metal oxide semiconductor) microchips,⁶² it failed to generate a polymer film on the LSPR biosensor. The long, branched hydrocarbon

chain of the initiator molecule prohibits the attachment of the silyl groups onto the silica gel surface, resulting in a low coupling efficiency.

In the second attempt, the initiator coupling efficiency was optimized by immobilizing the initiator molecules in two steps. First, *aminopropyltriethoxysilane* (**initiator 1**) was coupled to the silica gel coated LSPR biosensor (Fig. 4-34a). In the second step, *bromoacetyl bromide* (**initiator 2**) was added to the surface (Fig. 4-34b).

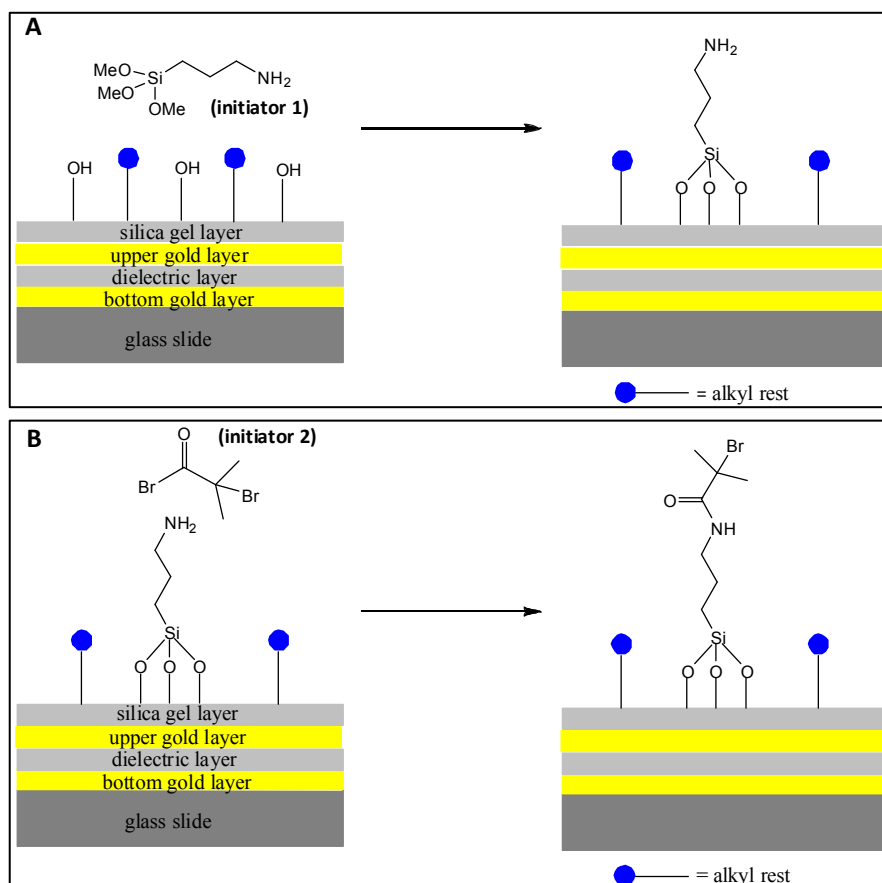


Figure 4-34. Two-steps immobilization of the ATRP initiators on the LSPR biosensor: (A) coupling of aminopropyltriethoxysilane (initiator 1) to the silica layer, (B) coupling of bromoacetyl bromide (initiator 2) to the terminal amino group of the immobilized silane.

Presence of nitrogen and bromine was detected in XPS, indicating a successful formation of a Br-terminated silane monolayer on the sensor surface (Fig. 4-35) due to the sterically less demanding *aminopropyltriethoxysilane*, which provides a higher accessibility to couple its silyl groups to the silica gel surface (Fig. 4-34a).

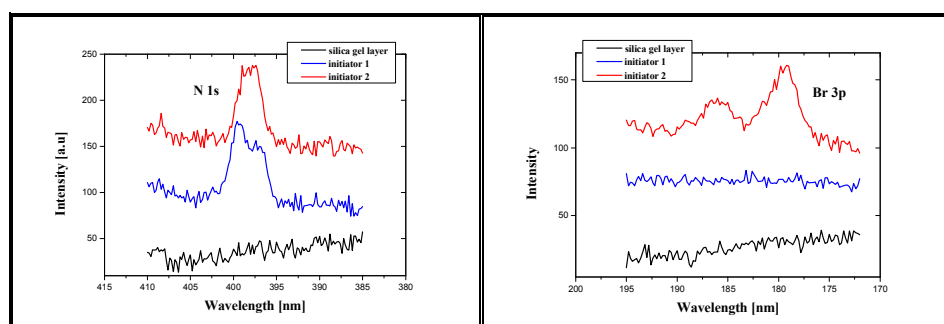


Figure 4-35. XP spectra of N 1s (left) and Br 3p (right) photoelectrons of the silica gel coated LSPR biosensor, functionalized by aminopropyltriethoxysilane (blue lines) and bromoacetyl bromide (red lines)

4.3.2.2.2. Surface initiated ATRP on the silica gel-coated LSPR biosensor

1. PEGMA graft polymer film

Polymerization of poly(ethylene glycol)methacrylate (PEGMA) on the initiator functionalized LSPR biosensor has been carried out successfully with help of Copper(I) bromide and 2,2'-bipyridine as the catalysts.

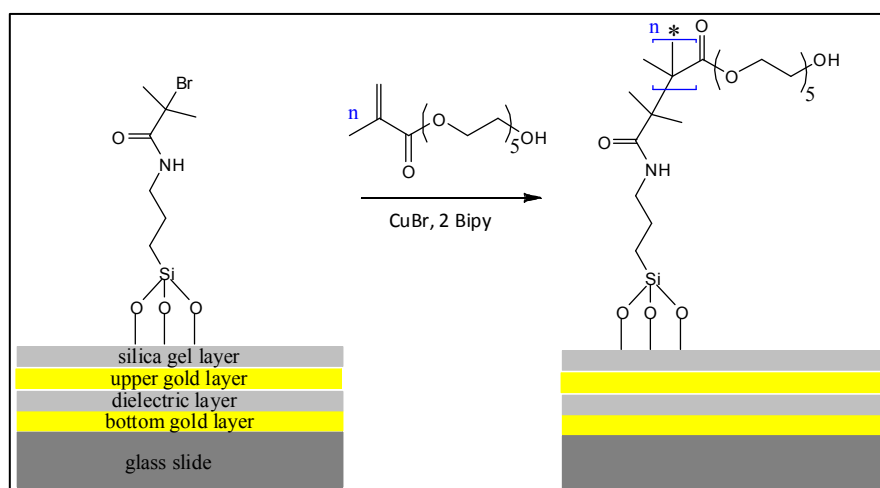


Figure 4-36. Atom Transfer Radical Polymerization of OEGMA monomers on a sol-gel coated LSPR biosensor

XP spectra revealed a successful formation of a PEGMA graft polymer film on the silica gel coated LSPR biosensor, as clearly indicated by the intensive C 1s and O 1s signals (Fig. 4-37). The SEM image displays a transparent polymer layer on the LSPR biosensor (Fig. 4-38).

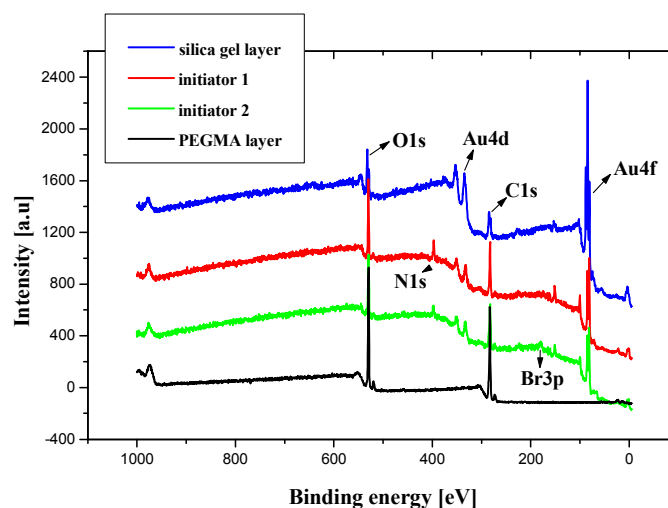


Figure 4-37. XP wide scan spectra of silica gel (black line), initiator 1 (red line), initiator 2 (green line), and PEGMA layer (blue line) on the LSPR biosensor.

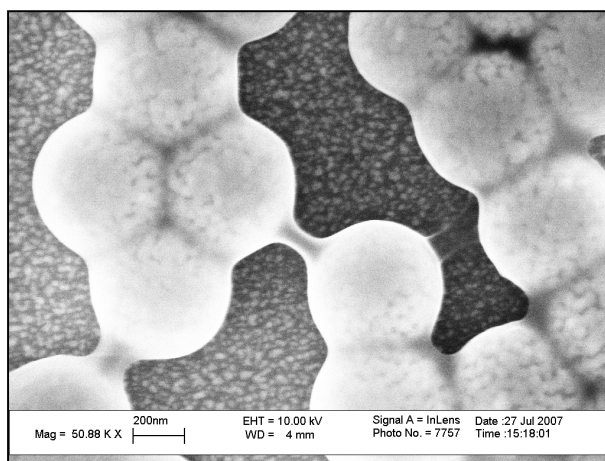


Figure 4-38. SEM image showing the LSPR biosensor coated with polymer layer.

Au 4f photoelectrons, which were still clearly visible after the attachment of the ATRP initiator, were completely shielded after the polymerization. Taking the inelastic mean free path for Au 4f photoelectrons in PEG layer of 3.4 nm into account,¹⁰⁶ the thickness of the PEGMA layer can be estimated to be at least 17 nm. Due to the roughness of the LSPR biosensor based on silica nanoparticles, the film thickness could not be measured by ellipsometry.

A high-resolution spectrum of C 1s photoemission peak of the PEGMA coated LSPR biosensor is shown in Fig. 4-39. The C 1s peak of the polymer film can be fitted with three unique carbon moieties: COOR (289.1 eV), COR (286.6 eV), and CH_x (285.2 eV). The ratio of the components C1 + C3 arising from the methyl methacrylate backbone to C2 arising from the pendant oligo(ethylene glycol) moiety is 3.98:10. This ratio is slightly higher than the theoretical value of 3:10 calculated from the stoichiometry of the polymer, assuming that an average value of n = 5 for PEGMA.

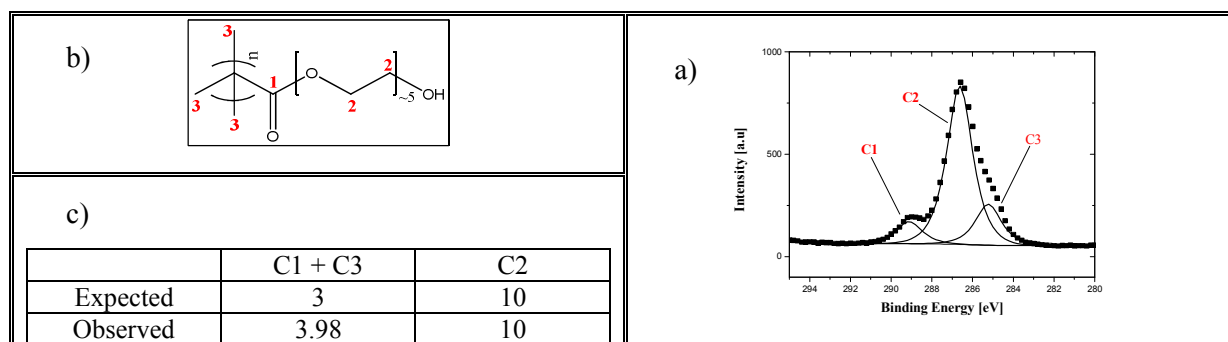


Figure 4-39. High-resolution spectra of the C 1s photoemission peak (a), peak assignment of the high-resolution C 1s spectrum used for quantification (b), and ratio of methyl methacrylate backbone C to pendant oligo(ethylene glycol) C atoms (c).

A high-resolution spectrum of the O 1s photoemission peak of the PEGMA coated LSPR biosensor is shown in Fig. 4-40. The O 1s peak of the polymer film can be fit with two oxygen moieties: COOR (533.6 eV) and COR (532.7 eV). The ratio of O 1s peak arising from the methyl methacrylate backbone to O 1s peak arising from the pendant oligo(ethylene glycol) moiety is 1.47:6. This ratio is also slightly higher than the theoretical value of 1:6 calculated from the stoichiometry of the polymer.

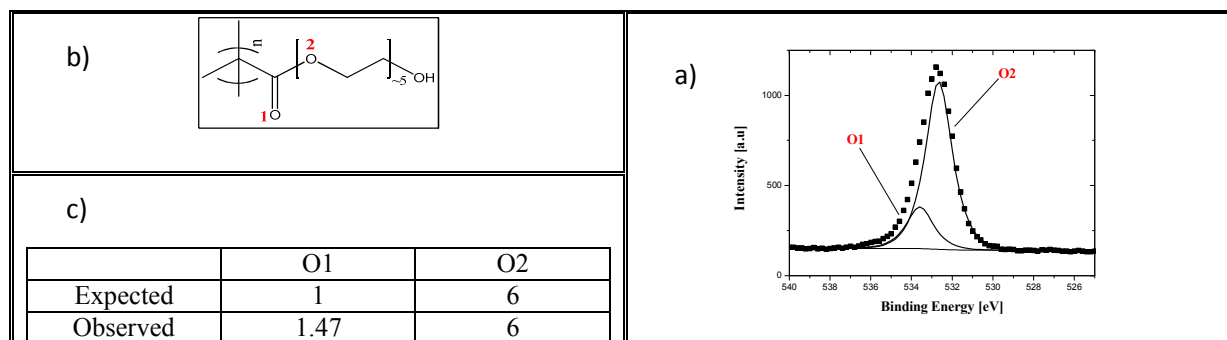


Figure 4-40. High-resolution spectra of the O 1s photoemission peak (a), peak assignment of the high-resolution O 1s spectrum used for quantification (b), and ratio of methyl methacrylate backbone O to pendant oligo(ethylene glycol) O atoms (c).

Thus, both experimentally determined ratios of C 1s and O 1s peaks suggest that the PEGMA monomer consists of a mixture of oligomers, and that in surface-initiated ATRP shorter OEGMA monomers are preferentially inserted into the growing polymer chain due to less steric hindrance. This trend was also observed by Ma et al.⁶¹

2. PEGMA/MMA graft copolymer film

Pure PEGMA graft polymer films possess a very high protein-resistance, which frequently shields the immobilized peptides from interaction with the corresponding antibodies. This can result in reduced detection efficiency due to an insufficient amount of coupled antibodies.

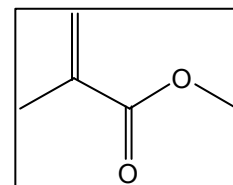


Figure 4-41. Methyl methacrylate (MMA)

Hence, a graft copolymer film of PEGMA and methyl methacrylate (MMA) was fabricated on the LSPR biosensor to attain a polymer coating with less protein resistance. MMA was chosen as the diluting monomer due to its moderate hydrophobicity, which should ensure a homogeneous monomer distribution in the copolymer. Moreover, PMMA itself is also widely used in the field of biomaterials, e.g., for microfluidic chips or laboratory-on-a-chip devices. Dilution of PEGMA by MMA might also improve the stability in vivo or in vitro compared to pure PEGMA-based coatings, which usually are prone to degrade enzymatically or by oxidation.⁶³

However, dilution of the OEGMA monomers by the use of MMA also decreases the number of functional groups, which are the starting points for peptide synthesis (Fig. 4-42). Thus, it decreases the number of peptides attached to the sensor surface.

Hence, a compromise between the amount of functional groups and the protein-repelling properties must be obtained by selecting a suitable PEGMA/MMA ratio.

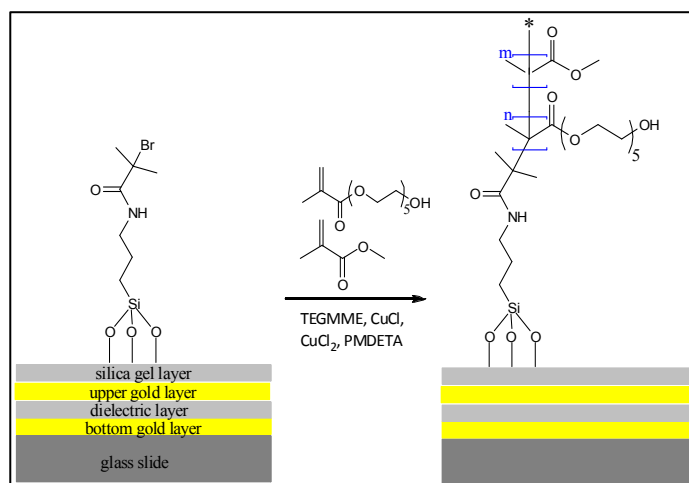


Figure 4-42. Atom Transfer Radical Polymerization of OEGMA/MMA monomers on a sol-gel coated LSPR biosensor

The polymerization was carried out in tri(ethylene glycol) monomethyl ether (TEGMME) using a $\text{CuCl} / \text{CuCl}_2 / \text{PMDETA}$ (N,N,N',N',N'' -pentamethyldiethylenetriamine) catalyst system, which was first reported by Kimani and Moratti.¹¹⁰

Two different ratios of OEGMA and MMA mole fractions were used in the polymerization solutions: 50/50 and 10/90.

The composition of the synthesized PEGMA/MMA graft copolymer film was determined by XPS from the ratio of the C 1s and O 1s signals arising from the methyl methacrylate backbone and from oligo(ethylene glycol) pendant. The ratio of $\underline{\text{C}}\text{-C}:\underline{\text{C}}\text{-O}$ should vary from 3:10 for a pure PEGMA- and 3:1 for a pure PMMA polymer film. The ratio of $\underline{\text{O}}=\text{C}:\underline{\text{O}}\text{-C}$ should vary between 1:6 for a pure PEGMA and 1:1 for a pure PMMA polymer film.

Table 4-16. Theoretical values for C 1s and O 1s signals arising from the methyl methacrylate backbone and from the oligo(ethylene glycol) pendant for pure PEGMA (left) and pure PMMA (right) films.

$\underline{\text{C}}\text{-C}:\underline{\text{C}}\text{-O}$	3:10	3:1
$\underline{\text{O}}=\text{C}:\underline{\text{O}}\text{-C}$	1:6	1:1

Copolymer films with 50 % PEGMA

Graft copolymer film synthesized from a monomer solution with 1:1 fraction of OEGMA/MMA resulted in a $\underline{\text{C}}\text{-C}:\underline{\text{C}}\text{-O}$ ratio of 3:7.1 and a $\underline{\text{O}}=\text{C}:\underline{\text{O}}\text{-C}$ ratio of 1:3.4 (Fig. 4-43).

The observed ratio of the C 1s peak arising from the methyl methacrylate backbone to the C 1s peak arising from the pendant oligo(ethylene glycol) moiety indicated a 68 % mole fraction of OEGMA monomer in the graft polymer film.

The observed ratio of the O 1s peak arising from the methyl methacrylate backbone to the C 1s peak arising from the pendant oligo(ethylene glycol) moiety was slightly higher than the expected value, which suggested that the shorter OEGMA monomers were preferentially inserted into the growing polymer chain.

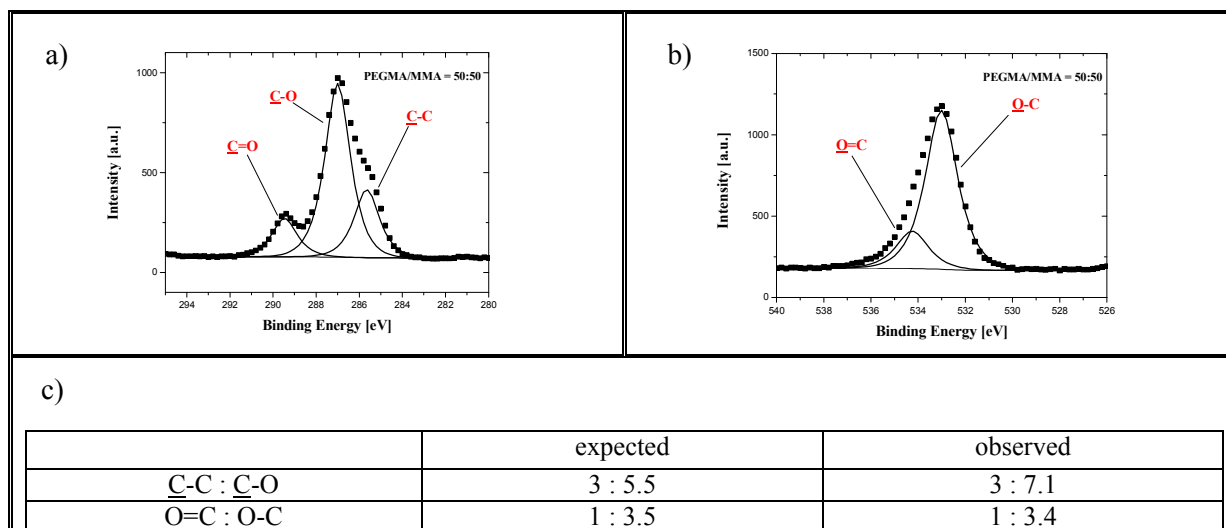


Figure 4-43. High-resolution spectra of C 1s (a) and O 1s (b) photoemission peaks from graft copolymer films with 50% PEGMA. Theoretical and experimental ratios for C 1s and O 1s signals arising from the methyl methacrylate backbone and from the oligo(ethylene glycol) pendant (c).

Copolymer films with 10 % PEGMA

Graft copolymer film synthesized from monomer solution with 1:9 fraction of OEGMA/MMA resulted in a $\underline{\text{C}}\text{-C}:\underline{\text{C}}\text{-O}$ ratio of 3:2.2 and a $\underline{\text{O}}\text{=C}:\underline{\text{O}}\text{-C}$ ratio of 1:1.3 (Fig. 4-44).

The observed ratio of the C 1s peak arising from the methyl methacrylate backbone to the C 1s peak arising from the pendant oligo(ethylene glycol) moiety indicated a 13 % mole fraction of OEGMA monomer in the graft polymer film.

The observed ratio of the O 1s peak arising from the methyl methacrylate backbone to the C 1s peak arising from the pendant oligo(ethylene glycol) moiety was slightly higher than the expected value, which suggested that the shorter OEGMA monomers were preferentially inserted into the growing polymer chain.

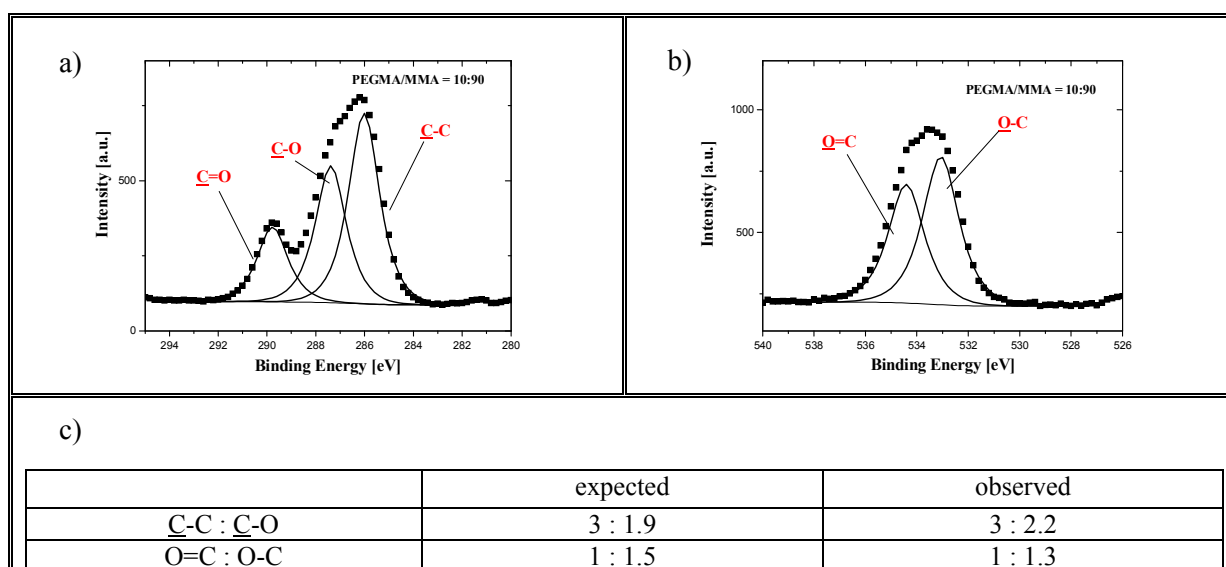


Figure 4-44. High-resolution spectra of C 1s (a) and O 1s (b) photoemission peaks from graft copolymer films with 10% PEGMA. Theoretical and experimental ratios for C 1s and O 1s signals arising from the methyl methacrylate backbone and from the oligo(ethylene glycol) pendant (c).

PEGMA/MMA (10:90) graft copolymer films with varying polymer film thickness were synthesized by varying the overall reaction time from 5 to 22 hours. The observed relationship between polymerization time and the resulting film thickness is depicted in Figure 4-45 (right). The data show that a polymer film with a thickness of ca. 80 nm is achieved for polymerization times longer than 15 hours. Increasing the reaction time from 15 to 22 hours does not significantly increase the thickness of the resulting polymer film. This observation is similar to that by Stadler et al. for graft polymer films with 100 % PEGMA (Fig 4-45, left),⁶² where reaction times of larger than 15 hours were reported to yield polymer films with a thickness of ca. 90 nm.

Important for the current work is that a copolymer film thickness of 50-60 nm can be achieved by setting the polymerization time between 9.5 and 10.5 hours. This thickness regime assures a high loading of functional groups. At the same time it does not exceed the surface sensitivity limit of the LSPR biosensor, which is restricted by the decay length of the evanescent electric field (~ 100 nm).¹¹¹

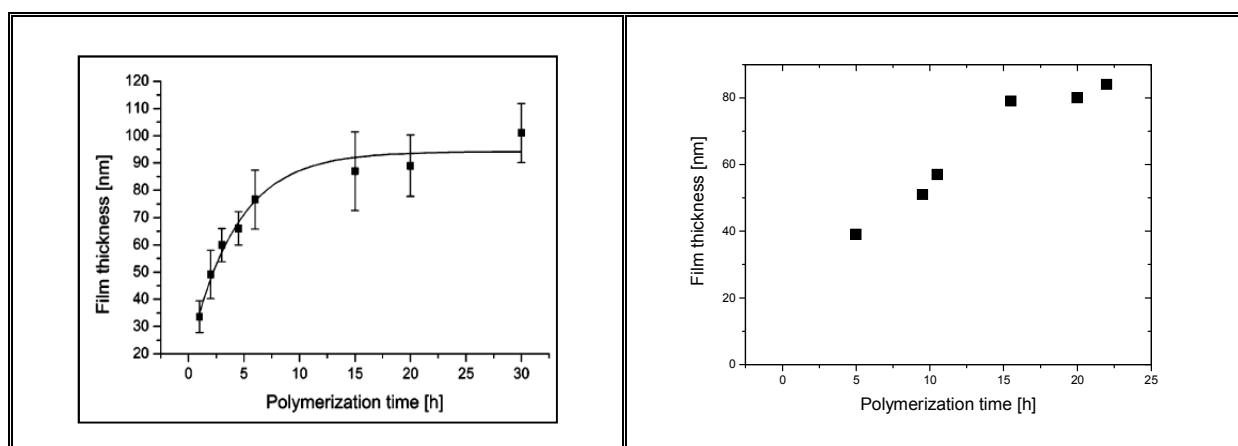


Figure 4-45. Film thickness versus polymerization time for pure PEGMA polymer films as determined by Stadler et al. (left). Film thickness versus polymerization time for PEGMA/MMA (10:90) copolymer film, which was experimentally determined in this work, shows the same trend (right).

4.3.2.2.3. LSPR response of graft copolymer films with different thicknesses

Graft copolymer films of different thickness were synthesized by varying the polymerization time (cf. Fig. 4-45, right). The shifts of the quadrupole LSPR peak, which were generated by the adsorption of the copolymer film on the LSPR sensor surface, were recorded and compiled in Figure 4-46, left. The LSPR responses to the different layer thickness of copolymer films with 10 % PEGMA show a linear behaviour with a slope of 1.34.

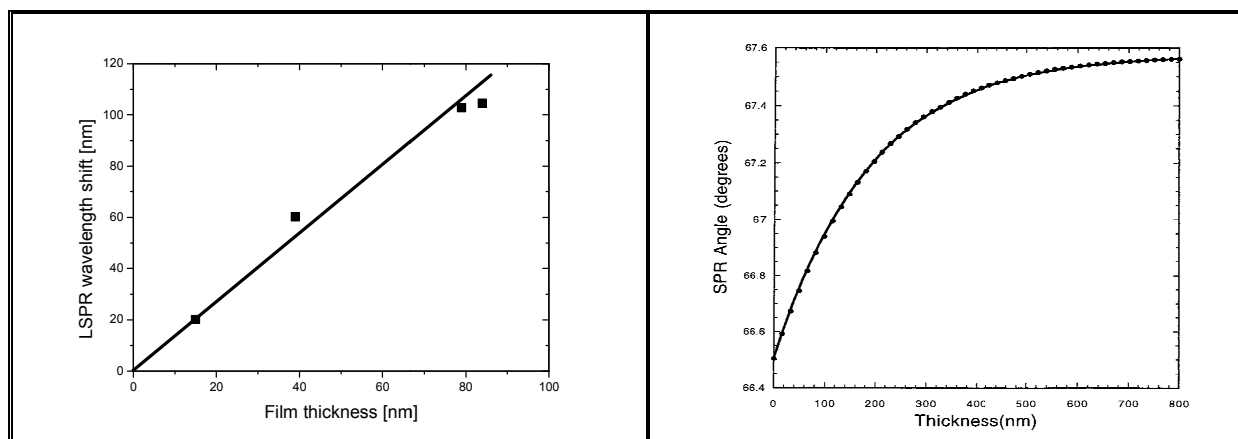


Figure 4-46. LSPR responses to different layer thickness of PEGMA/MMA 10:90 graft polymer films (left). Calculated SPR responses versus layer thickness based on Maxwell's equations (right).¹⁰

These experimental findings are in line with the calculated SPR response on Maxwell's equations (Fig. 4-46, right) for adsorbed films with a bilayer structure and particular values of m , n_a , n_s , and d (Fig. 4-53).¹⁰

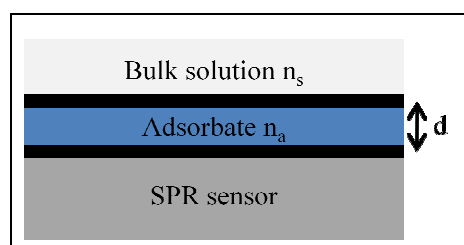


Figure 4-47. Schematic diagram of a bilayer structure involving an adsorbate a of thickness d and refractive index n_a directly on the SPR sensor surface. A solution s of refractive index n_s lies above the adsorbate film.¹⁰

In both cases, a linear relationship between the sensor response and the film thickness is observed in the thickness regime below 100 nm.

4.3.2.2.4. Functionalization of the protein-resistant coating on the LSPR biosensor

To enable the integration of amino acids onto the polymer-coated LSPR biosensor via peptide bonding, PEGMA side chains were functionalized by amino groups. Amino functional groups were introduced by esterification using Fmoc- β -Alanine, whose carboxyl groups were activated in situ by N,N' -diisopropyl carbodiimide (DIC) and N -methylimidazole (NMI) (Fig. 4-48). Subsequently, the N -terminal Fmoc groups were removed by 20 % piperidine in N,N -dimethylformamide. To provide a better accessibility for the growing peptide chains, three β -alanine residues were consecutively coupled to the graft polymer film to generate a NH_2 -(β -alanine)₃ sequence.

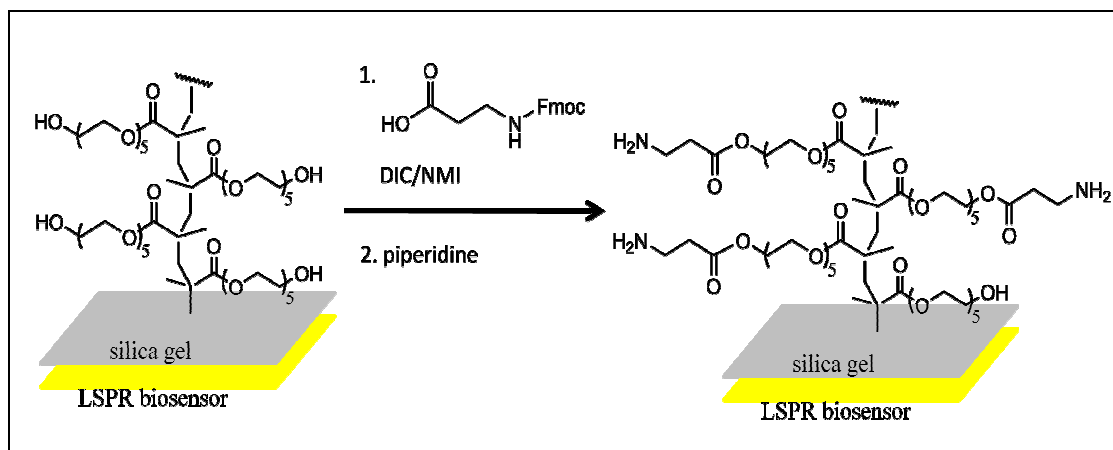


Figure 4-48. Functionalization of PEGMA side chain by Fmoc-β-alanine

The density of the integrated amino groups was determined by measuring the concentration of the dibenzofulvene-piperidine adduct of the piperidine-mediated Fmoc deprotection at 301 nm by UV-Vis spectroscopy. It varied with the grafting composition: a pure PEGMA polymer film yielded a density of 10 nmol/cm² while a copolymer film with 10 % PEGMA achieved a density of 1.3 nmol/cm².

However, a graft copolymer film with 50 % PEGMA only resulted in a surface functional density of 0.4 nmol/cm², which was probably caused by ineffective coupling of β-Alanine.

Table 4-17. Densities of the amino terminal groups on polymer-coated LSPR biosensor with different grafting composition

Monomer	pure PEGMA	PEGMA/MMA (50:50)	PEGMA/MMA (10:90)
[Amino group]	10 nmol/cm ²	0.4 nmol/cm ²	1.3 nmol/cm ²

4.3.3. Stability of the protein-resistant polymer -coated LSPR biosensor in the peptide printing procedure

One of the requirements in implementing the graft polymer-coated LSPR biosensor as a solid support in the peptide array synthesis is its stability against harshest conditions emerging in the generation of the arrays. These are represented by treatments with different organic solvents, buffers, and the final TFA (trifluoroacetic acid)-mediated side-group deprotection. In this work, the stability of the PEGMA film-coated LSPR nanobiosensor was investigated with respect to the three following chemical treatments.

4.3.3.1. Blocking of residual hydroxyl groups of the polymer film

In the capping step, samples were treated with a solution of acetic anhydride/*N,N*-diisopropylethylamine/*N,N*-dimethylformamide overnight to block residual hydroxyl groups.

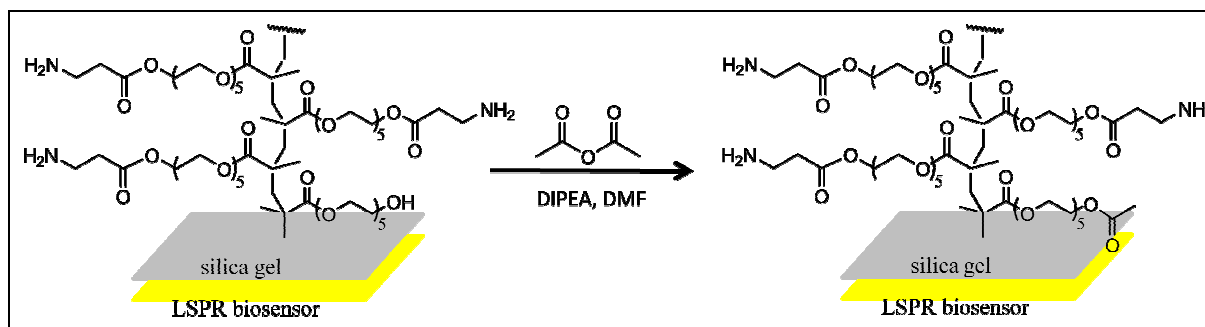


Figure 4-49. Blocking of residual hydroxyl groups on PEGMA

Images taken by SEM revealed the condition of the polymer-coated LSPR biosensor before and after the capping reaction (Fig. 4-50). A visible decrease in film thickness was not noticed.

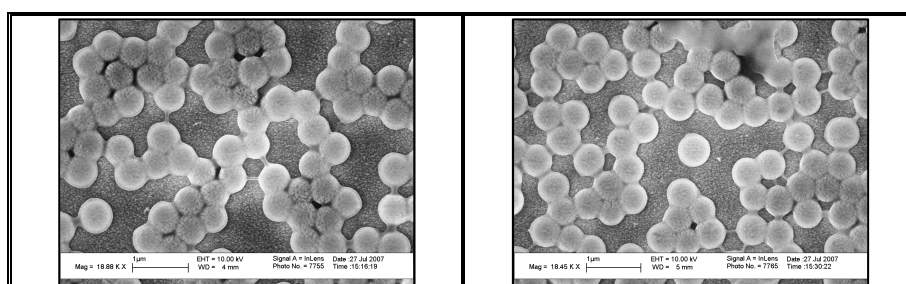


Figure 4-50. SEM image of the polymer-coated LSPR biosensor before (left) and after (right) the capping reaction

4.3.3.2. Removal of Fmoc protection groups by piperidine

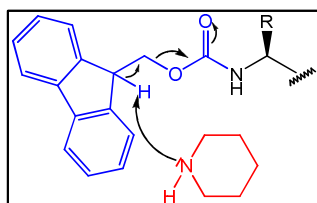


Figure 4-51. Removal of Fmoc groups (blue) by piperidine (rot)

In the combinatorial peptide array synthesis via laser printing, the 20 different amino acids are embedded in solid toner particles. The N-terminal groups on the amino acids are Fmoc protected, which is base-labile. In every synthesis cycle, Fmoc groups were removed by incubation in a solution of 20 v% piperidine in DMF for 20 minutes before the next amino acid layer was printed. SEM images display no visible change in film thickness after treatment with piperidine solution (Fig. 4-52).

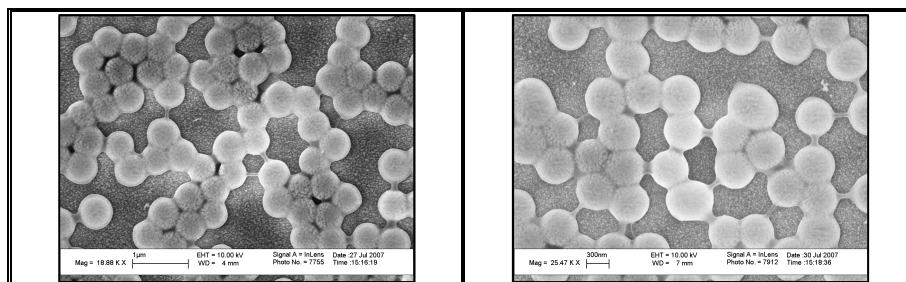


Figure 4-52. SEM images of the polymer-coated LSPR biosensor before (left) and after (right) removal of Fmoc groups

4.3.3.3. Removal of side-chain protecting groups by trifluoroacetic acid

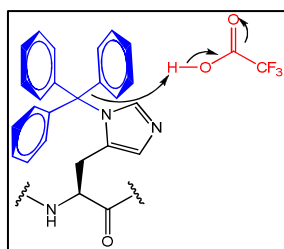


Figure 4-53. Removal of side-chain protection groups by TFA.

Side-chain amino groups in the Fmoc-amino acids are protected by acid-labile groups such as tert-Butyloxycarbonyl, tert-Butyl, or Trityl. Removal of the side-chain protecting groups occurs at the end of the peptide synthesis by incubation in 51 v% TFA, 44 v% methylene chloride, 3 v% TIBS and 2 v% water three times for 30 minutes. SEM images display no visible change in film thickness after treatment with TFA solution (Fig. 4-54).

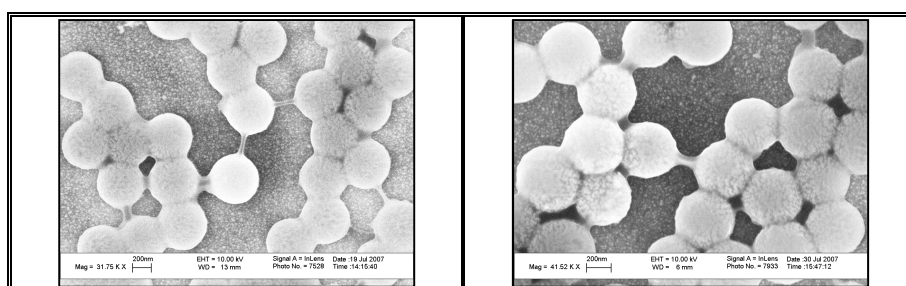


Figure 4-54. SEM images of the polymer-coated LSPR biosensors before (left) and after (right) removal of side-chain protecting groups

4.3.3.4. Treatment of graft polymer-coated LSPR biosensor with acetic acid, piperidine, and trifluoroacetic acid

In the last stability test, the polymer-coated LSPR biosensor was successively treated with the capping solution, 20 % piperidine, and 51 % trifluoroacetic acid. The SEM images showed a slight decrease in film thickness of the PEGMA coating after treatment with all three reagents.

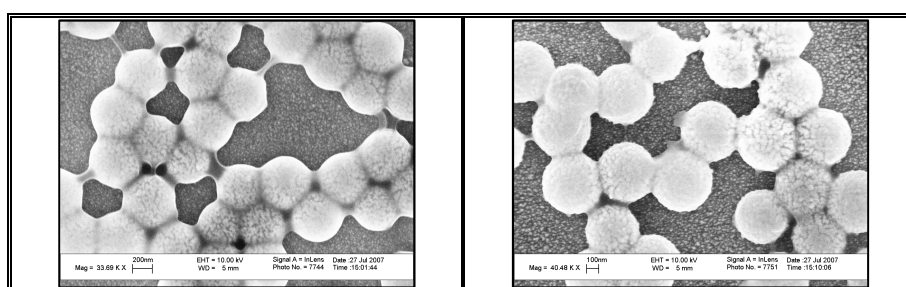


Figure 4-55. SEM images of the polymer-coated LSPR biosensor before (left) and after (right) treatment with capping solution, 20 % piperidine, and 51 % trifluoroacetic acid

XP spectra of the sample were taken prior to and after treatment with the blocking reagent and removal of the protection groups by piperidine and TFA (Fig. 4-56). O 1s and C 1s signals before and after treatment display only a slight change in the O 1s and C 1s peaks, indicating almost no alteration in the composition of the polymer coating.

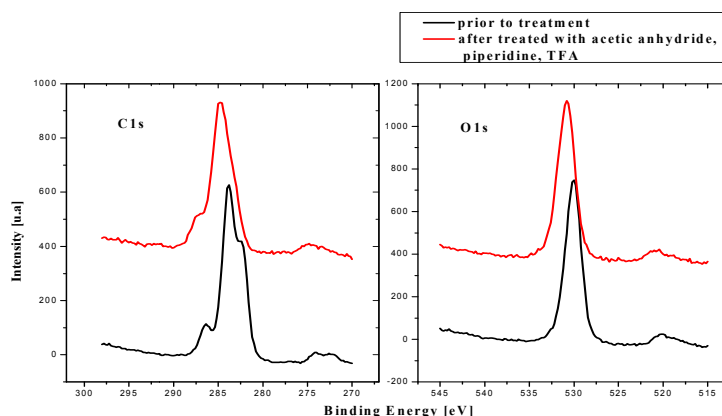


Figure 4-56. High-resolution spectra of O 1s and C 1s photoelectrons of the LSPR biosensor, coated with an amino-functionalized PEGMA layer (black line) and after treatment with acetic anhydride, piperidine, trifluoroacetic acid (red line)

4.3.4. Conclusion

A protein-repelling layer has been successfully synthesized on the LSPR biosensor via atom transfer radical polymerization (ATRP) (Fig. 4-57). First, a silica gel coating was fabricated to stabilize the sensor and to provide a high loading of hydroxyl functional groups. ATRP initiators were then coupled to the silica gel surface in two steps by silanization and esterification to enhance the coupling efficiency. Subsequently, polymerization was carried out at ambient temperature with OEGMA as the monomer and Cu(I) complex as the catalyst, resulting in a PEGMA polymer film.

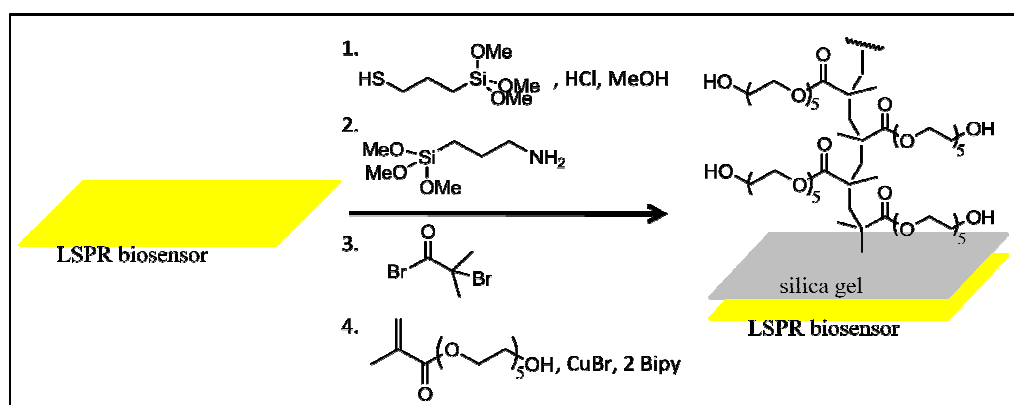


Figure 4-57. Synthesis route for a PEGMA coating on the LSPR biosensor via ATRP: (1) sol-gel coating, (2) attachment of the first ATRP initiator, (3) attachment of the second ATRP initiator, (4) polymerization of PEGMA monomer.

However, pure PEGMA graft polymer films possess a very high protein-resistance, which frequently shields the immobilized peptides from interaction with the corresponding antibodies. This can result in reduced detection efficiency due to an insufficient amount of coupled antibodies.

Hence, in the second approach a graft copolymer film was synthesized on the sensor surface with MMA as the diluting monomer to reduce the protein-resistance of the polymer film. Figure 4-58 displays the scheme of PEGMA/MMA graft copolymer synthesis on the LSPR biosensor. The first to the third step are analogous to the synthesis route of a pure PEGMA coating. The “grafting from” copolymerization was carried out in TEGMME with a CuCl/CuCl₂/PMDETA catalyst system.

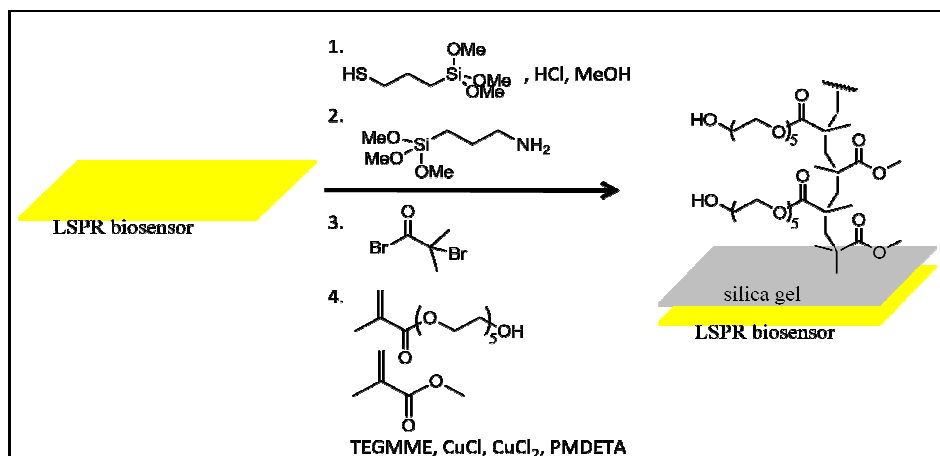


Figure 4-58. Synthesis route for a PEGMA/MMA coating on the LSPR biosensor via ATRP: (1) sol-gel coating, (2) attachment of the first ATRP initiator, (3) attachment of the second ATRP initiator, (4) polymerization of PEGMA and MMA monomers.

Graft copolymer films with 10 % PEGMA and a thickness of 50-60 nm were successfully synthesized by setting the polymerization time between 9.5 and 10.5 hours. This thickness regime was required to ensure a high-loading of amino functional groups, which were the starting point for the peptide array synthesis. At the same time it does not exceed the surface sensitivity limit of the LSPR biosensor.

The LSPR wavelength shifts due to the adsorption of the copolymer films with 10 % PEGMA of different thickness were experimentally determined. As expected, a linear relationship between LSPR response and film thickness was observed for the thickness regime below 100 nm.

The stability of the polymer-coated LSPR biosensor was tested in various chemical reactions, which are inevitable in the synthesis of peptide array via laser printing technology. XPS and SEM analysis showed that the protein resistant layer on the LSPR biosensor was stable under these harsh chemical conditions. This is one of the requirements for the application of the LSPR biosensor as a solid support in peptide array synthesis.

4.4. Label-free detection of antigen-antibody interactions occurring on a LSPR biosensor coated with a protein-resistant layer

In order to interrogate antibody-antigen interactions occurring on the peptide chips, a label-free detection method based on localized surface plasmon resonance (LSPR) was used. Label-free detection offers the advantages of reducing the time and cost demands because they avoid all steps associated with applying and processing the label. Moreover, in contrast to label-based methods they facilitate the detection of low-affinity binding events.

Local refractive index changes such as those induced by biomolecular interactions at the sensor surface can be monitored via the LSPR peak shift, which is proportional to the change in mass on the surface. Thus, LSPR biosensors are valuable tools for both *in situ* detection of binding kinetics and the quantification of the surface-bound molecules.

A qualitative comparison between label-based and label-free analysis was made in an antibody assay with respect to the performances of both techniques in detecting biomolecules. Two techniques were used to fabricate arrays on the LSPR biosensor: spotting of fluorescent-labeled antibodies and particle-based peptide synthesis (cf. chapter 2.1.3).

In a proof-of-principle experiment, an array of fluorescent-labeled antibodies was formed on the sensor surface by a spotting robot and subsequently detected by means of a fluorescent scanner and the LSPR imaging technique.

In the final part of this thesis, the polymer-coated LSPR biosensor was used as the solid substrate in the synthesis of a peptide array via particle-based synthesis, and then used as a tool for detecting biomolecular interactions occurring on the peptide array (Fig. 4-59).

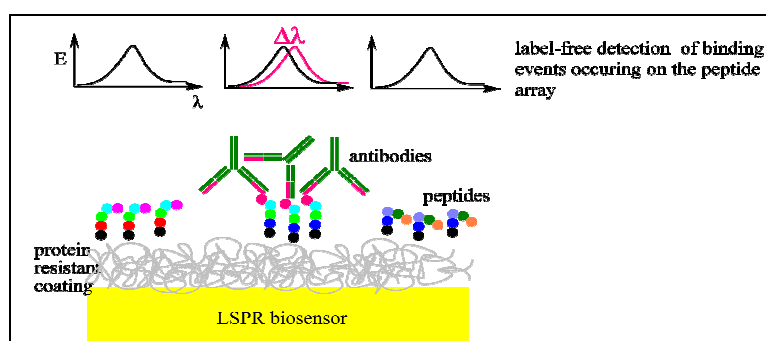


Figure 4-59. The LSPR biosensor served as a solid substrate in the synthesis of a peptide array and as a detection tool in the antibody assaying process.

4.4.1. LSPR biosensor as label-free detection tool

Detection limit

The detection limit of the biosensing system must be determined before applying the LSPR biosensor in the analysis of antibody-antigen interactions. The detection limit was estimated based on the mass sensitivity study of Buecker et al. for optically responsive nanoparticle layers.¹¹¹

Buecker et al. measured the adsorption induced wavelength shift and related these values to the mass density of the deposited films as determined by XPS or ELISA (Enzyme-linked

Immunosorbent Assay). A linear relationship is found yielding a sensitivity factor of 0.027 nm/(ng/cm²) for the quadrupole resonance peak.

The sensitivity of 0.027 nm/(ng/cm²) for molecular adsorption translates into a detection limit of **37 ng/cm²**, assuming that a spectral shift of 1 nm can still be detected.

Principle of LSPR image generation

The samples were scanned with a specific lateral resolution and the UV-Vis extinction spectra of each measured position (pixel) were recorded. The exact description of the optical set-up can be found in chapter 3.4.

The scan data is recorded in four dimensions: two dimensions corresponding to the lateral (x, y) coordinates of the measured pixel, the wavelength of the incident light, and the corresponding extinction. This spectrum is then translated into a 3-dimensional LSPR-image by displaying the (x,y) coordinates and the extinction maximum position of a selected wavelength regime in a color code (Fig. 4-60).⁸³

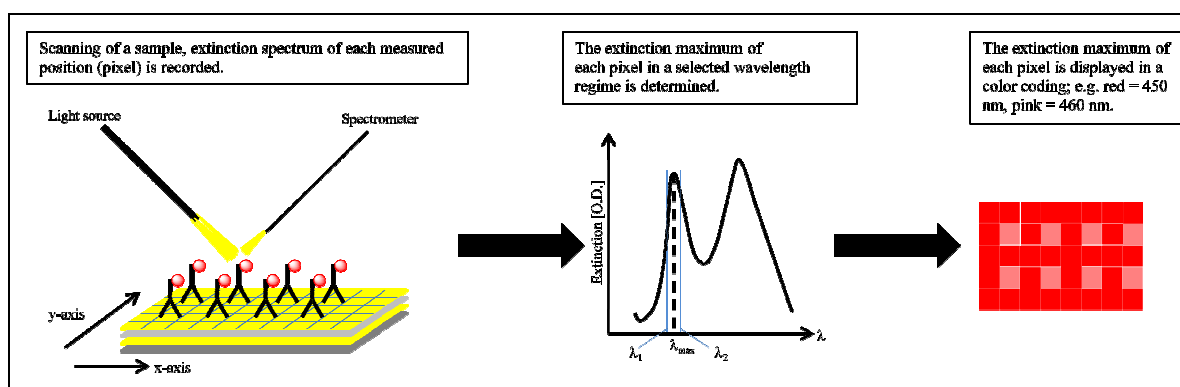


Figure 4-60. Principle of LSPR images generation

4.4.2. Fabrication of an antibody array on a LSPR biosensor by spotting technique

In a proof-of-principal experiment, AlexaFluor 647-labeled mouse anti-HA was coupled to a LSPR biosensor. The sensor geometry consisted of a 100 nm gold film as the bottom gold layer, a 250 nm polycrystalline silica film as the intermediate dielectric layer, and gold colloids deposited by seeding/plating as the upper gold layer.

An array of 25x25 spots with a distance of 600 μm was formed by spotting small droplets containing 2 nl of the fluorescent-labeled antibody (0.08 ml/ml). Implying that each droplet covered a surface area with a diameter of ~280 μm, an antibody density of 290 ng/cm² is calculated. The spotted structure was clearly resolved by the use of a fluorescence scanner (Fig. 4-61).

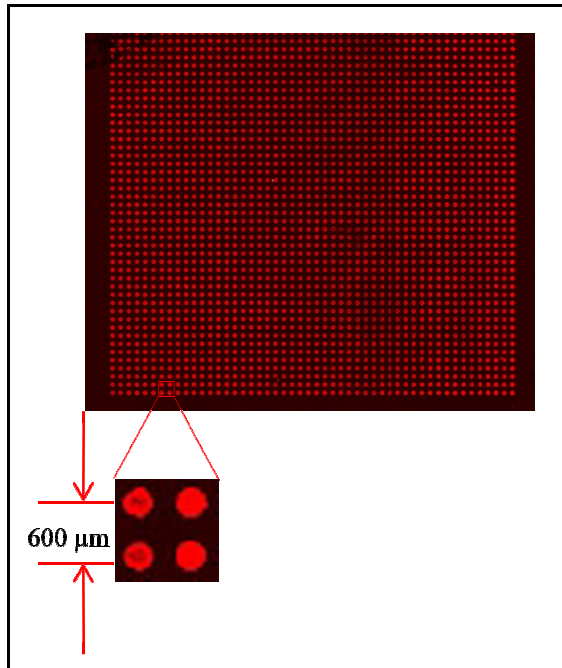


Figure 4-61. Fluorescence image of a AlexaFluor 647-labeled mouse anti-HA antibody array on a LSPR biosensor. The center-to-center distance corresponds to 600 μm.

4.4.1.1. Qualitative analysis by LSPR imaging

The sample was then scanned with a spatial resolution of 110 μm and a total scan area of 77.44 mm². The UV-Vis spectra of all measured positions were recorded. An LSPR image of the sample was generated for a selected wavelength regime around the quadrupole resonance peak (Fig. 4-62 a).

A pattern of squares with a regular distance of 600 μm is visible in a lighter shade than the surrounding background. This grid of lighter colors represents the antibody spots. Note, that the round spots are transferred into a rectangular image due to the relatively low resolution of the scan.

Figure 4-62 b and c display the extinction spectra of one antibody spot and the corresponding background from the left-bottom part of the sample. The wavelength difference between the extinction maxima positions of the quadrupole peaks measured for the antibody spot and for the background amounts to 8 nm.

Also of notice in the LSPR image is a gradual and regular shift of the background encoding. The left-bottom part displays a red-orange color which gradually shifts to orange-yellow at the right-top part of the image. This arises from the inhomogeneity of the extinction maxima, and is primarily caused by the thickness variation of the polycrystalline silica film serving as the dielectric layer in the LSPR biosensor.⁹ Further discussion on the dependence of the optical homogeneity on the intermediate dielectric layer can be found in chapter 4.3.4.2.

In Figure 4-63, a LSPR image of the same antibody array in the wavelength regime around the dipole resonance peak is shown. The array pattern was less explicitly resolved due to a higher background irregularity, since the dipole peak is more sensitive to inhomogeneities of the intermediate dielectric layer. The wavelength difference between the extinction maxima positions of the quadrupole peaks measured for the antibody spot and for the background amounts to 9 nm.

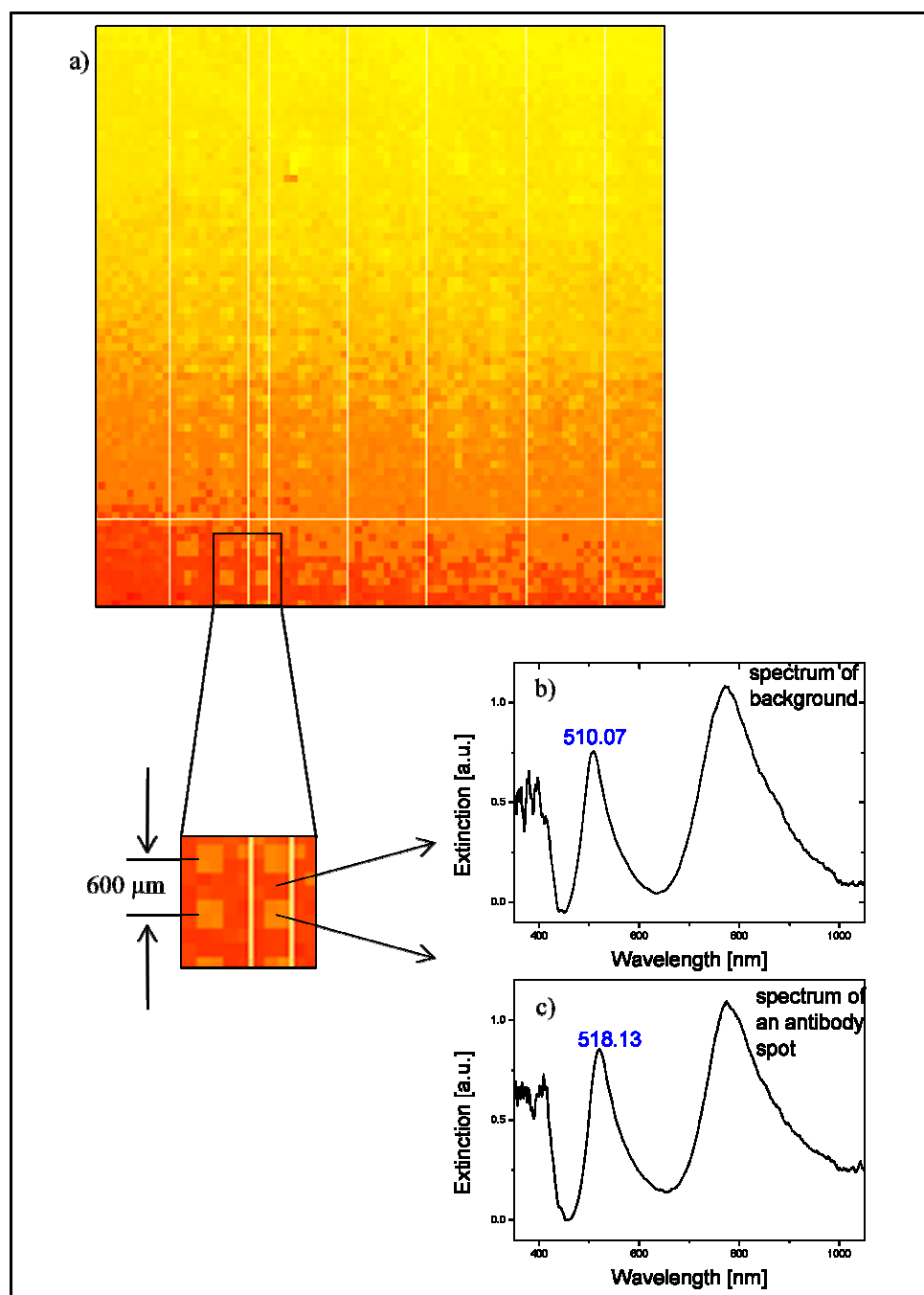


Figure 4-62. a) LSPR imaging of an antibody-array in the wavelength regime around the quadrupole resonance peak. The wavelength shift of the extinction maxima due to antibody coupling amounts to ~ 8 nm, as determined from the extinction spectra of the background (b) and the antibody spots (c).

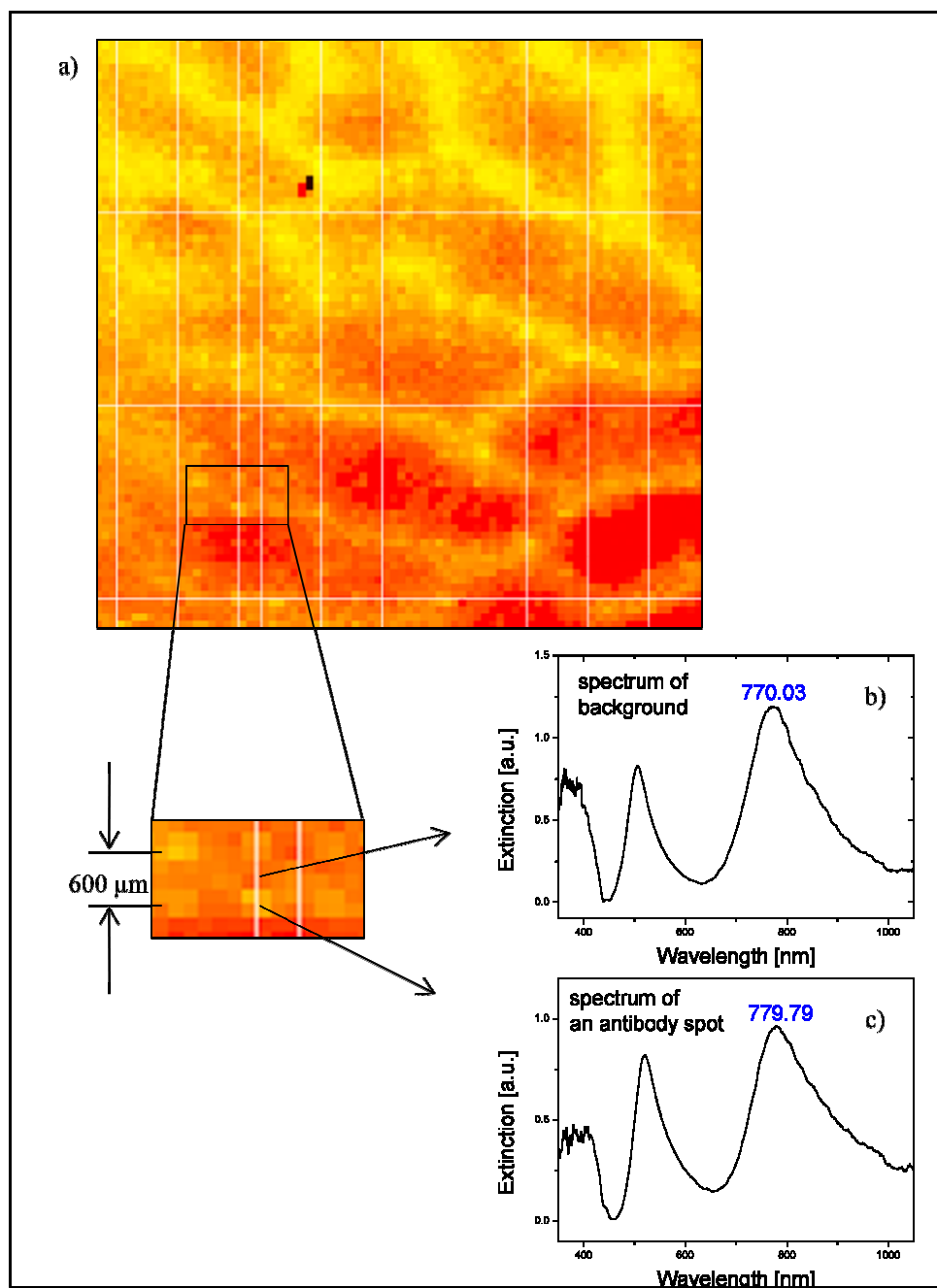


Figure 4-63. LSPR imaging of an antibody array in the wavelength regime around the dipole resonance peak. The wavelength shift of the extinction maxima due to antibody coupling amounts to ~ 9 nm, as determined from the extinction spectra of the background (b) and the antibody spots (c).

4.4.1.2. Quantitative analysis by LSPR resonance shift

The amount of antibody bound to the biosensor can be estimated by considering the measured wavelength shifts in the LSPR quadrupole resonance and the mass sensitivity factor. Using the measured wavelength shifts of 8 nm in the quadrupole regime and a mass sensitivity factor of $0.027 \text{ nm}/(\text{ng}/\text{cm}^2)$ determined by Buecker et al.¹¹¹, the amount of surface-bound antibody can be estimated to $296 \text{ ng}/\text{cm}^2$. This value is close to the calculated mass density of $290 \text{ ng}/\text{cm}^2$ generated by the spotting application. This result shows that the LSPR biosensor described in this thesis has the potential to facilitate the detection of molecular interactions in a miniaturized array format, as well as the quantification of surface-bound molecules.

LSPR based biosensors with similar geometry were constructed by Endo et al. and were used for detecting biomolecular interactions, such as antibody-antigen coupling (Fig. 4-64a (A)). The sensor geometry consisted of a silica nanoparticle monolayer (with a diameter of 100 nm) sandwiched between the top and the bottom gold layers (both with a thickness of 30 nm) that were deposited using thermal evaporation (Fig. 4-64a (D)). Antibody-antigen interactions were detected by comparing the peak intensity before and after the reaction. The change in absorbance strength was directly related to the applied antigen concentration.¹¹²⁻¹¹⁷

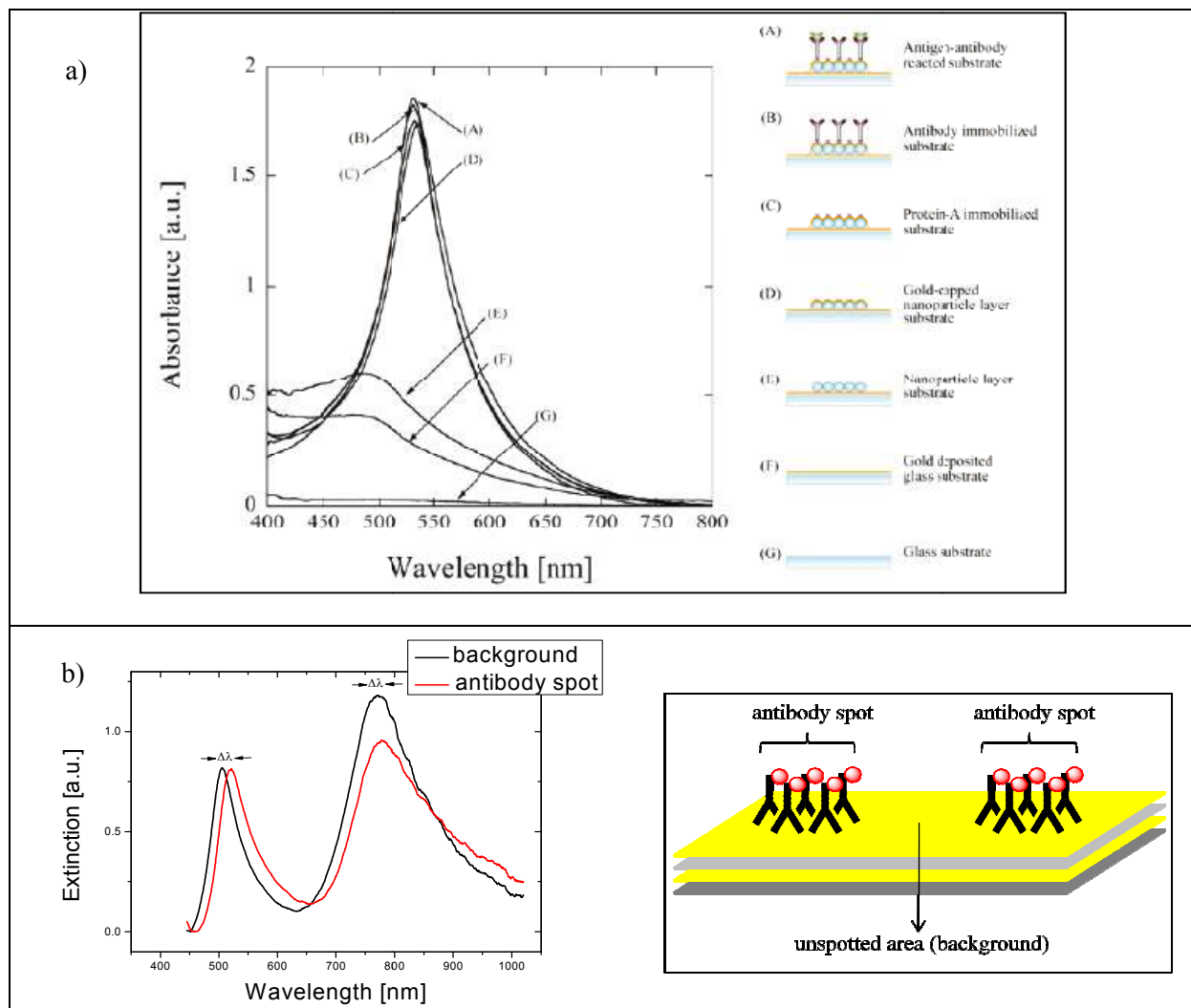


Figure 4-64. (a) Optical spectra of the LSPR-based biosensor constructed by Endo et al. Antigen-antibody coupling was detected by observing the change in peak intensity before (B) and after the reaction (A).¹¹² (b) Optical spectra of our LSPR-based biosensor. Binding events were detected by observing the wavelength shift in the LSPR peaks of the antibody spots and the unspotted area (background).

On the contrary, binding events occurring on our LSPR biosensor surface were detected by monitoring the wavelength shift ($\Delta\lambda$) in the LSPR peaks position (Fig. 4-64b). The shift ($\Delta\lambda$) in the LSPR resonance peak caused by molecular adsorption can be deduced by the following theoretical consideration. The extinction (E) of a metallic nanoparticle is given by

$$E(\lambda) \propto \left[\frac{\varepsilon_m''}{(\varepsilon_m' + \chi\varepsilon_d)^2 + \varepsilon_m''^2} \right] \text{ (Eq. 4-1)}$$

where ε_m' and ε_m'' are the real and imaginary components of the metal dielectric function, and ε_d is the dielectric constant of the dielectric medium, λ is the excitation wavelength, and χ is a form factor describing the nanoparticle's aspect ratio. For a spherical nanoparticle with $|\varepsilon_m'| \gg \varepsilon_m''$, equation 4-1 has a maximum when $\varepsilon_m' \approx -2\varepsilon_d$. This is observed as the LSPR peak in the extinction spectra.

A growth in magnitude of the dielectric constant of the surrounding medium (e.g. by molecular adsorption) would increase the polarization charges on the dielectric side of the interface, which is responsible for the weakening of the total restoring force. Hence, the position of the LSPR peak maximum will shift to the higher wavelength.¹¹⁸

Compared to the LSPR sensors constructed by Endo et al. our sensors work in a more straightforward manner. The surface of the LSPR sensor described in this work is scanned and the extinction spectra were recorded after the antibody assaying process only. Molecular adsorption is detected by a comparison of the LSPR peak maxima of the antibody spots and blank area (background). This renders the recording and comparison of the extinction spectra before and after the binding event unnecessary, and therefore removes a source of inaccuracy and error in detecting molecular adsorption provided that the background is optically homogeneous.

Another advantage of our LSPR biosensor is the number of resonance peaks generated by the sensor geometry. Two distinct peaks -dipole and quadrupole resonances- were detected in the UV-Vis region, which both can be used for the read-out of binding events.

4.4.2. Fabrication of a peptide array on a LSPR biosensor by particle-based technique for peptide synthesis

4.4.2.1. Generation of a peptide array on a LSPR biosensor by partial particle-based synthesis

A peptide array with 3x20 permutations of the hemagglutinin/HA (YPYDVPDYA) epitope was synthesized on a polymer-coated LSPR biosensor *partially* by the particle-based technique.

The sensor geometry consisted of a 100 nm gold film as the bottom gold layer, a 250 nm polycrystalline silica film as the intermediate dielectric layer, and gold colloids deposited by seeding/plating as the upper gold layer. The LSPR biosensor was coated with a copolymer film composed of 50 % PEGMA and 50 % MMA.

Variants of the above HA epitope were generated by means of the peptide printer. For this purpose, the *second (Y)*, *third (D)*, and *sixth (D)* amino acid in the original sequence of the HA epitope were permuted using all 20 different proteinogenic amino acids. These three positions in the HA epitope were chosen to be permuted due to their function as the *key positions* in the interaction of HA with its corresponding antibody. The remaining positions of the sequence were not varied and inserted into the peptide sequence by liquid-phase synthesis.

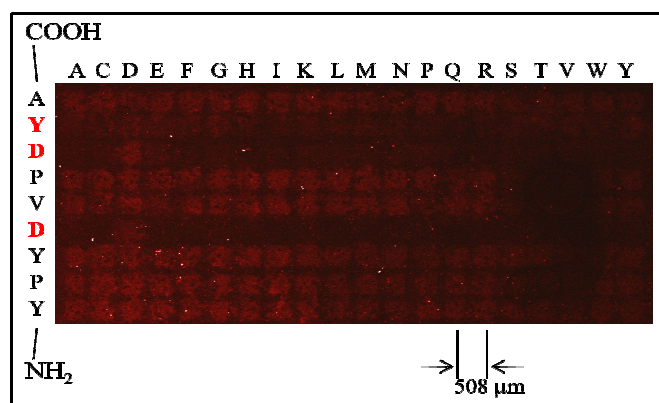


Figure 4-65. Fluorescence image of a peptide array with 60 permuted HA epitopes, which was incubated with specific antibody (rabbit anti-HA) and secondary antibody (Alexa Fluor 647-conjugated goat anti-rabbit). In the 2nd, 3rd, and 6th rows, the 2nd, 3rd, and 6th amino acid of the sequence was permuted, respectively. The center-to-center distance of the spots corresponds to 508 μm .

After incubating the array with a specific antibody (rabbit anti-HA) and a secondary antibody (Alexa Fluor 647-conjugated goat anti-rabbit), the structure of the array is clearly displayed in the image taken by a fluorescence scanner (Fig. 4-65). All of the permuted peptide epitopes showed the expected staining pattern.¹¹⁹

LSPR Imaging

Before scanning the sample to generate a LSPR image, the optical properties of the LSPR biosensor were first examined to exclude any damage caused by the mechanical and chemical stress occurring during the peptide array formation and staining. The extinction spectrum of the sample shows three distinct resonance peaks, indicating an intact optical response of the sensor (Fig. 4-66).

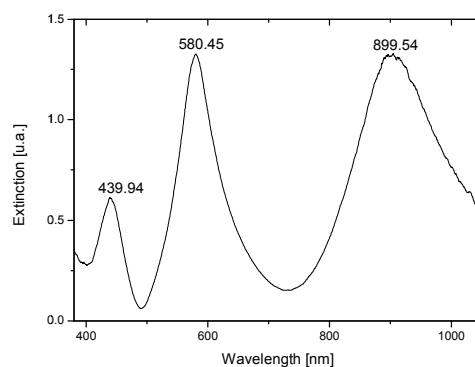


Figure 4-66. Extinction spectra of the LSPR biosensor after peptide synthesis and antibody assay.

The sample was then scanned with a spatial resolution of 100 μm , and the UV-Vis spectra of all measured points were recorded. LSPR images of the peptide array were then generated by the technique depicted in Fig. 4-60.

Figure 4-67 shows the LSPR image of the peptide array in the wavelength regime around the quadrupole resonance peak. However, no array pattern can be observed on this image.

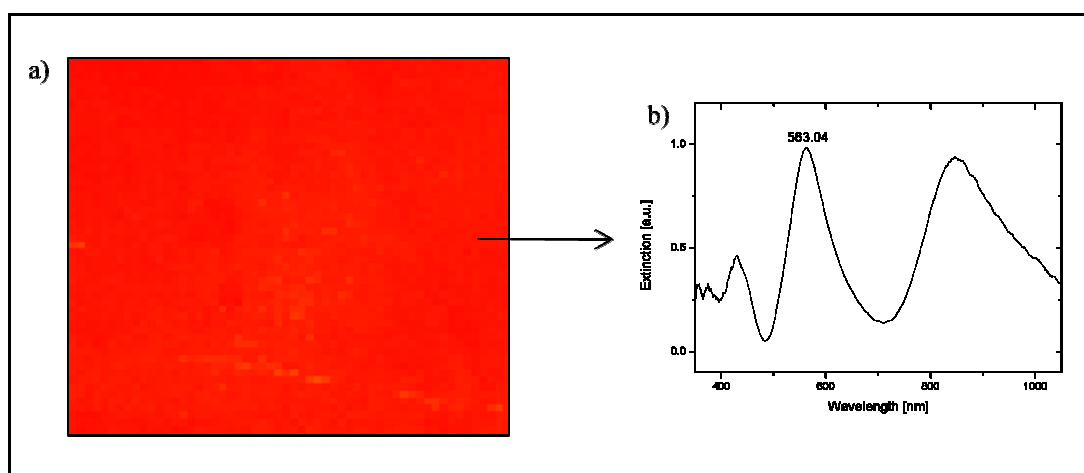


Figure 4-67. LSPR imaging of a peptide array with permuted HA epitope in the wavelength regime around the quadrupole resonance peak (a).

The UV-Vis spectrum of a measured pixel shows a quadrupole peak with a maximum at 563 nm wavelength (b).

In the wavelength regime around the dipole resonance peak (Fig. 4-68), an irregular pattern was displayed in the LSPR image. However, it can be excluded that this pattern was generated by the peptide-antibody spots, since the distance between spot centers amounts to ~ 1.5 cm.

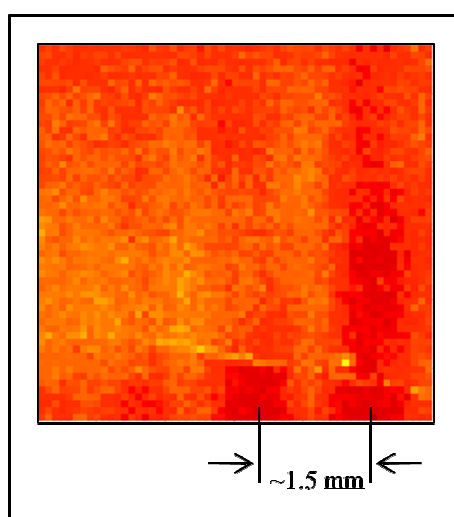


Figure 4-68. LSPR imaging of a peptide array with permuted HA epitope in the wavelength regime around the dipole resonance peak.

As a result, both LSPR resonance peaks in the wavelength regimes around the quadrupole and dipole resonance peaks failed to generate an image of the peptide-antibody spots. This is most likely caused by a very small difference in extinction maxima position for the peptide-antibody spots and the background due to a concentration of peptides and coupled antibodies, which is below the detection limit (37 ng/cm^2) of the LSPR biosensor.

4.4.2.2. Total synthesis of a peptide array on a LSPR biosensor by particle-based technique

Finally, a complete (full-sequence) synthesis of a peptide array was carried out on the polymer-coated LSPR biosensor using the particle-based synthesis.

The sensor geometry consisted of a 100 nm gold film as the bottom gold layer, a 250 nm polycrystalline silica film as the intermediate dielectric layer, and gold colloids deposited by seeding/plating as the upper gold layer. The LSPR biosensor was coated by a copolymer film composed of 10 % PEGMA and 90 % MMA.

An array with 9x20 permutations of the hemagglutinin/HA (YPYDVPDYA) epitope was synthesized on a polymer-coated LSPR biosensor by the particle-based technique. Every amino acid in the sequence (YPYDVPDYA) was substituted by one of the 20 proteinogenic amino acids.

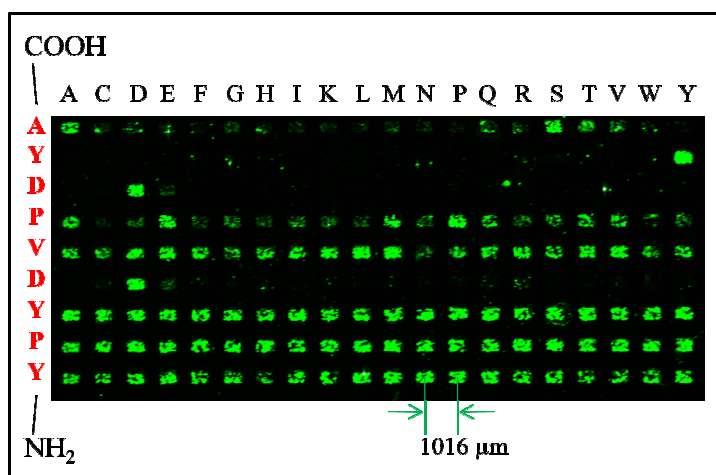


Figure 4-69. IR-image of a peptide array with different permuted HA epitope, which was incubated with specific antibody (800 CW-conjugated mouse anti-HA).

Every amino acid position was substituted by one of the 20 different proteinogenic amino acids.

In the 1st row the 1st amino acid of the sequence was permuted, etc.

The center-to-center distance of the spots amounts to 1016 μm .

After incubating the array with a specific antibody (800 CW-conjugated mouse anti-HA), the array structure is clearly observed in the image recorded by an IR scanner (Fig. 4-69). All of the permuted peptide epitopes showed the expected staining pattern.¹¹⁹

LSPR Imaging

The optical properties of the LSPR biosensor were first examined to exclude any damage caused by the mechanical and chemical straining conditions of the peptide printing process. Three distinct resonance peaks were observed in the optical spectrum of the sample before the synthesis of the peptide array (Fig. 4-71a), which can be assigned to the octapole, quadrupole and dipole resonances.

After the whole peptide synthesis- and antibody assay process the quadrupole and dipole resonances are split into two or more peaks (Fig. 4-71b). One possible cause for the peak splitting is silica particle residues of the amino acids toner particles, which were accumulated on the LSPR sensor surface during the peptide synthesis (Fig. 4-70).

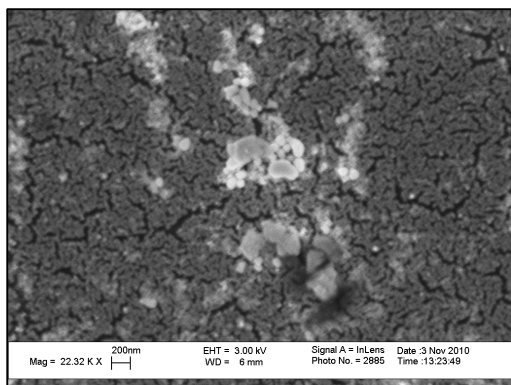


Figure 4-70. SEM image of the polymer coated LSPR biosensor after peptide printing- and antibody assaying processes showing the silica particle residues from the amino acid toner particles.

After sonicating the sample for 9 min, most silica particle residues were removed. The LSPR spectrum is shown in Figure 4-71c. Although the spectrum profile was altered, three resonance peaks corresponding to the octapole, quadrupole, and dipole resonances could still be identified.

The sample was then scanned with a spatial resolution of 70 μm , and the UV-Vis spectrum of each measured point was recorded. LSPR images of the peptide array were then generated by the technique depicted in Fig. 4-60. The wavelength shift in the octapole resonance maxima was chosen to generate the LSPR image due to its relatively small FWHM compared to the quadrupole and dipole resonances (cf. Fig. 4-71c). The LSPR image of the sample in the wavelength regime around the octapole peak is displayed in Fig. 4-72.

UV-Vis extinction spectra of three positions in the array with three different LSPR peak maxima are displayed in Fig. 4-73. These shifts in the LSPR peak maximum reflect the different amounts of adsorbed molecules. The LSPR spectrum displayed in black (Fig. 4-73a) shows the lowest value of the LSPR peak maximum (480.56 nm), indicating the unspotted area of the sample. The LSPR spectrum displayed in brown (Fig. 4-73b) shows the intermediate value of the LSPR peak maximum (492.38 nm), indicating peptide spots in the sample. The LSPR spectrum displayed in red (Fig. 4-73c) shows the highest LSPR peak maximum (498.28 nm), indicating the peptide spots in the sample with a higher adsorbed mass than the LSPR spectrum in brown, probably due to binding of specific antibodies.

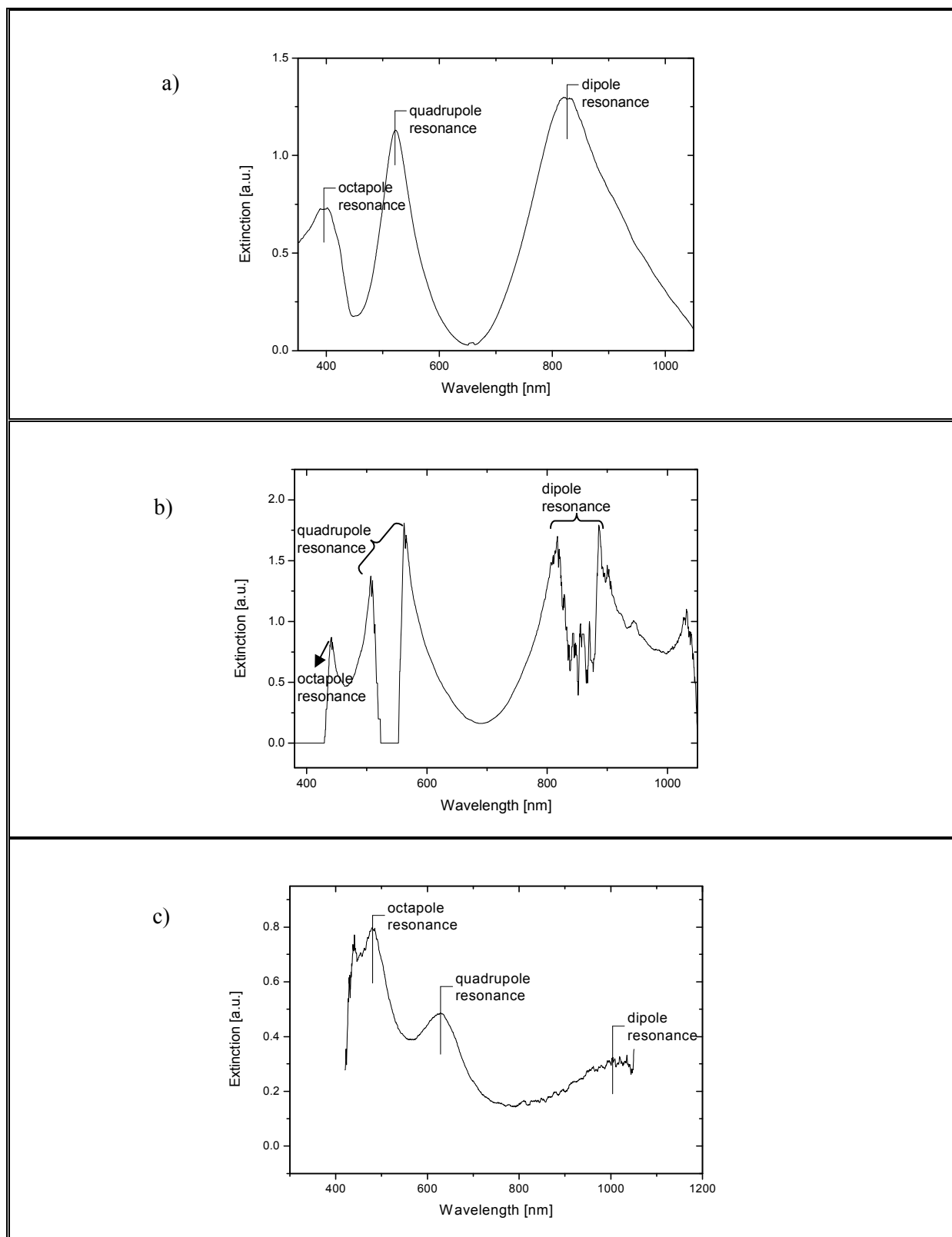


Figure 4-71. UV-Vis spectra of the LSPR biosensor

- (a) before the peptide printing- and antibody assaying processes
- (b) after the peptide printing- and antibody assaying processes
- (c) after the peptide printing-, the antibody assaying processes, and 9 min sonification

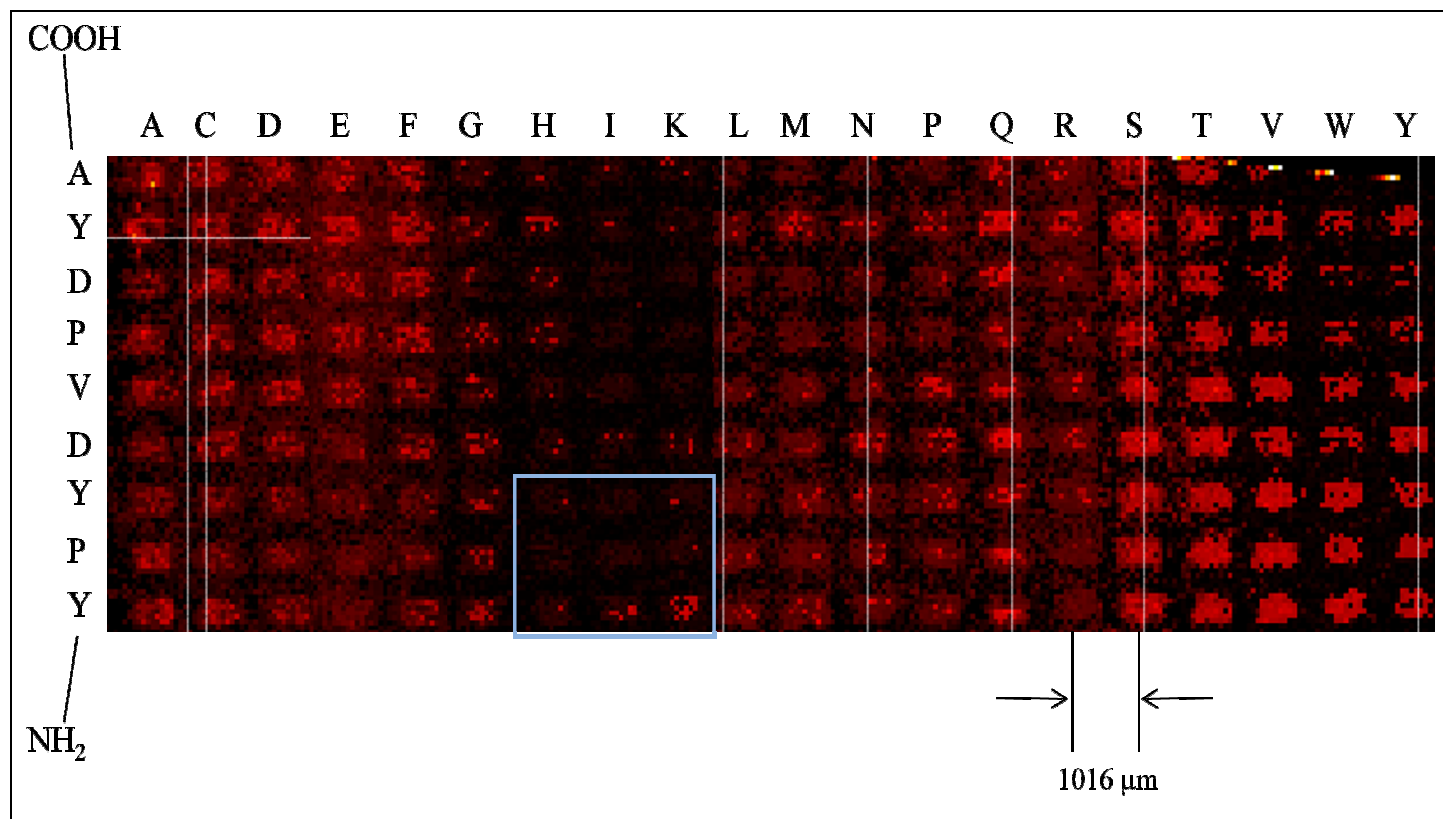


Figure 4-72. LSPR imaging of a peptide array with permuted HA epitope, incubated with specific antibody (800 CW-conjugated mouse anti-HA), in the wavelength regime around the octapole resonance peak. The lateral resolution of the scanning device amounts to 70 μm.

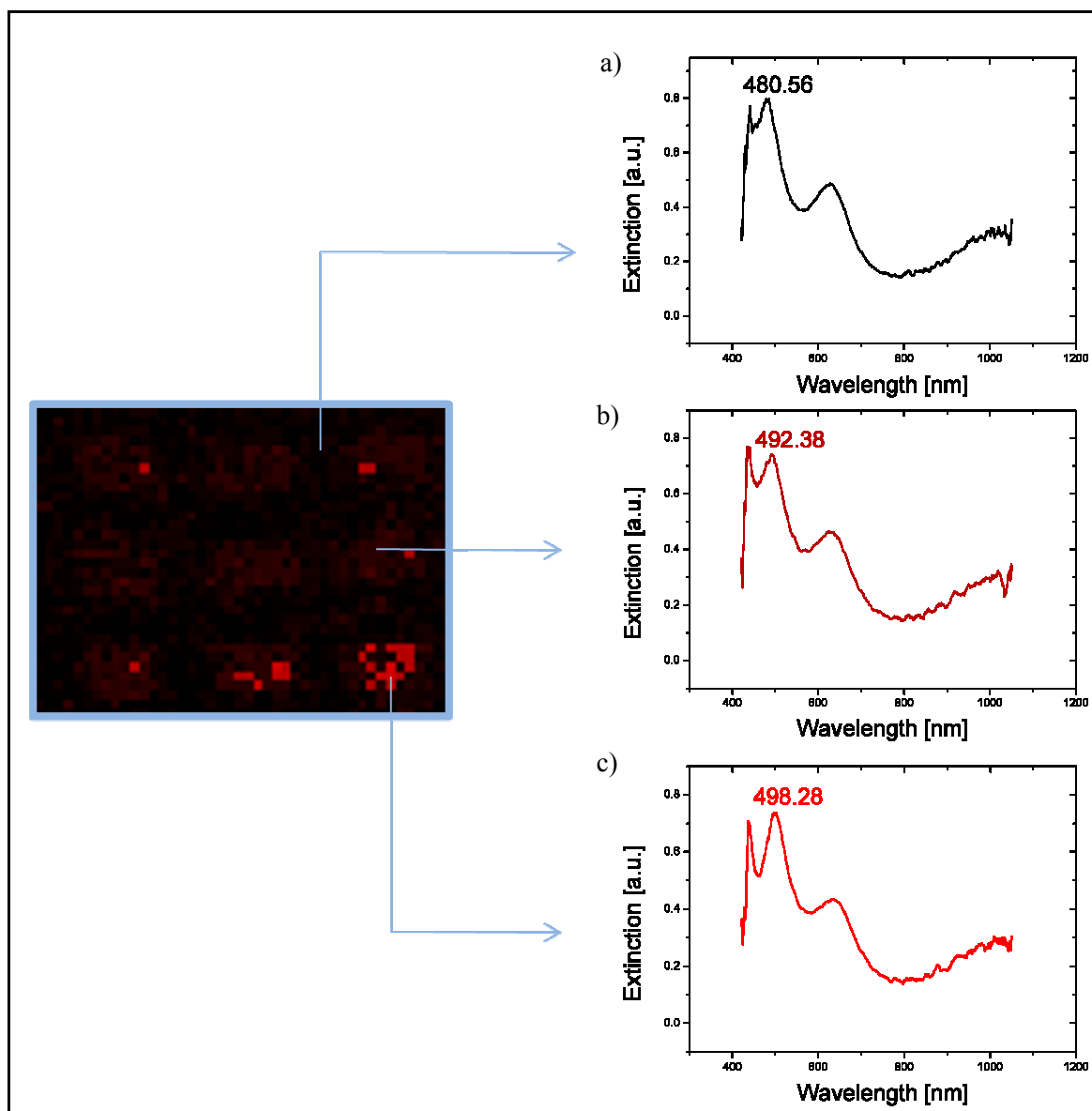


Figure 4-73. UV-Vis extinction spectra of three positions in the array, with different LSPR peak wavelengths, indicating three different amounts of adsorbed molecules.

- (a) The LSPR spectrum displayed in black shows the lowest LSPR peak maximum (480.56 nm), indicating the unspotted area of the sample.
- (b) The LSPR spectrum displayed in brown shows the middle LSPR peak maximum (492.38 nm), indicating the peptide spots in the sample.
- (c) The LSPR spectrum displayed in red shows the highest LSPR peak maximum (498.28 nm), indicating the peptide spots in the sample with a higher adsorbed mass than the LSPR spectrum in brown, probably due to binding of specific antibodies.

In Figure 4-74, the label-based detection (IR-scanner image) is compared with the label-free detection technique based on LSPR resonance shifts. The entire peptide array with 9x20 different HA epitope variants on the sensor was displayed in the LSPR image. However, the IR-scanner image and the LSPR image show different results regarding the positions of peptide spots with HA epitope variants which are recognized by the specific antibody (800 CW-conjugated mouse anti-HA).

The IR-scanner image (Fig. 4-74, top) shows that the HA-epitope variants permuted in the 1st, 2nd, 3rd, and 6th amino acid of the sequence were not bound by the specific antibody. This means that these positions were substantial in the antibody-antigen recognition mechanism. On the other hand, the LSPR image shows minor antibody coupling in the 7th, 8th, and 9th columns, which indicates that substitution of amino acids in the HA sequence by *histidine*, *isoleucine*, and *lysine* could hinder the antibody-antigen coupling.

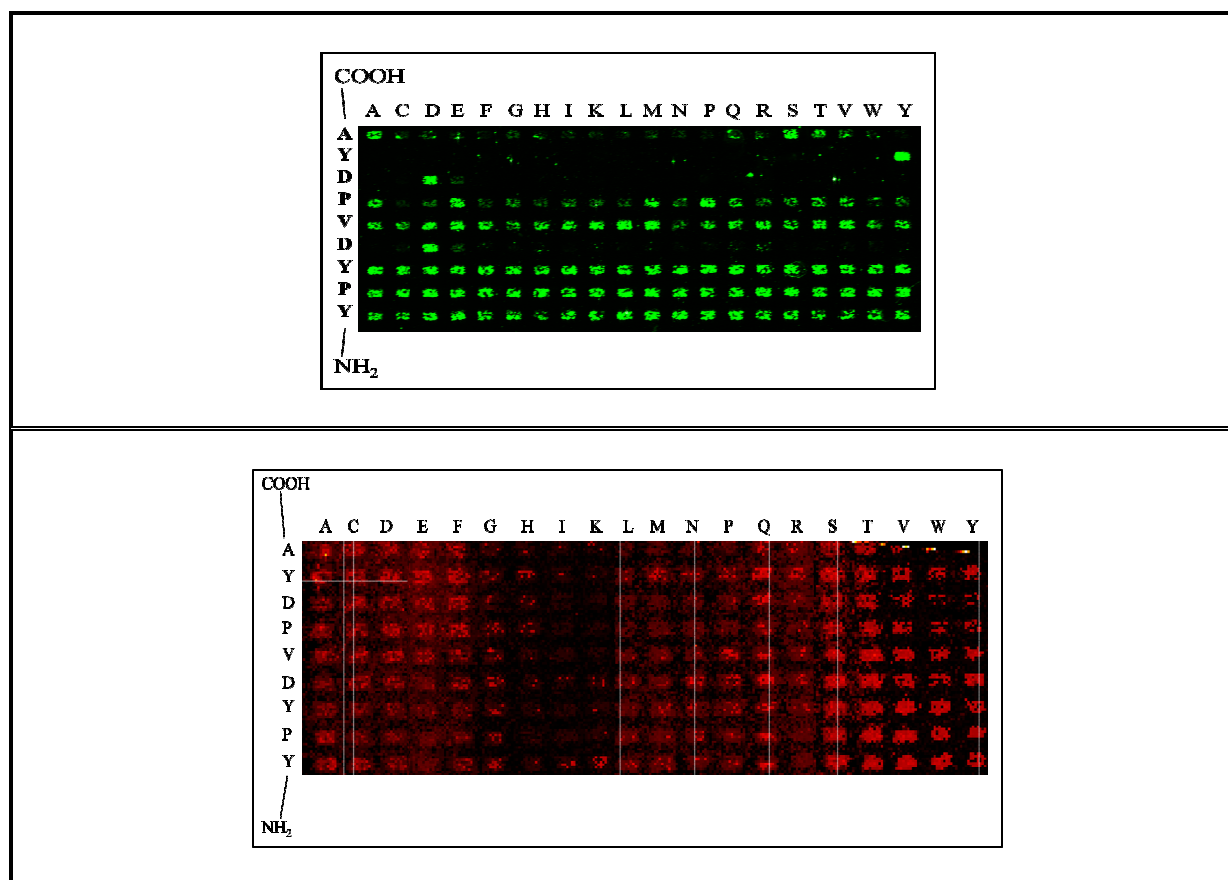


Figure 4-74. Comparison of label-based (top) and label-free (bottom) detection of antibody-antigen interactions on a peptide array.

There are two possible effects which could contribute to the difference in the results of label-based and label-free detection of antibody-antigen binding events. The first possibility is that the amount of antibody coupled to the sensor was lower than the detection limit of the LSPR biosensor. In this case, the LSPR spectrum displayed in red (Fig. 4-73c) which shows the highest LSPR peak maximum (498.28 nm) merely represents spots on the biosensor with a larger amount of peptides than the LSPR spectrum in brown (Fig. 4-73b). In the second possibility, the wavelength shifts in the resonance peak were induced by the surface-bound silica particle residues, which were not removed through sonification.

There are several factors which still have to be optimized in order to routinely use the LSPR biosensor for a label-free detection of biomolecular interactions occurring on the peptide array. Based on the results obtained in this thesis, the most crucial parameter is the analytical

method used to determine the LSPR resonance shift. Instead of using only the wavelength shift in octapole resonance (Fig. 4-72) to detect antibody coupling, the quadrupole and dipole resonance peaks should also be used for analysis. As described in chapter 4.2.4.4., these two peaks allow a higher sensitive read-out of binding events on the sensor surface. However, due to the large FWHMs of these two resonance peak in this particular sample, they could not be used to generate LSPR images. A more complex spectra processing software should be utilized, which can automatically fit the quadrupole and dipole resonance peaks of each measured point on the sample by a Pseudo-Voigt function described in Equation 3-1. The maxima of the fitted peaks could be then identified easily and the wavelength shift of the maxima, induced by antibody coupling, could be used to detect the binding events.

The LSPR imaging technique detects binding events by monitoring the wavelength shifts in the resonance peaks. This shift in wavelength is induced by the change in refractive index of surrounding medium when molecules adsorb onto the sensor surface. Hence, only the change in mass of surface-bound molecules is detected by this method. The type of the molecule bound to the sensor surface cannot be differentiated by this method. Therefore, it is pivotal that the amount of surface-bound peptide -synthesized by the laser printing method- is kept relatively constant for all peptide spots. Only then a successful identification of antibody coupling efficiency can be achieved by monitoring the wavelength shifts.

The third factor that must be optimized is the sensitivity of the LSPR biosensor. Application of silver instead of gold as the metal layer in the sensor geometry should be considered due to its sharper and more intense LSPR bands, although with some loss in chemical stability of the sensor.

A low mass density of surface-bound antibodies was likely induced by the high protein-resistance of the graft copolymer coating with 10 % PEGMA. A lower percentage of PEGMA in the copolymer film should be considered in the fabrication of the polymer coating to reduce the surface's protein repelling ability and increase the access of the antibody into the surface-bound peptides.

Another option in the label-free detection of biomolecular interactions in array format using LSPR biosensor is to transfer the peptide arrays from a prequel substrate onto the sensor surface under mild conditions. This new synthesis route could not only prevent the accumulation of silica particle residues on the sensor surface and the induced alternation of the LSPR spectrum, but also significantly reduce the time needed for one set of experiment.

4.4.3. Conclusion

In this chapter, the fabricated optical biosensor based on LSPR was used as a detection tool in label-free analysis of biomolecular interactions.

In a proof-of-principle experiment, an array of fluorescent-labeled antibodies was formed on the sensor surface by a spotting robot and subsequently detected by means of a fluorescent scanner and the LSPR imaging technique. The LSPR image, recorded with a lateral resolution of 110 μm in the wavelength regime of the quadrupole resonance peak, displayed an array of spots which corresponds to the fluorescence image. This indicates a successful detection of molecular binding on the sensor surface by observing a shift in the LSPR resonance maxima.

Moreover, the quantity of antibodies bound to the sensor surface was correctly predicted by using the measured wavelength shifts of 8 nm in the quadrupole regime and a mass sensitivity factor of 0.027 nm/(ng/cm²) determined by Buecker et al.¹¹¹ This result shows that the LSPR

biosensor described in this thesis has the potential to allow the detection of molecular interactions in a miniaturized array format in a quantitative manner.

In the final part of this thesis, the polymer-coated LSPR biosensor was successfully applied as the solid substrate in the synthesis of a peptide array via the particle-based technique, and then used as a tool for detecting biomolecular interactions occurring on the peptide array. An array with 9x20 variants of the hemagglutinin/HA epitope (YPYDVPDYA) was synthesized on a polymer-coated LSPR biosensor and incubated with an IR-dye conjugated specific antibody. The binding events occurring on the sensor were then detected by means of an IR-scanner and the LSPR imaging technique.

The LSPR image with a lateral resolution of 70 μm in the wavelength regime of the octapole resonance peak was successfully generated, displaying the entire spots of the HA epitope variants formed on the sensor surface. However, there is a significant difference in the results from label-based and label-free detection with regard to the HA epitope variants which were recognized and specifically bound by the anti-HA antibodies. This might be caused by a mass density of antibodies coupled to the surface-bound peptide which is below the detection limit of the LSPR biosensor.

Therefore, several important parameters still have to be optimized in order to use the LSPR biosensor for the label-free and quantitative detection of antibody-antigen interactions in high-density peptide arrays fabricated by the printing method. The read-out of the wavelength maxima of the dipole and quadrupole resonance peaks must be facilitated by automatically fitting the individual extinction peaks to a Pseudo-Voigt function. The amount of surface-bound peptide -synthesized by the laser printing method- should be kept relatively constant for all peptide spots to avoid errors in the quantification of binding affinities. The sensitivity of the LSPR biosensor must be enhanced, for example by using silver instead of gold as the metal layer in the sensor. Copolymer film with a lower fraction of PEGMA should be synthesized as the sensor coating to reduce the protein resistance and improve the access of antibodies to the surface-bound peptides. Another option in combining the peptide arrays and the LSPR biosensor is to transfer the peptide arrays from a prequel substrate onto the sensor surface under mild conditions.

In summary, the LSPR biosensor optimized in this thesis has been successfully used as the solid substrate in the synthesis of high-density peptide arrays by the particle-based printing technique. The polymer coated LSPR biosensor has shown a high stability against the harsh chemical and mechanical conditions of the peptide printing process and a high non-specific protein resistance in the staining process. The optical response of the sensor was partially altered but still intact, indicated by the three visible resonance peaks (octapole, quadrupole, and dipole) in the UV-Vis extinction spectra. A LSPR image has been generated by using the octapole resonance peak, which clearly showed all peptide spots formed on the sensor surface. However, the attempt to label-free detect the antibody amount coupled to the surface-bound peptides, has failed. This was caused most probably by a low concentration of antibodies and accumulation of silica particles residues on the LSPR sensor surface. Several optimization steps must be taken in order to fully utilize the LSPR biosensor as a label-free detection tool for antibody-antigen interactions.

This result shows that by using comparatively simple, cheap instrumentation and preparation steps, a label-free, LSPR-based detection of biomolecular interactions in high-density peptide arrays can be achieved. In the future, it will allow a high-throughput screening of disease-specific markers and the identification of diseases in their early, treatable stages.

5. Optical biosensors based on WGM

5.1. Introduction

Optical label-free detectors, such as the well-established surface plasmon resonance (SPR) sensor, are generally favored for their ability to obtain quantitative data on intermolecular binding. However, sensitivity to single binding events has not materialized due to the problem that a given photon in the exciting light interacts only once with an adsorbate.²²⁻²³

Optical microcavities have been introduced as a powerful tool to achieve label-free detection of single molecules because the resonant recirculation of light within a microcavity allows the light to interact with the adsorbate molecules many more times. Armani et al demonstrated a label-free, single-molecule detection of interleukin-2 in serum using an optical sensor based on an ultrahigh quality (Q) factor ($Q > 10^8$) whispering-gallery microcavity.

The application of high-Q WGM (Whispering Gallery Modes) sensing in the biotechnology is restrained however, by the limited miniaturization potential and demands on mechanical precision. This is caused by the limitation in minimum particle size of WGM cavities imposed by the demand for high Q-factors.

In this work, the potential of small particles with low Q-factors for biosensing applications was investigated as a joint project with Andreas Weller et al. Due to the low Q-factors of these small cavities, particles with diameters below 6 μm exhibit only $q = 1$ modes, thereby causing simplification of the WGM spectrum and facilitating the read-out of resonance shift upon molecular adsorption. The feasibility of this low-Q WGM sensor was demonstrated by monitoring the resonance shift caused by adsorption of multiple layers of polyelectrolytes onto the surface of particles with 2 μm diameter. The detection limit of the WGM sensor can be determined by measuring the resonance shift as a function of the layer thickness.¹⁴

5.2. Theory

WGM can be viewed as light travelling along the inner circumference of the particles at incidence angles above the critical angle for total internal reflection (TIR). WGMs occur at discrete frequencies that depend on the index of refraction n_s and the radius a of the particle. On the outside, an exponentially decaying evanescent field exists, which is sensitive to changes of the dielectric function in the intimate vicinity of the cavity. Thus, biomolecular adsorption on the outer cavity surface can be detected by either the shift in the resonance position or the change of the Q-factor.

The study of the electrodynamics of a dielectric sphere is required in order to understand the resonance condition of the whispering-gallery waves.¹²⁰⁻¹²²

5.2.1. Basic equations

The solutions for Maxwell's equation for a monochromatic field

$$\text{rot } \mathbf{E} = ik\mathbf{H}, \quad \text{rot } \mathbf{H} = -ik\mathbf{E}$$

inside the dielectric sphere ($r \leq a$) has the form

$$U_{mn}^i(r, \theta, \varphi) = C_i P_n^m(\cos \theta) (kr)^{1/2} j_n(kr) e^{\pm im\varphi}$$

and outside the dielectric sphere ($r > a$)

$$U_{mn}^e(r, \theta, \varphi) = C_e P_n^m(\cos \theta) (kr)^{1/2} h_n^{(1)}(k_0 r) e^{\pm im\varphi}$$

In these so-called Debye potentials, $P_n^m(\cos \theta)$ are the adjoint Legendre polynomials, $j_n(kr)$ the Bessel function, $h_n^{(1)}(k_0 r)$ the Hankel functions. Bessel functions describe standing waves in the radial direction of spherical coordinates, while Hankel functions describe the spherical waves propagating outside the dielectric sphere and in the radial direction away from the centre of the sphere. $C_{i,e}$ are arbitrary constants, where indexes i and e stand for inside and outside the sphere. m and n are parameters with $n \in \mathbb{N}$, $m \in \mathbb{N}$, and $|m| \leq n$. The wave vector inside the dielectric sphere is described as $k = \frac{2\pi}{\lambda} n_s$, the one outside the sphere as $k_0 = \frac{2\pi}{\lambda}$, where n_s is the refractive index of the dielectric sphere and λ the wavelength in vacuum.

Whispering gallery modes can be divided into two subgroups regarding the polarization: transversal electric (TE), and transversal magnetic (TM) modes. In spherical coordinates, TE-modes can be derived from electromagnetic fields with zero E-component in the radial direction, while the magnetic field of the TM-modes is zero in the radial direction.

The characteristic equation for the TE field is

$$\frac{H_{n-1}^{(2)}(k_0 r)}{H_n^{(2)}(k_0 r)} = n_s \frac{J_{n-1}(kr)}{J_n(kr)}$$

and for the TM field

$$-n + k_0 r \frac{H_{n-1}^{(2)}(k_0 r)}{H_n^{(2)}(k_0 r)} = -\frac{n}{n_s^2} + \frac{k_0 r}{n_s} \frac{J_{n-1}(kr)}{J_n(kr)}$$

Here, $k = n_s k_0$ with $k_0 = \frac{2\pi}{\lambda} n_m$ and n_m is the refractive index of the outside medium. J_n and $H_n^{(2)}$ describe the spherical Bessel- and Hankel functions. These characteristic equations determine the relation between the wave length λ (or the wave number k) of the WGM resonances and the sphere radius a .

For a small index n , the oscillating field fills almost the entire volume of the sphere and therefore cannot be called a WGM. If $m \neq n$, the mode acquires an oscillating transverse structure, which increases with increasing the difference $n - m$. Therefore, it is reasonable to call a WGM a wave which has large and identical number of n and m .

For a given radius of the sphere there is an infinite set of the corresponding eigenfrequencies. Thus, it is necessary to introduce the third index q , with $q = 1$ as the solution with the highest λ for a given parameter n , $q = 2$ as the solution with the second highest λ for a given parameter n , etc.

For example, a polystyrol sphere ($n_s = 1.59$) with a radius of 15 μm and air as the outside medium has the following resonance wavelengths for a given $n = 247$:

Table 5-1. Resonance wavelength for $n = 247$ with different q -values.

q	TE	TM
1	580.8 nm	579.1 nm
2	561.2 nm	560.0 nm
3	545.8 nm	544.3 nm

5.2.2. Approximation for $q = 1$ mode

The Hankel and Bessel functions are well approximated by Airy functions ¹²⁰

$$\sqrt{z}J_n(z) = \sqrt{2} \left(\frac{n}{2}\right)^{1/6} Ai(\zeta)$$

$$\sqrt{z}H_n(z) = \sqrt{2} \left(\frac{\psi}{2 \sinh \eta}\right)^{1/4} [Ai(\psi) - iBi(\psi)]$$

where $\zeta = \left(\frac{2}{n}\right)^{1/3} (n - z)$; $\eta(z) = \text{arcosh} \left(\frac{n}{z}\right)$; $\psi = \left[\frac{3}{2}n (\eta - \tanh \eta)\right]^{2/3}$.

Using the Airy functions, the resonance frequencies of the $q = 1$ mode can be approximated by the following analytical expressions for transverse electric (TE) and transverse magnetic (TM) fields, respectively:

$$\omega_n^{TE} \approx \frac{c}{R\sqrt{\varepsilon\mu}} \left[\nu + 1.85576 \nu^{1/3} - \frac{1}{\mu} \sqrt{\frac{\varepsilon\mu}{\varepsilon\mu - 1}} + O(\nu^{-1/3}) \right] \quad (1a)$$

$$\omega_n^{TM} \approx \frac{c}{R\sqrt{\varepsilon\mu}} \left[\nu + 1.85576 \nu^{1/3} - \frac{1}{\varepsilon} \sqrt{\frac{\varepsilon\mu}{\varepsilon\mu - 1}} + O(\nu^{-1/3}) \right] \quad (1b)$$

Here, $\nu = n + 0.5$ and ε and μ are the dielectric permittivity and magnetic permeability of the particle. The quantum number m does not enter the formulas due to the spherical symmetry of the system. For deviations from spherical symmetry, the degeneration in m is resolved and the mode splitting can be calculated as

$$\omega_{mn} \approx \omega_n \left[1 - \frac{dR}{R} \left(2 + 3 \frac{n^2 - m^2}{n^2} \right) \right] \quad (2)$$

where dR is the deviation of the minor axis of the spheroid from the initial radius of the sphere.

5.2.3. Q-factor

The quality factor, Q , of a resonator is related to the lifetime of light energy in the resonator mode. The Q -factor is fundamentally restricted by the radiative emission, which is unavoidable in open dielectric resonators. Losses in dielectric WGM cavities originate from material absorption and scattering, scattering at the interface due to surface roughness, and a loss related to the curvature of the reflecting surface.

The theoretical Q -factor of a WGM with the parameters q and n is calculated as

$$Q_{nq} = \frac{n + \frac{1}{2}}{2} \left[\frac{\varepsilon(\varepsilon\mu - 1)}{\mu} \right]^{1/2} \exp(2T_{nq})$$

$$T_{nq} = \left(n + \frac{1}{2} \right) \left[\text{arcosh}(\varepsilon\mu)^{1/2} - \left(\frac{\varepsilon\mu - 1}{\varepsilon\mu} \right)^{1/2} \right] + \left(\frac{n + \frac{1}{2}}{2} \right)^{1/3} \zeta_q \left(\frac{\varepsilon\mu - 1}{\varepsilon\mu} \right)^{1/2} + \frac{1}{\varepsilon}$$

Because the roots ζ_q of the Airy function are negative, the value of T_{nq} decreases with increasing the root number q . For this reason, the mode Q -factor rather rapidly decreases with increasing q .

5.2.4. WGM for biosensing

Arnold and coworkers derived the sensitivity, $\Delta\lambda/\lambda$, of WGM biosensors for the adsorption of very thin adsorption layers ($d \ll \lambda$) from a perturbation theoretical approach.²²

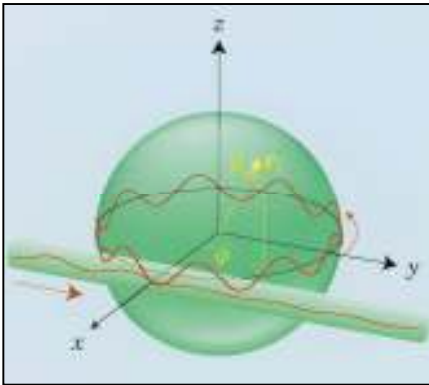


Figure 5-1. Protein molecule at position r_i on the surface of a sphere near an optical fiber core.

The studied configuration is shown in Figure 5-1. Light from a tunable laser is coupled into a WGM of the sphere from an optical fiber and circulates about the equator. Resonant modes are detected from dips in the transmission through the fiber. A protein molecule diffuses to the sphere's surface from the surrounding aqueous medium and is adsorbed at position r_i , where it interacts with the evanescent field of the WGM. The index i distinguishes each adsorbed protein molecule. This interaction polarizes the molecule, shifting the frequency of the mode.

The frequency shift is given by a surprisingly simple formula:

$$\frac{\Delta\lambda}{\lambda} \cong -\frac{\alpha_{ex}\sigma_p}{\epsilon_0(n_s^2 - n_m^2)R}$$

where n_s and n_m are the refractive indices of the sphere and the surrounding medium, R denotes the sphere's radius and σ_p is the protein surface density. The excess polarizability α_{ex} of the protein molecule is roughly proportional to the mass of the molecule.

The linear dependence of $\Delta\lambda/\lambda$ on α_{ex}/R has been confirmed experimentally for particles with high Q -factors, i.e. for particles with diameter of some tens to some hundreds of microns.

5.2.5. Excitation of WGM

In practice, WGMs are excited by near-surface fields such as near-surface TIR (total internal reflection) waves, planar, or fiber waveguides. The efficient coupling requires the spatial overlap of the evanescent fields of the cavity and the source of excitation. The distance between the evanescent fields of excitation source and particle, respectively, must be controlled with nanometer precision, thereby complicating the applicability of most WGM systems.

In his diploma thesis Weller avoided the crucial evanescent field coupling by exciting the mode spectrum from the inside of the cavity by means of a fluorescent dye, thus largely widening applicability and ease of usage of WGM sensors in in-situ micro-sensing applications.^{14,122}

The dye molecules inside the cavity were excited by means of a Raman microscope, which is highly effective as its tight laser focus can be placed into the center of the beads (Fig. 5-2). The excited dye molecules emit in arbitrary direction, accidentally also populating cavity modes. Thus, particularly dye molecules in proximity of the particle surface contribute to WGM excitation.

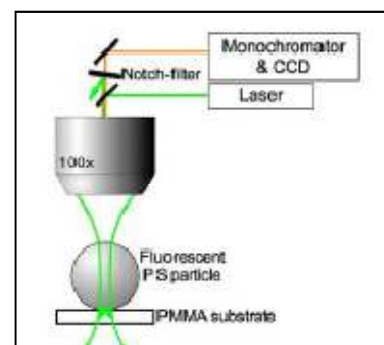


Figure 5-2. Experimental set-up for excitation and detection of WGM in fluorescent-dyed polystyrene beads by means of a Raman microscope.

5.2.6. Determination of the sphere radius

To compare the experimentally determined sensitivity of a spherical WGM sensor to theoretical prediction, the particle radius has to be calculated precisely as the wavelength shift due to changes in the immediate environment of the particle is inversely proportional to R .

By combining the equations (1) and (2), the WGM resonance positions can be written as

$$\lambda_n^{TE} \approx P * \left(\frac{1}{2\pi\sqrt{\varepsilon\mu}} \left[\nu + 1.85576 \nu^{\frac{1}{3}} - \frac{1}{\mu} \sqrt{\frac{\varepsilon\mu}{\varepsilon\mu - 1}} \right] \right)^{-1}$$

$$\lambda_n^{TM} \approx P * \left(\frac{1}{2\pi\sqrt{\varepsilon\mu}} \left[\nu + 1.85576 \nu^{\frac{1}{3}} - \frac{1}{\varepsilon} \sqrt{\frac{\varepsilon\mu}{\varepsilon\mu - 1}} \right] \right)^{-1}$$

$$\text{with } P = \left[\frac{1}{R} - 2 \frac{dR}{R} \right]^{-1}.$$

Using these equations the particle radius can be determined precisely by a least-square fit to the experimentally determined WGM positions as a function of the parameter P . A reasonable trade-off between miniaturization and spectrum quality was found for particles with a diameter of 2 μm .

5.3. Materials and Methods

5.3.1. Chemicals

Sulfonated polystyrene (PS) particles of different size (Polysciences), xylene (96%, Merck), Nile red fluorescent dye (HPLC grade, Fluka), poly(allylamine hydrochloride) (PAH, MW 15000 Da) and poly(sodium 4-styrenesulfonate) (PSS, MW 70000 Da), and bovine serum albumin (BSA, 98%, MW 66000 Da) (all Sigma Aldrich) were used as received. Deionized water (>18 M Ωcm) was produced by a MilliQ plus system.

5.3.2. Inking

A 500 μl saturated solution of Nile red in xylene was placed on top of 8 ml of a PS particle suspension diluted ~40 fold by means of deionized water. The resulting phase-separated system was gently shaken until the xylene had evaporated. The remaining aqueous phase was centrifuged at 5000 rpm and the supernatant removed in order to obtain a concentrated suspension of dye-inked PS particles.

5.3.3. Deposition of polyelectrolytes

PAH and PSS were both adsorbed from either salt-free or 0.5 M NaCl aqueous solutions at a concentration of 1mg/ml, respectively. Three washing steps were applied before and after exposure of the particles to the particular PE solution.

5.3.4. Raman measurement

A Dilor LabRam Raman microscope was used to excite the dye and detect the radiation scattered from the particles. The particles were first immobilized on a poly(methylmethacrylate) (PMMA) substrate and then placed in the focus of a 100x objective. For excitation of the fluorescent dye, a cw Ar ion laser was coupled into the

microscope at a radiant power of 15 mW, yielding a focus of 3 μm diameter. The emitted light was re-collected by the 100x objective and separated from the excitation by means of a Notch filter. The spectral range of the detection unit was 520–660 nm at an optical resolution of $\delta\lambda = 0.03$ nm.

5.4. Results and Discussion

A well-characterized system was selected to study the resonance shift of the WGM sensor in dependence of the adsorbate film thickness. Positively charged poly(allylamine hydrochloride) (PAH) and negatively charged poly(sodium 4-styrenesulfonate) (PSS) were deposited successively onto polystyrene particles (diameter = 2 μm) from 0.5 M NaCl aqueous solutions. To exclude the impact of salt crystallites remaining in the polyelectrolyte layers, both polyelectrolytes were also adsorbed from salt-free solutions.¹²³⁻¹²⁵

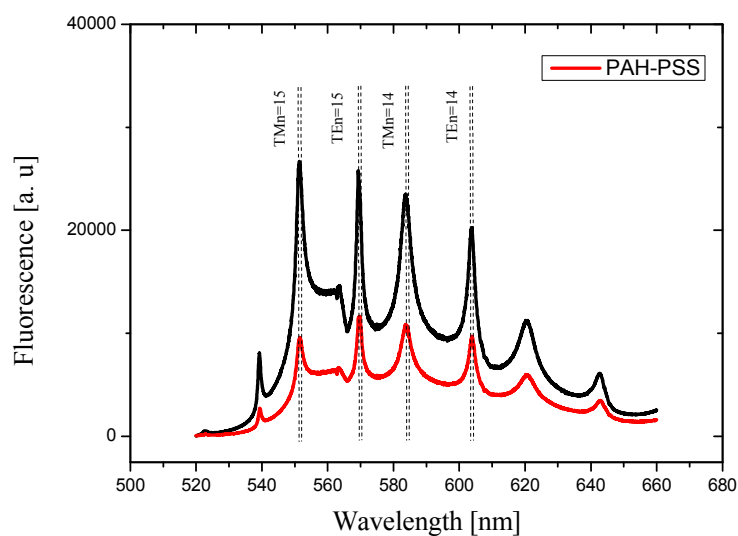


Figure 5-3. Emission spectra from a fluorescent-doped 2 μm sulfonated polystyrene particle before (black line) and after (red line) adsorption of a PAH/PSS-bilayer from aqueous solution.

Figure 5-3 shows the emission spectra taken from a 2 μm sulfonated polystyrene particle which was coupled with Nile red fluorescent dyes (black line). Peaks at 553 nm and 571 nm can be assigned to the transversal magnetic and transversal electric modes with the quantum number $n = 15$. TM and TE modes of the quantum number $n = 14$ exhibited the emission peaks at 585 nm and 605 nm.¹²² A shift in the emission spectra was observed after adsorption of one PAH-PSS layer pair (red line) from a salt-free solution.

In Figure 5-4 the resonance shift is plotted as a function of the adsorbate's film thickness for deposition from salt-free and 0.5 M NaCl solution. The film thickness was taken from neutron reflectometry measurements by Lösche et al, which studied the dependence of polyelectrolyte film thickness on the ionic strength of the solution used for the preparation.¹⁷ A film thickness of 8 \AA had been observed for deposition of a single PAH/PSS-bilayer under salt-free conditions. Adsorption of the layer pair from a 0.5 M NaCl solution had obtained a film thickness of 35.6 \AA , with a contribution of PSS to the layer pair thickness of 76 %.

Both experimental series (salt-free and 0.5 M NaCl) show the same behavior including an increase in the slope for thickness values beyond 40 \AA (Fig. 5-4). A linear fit of the data from 1 to ~ 40 \AA yields a slope of 0.038 nm/ \AA . This result was then used to determine the detection limit of the WGM sensor. By assuming a spectral resolution of 0.1 nm and using a

polyelectrolyte mass density¹⁷ of 0.81 g/cm^3 , a mass sensitivity limit of 3 fg can be achieved by the WGM sensor.

A distinct increase in the slope for thicknesses beyond 40 \AA can be related to experimental uncertainties. By using surface-adsorbed particles, the contact area between particle and interface remains uncoated, resulting in smaller shift in the regime below 40 \AA . Moreover, polyelectrolytes are known to form thicker adsorption layers after the first few double layers, an effect which was not considered in the work of Lösche et al. Thus, the PE layer thickness could possibly be underestimated in the latter regime. In addition, the accumulation of material underneath the particles during the drying process might come into play at higher layer thickness.

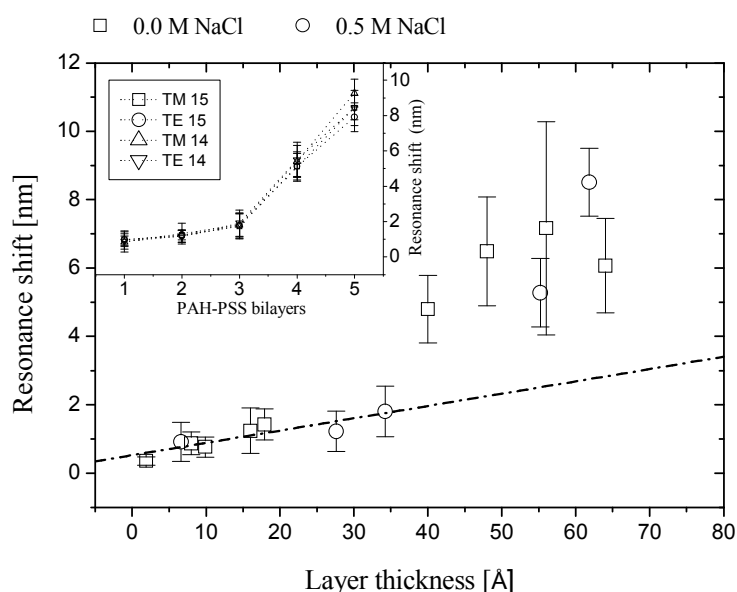


Figure 5-4. Measured shifts of the WGM resonance peaks of fluorescent-doped sulfonated polystyrene beads ($d = 2 \mu\text{m}$) due to adsorption of polyelectrolyte (PE) multilayers.¹⁴ PE adsorption was performed from 0.5 M NaCl aqueous solution (rectangles) as well as from salt-free solution (circles). The inset shows the measured shifts for four different modes in dependence of the number of adsorbed PE layers prepared from 0.5 M NaCl solution. The main graph displays the average over these four modes. A linear fit of the peak shifts up to a PE thickness of 40 \AA (dash-dotted line) yields a slope of 0.038 nm/\AA .

5.5. Summary and Conclusion

Whispering gallery modes of fluorescence-doped sulfonated polystyrene particles with a diameter of $2 \mu\text{m}$ were studied with respect to their resonance shift after adsorption of polyelectrolyte multilayers. Due to the low Q-factor, these small cavities exhibit only $q = 1$ modes, causing drastic simplification in the WGM spectrum. At the same time, the small size of the particles facilitates the implementation of the WGM sensor in miniaturized systems.

Oppositely charged poly(allylamine hydrochloride) (PAH) and poly(sodium 4-styrenesulfonate) (PSS) were deposited alternately onto PS particles (diameter = $2 \mu\text{m}$) from salt-free and 0.5 M NaCl aqueous solutions. Both experimental series display the same behavior when their resonance shifts are plotted as a function of the film thickness. A slope of 0.038 nm/\AA was obtained from a linear fit to the experimental data.

The sensitivity factor of 0.038 nm/\AA can be translated into a detection limit of 3 fg by assuming a spectral resolution of 0.1 nm and a polyelectrolyte mass density¹⁷ of 0.81 g/cm^3 .

With a mass sensitivity of 3 fg, this WGM based sensor is highly competitive in the field of label-free detection techniques.

6. Summary and Conclusion

6.1. Optical biosensor based on localized surface plasmon resonance (LSPR)

Optically responsive substrates based on Localized Surface Plasmon Resonance (LSPR) were developed and optimized to serve both as a solid support for the peptide arrays and for the detection of antibody-antigen interactions in an array format. LSPR is an optical phenomenon generated by collective oscillations of the electron gas in metal nanostructures surrounded by a dielectric material. The position of the resonance maxima is controlled among others by the dielectric constant/refractive index of the surrounding medium. Molecular adsorption at the surface of the metal nanostructures changes the local refractive index. This change in refractive index can be observed as a shift in the wavelength of the resonance peaks and forms the basis of LSPR biosensor operation.

In this thesis, biosensors using the localized surface plasmon resonances of metallic gold were constructed. Gold was chosen because of its high chemical stability. The LSPR biosensor geometry consists of two gold layers and an intermediate dielectric layer in-between (Fig. 6-1, left). These 3-layer biosensors show pronounced resonance peaks in the UV-Vis region of the electromagnetic spectrums, at approximately 350 nm (octapole resonance peak), 500 nm (quadrupole resonance peak) and 750 nm (dipole resonance peak), respectively (Fig. 6-1, right).

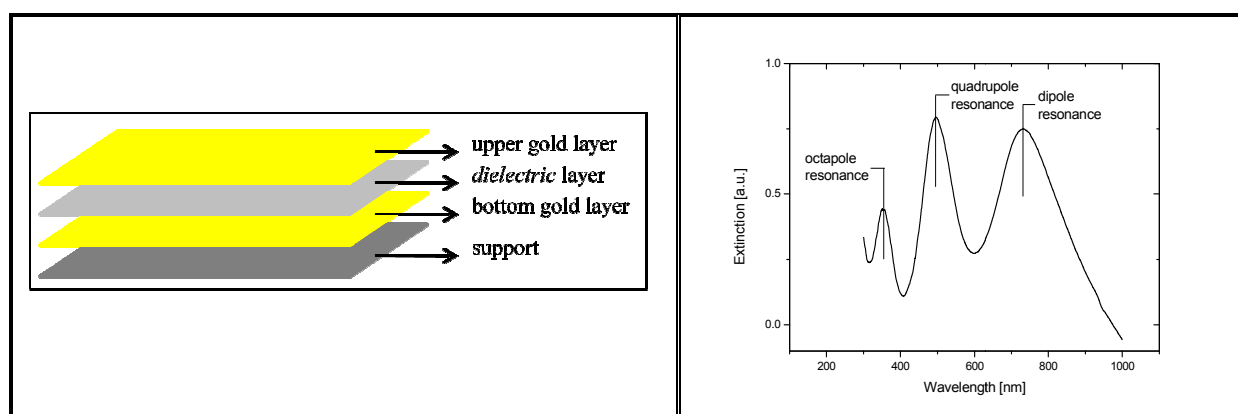


Figure 6-1. (left) Schematic drawing of the LSPR biosensor developed and optimized in this work. The sensor geometry consists of two gold layer and an intermediate dielectric layer between the two metal films. (right) The UV-Vis extinction spectrum of the LSPR biosensor shows three resonance peaks: octapole (around 350 nm), quadrupole (around 500 nm), and dipole (around 750 nm).

It was shown that the extinction spectra of the LSPR biosensors optimized in this dissertation, correlate with the theoretical calculations made by Westcott et al.⁹⁷ for silica-gold nanoshells in water based on Mie scattering theory. Importantly, it is shown that the number and the wavelength of the excited resonance modes on the sensor increase with increasing core size. This shows that the optical properties of the LSPR sensor system, such as the position of the plasmon resonances, can be tuned by modifying the dimension of the dielectric layer.

Different sensor geometries were constructed and optimized in terms of three aspects pivotal to the performance of the sensors when used for the detection of biomolecular interactions in miniaturized format: plasmon line shape, optical homogeneity, and sensitivity towards the surrounding dielectric medium. Three geometries of the intermediate dielectric layer were investigated: a silica nanoparticle monolayer, a homogeneous silica film, and a composite structure of a silica nanoparticle monolayer and a homogeneous silica film. While the lower gold layer was exclusively prepared by Physical Vapor Deposition (PVD), the performances

of PVD as well as metal deposition from solution by seeding/plating were investigated as the deposition technique for the upper gold layer.

The *plasmon line shape*, which determines the accuracy of a spectroscopic measurement, was quantitatively assessed by the normalized Full Width at Half Maximum (FWHM), defined as $L = \frac{FWHM \text{ (Full Width at Half Maximum)}}{I \text{ (Intensity)}}$. A small L value will enable an exact read-out of the resonance maximum. Two important aspects were evaluated from the study of different LSPR biosensor structures. First, both the dipole and quadrupole resonance peaks strongly depend on the surface coverage of the silica particle monolayer and the normalized FWHM decreases with the increasing surface coverage. Second, the lowest normalized FWHM was accomplished in the quadrupole resonance mode of the LSPR biosensor prepared by seeding and plating in the fabrication of the upper gold layer, with a composite structure of a homogeneous silica film (thickness = 50 nm) and a silica particle monolayer ($d = 510$ nm) as the intermediate dielectric layer.

For parallel detection of binding events on a peptide array, it is necessary that surface areas with both unoccupied and occupied binding sites exhibit little variation in the resonance maximum position. To determine the *optical homogeneity* of the sensor, the extinction spectra of several arbitrarily chosen positions on a LSPR biosensor were recorded. The variations in the wavelength of the dipole and quadrupole resonances were then analyzed for different sensor preparation techniques. In a comparison between simple incubation and optimized spin coating in the preparation step for the intermediate dielectric layer, spin coating yielded a lower variation of the peak position for both quadrupole and dipole resonances. It was also found that both techniques generate less variation in peak position for the quadrupole resonance than for the dipole resonance. In the comparison of seeding/plating and PVD as the deposition technique for the upper gold layer, the quadrupole resonance peak of LSPR biosensor prepared by PVD shows the least variation.

A high *sensitivity* of the LSPR biosensors towards the surrounding medium is essential to detect biomolecular interactions in miniaturized format. Sensitivity tests were performed by observing the fibrinogen-induced shift of the dipole and quadrupole resonance maxima. Using spin coating in the preparation of silica nanoparticle monolayers has improved the sensitivity of both dipole and quadrupole resonances compared to LSPR sensors prepared by the simple incubation method. In the comparison of seeding/plating and PVD as the deposition technique of the upper gold layer, both techniques show advantages and disadvantages. Seeding/plating shows a higher sensitivity in the dipole resonance compared to PVD, while the PVD technique generates a larger shift in the quadrupole resonance.

Regarding the three aspects (plasmon line shape, optical homogeneity, and sensitivity), the most suitable geometry for the LSPR biosensor application in label-free detection of biomolecular interactions in array format was found to consist of a 100 nm gold film as the bottom gold layer, a 250 nm homogeneous silica film as the intermediate dielectric layer, and gold colloids prepared by seeding/plating as the upper gold layer (Fig. 6-2).

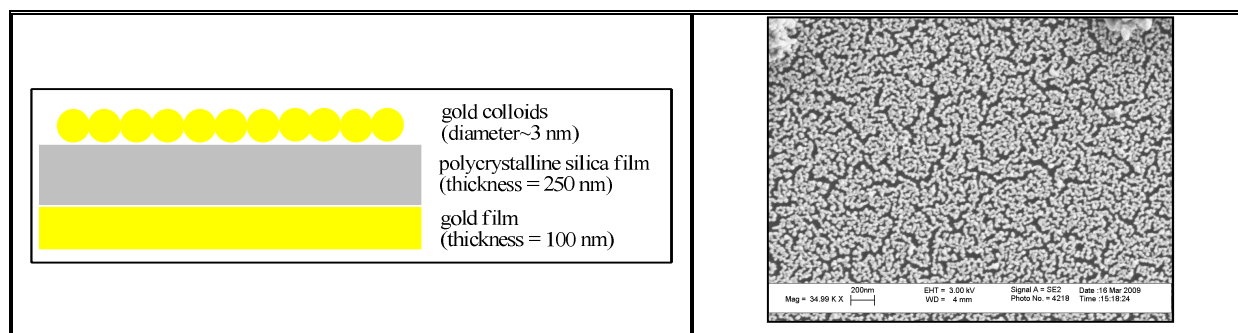


Figure 6-2. The most suitable LSPR biosensor geometry for the application in label-free detection of biomolecular interactions in array format: (a) a schematic viewing, (b) a SEM image of the sensor surface.

6.2. Protein resistant coating on the LSPR biosensor based on poly(ethylene glycol)

Suppression of nonspecific protein adsorption is crucial for achieving sufficient bioassay selectivity and sensitivity in the diagnostic assays and biosensors based on specific recognition of antigen-antibody pairs. Therefore, the successfully designed LSPR biosensor has to be coated with a protein-resistant layer before it can be used as a solid support for peptide array formation. A protein-resistant coating based on poly(ethylene glycol) methacrylate (PEGMA) was introduced to the sensor surface via Atom Transfer Radical Polymerization (ATRP) in this thesis. A PEGMA graft polymer film was chosen as the protein-repelling layer due to the advantages of polymer coatings compared to self-assembled PEG monolayers. Polymer films possess thicker and more robust architecture and chemistry, and their three-dimensional layer geometries provide a high loading of functional groups for the linkage of the generated peptides. The mild reaction conditions of ATRP should facilitate its application on the chemically-sensitive LSPR biosensor. Besides a high tolerance towards various functional groups, ATRP produces polymers with a narrow molecular weight distribution, which provides a high control over the film thickness.

Prior to synthesis of the protein-resistant layer, the LSPR biosensor was first coated with a layer of silica gel. The three-dimensional structure of the silica layer stabilizes the chemically and mechanically sensitive sensor and provides a high loading of hydroxyl functional groups. ATRP initiators were coupled to the hydroxyl groups of the silica gel in two steps (silanization and esterification) to enhance the coupling efficiency. Subsequently, polymerization was carried out at ambient temperature with OEGMA as the monomer and Cu(I) complex as the catalyst, resulting in a PEGMA polymer film (Fig. 6-4).

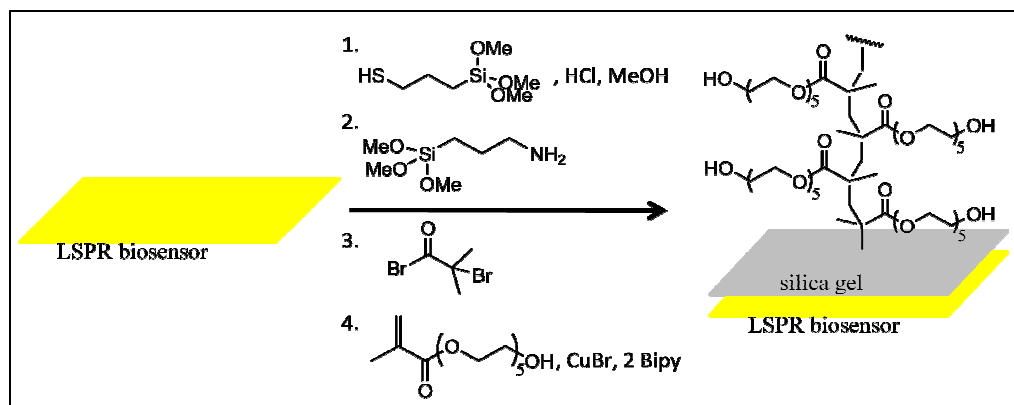


Figure 6-3. Synthesis route for a PEGMA coating on the LSPR biosensor via ATRP: (1) sol-gel coating, (2) surface immobilization of the first ATRP initiator, (3) surface immobilization of the second ATRP initiator, (4) polymerization of OEGMA monomer.

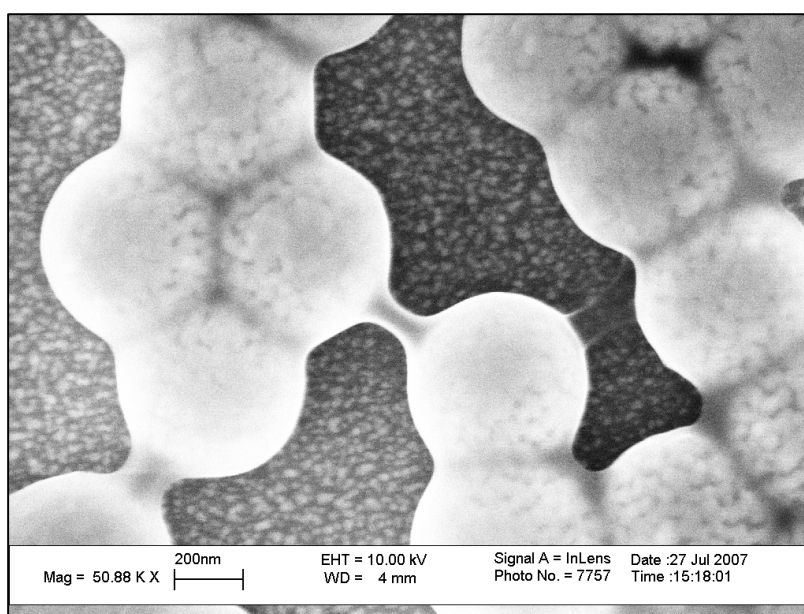


Figure 6-4. SEM image of a LSPR biosensor coated with a PEGMA graft polymer film.

However, graft polymer films with 100 % PEGMA fraction possess a very high protein-resistance. This frequently shields the peptides immobilized on the sensor surface from interacting and binding to the corresponding antibodies. As a result, the detection efficiency is reduced due to an insufficient amount of antibodies coupled to the surface-bound peptides. In the second approach, a graft copolymer film was therefore synthesized on the sensor surface with MMA as the diluting monomer. This reduces the protein-resistance of the polymer film. The first to the third step are analogous to the synthesis route for a pure PEGMA coating. The “grafting from” copolymerization was carried out in TEGMME with a $\text{CuCl}/\text{CuCl}_2/\text{PMDETA}$ catalyst system (Fig. 6-5). Two different ratios of PEGMA/MMA mole fractions were used in the polymerization solutions: 50/50 and 10/90.

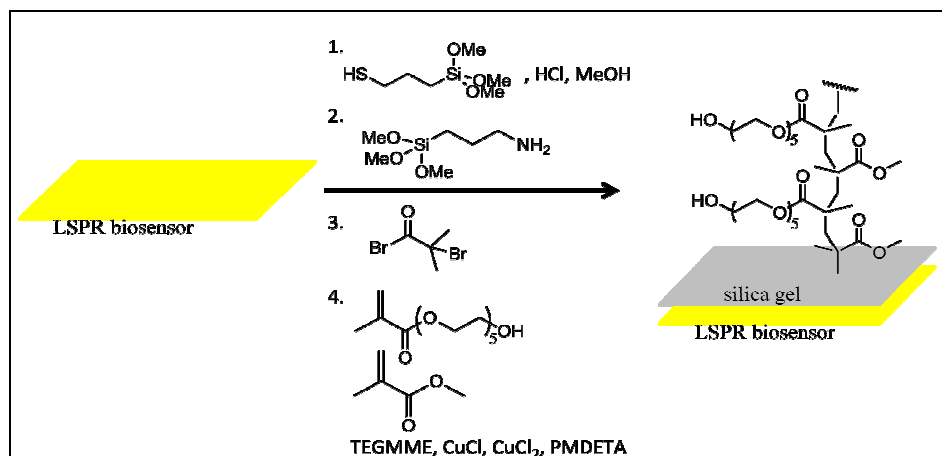


Figure 6-5. Synthesis route for a PEGMA/MMA coating on the LSPR biosensor via ATRP: (1) sol-gel coating, (2) surface immobilization of the first ATRP initiator, (3) surface immobilization of the second ATRP initiator, (4) polymerization of OEGMA and MMA monomers.

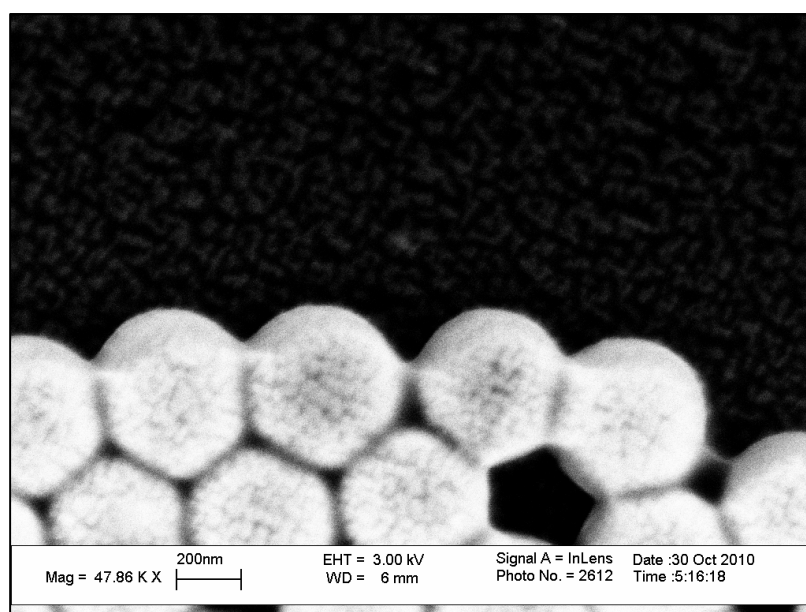


Figure 6-6. SEM image of a LSPR biosensor coated with a graft copolymer film with 10 % PEGMA.

Graft copolymer films with 10 % PEGMA and a thickness of 50-60 nm were successfully synthesized by setting the polymerization time between 9.5 and 10.5 hours (Fig. 6-7, left). This thickness regime is required to ensure a high-loading of amino functional groups, which serve as the starting point for the subsequent peptide array synthesis. At the same time, this film thickness regime does not exceed the surface sensitivity regime of the LSPR biosensor. Furthermore, the LSPR wavelength shifts due to the adsorption of the copolymer films with 10 % PEGMA of different thickness were experimentally determined. As expected, a linear relationship between LSPR response and film thickness was observed for the thickness regime below 100 nm (Fig. 6-7, right).

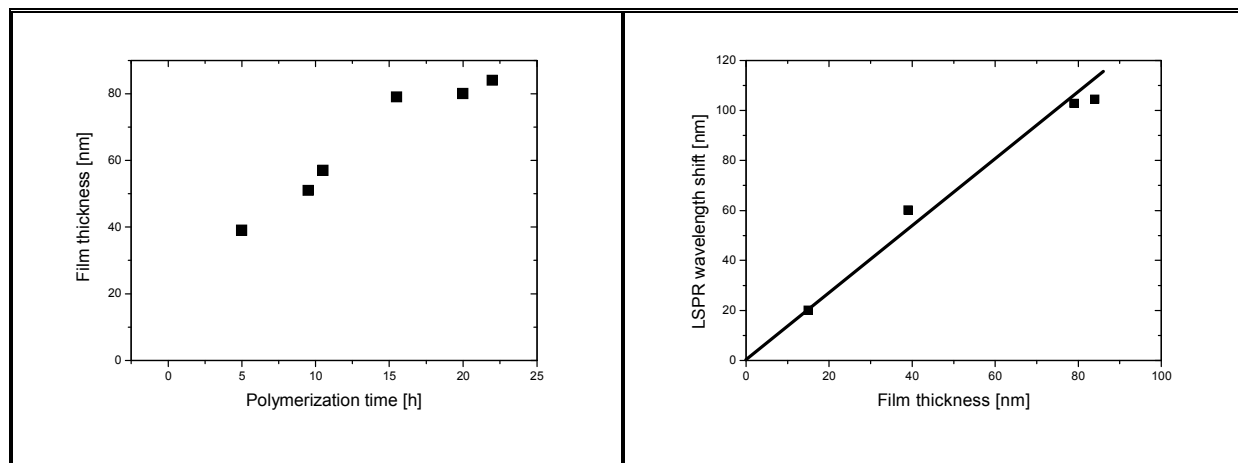


Figure 6-7. (left) Film thickness versus polymerization time for PEGMA/MMA (10:90) copolymer film. (right) LSPR responses to different layer thickness of PEGMA/MMA 10:90 graft polymer films

The stability of the polymer-coated LSPR biosensor was tested in various chemical reactions, which are inevitable in the synthesis of peptide arrays via laser printing technology. XPS and SEM analysis showed that the protein resistant layer on the LSPR biosensor is stable under these harsh chemical conditions. This requirement represents one of the challenges in the application of the LSPR biosensor as a solid support in the peptide array synthesis via the laser printing technique.

In order to generate surface-immobilized amino groups on the LSPR biosensor, β -alanine was coupled to the hydroxyl end groups of the protein resistant layer. The three-dimensional layer geometry of the PEGMA-based polymer coatings ensure a high loading of the amino functional groups, which act as anchors for peptide immobilization.

6.3. Label-free detection of biomolecular interactions on the polymer coated LSPR biosensors

Label-free detection offers the advantages of reducing the time and cost demands of the preparation, because all steps associated with applying and processing the label are avoided. Furthermore, in contrast to label-based methods, label-free analysis facilitates the detection of low-affinity binding events. Local refractive index changes such as those induced by biomolecular interactions at the sensor surface can be monitored via the LSPR peak shift in a highly sensitive manner. This LSPR peak shift is proportional to the change in mass on the surface. Thus, LSPR biosensors are valuable tools for both *in situ* detection of binding kinetics and the quantification of the surface-bound molecules.

The polymer coated LSPR biosensor developed in this work was used as a detection tool in label-free analysis of biomolecular interactions in array format. In a proof-of-principle experiment, an array of fluorescent-labeled antibodies was formed on the sensor surface by a spotting robot and subsequently detected by means of a fluorescent scanner and the LSPR imaging technique. A LSPR image with a lateral resolution of 110 μm in the wavelength regime of the quadrupole resonance peak was generated, displaying an array of spots which corresponds to the fluorescence image (Fig. 6-8). This indicates a successful detection of molecular binding on the sensor surface by observing a shift in the LSPR resonance maxima. Moreover, the quantity of antibody bound to the sensor surface was correctly predicted as 296 ng/cm^2 using the measured wavelength shifts of 8 nm in the quadrupole regime and a mass sensitivity factor of 0.027 $\text{nm}/(\text{ng}/\text{cm}^2)$.¹¹¹ This result shows that the LSPR biosensor

described in this thesis has the potential to allow the detection of molecular interactions in a miniaturized array format in a quantitative manner.

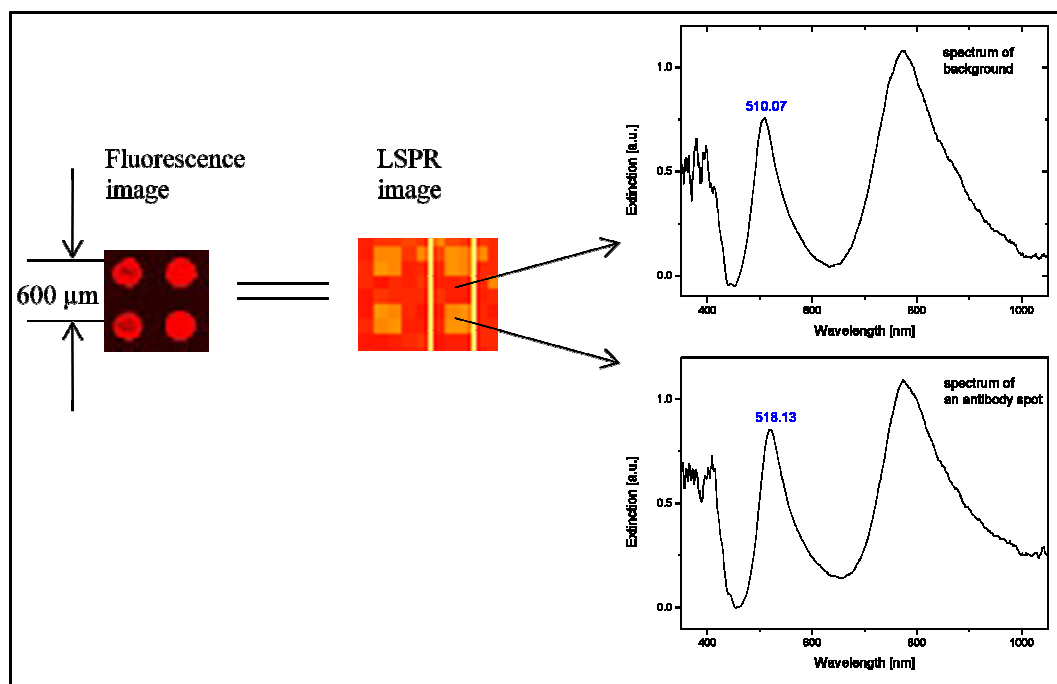


Figure 6-8. Fluorescence- and LSPR image of antibody spots on the LSPR biosensor. A wavelength shift in the quadrupole resonance peak of ~ 8 nm was induced by the antibody adsorption as shown in the UV-Vis spectra. By using the wavelength shift and a mass sensitivity factor of $0.027 \text{ nm}/(\text{ng}/\text{cm}^2)$, the amount of surface-bound antibody was correctly predicted as $296 \text{ ng}/\text{cm}^2$.

In the final part of this thesis, the polymer-coated LSPR biosensor was successfully applied as the solid substrate in the synthesis of a peptide array via the laser printing technique, and then utilized for detecting biomolecular interactions occurring on the peptide array. An array with 9×20 variants of the hemagglutinin/HA epitope (YPYDVPDYA) was synthesized on a polymer-coated LSPR biosensor and incubated with an IR-dye conjugated specific antibody. The binding events occurring on the sensor were then detected by means of an IR-scanner and the LSPR imaging technique.

The LSPR image with a lateral resolution of $70 \mu\text{m}$ in the wavelength regime of the octapole resonance peak was successfully generated, displaying the entire spots of the HA epitope variants formed on the sensor surface (Fig. 6-9). The evaluation of the molecular binding on the LSPR biosensor was achieved by monitoring the wavelength shift of the octapole resonance (Fig. 6-10). It should be noted, that the octapole resonance possesses the lowest sensitivity among the three resonance peaks. However, due to the large FWHMs of the quadrupole and dipole resonances as observed after the laser printing process, these two peaks in this particular sample could not be used to generate LSPR images.

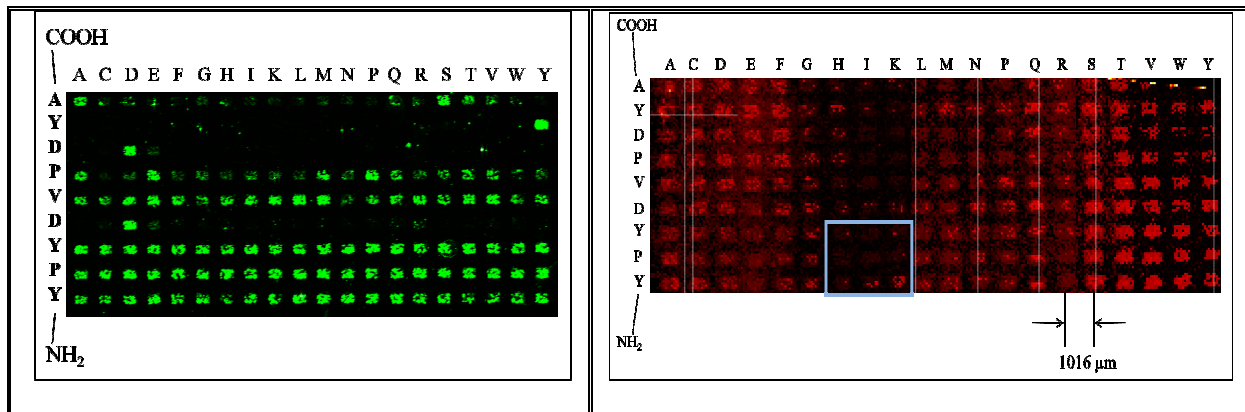


Figure 6-9. IR scanner (left) and LSPR (right) image of a peptide array consisting of 9x20 HA variants on the polymer-coated LSPR biosensor. The entire array was incubated with specific antibody (800 CW conjugated mouse anti-HA)

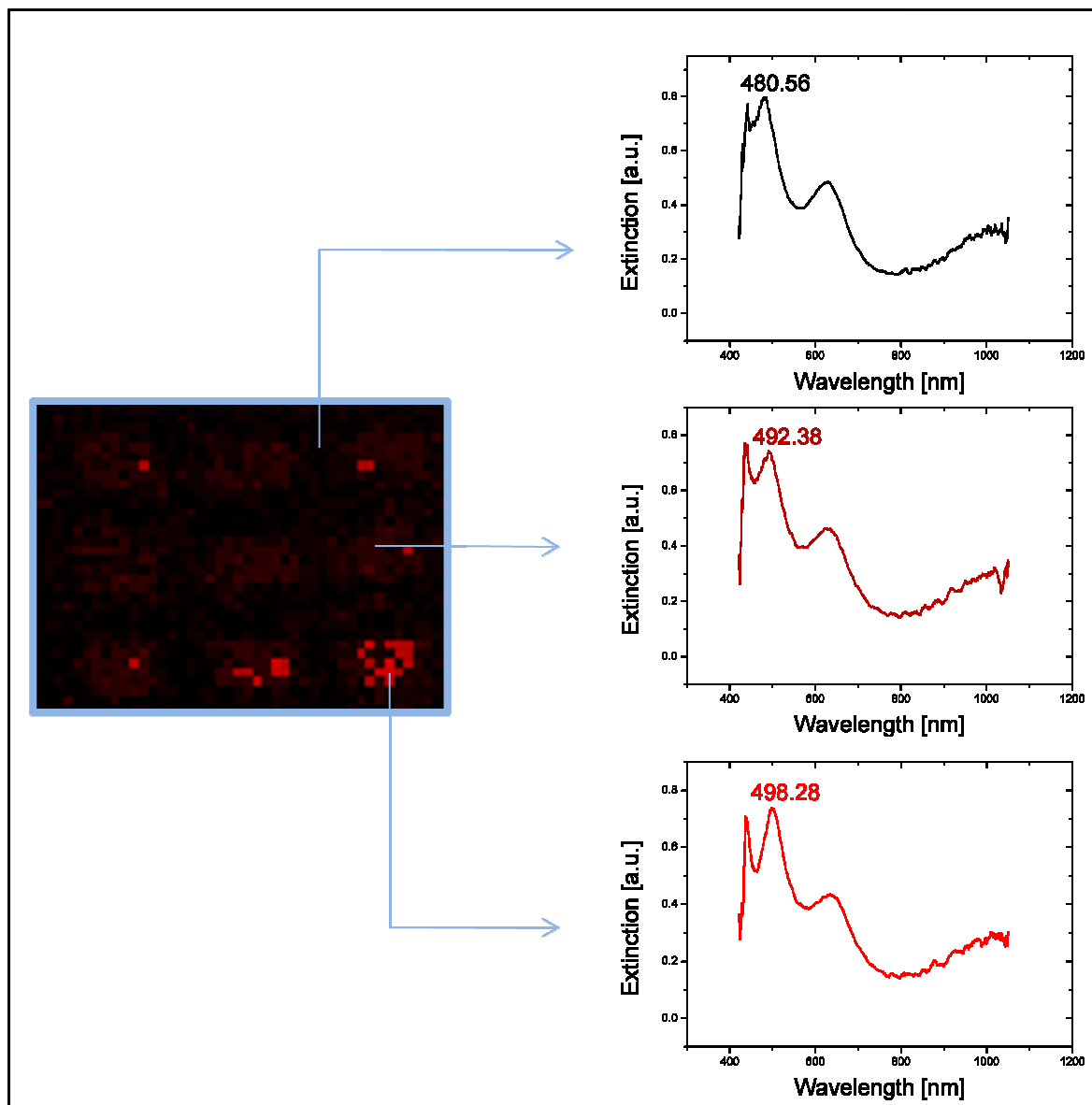


Figure 6-10. UV-Vis extinction spectra of three positions in the array, with different position of the octapole resonance maxima indicating three different amounts of adsorbed molecules. (a) The LSPR spectrum displayed in black shows the lowest LSPR peak position (480.56 nm), indicating the unspotted area of the sample. (b) The LSPR spectrum displayed in brown shows the middle LSPR peak position (492.38 nm), indicating the peptide spots in the sample. (c) The LSPR spectrum displayed in red shows the highest LSPR peak position (498.28 nm), indicating the peptide spots in the sample with a higher adsorbed mass than the LSPR spectrum in brown, probably due to binding of specific antibodies.

A significant difference in the results from label-based and label-free detection is displayed with regard to the HA epitope variants recognized and specifically bound by the anti-HA antibodies (Fig. 6-9). One plausible cause for this discrepancy is a mass density of antibodies coupled to the surface-bound peptide which is below the detection limit of the LSPR biosensor (37 ng/cm^2). Another possible cause for the wavelength shifts in the resonance peak would be the surface-bound silica particle residues, which were not removed through sonification.

In summary, the protein-resisting polymer coated LSPR biosensor described and optimized in this thesis was successfully applied as the solid substrate in the peptide array synthesis via particle-based and printing technique. The sensor was stable against the harsh chemical and mechanical conditions of the peptide printing and preserved its optical properties. The UV-Vis spectra of the sensor surface revealed three resonance peaks, which can be assigned to as the octapole, quadrupole, and dipole peaks. A LSPR image was generated by using the wavelength shift of the octapole resonance, displaying the entire peptide spots on the sensor surface. Several important parameters still have to be optimized in order to routinely use the LSPR biosensor in label-free and quantitative detection of antibody-antigen interactions that is compatible with high-density peptide array fabricated by the laser printing method. The read-out of the wavelength maxima of the dipole and quadrupole resonance peaks must be facilitated by automatically fitting the peaks into a Pseudo-Voigt function. The amount of surface-bound peptide -synthesized by the laser printing method- should be kept relatively constant for all peptide spots to avoid false positive results. The sensitivity of the LSPR biosensor must be enhanced, for example by using silver instead of gold as the metal layer in the sensor. Copolymer film with a lower fraction of PEGMA should be synthesized as the sensor coating to reduce the protein resistance and increase the antibody access to the surface-bound peptide. Transferring the peptide arrays from a prequel substrate onto the sensor surface under mild conditions is another option in combining the LSPR biosensor and the peptide printing technique in order to reduce the harsh chemical and mechanical conditions experienced by the biosensor upon peptide array generation.

In the future, the LSPR biosensor optimized in this thesis will allow a high-throughput screening of disease-specific markers by the label-free detection of antibody-antigen binding occurring on surface-bound peptide arrays. This will enable the identification of diseases in their early, treatable stages.

6.4. Optical biosensors based on Whispering Gallery Modes (WGM)

Whispering gallery modes of fluorescence-doped sulfonated polystyrene particles with a diameter of $2 \mu\text{m}$ were studied with respect to their resonance shift after adsorption of polyelectrolyte multilayers. Oppositely charged poly(allylamine hydrochloride) (PAH) and poly(sodium 4-styrenesulfonate) (PSS) were deposited alternately onto PS particles (diameter = $2 \mu\text{m}$) from salt-free and 0.5 M NaCl aqueous solutions. Both experimental series display the same behavior when their resonance shifts are plotted as a function of the film thickness. A slope of $0.038 \text{ nm}/\text{\AA}$ was obtained from a linear fit to the experimental data.

The sensitivity factor of $0.038 \text{ nm}/\text{\AA}$ can be translated into a detection limit of 3 fg by assuming a spectral resolution of 0.1 nm and a polyelectrolyte mass density¹⁷ of 0.81 g/cm^3 . With a mass sensitivity of 3 fg , this WGM based sensor is highly competitive in the field of label-free detection techniques.

Bibliography

- 1 Willets, K. A. & Van Duyne, R. P. Localized surface plasmon resonance spectroscopy and sensing. *Annu Rev Phys Chem* **58**, 267-297, doi:DOI 10.1146/annurev.physchem.58.032806.104607 (2007).
- 2 Stadler, V. *et al.* Combinatorial synthesis of peptide arrays with a laser printer. *Angewandte Chemie, International Edition* **47**, 7132-7135, doi:DOI 10.1002/anie.200801616 (2008).
- 3 Himmelhaus, M. & Takei, H. Cap-shaped gold nanoparticles for an optical biosensor. *Sensor Actuat B-Chem* **63**, 24-30 (2000).
- 4 Takei, H., Himmelhaus, M. & Okamoto, T. Absorption spectrum of surface-bound cap-shaped gold particles. *Opt Lett* **27**, 342-344 (2002).
- 5 Knoll, W. Interfaces and thin films as seen by bound electromagnetic waves. *Annu Rev Phys Chem* **49**, 569-638 (1998).
- 6 Ocean Optics, I. <<http://www.oceanoptics.com/technical/hr4000.pdf>> (
- 7 <http://en.wikipedia.org/wiki/File:Microarray2.gif>.
- 8 Stanley L. Flegler, J. W. H., Jr, Karen L. Klomparens. *Scanning and Transmission Electron Microscopy -An Introduction-*. (W. H. Freeman and Company, 1993).
- 9 Albert, G. *Herstellung und Charakterisierung polykristalliner Goldschichten zur Verwendung in der Nanolithographie* Diplom Physiker thesis, University of Heidelberg.
- 10 Jung, L. S., Campbell, C. T., Chinowsky, T. M., Mar, M. N. & Yee, S. S. Quantitative Interpretation of the Response of Surface Plasmon Resonance Sensors to Adsorbed Films. *Langmuir* **14**, 5636-5648 (1998).
- 11 Jeon, S. I., Lee, J. H., Andrade, J. D. & De Gennes, P. G. Protein-Surface Interactions in the Presence of Polyethylene Oxide. *J Colloid Interf Sci* **142**, 149-158 (1991).
- 12 Kamigaito, M., Ando, T. & Sawamoto, M. Metal-catalyzed living radical polymerization. *Chem Rev* **101**, 3689-3745, doi:Doi 10.1021/Cr9901182 (2001).
- 13 Ionov, L., Synytska, A., Kaul, E. & Diez, S. Protein-Resistant Polymer Coatings Based on Surface-Adsorbed Poly(aminoethyl methacrylate)/Poly(ethylene glycol) Copolymers. *Biomacromolecules* **11**, 233-237, doi:Doi 10.1021/Bm901082y (2010).
- 14 Weller, A., Liu, F. C., Dahint, R. & Himmelhaus, M. Whispering gallery mode biosensors in the low-Q limit. *Appl Phys B-Lasers O* **90**, 561-567, doi:DOI 10.1007/s00340-007-2893-2 (2008).
- 15 Kidambi, S., Chan, C. & Lee, I. S. Selective depositions on polyelectrolyte multilayers: Self-assembled monolayers of m-dPEG acid as molecular template. *J Am Chem Soc* **126**, 4697-4703, doi:Doi 10.1021/Ja039359o (2004).

- 16 Breitling, F., Nesterov, A., Stadler, V., Felgenhauer, T. & Bischoff, F. R. High-density peptide arrays. *Mol Biosyst* **5**, 224-234, doi:Doi 10.1039/B819850k (2009).
- 17 Losche, M., Schmitt, J., Decher, G., Bouwman, W. G. & Kjaer, K. Detailed structure of molecularly thin polyelectrolyte multilayer films on solid substrates as revealed by neutron reflectometry. *Macromolecules* **31**, 8893-8906 (1998).
- 18 Service, R. F. Protein chips - Searching for recipes for protein chips. *Science* **294**, 2080-2082 (2001).
- 19 Min, D. H. & Mrksich, M. Peptide arrays: towards routine implementation. *Curr Opin Chem Biol* **8**, 554-558, doi:DOI 10.1016/j.cbpa.2004.08.007 (2004).
- 20 Cooper, M. A. Label-free screening of bio-molecular interactions. *Anal Bioanal Chem* **377**, 834-842, doi:DOI 10.1007/s00216-003-2111-y (2003).
- 21 Huang, N. P. *et al.* Poly(L-lysine)-g-poly(ethylene glycol) layers on metal oxide surfaces: Surface-analytical characterization and resistance to serum and fibrinogen adsorption. *Langmuir* **17**, 489-498 (2001).
- 22 Arnold, S., Khoshsima, M., Teraoka, I., Holler, S. & Vollmer, F. Shift of whispering-gallery modes in microspheres by protein adsorption. *Opt Lett* **28**, 272-274 (2003).
- 23 Vollmer, F. & Arnold, S. Whispering-gallery-mode biosensing: label-free detection down to single molecules. *Nat Methods* **5**, 591-596, doi:Doi 10.1038/Nmeth.1221 (2008).
- 24 Service, R. F. Proteomics ponders prime time. *Science* **321**, 1758-1761 (2008).
- 25 Fodor, S. P. A. *et al.* Light-Directed, Spatially Addressable Parallel Chemical Synthesis. *Science* **251**, 767-773 (1991).
- 26 Lipshutz, R. J., Fodor, S. P. A., Gingeras, T. R. & Lockhart, D. J. High density synthetic oligonucleotide arrays. *Nat Genet* **21**, 20-24 (1999).
- 27 Frank, R. Spot-Synthesis - an Easy Technique for the Positionally Addressable, Parallel Chemical Synthesis on a Membrane Support. *Tetrahedron* **48**, 9217-9232 (1992).
- 28 Frank, R. The SPOT synthesis technique - Synthetic peptide arrays on membrane supports - principles and applications. *J Immunol Methods* **267**, 13-26, doi:Pii S0022-1759(02)00137-0 (2002).
- 29 Hilpert, K., Winkler, D. F. H. & Hancock, R. E. W. Peptide arrays on cellulose support: SPOT synthesis, a time and cost efficient method for synthesis of large numbers of peptides in a parallel and addressable fashion. *Nat Protoc* **2**, 1333-1349, doi:DOI 10.1038/nprot.2007.160 (2007).
- 30 Beyer, M. *et al.* Combinatorial synthesis of peptide arrays onto a microchip. *Science* **318**, 1888-1888, doi:DOI 10.1126/science.1149751 (2007).
- 31 Cooper, M. A. Optical biosensors in drug discovery. *Nat Rev Drug Discov* **1**, 515-528, doi:Doi 10.1038/Nrd838 (2002).

-
- 32 Cooper, M. A. Optical biosensors: where next and how soon? *Drug Discov Today* **11**, 1061-1067, doi:DOI 10.1016/j.drudis.2006.10.003 (2006).
- 33 Rao, C. N. R. *Nanomaterials Chemistry*. doi:10.1002/9783527611362 (2007).
- 34 Homola, J. in *Springer Series on Chemical Sensors and Biosensors* Vol. 4 (ed O. S. Wolfbeis) (Springer, Berlin, Heidelberg, New York, 2006).
- 35 Smith, E. A. & Corn, R. M. Surface plasmon resonance imaging as a tool to monitor biomolecular interactions in an array based format. *Appl Spectrosc* **57**, 320a-332a (2003).
- 36 Hutter, E. & Fendler, J. H. Exploitation of localized surface plasmon resonance. *Adv Mater* **16**, 1685-1706, doi:DOI 10.1002/adma.200400271 (2004).
- 37 Brockman, J. M., Nelson, B. P. & Corn, R. M. Surface plasmon resonance imaging measurements of ultrathin organic films. *Annu Rev Phys Chem* **51**, 41-63 (2000).
- 38 Steiner, G. Surface plasmon resonance imaging. *Anal Bioanal Chem* **379**, 328-331, doi:DOI 10.1007/s00216-004-2636-8 (2004).
- 39 Lee, H. J., Wark, A. W. & Corn, R. M. Microarray methods for protein biomarker detection. *Analyst* **133**, 975-983, doi:Doi 10.1039/B717527b (2008).
- 40 Lee, H. J., Nedelkov, D. & Corn, R. M. Surface plasmon resonance imaging measurements of antibody arrays for the multiplexed detection of low molecular weight protein biomarkers. *Anal Chem* **78**, 6504-6510, doi:Doi 10.1021/Ac060881d (2006).
- 41 Haes, A. J., Chang, L., Klein, W. L. & Van Duyne, R. P. Detection of a biomarker for Alzheimer's disease from synthetic and clinical samples using a nanoscale optical biosensor. *J Am Chem Soc* **127**, 2264-2271 (2005).
- 42 Harris, J. M. (Plenum Press, New York, 1992).
- 43 Heuberger, M., Drobek, T. & Spencer, N. D. Interaction forces and morphology of a protein-resistant poly(ethylene glycol) layer. *Biophys J* **88**, 495-504, doi:DOI 10.1529/biophysj.104.045443 (2005).
- 44 Patel, S., Tirrell, M. & Hadziioannou, G. A Simple-Model for Forces between Surfaces Bearing Grafted Polymers Applied to Data on Adsorbed Block Copolymers. *Colloid Surface* **31**, 157-179 (1988).
- 45 Carignano, M. A. & Szleifer, I. On the Structure and Pressure of Tethered Polymer Layers in Good Solvent. *Macromolecules* **28**, 3197-3204 (1995).
- 46 Szleifer, I. Statistical thermodynamics of polymers near surfaces. *Curr Opin Colloid In* **1**, 416-423 (1996).
- 47 Szleifer, I. Protein adsorption on surfaces with grafted polymers: A theoretical approach. *Biophys J* **72**, 595-612 (1997).

-
- 48 Szleifer, I. Protein adsorption on tethered polymer layers: effect of polymer chain architecture and composition. *Physica A* **244**, 370-388 (1997).
- 49 Barbey, R. *et al.* Polymer Brushes via Surface-Initiated Controlled Radical Polymerization: Synthesis, Characterization, Properties, and Applications. *Chem Rev* **109**, 5437-5527, doi:Doi 10.1021/Cr900045a (2009).
- 50 Prime, K. L. & Whitesides, G. M. Adsorption of Proteins onto Surfaces Containing End-Attached Oligo(ethylene oxide): A Model System Using Self-Assembled Monolayers. *J Am Chem Soc* **115**, 10714-10721 (1993).
- 51 Bain, C. D. *et al.* Formation of Monolayer Films by the Spontaneous Assembly of Organic Thiols from Solution onto Gold. *J Am Chem Soc* **111**, 321-335 (1989).
- 52 Gombotz, W. R., Guanghui, W., Horbett, T. A. & Hoffman, A. S. Protein Adsorption to Poly(Ethylene Oxide) Surfaces. *J Biomed Mater Res* **25**, 1547-1562 (1991).
- 53 Jiang, X. P. & Hammond, P. T. Selective deposition in layer-by-layer assembly: Functional graft copolymers as molecular templates. *Langmuir* **16**, 8501-8509, doi:Doi 10.1021/La0004146 (2000).
- 54 Chen, K. M., Jiang, X. P., Kimerling, L. C. & Hammond, P. T. Selective self-organization of colloids on patterned polyelectrolyte templates. *Langmuir* **16**, 7825-7834, doi:Doi 10.1021/La000277c (2000).
- 55 Kumar, A., Biebuyck, H. A. & Whitesides, G. M. Patterning Self-Assembled Monolayers: Applications in Materials Science. *Langmuir* **10**, 1498-1511 (1994).
- 56 Kumar, A. & Whitesides, G. M. Patterned Condensation Figures as Optical Diffraction Gratings. *Science* **263**, 60-62 (1994).
- 57 Wilbur, J. L., Kumar, A., Kim, E. & Whitesides, G. M. Microfabrication by Microcontact Printing of Self-Assembled Monolayers. *Adv Mater* **6**, 600-604 (1994).
- 58 Herrwerth, S. *et al.* Covalent coupling of antibodies to self-assembled monolayers of carboxy-functionalized poly(ethylene glycol): Protein resistance and specific binding of biomolecules. *Langmuir* **19**, 1880-1887, doi:Doi 10.1021/La026327q (2003).
- 59 Matyjaszewski, K. & Xia, J. H. Atom transfer radical polymerization. *Chem Rev* **101**, 2921-2990, doi:Doi 10.1021/Cr940534g (2001).
- 60 Lee, B. S., Chi, Y. S., Lee, K. B., Kim, Y. G. & Choi, I. S. Functionalization of poly(oligo(ethylene glycol)methacrylate) films on gold and Si/SiO₂ for immobilization of proteins and cells: SPR and QCM studies. *Biomacromolecules* **8**, 3922-3929, doi:Doi 10.1021/Bm7009043 (2007).
- 61 Ma, H. W., Wells, M., Beebe, T. P. & Chilkoti, A. Surface-initiated atom transfer radical polymerization of oligo(ethylene glycol) methyl methacrylate from a mixed self-assembled monolayer on gold. *Adv Funct Mater* **16**, 640-648, doi:DOI 10.1002/adfm.200500426 (2006).
- 62 Stadler, V. *et al.* Multifunctional CMOS microchip coatings for protein and peptide Arrays. *J Proteome Res* **6**, 3197-3202, doi:Doi 10.1021/Pr0701310 (2007).

-
- 63 Stadler, V. *et al.* PEGMA/MMA copolymer graftings: Generation, protein resistance, and a hydrophobic domain. *Langmuir* **24**, 8151-8157, doi:Doi 10.1021/La800772m (2008).
- 64 Chen, S. F., Zheng, J., Li, L. Y. & Jiang, S. Y. Strong resistance of phosphorylcholine self-assembled monolayers to protein adsorption: Insights into nonfouling properties of zwitterionic materials. *J Am Chem Soc* **127**, 14473-14478, doi:Doi 10.1021/Ja054169u (2005).
- 65 Chang, Y., Chen, S. F., Zhang, Z. & Jiang, S. Y. Highly protein-resistant coatings from well-defined diblock copolymers containing sulfobetaines. *Langmuir* **22**, 2222-2226, doi:Doi 10.1021/La052692v (2006).
- 66 Chang, Y. *et al.* Hemocompatible Mixed-Charge Copolymer Brushes of Pseudozwitterionic Surfaces Resistant to Nonspecific Plasma Protein Fouling. *Langmuir* **26**, 3522-3530, doi:Doi 10.1021/La903172j (2010).
- 67 Svanberg, S. *Atomic and Molecular Spectroscopy -Basic Aspects and Practical Applications-*. Third edn, (Springer, 2001).
- 68 Hunsperger, R. G. *Integrated Optics -Theory and Technology-*. Sixth edn, (Springer, 2009).
- 69 Fitzpatrick, L. E. in *Encyclopedia of Materials Characterization* (ed Charles A. Evans C. Richard Brundle, Jr.) (Manning Publications Co., Greenwich, 1992).
- 70 M. Henzler, W. G. *Oberflächenphysik des Festkörpers*. (Teubner 1991).
- 71 Smith, G. C. *Surface Analysis by Electron Spectroscopy: Measurement and Interpretation.*, (Plenum Press, 1994).
- 72 John C. Vickerman, R. W., Buddy Ratner, David Castner, and Hans & Joerg. (John Wiley & Sons, 1997).
- 73 K. Oura, V. G. L., A. A. Saranin, A. V. Zotov, M. Katayama. *Surface Science -an Introduction-*. (Springer, 2003).
- 74 Ahn, J. S., Hammond, P. T., Rubner, M. F. & Lee, I. Self-assembled particle monolayers on polyelectrolyte multilayers: particle size effects on formation, structure, and optical properties. *Colloid Surface A* **259**, 45-53, doi:DOI 10.1016/j.colsurfa.2005.02.008 (2005).
- 75 Stamm, M. *Polymer Surfaces and Interfaces*. (Springer, 2008).
- 76 Li, L. P. *et al.* Fabrication of hemispherical cavity arrays on silicon substrates using laser-assisted nanoimprinting of self-assembled particles. *Nanotechnology* **15**, 333-336, doi:Pii S0927-4484(04)69820-5 (2004).
- 77 Waly, N. Ph.D. thesis, University of Heidelberg, (ongoing).
- 78 Grabar, K. C. *et al.* Two-dimensional arrays of colloidal gold particles: A flexible approach to macroscopic metal surfaces. *Langmuir* **12**, 2353-2361 (1996).

- 79 Stadler, V. *et al.* Combinatorial synthesis of peptide arrays with a laser printer. *Angew Chem Int Edit* **47**, 7132-7135, doi:DOI 10.1002/anie.200801616 (2008).
- 80 Christopher Schirwitz, I. B., Kai König, Alexander Nesterov,, Simon Fernandez, T. F., Klaus Leibe, Gloria Torralba,, Michael Hausmann, V. L., Volker Stadler, & Frank Breitling, a. F. R. B. Combinatorial peptide synthesis on a microchip. *Current Protocols in Protein Science* **57**, 18.12.11-18.12.13 (2009).
- 81 *Balanced Deuterium Tungsten Halogen Source*, <http://www.mikropack.de/d/spectro/pdf_downloads/light_sources.pdf> (
- 82 *Silica/Silica Optical Fiber*, <http://www.polymicro.com/productpdfs/FV_12-04.pdf> (
- 83 Zimmer, M. *Aufbau und Evaluierung eines orts aufgelösten UV-Vis-Spectrometers* Diplom thesis, University of Heidelberg, (2005).
- 84 Himmelhaus, M. & Takei, H. Self-assembly of polystyrene nano particles into patterns of random-close-packed monolayers via chemically induced adsorption. *Phys Chem Chem Phys* **4**, 496-506 (2002).
- 85 Dahint, R. *et al.* Optically responsive nanoparticle layers for the label-free analysis of biospecific interactions in array formats. *Biosens Bioelectron* **22**, 3174-3181, doi:DOI 10.1016/j.bios.2007.02.012 (2007).
- 86 Kaltenpoth, G., Himmelhaus, M., Slansky, L., Caruso, F. & Grunze, M. Conductive core-shell particles: An approach to self-assembled mesoscopic wires. *Adv Mater* **15**, 1113-+, doi:DOI 10.1002/adma.200304834 (2003).
- 87 Brown, K. R. & Natan, M. J. Hydroxylamine seeding of colloidal Au nanoparticles in solution and on surfaces. *Langmuir* **14**, 726-728 (1998).
- 88 Ji, T. H., Lirtsman, V. G., Avny, Y. & Davidov, D. Preparation, characterization, and application of Au-shell/polystyrene beads and Au-shell/magnetic beads. *Adv Mater* **13**, 1253-1256 (2001).
- 89 McLellan, J. M., Geissler, M. & Xia, Y. N. Edge spreading lithography and its application to the fabrication of mesoscopic gold and silver rings. *J Am Chem Soc* **126**, 10830-10831, doi:Doi 10.1021/Ja0470766 (2004).
- 90 Glazer, M., Fidanza, J., McGall, G. & Frank, C. Colloidal silica films for high-capacity DNA probe arrays. *Chem Mater* **13**, 4773-4782, doi:Doi 10.1021/Cm010578n (2001).
- 91 Liu, F. K., Chang, Y. C., Ko, F. H., Chu, T. C. & Dai, B. T. Rapid fabrication of high quality self-assembled nanometer gold particles by spin coating method. *Microelectron Eng* **67-8**, 702-709, doi:Doi 10.1016/S0167-9317(03)00175-8 (2003).
- 92 Davies, J. T. *Interfacial Phenomena*. Second edn, (Academic Press, 1963).
- 93 Denkov, N. D. *et al.* Mechanism of Formation of 2-Dimensional Crystals from Latex-Particles on Substrates. *Langmuir* **8**, 3183-3190 (1992).

-
- 94 Retsch, M. *et al.* Fabrication of Large-Area, Transferable Colloidal Monolayers Utilizing Self-Assembly at the Air/Water Interface. *Macromol Chem Phys* **210**, 230-241, doi:DOI 10.1002/macp.200800484 (2009).
- 95 Retsch, M. *et al.* Parallel Preparation of Densely Packed Arrays of 150-nm Gold-Nanocrescent Resonators in Three Dimensions. *Small* **5**, 2105-2110, doi:DOI 10.1002/smll.200900162 (2009).
- 96 Wu, D. J., Xu, X. D. & Liu, X. J. Influence of dielectric core, embedding medium and size on the optical properties of gold nanoshells. *Solid State Commun* **146**, 7-11, doi:DOI 10.1016/j.ssc.2008.01.038 (2008).
- 97 Westcott, S. L., Jackson, J. B., Radloff, C. & Halas, N. J. Relative contributions to the plasmon line shape of metal nanoshells. *Phys Rev B* **66**, -, doi:Artn 155431 DOI 10.1103/Physrevb.66.155431 (2002).
- 98 Pena, O., Pal, U., Rodriguez-Fernandez, L. & Crespo-Sosa, A. Linear optical response of metallic nanoshells in different dielectric media. *J Opt Soc Am B* **25**, 1371-1379 (2008).
- 99 Kelly, K. L., Coronado, E., Zhao, L. L. & Schatz, G. C. The optical properties of metal nanoparticles: The influence of size, shape, and dielectric environment. *J Phys Chem B* **107**, 668-677, doi:Doi 10.1021/Jp026731y (2003).
- 100 Zhou, F., Li, Z. Y., Liu, Y. & Xia, Y. N. Quantitative Analysis of Dipole and Quadrupole Excitation in the Surface Plasmon Resonance of Metal Nanoparticles. *J Phys Chem C* **112**, 20233-20240, doi:Doi 10.1021/Jp807075f (2008).
- 101 Johnson, P. B. & Christy, R. W. Optical Constants of the Noble Metals. *Phys. Rev. B* **6**, 4370-4379 (1972).
- 102 Rampi, M. A., Schueller, O. J. A. & Whitesides, G. M. Alkanethiol self-assembled monolayers as the dielectric of capacitors with nanoscale thickness. *Appl Phys Lett* **72**, 1781-1783 (1998).
- 103 Hao, E., Schatz, G. C. & Hupp, J. T. Synthesis and optical properties of anisotropic metal nanoparticles. *J Fluoresc* **14**, 331-341 (2004).
- 104 Hench, L. L. & West, J. K. The Sol-Gel Process. *Chem Rev* **90**, 33-72 (1990).
- 105 Wang, J., Pamidi, P. V. A. & Zanette, D. R. Self-assembled silica gel networks. *J Am Chem Soc* **120**, 5852-5853 (1998).
- 106 Cumpson, P. J. Estimation of inelastic mean free paths for polymers and other organic materials: use of quantitative structure-property relationships. *Surf Interface Anal* **31**, 23-34 (2001).
- 107 Castner, D. G., Hinds, K. & Grainger, D. W. X-ray photoelectron spectroscopy sulfur 2p study of organic thiol and disulfide binding interactions with gold surfaces. *Langmuir* **12**, 5083-5086 (1996).
- 108 Tsao, M. W. *et al.* Formation and characterization of self-assembled films of thiol-derivatized poly(dimethylsiloxane) on gold. *Macromolecules* **30**, 5913-5919 (1997).

-
- 109 Singh, J. & Whitten, J. E. Adsorption of 3-Mercaptopropyltrimethoxysilane on Silicon Oxide Surfaces and Adsorbate Interaction with Thermally Deposited Gold. *J Phys Chem C* **112**, 19088-19096, doi:Doi 10.1021/Jp807536z (2008).
- 110 Kimani, S. M. & Moratti, S. C. Synthesis of five-arm star polymers with an inositol core by atom transfer radical polymerisation at ambient temperature. *Macromol Rapid Comm* **27**, 1887-1893, doi:DOI 10.1002/marc.200600476 (2006).
- 111 Buecker, P., Trileva, E., Himmelhaus, M. & Dahint, R. Label-free biosensors based on optically responsive nanocomposite layers: Sensitivity and dynamic range. *Langmuir* **24**, 8229-8239, doi:Doi 10.1021/La8003883 (2008).
- 112 Endo, T. *et al.* Multiple label-free detection of antigen-antibody reaction using localized surface plasmon resonance-based core-shell structured nanoparticle layer nanochip. *Anal Chem* **78**, 6465-6475, doi:Doi 10.1021/Ac0608321 (2006).
- 113 Endo, T., Kerman, K., Nagatani, N., Takamura, Y. & Tamiya, E. Label-free detection of peptide nucleic acid-DNA hybridization using localized surface plasmon resonance based optical biosensor. *Anal Chem* **77**, 6976-6984, doi:Doi 10.1021/Ac0513459 (2005).
- 114 Endo, T., Kerman, K., Nagatani, N. & Tamiya, E. Excitation of localized surface plasmon resonance using a core-shell structured nanoparticle layer substrate and its application for label-free detection of biomolecular interactions. *J Phys-Condens Mat* **19**, -, doi:Artn 215201 DOI 10.1088/0953-8984/19/21/215201 (2007).
- 115 Endo, T., Takizawa, H., Yanagida, Y., Hatsuzawa, T. & Tamiya, E. Construction of a Biosensor Operating on the Combined Principles of Electrochemical Analysis and Localized Surface Plasmon Resonance for Multiple Detection of Antigen-Antibody and Enzymatic Reactions on the Single Biosensor. *Sensor Mater* **20**, 255-265 (2008).
- 116 Endo, T. *et al.* Localized surface plasmon resonance based optical biosensor using surface modified nanoparticle layer for label-free monitoring of antigen-antibody reaction. *Sci Technol Adv Mat* **6**, 491-500, doi:DOI 10.1016/j.stam.2005.03.019 (2005).
- 117 Hiep, H. M., Kerman, K., Endo, T., Saito, M. & Tamiya, E. Nanostructured biochip for label-free and real-time optical detection of polymerase chain reaction. *Anal Chim Acta* **661**, 111-116, doi:DOI 10.1016/j.aca.2009.12.006 (2010).
- 118 Stewart, M. E. *et al.* Nanostructured plasmonic sensors. *Chem Rev* **108**, 494-521, doi:Doi 10.1021/Cr068126n (2008).
- 119 Felgenhauer, T., Bischoff, R. & Stadler, V. (German Cancer Research Center Heidelberg, 2010).
- 120 Oraevsky, A. N. Whispering-gallery waves. *Quantum Electron+* **32**, 377-400, doi:Doi 10.1070/Qe2002v032n05abeh002205 (2002).
- 121 Matsko, A. B. & Ilchenko, V. S. Optical resonators with whispering-gallery modes - Part I: Basics. *Ieee J Sel Top Quant* **12**, 3-14, doi:Doi 10.1109/Jstqe.2005.862952 (2006).

-
- 122 Weller, A. *Whispering Gallery Modes und Fabry-Perot Resonanzen in fluoreszenzten mikroskopischen Polystyrol-Kugeln* Diplom-Physiker thesis, of Heidelberg, (2005).
- 123 Caruso, F., Lichtenfeld, H., Donath, E. & Mohwald, H. Investigation of electrostatic interactions in polyelectrolyte multilayer films: Binding of anionic fluorescent probes to layers assembled onto colloids. *Macromolecules* **32**, 2317-2328 (1999).
- 124 Lourenco, J. M. C. *et al.* Counterions in poly(allylamine hydrochloride) and poly(styrene sulfonate) layer-by-layer films. *Langmuir* **20**, 8103-8109, doi:Doi 10.1021/La049872v (2004).
- 125 Clark, S. L., Montague, M. F. & Hammond, P. T. Ionic effects of sodium chloride on the templated deposition of polyelectrolytes using layer-by-layer ionic assembly. *Macromolecules* **30**, 7237-7244 (1997).

Acknowledgement

Firstly and most importantly, I thank my advisor Prof. Dr. Reiner Dahint. Without his kind supervision and constant support this thesis would not have been possible. In particular, I am grateful for the various scientific discussions we had during the last years.

I wish to express my gratitude to Prof. Dr. Michael Grunze for the opportunity to be a part of his research group, for the scientific discussion in the group seminar, and for providing us with all required surface analytical tools.

I am deeply grateful to Dr. Thomas Felgenhauer, who introduced me to the long peptide synthesis, for his help and support. I thank PD Dr. Frank Breitling, PD Dr. Ralf Bischoff, and Dr. Volker Stadler for the chance to use the peptide printer and all chemicals necessary for my research conducted at the “Chip-based peptide array” group of the DKFZ. I would like to thank Christopher Schirwitz for providing me helpful knowledge regarding the synthesis of the protein-resisting polymer layer. I thank Jürgen Kretschmer for sharing his lab space with me.

I am thankful to PD Dr. Michael Himmelhaus, who first introduced me to the nanoparticles-based research and evoked my interest in surface chemistry during my job as a part-time student in his research group. Also, I thank him for the guidance in my research related to the application of the WGM sensor.

I am indebted to my many colleagues for their support during my diploma and PhD theses. I would like to thank Georg Albert, the constant source of glass substrates for all of us. I am grateful to Vasili Stumpf, who assisted me in some time-crucial experiments. I thank Elka Trivela for introducing me to SEM, Dr. Xinyu Cao and Nikolaus Meyerbroker for the introduction to XPS and related software, Dr. Petra Bucker, Dr. Mario Beyer, and Andrea Seehuber for the helpful scientific discussions and advices during our group meetings.

I thank my old “roommates” from INF 229: Dr. Brett Andrzejewski, Dr. Xinyu Cao, Dominique Vereault, and Christina Leinweber for a nice time and for partially starting our PhD-journey together. I am grateful for sharing the lab/office with Haci Güvenc, Anna Grab, and specially Noha Waly in these last few years, with which I can always share and discuss any kind of problems.

I am grateful to my family, which has always been my source of strength and motivation. I thank both my sisters, who came and accompany me in this faraway country. I thank my parents, who always did their best in providing us with good education, ultimately giving me the opportunity to choose this academic path. For most I thank Christian, without his support I would never have come this far.

Disertasi S3 di jurusan Kimia Fisika ini Fanny persembahkan untuk Papa dan Mama tersayang.

Erklärungen gemäß § 8 (3) b) und c) der Promotionsordnung:

- (1) Ich erkläre hiermit, dass ich die vorgelegte Dissertation selbst verfasst und mich keiner anderen als der von mir ausdrücklich bezeichneten Quellen und Hilfen bedient habe.
- (2) Ich erkläre hiermit, dass ich an keiner anderen Stelle ein Prüfungsverfahren beantragt bzw. die Dissertation in dieser oder anderer Form bereits anderweitig als Prüfungsarbeit verwendet oder einer anderen Fakultät als Dissertation vorgelegt habe.

Heidelberg, den 16.12.2010

Fanny Caroline Liu.